



**University of
Nottingham**
UK | CHINA | MALAYSIA

**Modification and Characterisation of Superior
Nickel-rich Layered Oxide Cathodes for Advanced
Lithium-ion Batteries for EVs Application**

Thesis submitted to the University of Nottingham for the degree of
Doctor of Philosophy, January 2025.

Xiaoqing Zhang

20319301

Supervised by

Philip Hall

Zheng Wang

Yonggao Xia

Signature Xiaoqing Zhang

Date 12/01/2025

Abstract

Significant focus has been directed towards Ni-rich cathodes in lithium-ion batteries (LIBs) as they have been shown to become the sustainable electrodes for electric vehicles (EVs) applications. Particularly, Ni-rich layered oxides (NLO) cathodes with stoichiometric ratios of Ni \geq 80% have gained substantial attention due to their impressive high energy density. Nonetheless, NLO compounds suffer several crucial problems such as Li⁺/Ni²⁺ cation mixing, structural degradation, side reactions, and micro-cracks. These problems deteriorate the battery performance, especially at high current density and high voltage. This PhD research focused on modifying polycrystalline NLO to alleviate these crucial problems. To this end, a novel sol/antisolvent method with boron-related materials has been developed to modify the different NLO materials or their precursors. The underlying mechanisms of the modification effects by the proposed sol/antisolvent method for the superior NLO cathodes for EV applications have also been studied. First, a high initial Coulombic efficiency and ultra-stable mechanical integrity of LiNi_{0.85}Co_{0.1}Mn_{0.05}O₂ are achieved. This is mainly because the modification with crystalline LiBO₂ nanoparticle coating and nanorod wrapping on NLO can provide double protection against electrolytes. Second, the innovative design of a three-in-one effect incorporating radially aligned structure and amorphous LiBO₂ coating and B-doping on NLO has proven compelling. This strategy has enabled extremely high discharge capacity and excellent cycling stability in LiNi_{0.83}Co_{0.05}Mn_{0.12}O₂ materials. Third, the benefits of radially aligned structure and B-doping extend to the ultra-high Ni content materials such as LiNiO₂ with improved Li/Ni ordering, resulting in markedly superior capacity retentions compared to the well-formed and similar-sized single-crystal LiNiO₂. This work demonstrates the efficacy of utilizing novel sol/antisolvent treatment with boron-related materials in advancing NLO cathode development. The findings establish viable strategies for creating superior NLO cathodes for the rigorous demands of EV applications.

Acknowledgments

Hereon, I would like to express my deepest appreciation to my supervisors, Prof. Philip Hall, Prof. Zheng Wang, and Prof. Yonggao Xia for providing me the opportunity to undertake this PhD research. Their guidance and encouragement have always inspired me to promote the PhD research. Their holistic suggestions have helped me to think deeply from multiple perspectives during my research. Also, I would like to express my deep thanks to Prof. Ya-Jun Cheng, who provided many suggestions and discussions about the papers and problems related to organic materials.

I also thank Dr. Ishioma Egun, Dr. Qiang Guo, Dr. Zhepu Shi, Dr. Zihou Li, Dr. Qing Ji, Dr. Fatima Zhra Chafi, Dr. Yitao Zheng, Jianwei Xiong, Fengzhen Chang, Zhuijun Xu, Said Amzil, Hui Wang, Xiang Liu, Mengyuan Wang, Ruoxuan Qi, Bingying Zhu, Longhao Cao, Xiaoying Fan, Laihao Liu, Jiapei Li, Yiyao Xiao, Chenkun Li, Zhao Wang, Tonghui Xu, Liling Dai, Wanli Wei, Xuanting Wu, Mengmeng Wang, Yujiao Xie, and Shou Ding, these friends and colleagues in University of Nottingham Ningbo China (UNNC) and Ningbo Institute of Materials Technology and Engineering (CNITECH) of the Chinese Academy of Sciences (CAS) for their companionships, discussions, mutual assistance, resource and information sharing.

Lastly, I would like to express my special thanks to my husband Dr. Ning Tang, my two kids Yiru Tang and Yuzhu Tang, my parents Jing Zhang and Ping Zhang, and my parents-

in-law Xueliang Wen and Xingliang Tang for their understanding and support throughout the PhD journey.

Affirmation

The content of this thesis is the product of my own work. This thesis has not been previously submitted for any degree. The publications and conferences are listed below based on the research:

List of Publications:

1. X. Zhang, J. Xiong, F. Chang, Z. Xu, Z. Wang, P. Hall, Y. Cheng, Y. Xia, Sol/Antisolvent Coating for High Initial Coulombic Efficiency and Ultra-stable Mechanical Integrity of Ni-Rich Cathode Materials, ACS Applied Materials & Interfaces, 14, pp.45272-45288 (2022).
2. X. Zhang, S. Amzil, Z. Wang, P. Hall, Y. Cheng, Y. Xia, With the Intrinsic Daisy-like Precursor to Develop Extreme High-Capacity and High-Stability Ni-rich Cathode Material by the Boron-related Smooth and Dense Coating and Near-Surface Doping (Manuscript Preparation).

List of Conferences:

1. X. Zhang, J. Xiong, Z. Wang, P. Hall, Y. Cheng, Y. Xia., Antisolvent Coating Approach to Construction of High Initial Coulombic Efficiency and Ultra-stable Mechanical Integrity of Ni-rich Cathode Materials, 4th Annual FoSE PGR Research Showcase of the University of Nottingham Ningbo China, Poster Presentation, Ningbo 2022.

Content

Abstract	I
Acknowledgments	II
Affirmation	IV
List of Tables	IX
List of Figures	XI
List of Abbreviations	XXI
Chapter 1 Introduction	1
<i>1.1. Background Study</i>	<i>1</i>
1.1.1. Lithium-ion Battery from Prototype to Commercialization	1
1.1.2. Lithium-ion Battery Applications: Rapid Development in Electric Vehicles (EVs).....	12
1.1.3. LMO, LFP, NCA, and NCM Batteries.....	16
1.1.4. Ni-rich NCM: One of the Most Promising Cathode for EVs.....	20
<i>1.2. Significance and Originality of the Thesis</i>	<i>26</i>
Chapter 2 Literature Review	31
<i>2.1. Four Main Factors Responsible for the Decaying of Ni-Rich NCM</i>	<i>31</i>
2.1.1. Li ⁺ /Ni ²⁺ cation mixing	31
2.1.2. Surface Structural Degradation.....	36
2.1.3. Side Reactions	43
2.1.4. Micro-cracks	51
<i>2.2. Current Modification Strategy</i>	<i>56</i>
2.2.1. Coating of Ni-rich Cathode Materials for Lithium-ion Batteries.....	56
2.2.2. Doping of Ni-rich Cathode Materials for Lithium-ion Batteries.....	62
2.2.3. Beyond Doping and Coating Strategies of Ni-rich Cathode Materials for Lithium-ion	

Chapter 3 Materials and Equipment	71
3.1. <i>Materials and Experimental Equipment.....</i>	<i>71</i>
3.2. <i>Electrochemical Property Test Equipment and Material Characterisation Instruments.....</i>	<i>75</i>
Chapter 4 Sol/Antisolvent Coating with Crystalline LiBO₂ for LiNi_{0.85}Co_{0.1}Mn_{0.05}O₂ Cathode Towards High Initial Coulombic Efficiency and Ultra-stable Mechanical Integrity	81
4.1. <i>Introduction</i>	<i>81</i>
4.2. <i>Experimental Section.....</i>	<i>86</i>
4.2.1. Pristine NCM and LiBO ₂ powders.....	86
4.2.2. Synthesis of LiBO ₂ -coated NCM by Sol/Antisolvent Wet Coating.....	87
4.2.3. Materials Characterisation.....	91
4.2.4. Electrochemical Tests	92
4.3. <i>Results and Discussion</i>	<i>93</i>
4.3.1. Successful Synthesising of LiBO ₂ -coated NCM by Sol/Antisolvent Wet Coating	93
4.3.2. XRD, TEM, and AFM Tests	98
4.3.3. Improved Rate Capability and High Current Cycling Performance after LiBO ₂ Coating with Electrochemical Study.....	110
4.3.4. Comparison of SEI Chemical Composition and Micro-cracks of NCM and LiBO ₂ -coated NCM after Cycling.....	122
4.4. <i>Conclusion</i>	<i>128</i>
Chapter 5 Sol/Antisolvent Combined Coating and Doping with Boron-related Materials for LiNi_{0.83}Co_{0.05}Mn_{0.12}O₂ Cathode Towards High Capacity and High Cycling Stability	131
5.1. <i>Introduction</i>	<i>131</i>
5.2. <i>Experimental Section.....</i>	<i>136</i>
5.2.1. Ni-rich LiNi _{0.83} Co _{0.05} Mn _{0.12} O ₂ Cathode Material (Daisy-Ni83) Preparation.....	136
5.2.2. Synthesis of Boron-related Coating and Doping Modified Ni-rich LiNi _{0.83} Co _{0.05} Mn _{0.12} O ₂	

Cathode Material with Intrinsic Radially Aligned Microstructure	140
5.2.3. Electrochemical and Thermal Stability Tests of Daisy-Ni83, Daisy-Ni83-Bthin, Daisy-Ni83-Bmiddle, and Daisy-Ni83-Bthick	144
5.2.4. Material Composition and Microstructure Characterisation of Daisy-Ni83, Daisy-Ni83-Bthin, Daisy-Ni83-Bmiddle, and Daisy-Ni83-Bthick	146
5.3. <i>Results and Discussion</i>	147
5.3.1. Four Factors Determining the Optimal Lithiation Calcination Condition for Daisy-Ni83 147	
5.3.2. Greatly Developed Cycling Stability at Different Cut-off Voltages at 4.3 V and 4.5 V after the Treatment of the Combined Boron-related Coating and Doping with Intrinsic Radially Aligned Microstructure	163
5.3.3. Modification Mechanism of Daisy-Ni83-Bthin and Daisy-Ni83-Bmiddle with the Analysis of ICP-OES, XRD, SEM-EDS, TEM, and XPS	181
5.4. <i>Conclusion</i>	210
Chapter 6 Sol/Antisolvent with Boron Treating for the Modification of LiNiO₂ Cathode	213
6.1. <i>Introduction</i>	213
6.2. <i>Experimental Section</i>	215
6.2.1. LiNiO ₂ , LiNiO ₂ -less B, and LiNiO ₂ -more B preparation	215
6.2.2. Electrochemical Tests and Material Characterisation	217
6.3. <i>Results and Discussion</i>	218
6.3.1. Electrochemical Performances of LiNiO ₂ , LiNiO ₂ -less B, and LiNiO ₂ -more B	218
6.3.2. Exploring the Origin of Different Electrochemical Performances for LiNiO ₂ , LiNiO ₂ -less B, and LiNiO ₂ -more B	237
6.4. <i>Conclusion</i>	247

Chapter 7 Conclusions and Prospects.....	249
7.1. <i>Conclusions</i>	249
7.2. <i>Prospects</i>	253
Bibliography.....	255

List of Tables

Table 1. 1. A pathway for realising the commercialization of LIBs.	11
Table 1. 2. Li-ion battery market in GWh/y, past development and future perspectives (Zubi et al., 2018).	14
Table 3. 1. Materials and reagents used in the study.	72
Table 3. 2. Main material characterisation instruments used in this study.	79
Table 4. 1. Crystal structure parameters of original NCM and LiBO ₂ -coated NCM.....	100
Table 4. 2. Surface morphology and mechanical parameters of NCM, 1b-NCM, and 2b-NCM by AFM	106
Table 4. 3. Young's modulus of NCM811, α -LiBO ₂ and γ -LiBO ₂	107
Table 4. 4. List of advantages of sol/antisolvent wet coating.....	108
Table 4. 5. Improvement of initial Coulombic efficiency of NLO by coating	116
Table 4. 6. Li-ion diffusion coefficients of NCM and LiBO ₂ -coated NCM by Randles-Sevcik equation	121
Table 5. 1. Maximum discharge capacity of each cathode material at 0.2, 0.5, and 1 C in the voltage range of 2.8 to 4.3 V synthesised at different calcination temperatures with 5% mole excess LiOH·H ₂ O.	149
Table 5. 2. I(003)/I(104) intensity ratios of XRD data to indicate the degree of Li/Ni disordering for LiNi _{0.83} Co _{0.05} Mn _{0.12} O ₂ cathode materials synthesised at 720 °C, 750 °C and 780 °C with 5% mole excess LiOH·H ₂ O.	155
Table 5. 3. Summary of 1 st cycle, 100 th cycle, and last cycle discharge capacity for different current density cycling in 2.8-4.3 V and 2.8-4.5 V (Initial 10 cycles performance at 0.1 C is also shown.).....	170
Table 5. 4. Electrochemical performance comparison between this work and other people's reports. .	177
Table 5. 5. ICP-OES analysis of Daisy-Ni83, Daisy-Ni83-Bthin, Daisy-Ni83-Bmiddle, and Daisy-Ni83- Bthick.	182
Table 5. 6. The intensity ratio of I(003)/I(104) for each active material	188
Table 6. 1. Summary of the initial discharge capacity, the last cycle discharge capacity, and the capacity retention with full cycles at 0.3 C in 2.8-4.3 V, 2.8-4.5 V, and 2.8-4.6 V for pristine LiNiO ₂ , LiNiO ₂ -	

less B, and LiNiO ₂ -more B.....	221
Table 6. 2. I(003)/I(104) ratio of pristine LiNiO ₂ , LiNiO ₂ -less B, and LiNiO ₂ -more B.....	239

List of Figures

Figure 1. 1. Possible classification of cathode reactions (Whittingham, 1976b).	3
Figure 1. 2. Oxides with lower p-orbital energy than sulphides (Manthiram, 2020).	5
Figure 1. 3. Cell construction of cylindrical type LIB (Zubi et al., 2018).	7
Figure 1. 4. Schematic of the configuration of rechargeable LIB with (C/LiCoO ₂) system (Liu et al., 2016).	8
Figure 1. 5. Broad application of LIBs (Ding et al., 2019, Liang et al., 2019).	12
Figure 1. 6. Illustration of an electric vehicle with no tailpipe emission (Konarov et al., 2017).	13
Figure 1. 7. Leading materials in LIB market from 1995 to 2016 and forecast to 2025 (Yoshino, 2014, Li et al., 2018).	15
Figure 1. 8. The global plug-in electric vehicles market share from 2010 to 2020 (Irle, 2021).	15
Figure 1. 9. Relationship between potential and capacity for electrode materials (Kanno, 2006, Osiak et al., 2014).	17
Figure 1. 10. Multi-dimension estimation of four main LIBs technologies for EVs (Ding et al., 2019).	18
Figure 1. 11. Different cathode materials with different voltages and capacity profiles (Markevich et al., 2019).	19
Figure 1. 12. Comparison of charge and discharge curves of NCM cathodes and LiCoO ₂ (Markevich et al., 2019).	22
Figure 1. 13. (a) Phase diagram of LiNiO ₂ , LiCoO ₂ , and LiMnO ₂ ; (b) Layered structure of Ni-rich NCM compound (Susai et al., 2018, Li et al., 2020b).	23
Figure 1. 14. Share of total LIBs for EVs by battery type from 2018 to 2040 with the prediction (Mitchell, 2020).	25
Figure 1. 15. Cathode shares in LIB markets based on installed GWh (Celine Buechel, 2021).	26
Figure 1. 16. Fundamental characteristics of NCM materials on the correlation of performance and safety with Ni content (Noh et al., 2013).	27
Figure 2. 1. TM-O octahedral complexes in NCM: (a) Ni, Mn, and Co reside at the octahedral site surrounded by six O atoms; (b) Local view of the TM-O octahedral complexes (Sun and Zhao, 2017).	32
Figure 2. 2. Schematic diagram of local collapse of inter-slab space due to Li ⁺ /Ni ²⁺ cation mixing during	

charging-discharging (Manthiram et al., 2017).....	33
Figure 2. 3. XRD patterns of LiNi _{0.8} Co _{0.1} Mn _{0.1} O ₂ : (a) with Li excess of 0%, (b) Li excess of 10%, and (c) Li excess of 20% (Wu et al., 2015).....	34
Figure 2. 4. 2D XANES mapping showing the Ni ³⁺ concentration of NCM (LiNi _{0.8} Co _{0.1} Mn _{0.1} O ₂) particles after cycling. (The colour scheme indicates the percentage of Ni ³⁺ : Ni ³⁺ / (Ni ³⁺ + Ni ²⁺)) (Yang et al., 2019).....	34
Figure 2. 5. Illustration of structural transformation in layered lithium metal oxides with cation disorder: (a) Well-ordered R$\bar{3}m$ structure; (b) The cation mixing phase with Fm$\bar{3}m$ structure; (c) R$\bar{3}m$ structure with Li vacancies in highly charged state; (d) Partially cation mixed phase with TM ions in Li slab (Liu et al., 2015).	37
Figure 2. 6. (a) First charge and discharge voltage curves of a NCM811/Li half-cell; and (b) The corresponding differential capacity (dQ/dV) plot (Märker et al., 2019).....	38
Figure 2. 7. Illustration of the phase change with Li/vacancy ordering for Li _x NiO ₂ with identification of different phases (Delmas et al., 1999, Bianchini et al., 2019).	40
Figure 2. 8. High-resolution synchrotron radiation diffraction analysis of N85CM cathodes during the first cycling process (Lai et al., 2020).....	41
Figure 2. 9. dQ/dV curves of three different NMC/graphite cells recorded at 0.1 C-rate (3 rd cycle) (Jung et al., 2017).....	42
Figure 2. 10. Surface reaction of Ni-rich materials in air (Cho et al., 2014).....	44
Figure 2. 11. Formation of the SEI layer after cycling of the Ni-rich cathode material in liquid electrolyte (Liu et al., 2015).	45
Figure 2. 12. Cell voltage vs. time of a NCM811-graphite cell over four charge/discharge cycles at 0.2 C and 25°C between 2.6 and 4.8 V, in a cell containing 400 μ L of 1.5 M LiPF ₆ in ethylene carbonate, glass fiber separators and 16.40 mg NCM811 (The corresponding gas analysis is shown below, the dashed lines stem from the graphite electrode) (Jung et al., 2017).....	49
Figure 2. 13. Mass spectroscopy profiles for the oxygen collected simultaneously during the measurement of in situ time-resolved X-ray diffraction and the corresponding temperature region of the phase transitions for NMC samples (Bak et al., 2014).	50
Figure 2. 14. Images of crack inside a NCM622 sample after 150 charge-discharge cycles (Kim et al., 2015).....	52

Figure 2. 15. Image of uncycled a NLO primary and secondary particles. The white dashed line delineates the boundary of a primary particle (Liu et al., 2017).....	53
Figure 2. 16. Schematic illustration of micro-crack growth and structural deterioration of a Ni-rich layered oxide cathode($\text{LiNi}_{0.76}\text{Co}_{0.14}\text{Al}_{0.70}\text{O}_2$) with different DOD cycling (Watanabe et al., 2014).....	54
Figure 2. 17. Mechanical property calculation of NCM811 under the boundary condition of tensile and compressive deformation based on density functional theory: (a) Directions where the tensile and compressive deformation is applied for the in-plane and out-of-plane; (b) Stress-strain curves for NCM811 under tensile and compressive deformation in both in- and out-of-plane directions (Min and Cho, 2018).	55
Figure 2. 18. Challenges and requirements of surface coatings for cathode materials (Nisar et al., 2021).	57
Figure 2. 19. Schematic diagram of four different coating processes:(a) Co-precipitation; (b) Sol-gel; (c) Dry coating; and (d) Chemical vapor deposition (CVD) (Zuo et al., 2017).	59
Figure 2. 20. Diagram of the design and synthesis of hybrid nanomembrane-encapsulated NCM cathode materials (Li et al., 2016).....	61
Figure 2. 21. Discharge capacities of NCM811 electrodes comprising undoped and doped active materials, in coin cells at 45°C (Weigel et al., 2019).	63
Figure 2. 22. Atomic configurations for the structure of (a) LiMO_2 , where M=transition metals (Ni, Co, and Mn), and the schematic structures for each of the defects, (b) Li vacancies (V_{Li}), (c) oxygen vacancy (V_{O}), (d) excess Ni (Ni_{Li}), (e) Li/Ni exchange ($\text{Li}_{\text{Ni}}-\text{Ni}_{\text{Li}}$), and (f) Ni migration (Ni^{mig}) (Min et al., 2017).....	65
Figure 2. 23. Strategies beyond doping and coating for improving the electrochemical performance of Ni-rich cathode materials: (a) Core-shell structure (Wu et al., 2019b); (b) Full concentration gradient structure (Lim et al., 2016); (c) Single-crystalline structure (Deng et al., 2022); (d) The refined radially aligned structure (Park et al., 2018).....	67
Figure 2. 24. (a) Li-ion diffusion pathways inside the randomly orientated primary particles and the radially aligned primary particles (Lee et al., 2019); (b) Differences in the local stress concentration and stress distribution among the secondary particles consisting of randomly oriented, radially oriented, and size-refined radially oriented particles (Ryu et al., 2020).	69
Figure 3. 1. BEQ horizontal high-temperature tubular furnace.....	74

Figure 3. 2. WZM 1.5 L double-tank ball mill machine.....	74
Figure 3. 3. MBRAUN UNI-lab glove box workstation.....	75
Figure 3. 4. Coin cell assembly showing each component.....	76
Figure 3. 5. Solartron Analytical 1400 cell test station.	77
Figure 3. 6. Wuhan LAND cell test system: left is the LANHE CT3002A system with 8 channels; right is the real test image.	77
Figure 4. 1. Design mechanism of the sol/antisolvent method in anhydrous environment for coating...	85
Figure 4. 2. Particle size distribution of $\text{LiNi}_{0.85}\text{Co}_{0.1}\text{Mn}_{0.05}\text{O}_2$ (NCM) powders.	87
Figure 4. 3. Schematic diagram of combined sol/antisolvent wet coating NCM with nano- LiBO_2 : First, NCM powder was mixed in LiBO_2 ethanol sol, followed by pumping THF as an antisolvent for depositing LiBO_2 on the NCM surface.	88
Figure 4. 4. Pictures of “Tyndall effect” of prepared LiBO_2 ethanol sol.....	90
Figure 4. 5. (a) No clear scattering of light on the irradiation of laser beam in sol after settlement for three and a half days; (b) Stronger scattering of light through the colloidal particles after adding THF into the upper LiBO_2 ethanol sol.....	91
Figure 4. 6. SEM images: (a) pristine NCM, (b) 1b-NCM, (c) 2b-NCM, (d-f) bandage-like nanorod wrapping the outmost layer of 1b-NCM; and EDS mapping of Ni, Co, Mn, O and B elements: (g-k) 1b-NCM.....	94
Figure 4. 7. SEM images of enlarged nanorods comprising tiny LiBO_2 nanoparticle aggregates.	96
Figure 4. 8. Lamella-shaped coating in sol/antisolvent method by using LiBO_2 ethanol sol placed for over fifteen days.	98
Figure 4. 9. XRD patterns and Rietveld refinement results of samples: (a) pristine NCM; (b) LiBO_2 -coated NCM.	99
Figure 4. 10. HRTEM images and corresponding FFT patterns for (a) pristine NCM; (b and c) LiBO_2 -coated NCM.....	101
Figure 4. 11. TG-DSC curves of samples at 30-820 °C at a heating rate of 10 °C/min in an argon atmosphere: (a) NCM powder and (b) LiBO_2 powder.	102
Figure 4. 12. The enlarged HRTEM image of LiBO_2 -coated NCM shows the phase transformation from the layered phase into the rock-salt phase with a purple curve indicating the boundary between the rock-salt phase and the LiBO_2 coating.....	103

Figure 4. 13. Selected regions of the XRD patterns of the pristine NCM and LiBO ₂ -coated NCM are shown in Figure 4. 9.	104
Figure 4. 14. AFM images and mechanical properties of the surface of NCM, 1b-NCM, and 2b-NCM by AFM.	105
Figure 4. 15. FTIR absorption spectra of LiBO ₂ , NCM, and LiBO ₂ -coated NCM.	109
Figure 4. 16. XRD pattern of the LiBO ₂ sample.	109
Figure 4. 17. Detailed electrochemical performance test data of NCM and LiBO ₂ -coated NCM:(a) Rate performances; (b) Cycling performances at 3 C between 2.8-4.3 V; (c and d) First cycle charge/discharge profiles from panel b at 0.2, 0.5, 1, 2, and 3 C, respectively; (e and f) dQ dV ⁻¹ curves at selected cycles of 1 st and 5 th cycle at 2 C, 1 st , 33 rd and 55 th cycle at 3 C; (g and h) First cycle charge-discharge characteristic curves showing improvement of ICE, and the corresponding dQ dV ⁻¹ curves.	112
Figure 4. 18. (a) Cycling performances of NCM and LiBO ₂ -coated NCM within the voltage range of 2.8-4.3 V at 1 C; (b and c) dQ dV ⁻¹ curves at selected cycles of 3 rd cycle and 10 th cycle at 0.2 C (Black is NCM, red is LiBO ₂ -coated NCM).	115
Figure 4. 19. CV curves of (a) NCM, (b) LiBO ₂ -coated NCM at varied scan rates within the voltage range of 2.8-4.3 V; (c) Corresponding plots for I_p vs $v^{1/2}$	121
Figure 4. 20. XPS survey scan of (a) NCM, (b) LiBO ₂ -coated NCM (the black line represents uncycled samples, the red line represents samples after 3 C cycling).	122
Figure 4. 21. XPS spectra of samples after 3 C cycling: (a, c) C 1s, O 1s of NCM; (b, d) C 1s, O 1s of LiBO ₂ -coated NCM; (e, g, and i) F 1s, P 2p and Li 1s of NCM; (f, h and j) F 1s, P 2p and Li 1s of LiBO ₂ -coated NCM; (k) The chemical composition ratio for CEI species in the interfacial layers (the atomic concentrations of C, O, F, P, and Li for different samples are listed).	123
Figure 4. 22. FIB-SEM characterisation of cathode electrodes made by NCM and LiBO ₂ -coated NCM after cycling.	126
Figure 5. 1. SEM morphologies of the precursor Ni _{0.83} Co _{0.05} Mn _{0.12} (OH) ₂ : (a and b) spherical-shape precursor, (c) a picture of daisy, (d, e, and f) cross-section images of precursor at different magnifications.	137
Figure 5. 2. XRD spectrum of the hydroxide precursor Ni _{0.83} Co _{0.05} Mn _{0.12} (OH) ₂	138
Figure 5. 3. XRD patterns of LiOH·H ₂ O after different drying treatments.	139

Figure 5. 4. XRD pattern of B ₂ O ₃ after milling.....	141
Figure 5. 5. Schematic diagram of the synthesis of the combined boron-related coating and doping-modified LiNi _{0.83} Co _{0.05} Mn _{0.12} O ₂ based on the intrinsic refined microstructure of daisy-like cross-section.....	142
Figure 5. 6. Transparent B ₂ O ₃ ethanol sol with the light scattering by laser beam.	144
Figure 5. 7. 1 C cycling performances of LiNi _{0.83} Co _{0.05} Mn _{0.12} O ₂ cathode materials synthesised at 720, 750, and 780 °C with 5% mole excess LiOH·H ₂ O between 2.8-4.3 V.	148
Figure 5. 8. 0.2 C cycling performances of LiNi _{0.83} Co _{0.05} Mn _{0.12} O ₂ cathode material synthesised at 780 °C with 5% mole excess LiOH·H ₂ O in the voltage range of 2.8-4.3 V and 2.8-4.5 V.....	149
Figure 5. 9. SEM images on the surface of the original Ni _{0.83} Co _{0.05} Mn _{0.12} (OH) ₂ precursor and LiNi _{0.83} Co _{0.05} Mn _{0.12} O ₂ cathode materials synthesised at different temperatures with 5% mole excess LiOH·H ₂ O: (a1-a3) precursor, (b1-b3) cathode material synthesised at 720 °C, (c1-c3) cathode material synthesised at 750 °C, (d1-d3) cathode material synthesised at 780 °C.....	151
Figure 5. 10. SEM images on the cross-section of the original Ni _{0.83} Co _{0.05} Mn _{0.12} (OH) ₂ precursor and LiNi _{0.83} Co _{0.05} Mn _{0.12} O ₂ cathode materials synthesised at different temperatures with 5% mole excess LiOH·H ₂ O: (a1-a2) precursor, (b1-b2) cathode materials synthesised at 720 °C, (c1-c2) cathode materials synthesised at 750 °C, (d1-d2) cathode materials synthesised at 780 °C (the red dashed boxes on the left are magnified as shown on the right).....	153
Figure 5. 11. XRD patterns of LiNi _{0.83} Co _{0.05} Mn _{0.12} O ₂ cathode materials synthesised at different temperatures with 5% mole excess LiOH·H ₂ O. the gray line represents 720 °C, the green line represents 750 °C, and the purple line represents 780 °C.	155
Figure 5. 12. XRD patterns of LiNi _{0.83} Co _{0.05} Mn _{0.12} O ₂ cathode material synthesised at 810 °C with 5% mole excess LiOH·H ₂ O (SEM images of such cathode material are inserted).....	156
Figure 5. 13. 0.2 C cycling performances of LiNi _{0.83} Co _{0.05} Mn _{0.12} O ₂ cathode material synthesised at 800 °C with 2% mole excess LiOH·H ₂ O (Daisy-Ni83) in the voltage range of 2.8-4.3 V and 2.8-4.5 V.	158
Figure 5. 14. XRD patterns of LiNi _{0.83} Co _{0.05} Mn _{0.12} O ₂ cathode material synthesised at 800 °C with 2% mole excess LiOH·H ₂ O (Daisy-Ni83).	158
Figure 5. 15. SEM images of LiNi _{0.83} Co _{0.05} Mn _{0.12} O ₂ cathode material synthesised at 800 °C with 2% mole excess LiOH·H ₂ O (Daisy-Ni83): (a1-a4) surface images at different magnifications, (b1-b4) cutaway images with an oblique angle, (c1-c4) cross-section images of a plane perpendicular to the	

sphere.....	160
Figure 5. 16. 0.2 C longer cycling performances of $\text{LiNi}_{0.83}\text{Co}_{0.05}\text{Mn}_{0.12}\text{O}_2$ synthesised at 800 °C with 2% mole excess $\text{LiOH}\cdot\text{H}_2\text{O}$ (Daisy-Ni83) in the voltage range of 2.8-4.3 V and 2.8-4.5 V (Charge/discharge curves within 2.8-4.3 V are inserted).....	162
Figure 5. 17. Cycling performance comparison of Daisy-Ni83, Daisy-Ni83-Bthin, Daisy-Ni83-Bmiddle, and Daisy-Ni83-Bthick: (a) 1 C cycling between 2.8-4.3 V; (b) 0.5 C cycling between 2.8-4.3 V; (c) 0.2 C cycling between 2.8-4.3 V; (d) 0.2 C cycling between 2.8-4.5 V.....	164
Figure 5. 18. First cycle electrochemical curves comparison for Daisy-Ni83, Daisy-Ni83-Bthin, Daisy-Ni83-Bmiddle, and Daisy-Ni83-Bthick: (a and b) charge/discharge profiles at 0.1 C for the cut-off voltage at 4.3 V and 4.5 V, respectively; (c and d) the corresponding dQ/dV curves at 0.1 C for the cut-off voltage at 4.3 V and 4.5 V, respectively.	167
Figure 5. 19. The histogram of capacity retention for Daisy-Ni83, Daisy-Ni83-Bthin, Daisy-Ni83-Bmiddle, and Daisy-Ni83-Bthick: (a-d) full cycles capacity retention at 1 C, 0.5 C, 0.2 C in 2.8-4.3 V and at 0.2 C in 2.8-4.5 V, respectively; (e-h) 100 cycles capacity retention at 1 C, 0.5 C, 0.2 C in 2.8-4.3 V and at 0.2 C in 2.8-4.5 V, respectively.	172
Figure 5. 20. (a, b) Charge/discharge profiles of Daisy-Ni83 and Daisy-Ni83-Bmiddle for 1 C cycling between 2.8-4.3 V from Figure 5. 17. Cycling performance comparison of Daisy-Ni83, Daisy-Ni83-Bthin, Daisy-Ni83-Bmiddle, and Daisy-Ni83-Bthick: (a) 1 C cycling between 2.8-4.3 V; (b) 0.5 C cycling between 2.8-4.3 V; (c) 0.2 C cycling between 2.8-4.3 V; (d) 0.2 C cycling between 2.8-4.5 V involving the 1 st cycle at 0.2 C, 11 th cycle at 0.5 C, and 16 th , 30 th , 60 th , 90 th , 120 th , 150 th cycle at 1 C. (c, d) Corresponding dQ/dV^{-1} curves of Daisy-Ni83 and Daisy-Ni83-Bmiddle for 1 C cycling between 2.8-4.3 V. (e) Rate performances of all samples between 2.8-4.3 V. (f) 3 C cycling performances of all samples in the voltage range of 2.8-4.3 V.....	173
Figure 5. 21. (a) EIS test results of Daisy-Ni83, Daisy-Ni83-Bthin, Daisy-Ni83-Bmiddle, and Daisy-Ni83-Bthick with Nyquist plots and fitting data; (b) Warburg plot used to calculate Li-ion diffusion coefficient; (c) the corresponding diffusion coefficients of Li-ion in each cathode material.....	179
Figure 5. 22. SEM images of different precursors and the corresponding cathode material of Daisy-Ni83(a1-a6), Daisy-Ni83-Bthin(b1-b6), Daisy-Ni83-Bmiddle(c1-c6), and Daisy-Ni83-Bthick(d1-d6) at different magnifications. (The large-sized B_2O_3 particles on the precursor of Daisy-Ni83-Bthick are circled by the yellow dotted lines.)	184

Figure 5. 23. Enlarged SEM image of the precursor of Daisy-Ni83-Bthick.	185
Figure 5. 24. XRD diffraction patterns of cathode material of Daisy-Ni83, Daisy-Ni83-Bthin, Daisy-Ni83-Bmiddle, and Daisy-Ni83-Bthick with high power Bruker D8 ADVANCE.	188
Figure 5. 25. Amplifications of selected 2-Theta regions from Figure 5. 24.	190
Figure 5. 26. EDS mapping of O, Ni, Mn, Co, and B elements for B-thin precursor, Daisy-Ni83-Bthin, and Daisy-Ni83-Bmiddle.	192
Figure 5. 27. TEM images of cathode material: (a1 and a2) Daisy-Ni83; (b1 and b2) Daisy-Ni83-Bthin, panel b2 is the enlarged image from the area in the green circled part shown in panel b1.	197
Figure 5. 28. TEM images of cathode material of Daisy-Ni83-Bmiddle: (a) the spherical secondary particle of Daisy-Ni83-Bmiddle with high-resolution TEM image; (b, c, and d) enlarged images for the local areas indicated as “I”, “II”, and “III” of the spherical particle in panel (a).	198
Figure 5. 29. EDS analysis on the coating layer and the near-surface area for cathode material of Daisy-Ni83-Bthin (The analysis area is at position “1” marketed in Figure 5. 27. TEM images of cathode material: (a1 and a2) Daisy-Ni83; (b1 and b2) Daisy-Ni83-Bthin, panel b2 is the enlarged image from the area in the green circled part shown in panel b1.).	200
Figure 5. 30. EDS compositional maps of the Ni, Co, Mn, O, and B elements for a secondary particle of Daisy-Ni83-Bthin from Figure 5. 27. TEM images of cathode material: (a1 and a2) Daisy-Ni83; (b1 and b2) Daisy-Ni83-Bthin, panel b2 is the enlarged image from the area in the green circled part shown in panel b1.	201
Figure 5. 31. B 1s peaks at XPS spectrum of cathode material powders: (a) Daisy-Ni83; (b) Daisy-Ni83-Bthin; (c) Daisy-Ni83-Bmiddle; and (d) Daisy-Ni83-Bthick.	202
Figure 5. 32. TEM images of Daisy-Ni83 and Daisy-Ni83-Bmiddle particles at different magnifications after the total 150 cycles at 1 C with the initial 10 cycles at 0.2 C and 5 cycles at 0.5 C between 2.8-4.3 V: (a1-a4) Daisy-Ni83 and (b1-b4) Daisy-Ni83-Bmiddle with complete coating.	204
Figure 5. 33. XPS C 1s, F 1s, P 2p, and Ni 2p spectra of the cathode electrode after 150 cycles at 1 C with the initial 10 cycles at 0.2 C and 5 cycles at 0.5 C between 2.8-4.3 V: (a-d) Daisy-Ni83 and (e-h) Daisy-Ni83-Bmiddle.	207
Figure 5. 34. DSC curves of the cathode powders in fully delithiated states at a scanning rate of 1°C/min in nitrogen atmosphere: (a) Daisy-Ni83(NoB), (b) Daisy-Ni83-Bthin(B-thin), (c) Daisy-Ni83-Bmiddle (B-middle), and (d) Daisy-Ni83-Bthick(B-thick).	208

Figure 6. 1. SEM images of Ni(OH) ₂ precursor at different magnifications: (a) various sized spherical secondary particles; (b) a high degree of roundness for a secondary particle; and (c, d) cross-sectional observations at different angles with a picture of Ni(OH) ₂ powder in a bottle inserted in panel (d).	217
Figure 6. 2. 0.3 C cycling performances of pristine LiNiO ₂ , LiNiO ₂ -less B, and LiNiO ₂ -more B at different cut-off voltages: (a) the voltage range of 2.8-4.3 V, (b) the voltage range of 2.8-4.5 V, and (c) the voltage range of 2.8-4.6 V.....	220
Figure 6. 3. Discharge capacity and Coulombic efficiency as a function of the cycle number from 2.7-4.3 V (a), and from 2.7-4.6 V (b) for the well-formed and similar-sized SC-LNO (Kim et al., 2022).	226
Figure 6. 4. Combined cycling data of LiNiO ₂ -more B and the well-formed and similar-sized SC-LNO: (a) with a cut-off voltage of 4.3 V, (b) with a cut-off voltage of 4.6 V.....	226
Figure 6. 5. The first and second cycles charge/discharge profiles of all samples at 0.1 C in 2.8-4.3 V(a), 2.8-4.5 V(b), and 2.8-4.6 V(c) from Figure 6. 2 and the corresponding dQ/dV curves at 0.1 C in 2.8-4.3 V for pristine LiNiO ₂ (d), LiNiO ₂ -less B(e), and LiNiO ₂ -more B(f).	228
Figure 6. 6. The dQ/dV curves at 0.1 C in 2.8-4.5 V and 2.8-4.6 V: (a, d) pristine LiNiO ₂ ; (b, e) LiNiO ₂ -less B, and (c, f) LiNiO ₂ -more B.	229
Figure 6. 7. (a) Rate performances of pristine LiNiO ₂ , LiNiO ₂ -less B, and LiNiO ₂ -more B between 2.8-4.3 V; (b) Rate performances of pristine LiNiO ₂ , LiNiO ₂ -less B, and LiNiO ₂ -more B between 2.8-4.5 V; (c) Charge/discharge curves at 0.01 C, 0.02 C, and 0.1 C between 2.8-4.3 V for pristine LiNiO ₂ ; (d) Charge/discharge curves at 0.01 C, 0.02 C, and 0.1 C between 2.8-4.3 V for LiNiO ₂ -more B.	235
Figure 6. 8. XRD patterns of (a) pristine LiNiO ₂ , (b) LiNiO ₂ -less B, (c) LiNiO ₂ -more B, and (d) enlarged XRD patterns of all LNO samples in 2-Theta ranges of 37° to 39° and 63° to 66°.....	238
Figure 6. 9. SEM images: (a1-a3) surface images of pristine LiNiO ₂ at different magnifications; (b1-b3) surface images of LiNiO ₂ -less B at different magnifications; (c1-c3) surface images of LiNiO ₂ -more B at different magnifications; and (d1-d3) surface images of Ni(OH) ₂ precursor at different magnifications.	244
Figure 6. 10. SEM images: (a1-a2) cross-section images of pristine LiNiO ₂ at different magnifications; (b1-b2) cross-section images of LiNiO ₂ -less B at different magnifications; (c1-c2) cross-section	

images of LiNiO_2 -more B at different magnifications; and (d1-d2) cross-section images of Ni(OH)_2 precursor at different magnifications. 245

Figure 6. 11. The cracked particles after 0.3 C cycling of LNO cathode: (a1, a2) pristine LiNiO_2 at the cut-off voltage of 4.3 V and 4.5 V; (b1, b2) LiNiO_2 -less B at the cut-off voltage of 4.3 V and 4.5 V; (c1, c2, c3) LiNiO_2 -more B at the cut-off voltage of 4.3 V, 4.5 V and 4.6 V. 246

List of Abbreviations

AFM	Atomic Force Microscope
BEVs	Battery-Electric Vehicles
C	Carbon Materials
CVD	Chemical Vapor Deposition
CV	Cyclic Voltammetry
CEI	Cathode-Electrolyte Interphase
DOD	Degree-of-Discharge
DSC	Differential Scanning Calorimetry
DSC-TG	Differential Scanning Calorimetry and Thermogravimetric Analyser
DMC	Dimethyl Carbonate
EVs	Electric Vehicles
EC	Ethylene Carbonate
EDS	Energy Dispersive X-ray Spectroscopy
EIS	Electrochemical Impedance Spectroscopy
FIB	Focused Ion Beam
FTIR	Fourier Transform Infrared Spectrometer
GCPL	Galvanostatic Cycling with the Potential Limitation
HEV	Hybrid Electric Vehicles
H	Hexagonal Structure
ICP-OES	Inductively Coupled Plasma Optical Emission Spectrometer
ICE	Initial Coulombic Efficiency
LIBs	Lithium-ion Batteries
Li-ion	Lithium ion
LCO	LiCoO ₂
LMO	LiMn ₂ O ₄
LFP	LiFePO ₄
LNO	LiNiO ₂
M	Monoclinic Structure.
NLO	Ni-rich Layered Oxides

NCA	$\text{Li}(\text{Ni}_x\text{Co}_y\text{Al}_z)\text{O}_2$ ($x+y+z=1$)
NCM	$\text{Li}(\text{Ni}_x\text{Co}_y\text{Mn}_z)\text{O}_2$ ($x+y+z=1$)
NMC	$\text{Li}(\text{Ni}_x\text{Mn}_y\text{Co}_z)\text{O}_2$ ($x+y+z=1$)
NCM111	$\text{LiNi}_{1/3}\text{Co}_{1/3}\text{Mn}_{1/3}\text{O}_2$
NCM523	$\text{LiNi}_{0.5}\text{Co}_{0.2}\text{Mn}_{0.3}\text{O}_2$
NCM622	$\text{LiNi}_{0.6}\text{Co}_{0.2}\text{Mn}_{0.2}\text{O}_2$
NCM811	$\text{LiNi}_{0.8}\text{Co}_{0.1}\text{Mn}_{0.1}\text{O}_2$
NMP	N-Methyl Pyrrolidone
PHEVs	Plug-in Hybrid Electric Vehicles
PC	Personal Computer
PVDF	Polyvinylidene Fluoride
PC-NLO	Polycrystalline Ni-rich Layered Oxides
R_s	Electrolyte Resistance
R_{ct}	Charge Transfer Resistance
SEI	Solid Electrolyte Interface
SEM	Scanning Electron Microscope
SAED	Selected Area Electron Diffraction
SOC	State of Charge
SC-NLO	Single-Crystalline Ni-Rich Layered Oxides
SC-LNO	Single-Crystal LiNiO_2
TR-XRD	Time-Resolved X-ray Diffraction
TEM	Transmission Electron Microscope
THF	Tetrahydrofuran
TM	Transition Metal
XANES	X-ray Absorption Near Edge Structure
XPS	X-ray Photoelectron Spectroscopy
XRD	X-ray Diffraction

Chapter 1 Introduction

This chapter reports the background study of the thesis, it includes a review of the development of lithium-ion battery (LIB) from prototype to commercialization, the study of LIBs undergoing rapid development in EVs application in recent years, the comparison of four main LIBs technologies for EVs, and the characteristic description of Ni-rich NCM as one of the most promising cathodes for EVs. The significance and originality of the thesis are described subsequently. The purpose is to recall the historical background of LIBs and to figure out the relationship between LIBs and Ni-rich layered oxide cathodes for the EVs application.

1.1. Background Study

1.1.1. Lithium-ion Battery from Prototype to Commercialization

Since the commercialization of LIBs by Sony in 1991, LIBs have been fully integrated into our daily lives (He et al., 2023). The applications of LIBs become more and more diverse including electric cars, power tools, medical devices, smart watches, drones, satellites, and utility-scale storage (Grey and Hall, 2020). Before the introduction of Ni-rich layered oxide cathodes in LIBs for EVs application, it is necessary to understand LIBs as electrochemical energy storage devices. The history of LIBs from prototype to commercialization is first studied. It is found that the discovery of new materials can result in the development of the energy density of LIBs. Adopting carbon materials as

the anode can solve the safety problems encountered by the commercialization of LIBs. To help the readers know the important criteria for evaluating LIBs, the theoretical capacity and energy density of LIBs are calculated, which are the fundamental limits for the different LIB systems (Grey and Hall, 2020).

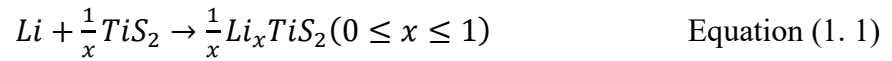
1.1.1.1. First Generation of Lithium-ion Battery

The prototype of LIBs was invented by M. Stanley Whittingham in 1976, worked in Exxon Research and Engineering Company, USA, he demonstrated the first lithium-based rechargeable battery (Li/TiS₂) system based on intercalation chemistry (Manthiram, 2020, Whittingham, 1976b, Whittingham, 1976a). Compared with first practical rechargeable batteries (lead-acid batteries), which was invented in 1859 by French scientist Gaston Planté and used as the power for a three-wheeled electric vehicle in 1881 (Kurzweil, 2010), the lithium titanium disulfide (Li_xTiS₂) battery system processes completely different cell reactions, due to the substances undergoing redox reactions was completely changed.

Whittingham's idea was inspired by the new superconductors of layered dichalcogenides of the transition metal atoms from groups IVB and VB in the periodic table reported in 1971 by F.R. GAMBLE etc. (Gamble et al., 1971, Cairns and Shimotake, 1969). In this first lithium-based rechargeable battery, lithium was used as the anode, TiS₂ as the cathode, and lithium hexafluorophosphate in propylene carbonate as the electrolyte to construct the Li/TiS₂ battery system. Lithium was intercalated into TiS₂ lattice during discharge, then extracted from TiS₂ electrode during charge. The

reversibility of this Li/TiS₂ system had been confirmed after 1100 times cycling at 4 mA (Whittingham, 1976a).

The ternary phases with the layered structure were formed by an intercalation reaction in this Li/TiS₂ battery system as shown below:



The topochemical method was adopted in Whittingham's work to analyse this cathode reaction in cells as shown in **Figure 1. 1**.

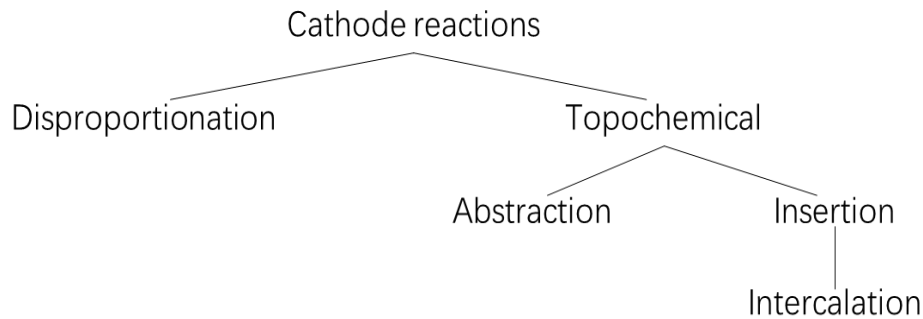


Figure 1. 1. Possible classification of cathode reactions (Whittingham, 1976b).

Based on the topochemical reaction of the cathode, the electrochemical reaction of layered TiS₂ with Li in the discharge/charge process occurs very rapidly and reversibly at ambient temperature. The existence of a non-stoichiometry ternary compound was further demonstrated by using Li⁷ nuclear magnetic resonance (Silbernagel and Whittingham, 1976).

The experimental energy density of Li/TiS₂ battery was found to be 480 Wh/kg (Whittingham, 1976a). The theoretical energy density E_d of Li/TiS₂ system can be calculated by the following calculation equations:

$$\Delta G = -nFE = -1 \times 96500 \times 2.5 = -241250 \text{ J/mol} = -241.25 \text{ KJ/mol} =$$

$$-67.01 \text{ Wh/mole} \quad \text{Equation (1. 2)}$$

$$E_d = \frac{\Delta G}{M_w} = \frac{67.01 \text{ Wh}}{0.11893 \text{ kg}} = 563.44 \text{ Wh/kg} \quad \text{Equation (1. 3)}$$

where ΔG is free energy change during discharge in KJ/mol, n is the corresponding mole electron transfer in mole, F is the Faraday's constant 96500 C/mol, E is the cell electromotive force as a reference in V, E_d is theoretical specific energy per mass in Wh/kg, M_w is the molecular weight of reactants in g/mol. The above equations are also applicable for calculating the theoretical energy densities of other battery systems.

Because of the advantages of smaller molecular weight and relatively higher cell electromotive force, the theoretical energy density of Li/TiS₂ battery is twice the theoretical energy density of Pb/PbO₂ lead-acid battery (246.18 Wh/kg with the electromotive force- E of 2.05 V) (Gong et al., 2015). However, due to the intrinsic safety concerns of internal short circuits triggered by lithium needles and dendrites with long branching structures during the recharging process, the first generation of rechargeable lithium-ion batteries (Li/TiS₂ system) had not been commercialized (Yan et al., 2020).

1.1.1.2. Discovery of LiCoO₂

According to Equation (1. 2) and Equation (1. 3) for calculating the energy density of the battery system, we know that higher electromotive force, more electron transfer, and smaller molecular weight of reactants can enhance the energy density. Higher energy density is favored for many different application scenarios. Ever since the invention of Li/TiS₂ battery system, researchers intended to develop a positive electrode (cathode)

with a layered structure, that has a larger energy density than Li_xTiS_2 battery. Based on the fundamental understanding that metal oxides have lower p-orbital energy than their corresponding sulphides, therefore increasing the cell voltage (**Figure 1. 2**), and knowing that lithium ion (Li-ion) may be mobile in solid electrolytes, J.B. GOODENOUGH etc. were enlightened in 1980 to speculate that close-packed oxygen arrays might be suitable for the mobility of Li-ions (Mizushima et al., 1980, Mizushima et al., 1981).

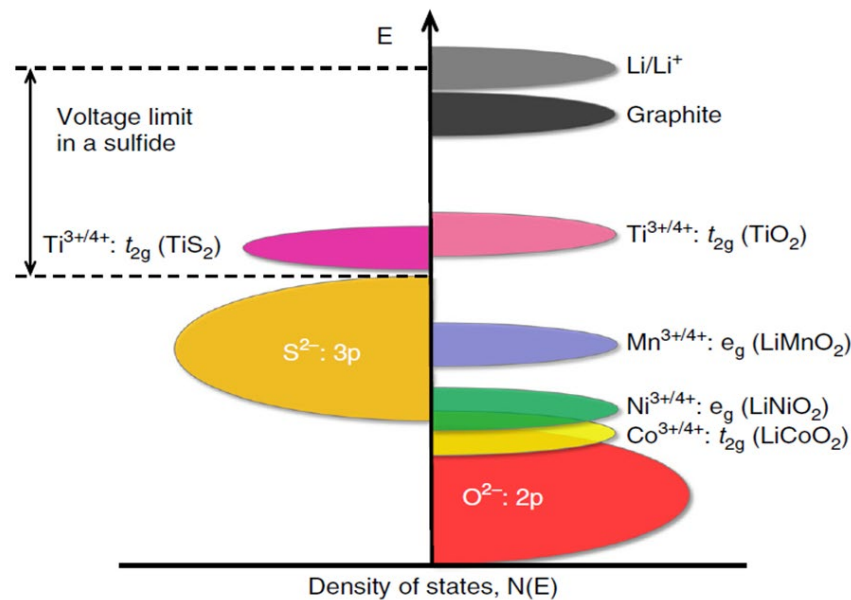


Figure 1. 2. Oxides with lower p-orbital energy than sulphides (Manthiram, 2020).

Based on the above hypothesis, transition-metal lithium oxides LiMO_2 were considered to crystallise in a layered structure. During the cell reaction, MO_2 phase with the layered structure would be generated through the removal of Li-ions from a high-voltage cell. Several transition-metal, V-Vanadium, Cr-Chromium, Co-Cobalt, and Ni-Nickel lithium oxides LiMO_2 were investigated. Results showed that LiCoO_2 is the most promising material for higher Li-ion mobilities (Mizushima et al., 1980, Mizushima et al., 1981).

Three factors were considered accounting for the superior property of LiCoO₂: (a) Li-ion diffusion becomes easier due to the larger space between oxygen layers facing the Li layer in LiCoO₂ than in the other LiMO₂ oxides, benefiting from the smaller ionic size of Co³⁺ (i.e. 0.545 Å for Co³⁺, 0.56 Å for Ni³⁺, 0.615 Å for V³⁺, 0.64 Å for Cr³⁺) (Shannon, 1976); (b) The oxygen layers are strongly polarised towards cobalt layers due to the low-spin state of Co(IV)/Co(III), which guarantees the stability of layered structure; (c) Cobalt and lithium ions existing in alternate layers in LiCoO₂ with good ordering, while the corresponding nickel compound would suffer from disordering.

Both the cell electromotive force and the theoretical energy density are much higher for Li/Li_xCoO₂ (0 ≤ x ≤ 1) system than for Li/Li_xTiS₂ system, with the value of 4 V and 1095.55 Wh/kg, respectively (Whittingham, 1976a, Mizushima et al., 1981). Energy density was enhanced from Li/Li_xTiS₂ system with the E_d of about 563 Wh/kg to Li/Li_xCoO₂ (0 ≤ x ≤ 1) system with the E_d of about 1100 Wh/kg. It can be concluded that the discovery of LiCoO₂ is a key milestone towards the practical application of lithium-ion batteries.

1.1.1.3. Commercialization of Lithium-ion Battery

Using lithium metal as an anode would trigger serious battery safety issues due to its high reactivity, low melting temperature and combustion (Brandt, 1994, Yang et al., 2024). Until Japanese scientist Yoshio Nishi considered using carbonaceous materials as anode for the electrochemical intercalation of lithium, LIBs had eventually achieved commercialization with their high energy density, high cycling stability, and good safety

(Yoshino, 2013, Ozawa, 1994). The first commercial model of LIB is C/LiCoO₂ system, C represents different kinds of carbon like the graphitizable carbon and the non-graphitizable carbon. Such C/LiCoO₂ battery system with a cylindrical construction was first put into use for the portable telephone by Sony Corporation in 1991, using lithium salt LiPF₆ dissolved in propylene carbonate as the electrolyte (Ozawa, 1994). An image of the cylindrical type LIB is shown in **Figure 1. 3**.

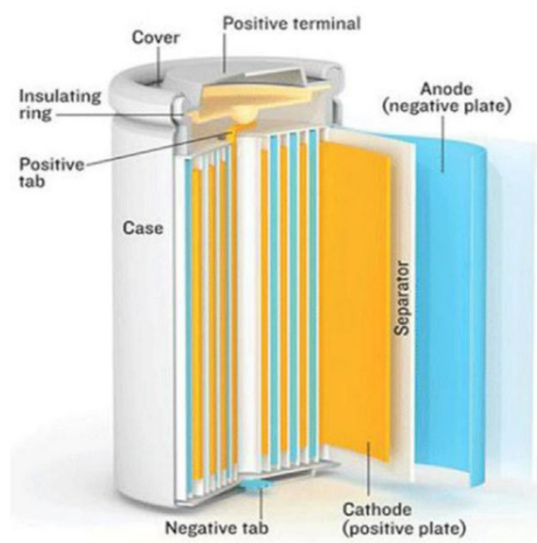


Figure 1. 3. Cell construction of cylindrical type LIB (Zubi et al., 2018).

In this first commercial model of (C/LiCoO₂) LIB system, both anode (C) and cathode (LiCoO₂) active components are layered materials, as illustrated in **Figure 1. 4**. During the charging and discharging process, lithium ions move back and forth between these two electrodes. Meanwhile, the electrons move in the opposite direction in the external circuit. Li ions are charge carriers in LIBs. Therefore, the capacity of the battery is directly proportional to the amount of Li ions that move between the cathode and anode through the electrolyte.

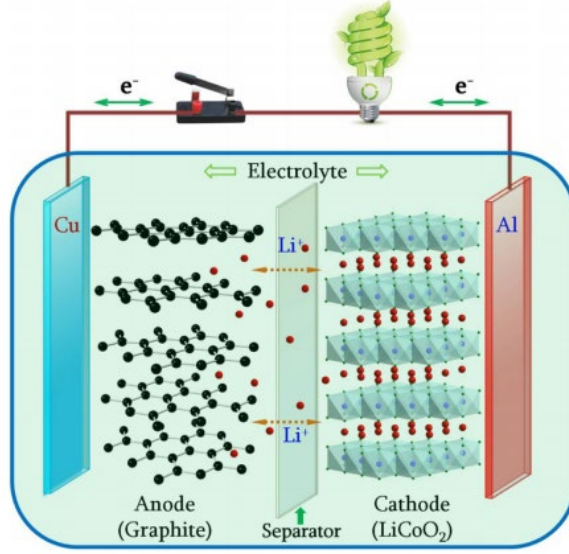
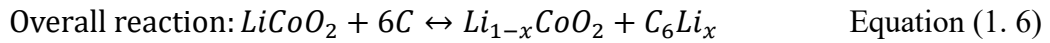
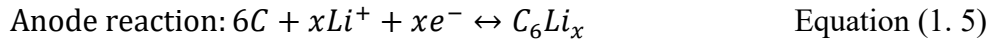
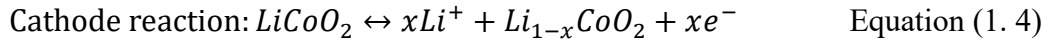


Figure 1. 4. Schematic of the configuration of rechargeable LIB with (C/LiCoO₂) system (Liu et al., 2016).

Different from the cell reactions of Li/LiCoO₂ battery system, the detailed cell reactions of C/LiCoO₂ battery system are shown below (Sun, 2015):



According to the above overall reaction of Equation (1. 6) and Equation (1. 2) and Equation (1. 3), and choosing electromotive force of 4.3 V (Konarov et al., 2017), the theoretical energy density of C/LiCoO₂ lithium-ion battery can be calculated to be 678.30 Wh/kg, higher than Li/TiS₂ system (563.44 Wh/kg) but lower than Li/LiCoO₂ system (1095.55 Wh/kg).

In addition, a simple estimation of theoretical energy density E_d can be shown below from a viewpoint of physical principle:

$$E_d = E_{nV} \times C_{sp} \quad \text{Equation (1. 7)}$$

where, E_{nV} is the nominal voltage of cell in V , C_{sp} is the theoretical specific capacity of the cell in mAh/g. The theoretical capacity of any material is given by:

$$C = nF \quad \text{Equation (1. 8)}$$

C represents capacity in mAh/g; n is the number of electrons exchanged; F is the Faraday's constant 96500 C/mol.

Concerning the cathode of LiCoO_2 :

$$C_{sp/c} = \frac{nF}{3.6 \times MW} = 273.89 \text{ mAh/g} \quad \text{Equation (1. 9)}$$

Concerning the anode of carbon:

$$C_{sp/a} = \frac{nF}{3.6 \times MW} = 371.99 \text{ mAh/g} \quad \text{Equation (1. 10)}$$

For C/ LiCoO_2 battery system, the cathode capacity is lower than the anode capacity. It means that the cell capacity of LIB (C/ LiCoO_2 system) is primarily determined by the cathode material.

It is worth mentioning that, considering the safety issue and longer life expectancy of LIBs for commercial application, the lower nominal voltage is applied. Therefore, the practical energy density is much lower than the above-calculated theoretical energy density. For example, the nominal voltage (voltage that the cell will exhibit through most of its discharge (Mikolajczak et al., 2011)) for a 18650 cell is 3.6 V, which is lower than the voltage (larger than 4.2 V) before the loss of oxygen for LiCoO_2 during charging (Tarascon and Armand, 2001), which is lower than the voltage before the start of oxygen loss during charging (Venkatraman et al., 2003). The practical energy density of 18650 C/ LiCoO_2 LIB is calculated based on the nominal voltage together with the corresponding molar electron transfer of 0.5 moles per redox reaction of Equation (1. 6)

to be 283.94 Wh/kg. The practical capacity of LiCoO_2 is limited to 136.95 mAh/g, only half of the theoretical capacity of 273.89 mAh/g.

Table 1. 1 summarises a pathway for realising the commercialization of LIBs. In short, the emergence of the first practical rechargeable battery Pb/PbO₂ system in 1859 is the first commercial model of energy conversions between chemical energy and electrical energy for energy storage and conversion application. Then in 1976, the prototype of the Li/TiS₂ LIB system appeared. The idea of TiS₂ as cathode was ignited by the new superconductors of layered dichalcogenides of the transition metals of groups IVB and VB in the periodic table. At the year of 1980, oxides replaced sulphides as cathode of LIB by Li/LiCoO₂ system resulting in larger cell voltage. While in the last stage of realising the successful commercialization of LIBs, the carbonous material was used as anode constructing C/LiCoO₂ system to host lithium for solving the intrinsic unsafety issues triggered by the lithium anode at the year of 1991.

The theoretical energy density of rechargeable battery had been developed from about 246 wh/kg for lead-acid battery to nearly 1100 wh/kg for Li/LiCoO₂ LIB battery. Because of the milestone contribution from M. Stanley Whittingham, J.B. Goodenough, and Yoshio Nishi, these three researchers won the Nobel Chemistry Prize in 2019 for the development of LIBs.

It can be concluded that each science and technology process is based on discoveries. Meanwhile, because of continuous development, LIBs have become fully integrated into our daily lives used in almost all portable electronic devices as mobile power source, making fossil fuels obsolete become possible. Undoubtedly, the review of the history of

LIB from prototype to commercialization can inspire thinking about the way to improve the promising Ni-rich layered oxides cathodes for LIBs for EVs application. Beyond the layered oxide cathodes like LiCoO_2 and LiNiO_2 , the spinel oxide cathodes like LiMn_2O_4 and polyanion oxide cathodes like LiFePO_4 were also explored from the 1980s to 1990s (Manthiram, 2020). Since the 1980s, the layered oxide cathodes have evolved with the substitution of Mn to give $\text{LiNi}_x\text{Co}_y\text{Mn}_z\text{O}_2$ and Al to give $\text{LiNi}_x\text{Co}_y\text{Al}_z\text{O}_2$ ($x+y+z=1$) (Manthiram and Goodenough, 2021).

Table 1. 1. A pathway for realising the commercialization of LIBs.

Year	Anode/ Cathode	Electromotive Force- E (V)	Theoretical- E_d (Wh/kg)	Inventors	Stage of LIB Commercialization
1859	Pb/PbO ₂	2.05	246	French scientist: Gaston Planté	Emerge of the first practical rechargeable battery in the world
1976	Li/TiS ₂	2.5	563	USA scientist: M. Stanley Whittingham	Prototype of LIB
1980	Li/LiCO ₂	4	1100	Japan & UK Scientists: K.Mizushima, J.B. Goodenough etc.	Oxides replaced sulphides as the cathode of LIB
1991	C/LiCoO ₂	4.3	678	Japan scientists: Yoshio Nishi, etc.	Commercialization of LIB by Sony corporation

1.1.2. Lithium-ion Battery Applications: Rapid Development in Electric Vehicles (EVs)

There are five main types of commercial LIBs, which use LiCoO_2 , LiMn_2O_4 , LiFePO_4 , $\text{Li}(\text{Ni}_x\text{Co}_y\text{Al}_z)\text{O}_2$, and $\text{Li}(\text{Ni}_x\text{Co}_y\text{Mn}_z)\text{O}_2$, ($x+y+z=1$) as cathode material, those batteries are referred to as LCO, LMO, LFP, NCA, and NCM batteries respectively. The numerous demands of LIBs originate from the stimulation of the information technology revolution and environmental & energy technology innovation revolution. The applications are broadened from consumer electronics & devices, to the new market of electric vehicles, like plug-in hybrid electric vehicles (PHEVs) and battery-electric vehicles (BEVs), as well as energy storage systems, such as integration with renewable energy resources to balance power generation and utilization (**Figure 1. 5**) (Ding et al., 2019, Liang et al., 2019).

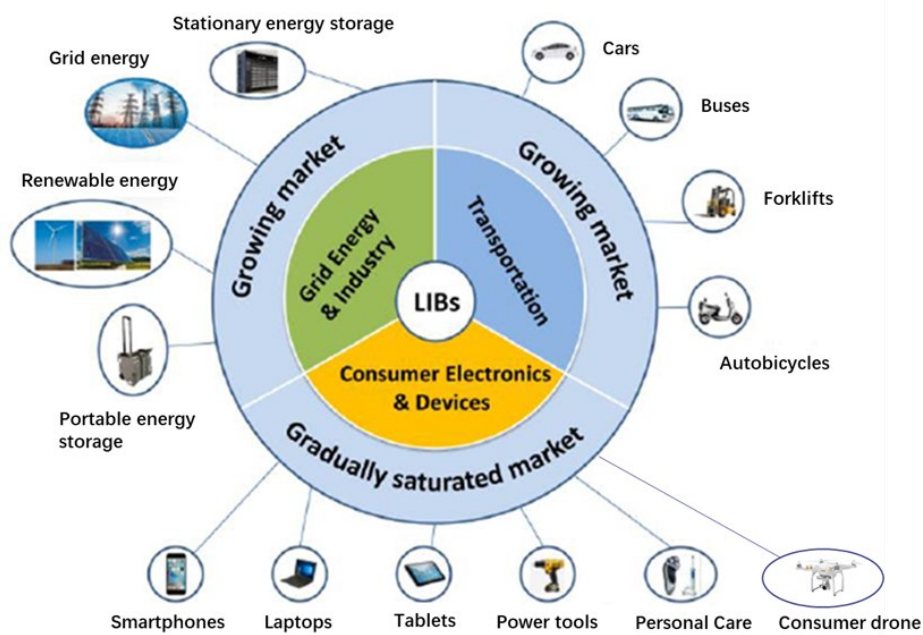


Figure 1. 5. Broad application of LIBs (Ding et al., 2019, Liang et al., 2019).

LIBs-based EVs have achieved fast development under the green philosophy as shown in **Figure 1. 6** with zero tailpipe emissions during running. Especially in urban areas, the toxic emissions from vehicles with internal combustion engines can be significantly reduced by the transport of EVs (Aijaz and Ahmad, 2022). Although vehicle electrification may increase air pollution damages in regions with high shares of coal-fired power plants, the development of clean electricity grids could be conducive to low damages from EVs in both climate change and air pollution (Tong and Azevedo, 2020).



Figure 1. 6. Illustration of an electric vehicle with no tailpipe emission (Konarov et al., 2017).

Table 1. 2 shows the LIBs market demand with the past development and future perspectives. Before 2015, LIBs demand for portable electronic devices occupied the main market. Wherein, in 2020, LIB demand for road-transport reached over 1.5 times than that of portable electronics with a capacity of 76 GWh, and would increase to 245 GWh in 2030, taking up to about 63% of the total LIBs demand. The total Li-ion battery market in GWh/y grows quickly after 2015, which is consistent with the growing market

of LIBs leading materials as shown in **Figure 1. 7**. The leading materials involve LMO, LCO, LFP, NCA, and NCM. Leading materials in LIB market grew dramatically from the 650 t in 1995 to 45,000 t in 2010, then 180,000 t in 2016, and it was predicted would reach 400,000 t in 2025. Wherein, LMO, LFP, NCA, and NCM (also written as NMC) batteries are mainly used for EVs, because of their advantages of more stable crystal structures, material abundance and lower cost compared to LCO (Ding et al., 2019). The percentage of LMO, LFP, NCA, and NCM has significantly increased from a small percentage in 1995 to about 50 % in 2010, almost 80 % in 2016, and is predicted to reach 84 % in 2025.

Table 1. 2. Li-ion battery market in GWh/y, past development and future perspectives (Zubi et al., 2018).

	2010	2015	2020	2025	2030
Cell phones	6	11	17	28	44
Tablets	1	7	12	17	25
PC	12	9	9	9	11
Portable electronics, other	3	4	7	12	20
Portable electronics, total	21	31	45	66	100
EV	0	11	65	115	200
PHEV	0	2	8	13	25
HEV	0	0	2	7	15
Road-transport, other	0	0	1	2	5
Road-transport, total	0	13	76	137	245
Storage in power supply	0	0	2	10	30
Other applications	1	1	2	7	15
Total	22	45	125	220	390

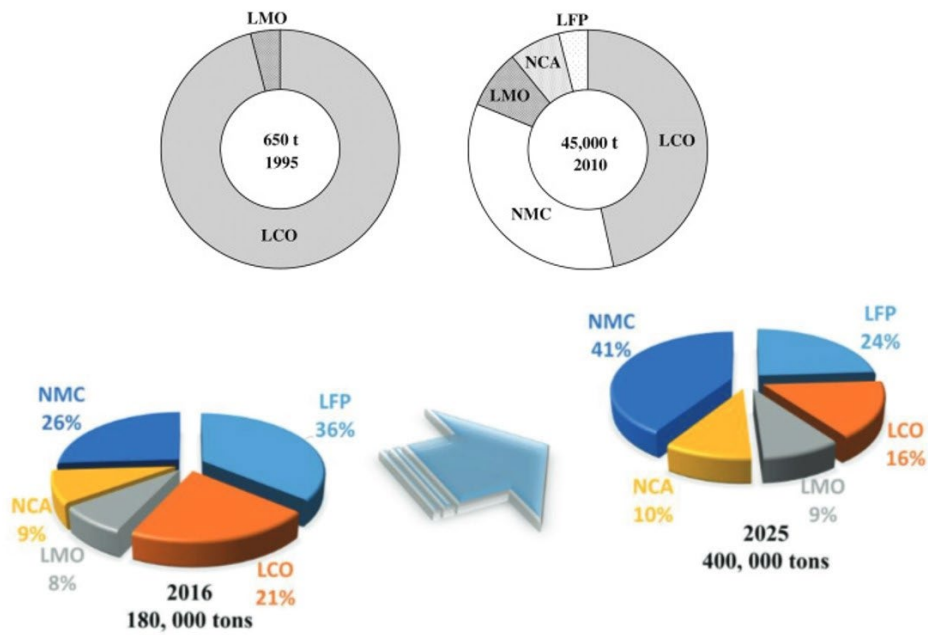


Figure 1. 7. Leading materials in LIB market from 1995 to 2016 and forecast to 2025 (Yoshino, 2014, Li et al., 2018).

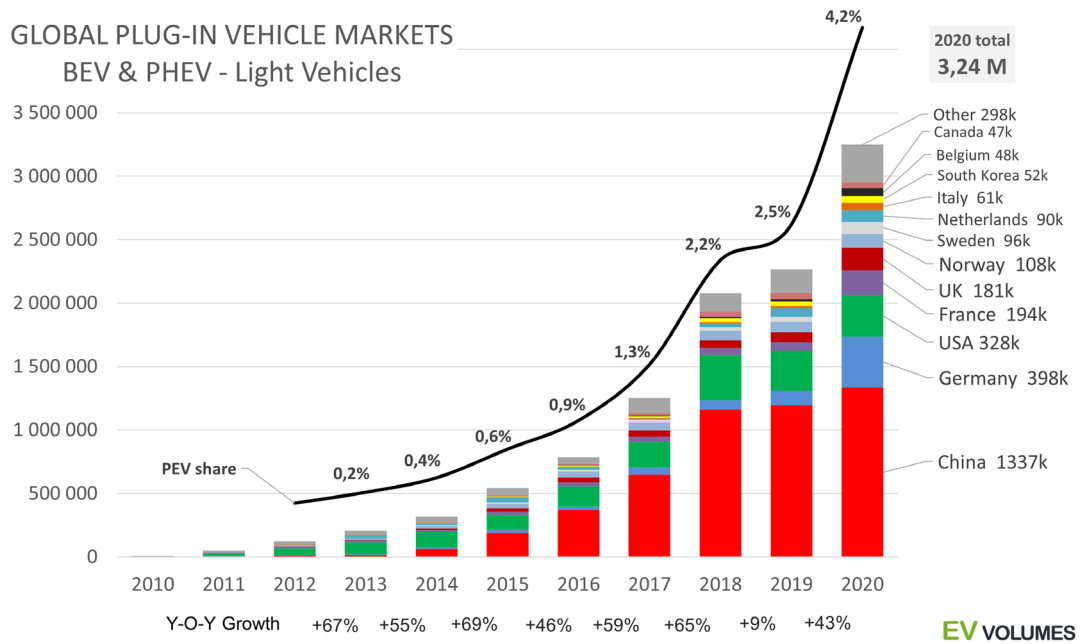


Figure 1. 8. The global plug-in electric vehicles market share from 2010 to 2020 (Irl, 2021).

Figure 1. 8 presents the global plug-in vehicle market share from 2010 to 2020 (Irle, 2021). Among different countries, China gains the greatest achievement, and occupied the largest plug-in EVs market size from 2016 to 2020, together with an increasing trend. According to the latest report on the development of global LIBs in GWh in 2023, global LIBs manufacturing grows much quicker than the previously predicted data (Sugumaran and Amutha Prabha, 2023). The previous expectations for 2025 with a 220 GWh LIB market as shown in **Table 1. 2** have already been exceeded in 2020 with a 250 GWh LIB market (Sugumaran and Amutha Prabha, 2023). Since such a good development momentum, the new expectation of the global LIB market in 2030 will reach 2000 GWh (Sugumaran and Amutha Prabha, 2023), which is about five times the predicted data in 2018. There is also a higher expectation from 259 to 2500 GWh within the years 2020-2030 with an average growth of 25.4 percent per year (Wu et al., 2022). The drastically rising demand for EVs has led to the enormous growth of LIB demand (Qiao et al., 2021).

1.1.3. LMO, LFP, NCA, and NCM Batteries

Figure 1. 9 represents the relationship between the potential and capacity of electrode materials (Kanno, 2006, Osiak et al., 2014). It is very useful to learn about the materials used for LIBs and to understand the function of electrodes in LIBs. As shown in **Figure 1. 9**, the positive electrode (i.e. cathode) is a metal oxide with high potential vs Li/Li⁺ compared with negative electrode (i.e. anode). The negative electrode varies from carbon material, nitrides, and silicon alloy to lithium metal. The battery potential is the

electric potential difference between the positive electrode and the negative electrode. From **Figure 1. 9**, it can be detected that the cathode material is the major determinant of battery performance, because it offers a much lower capacity than anode material does. The charging and discharging capacities of batteries are limited by the cathode material. So, the naming principle for LIBs is after the cathode material (Chen et al., 2020).

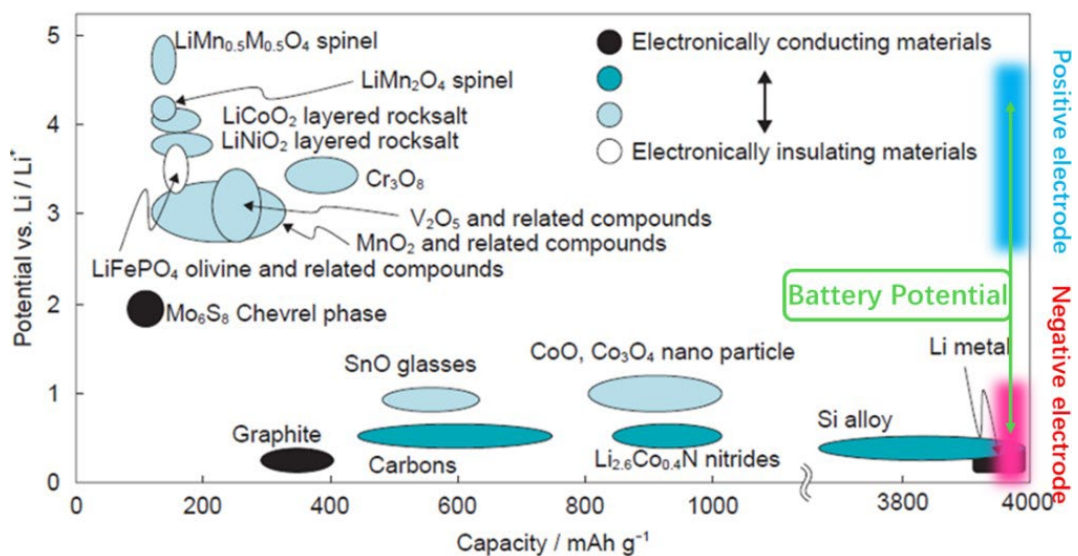


Figure 1. 9. Relationship between potential and capacity for electrode materials (Kanno, 2006, Osiak et al., 2014).

Five aspects of battery technology are compared for the conventional EVs-used LIBs, including energy density, power density, safety, cost, and life span for these four main LIBs (LFP, LMO, NCA, and NCM) in **Figure 1. 10** (Ding et al., 2019). LFP batteries provide the highest safety standard and longest lifetime, while NCA and NMC provide the highest energy density, and LMO exhibits a moderate level for each aspect. LFP and NCM batteries dominate the Chinese market for EV applications (Sybil Pan, 2023).

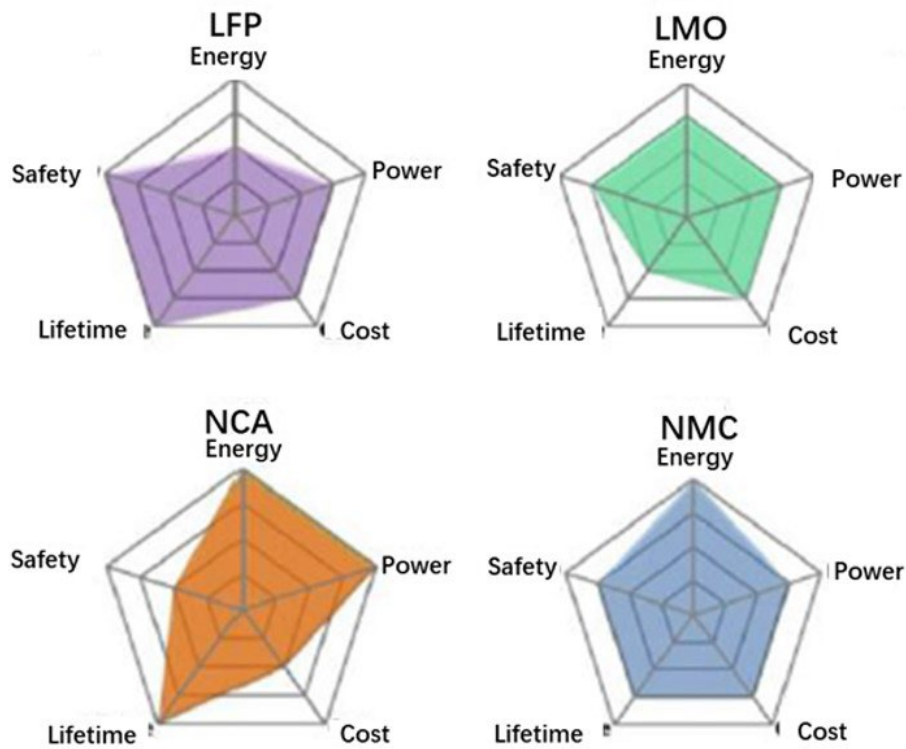


Figure 1. 10. Multi-dimension estimation of four main LIBs technologies for EVs (Ding et al., 2019).

The crystal structures of each cathode material together with the different voltages and capacity profiles are shown in **Figure 1. 11** (Markevich et al., 2019). Theoretically, the amount of energy that a battery can supply corresponds to the area under the discharge curve. The energy difference among LFP, LMO, and NCM (or named NMC) batteries, as shown in **Figure 1. 10**, can be easily comprehended by comparing the areas under the different discharge curves as shown in **Figure 1. 11**. Meanwhile, the discharge curve is strongly related to operating conditions like the C-rate and operating temperature (Shepard, 2021). The NCM in **Figure 1. 11** is referred to the compound $\text{LiNi}_{0.33}\text{Co}_{0.33}\text{Mn}_{0.33}\text{O}_2$.

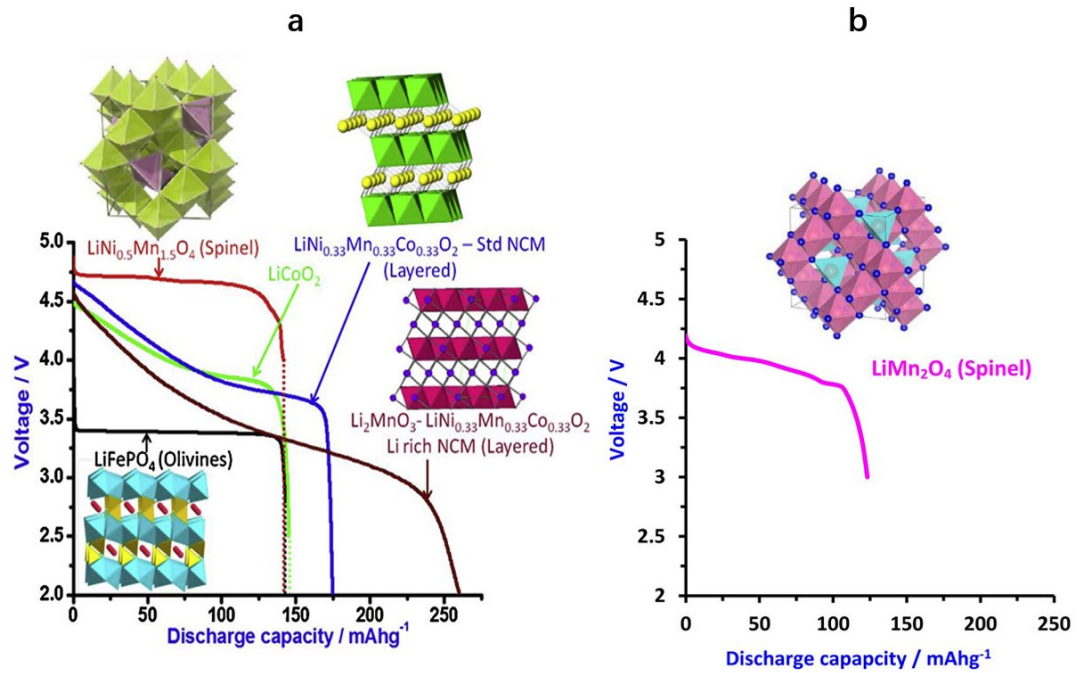


Figure 1. 11. Different cathode materials with different voltages and capacity profiles (Markevich et al., 2019).

Inside LIBs, lithium ions are shuttled between the cathode and anode while electrons move in the opposite direction through the external wire to accomplish the electrochemical process. The performance of LIBs can be simulated based on the pseudo-two-dimensional mechanism model, which is composed of the Li-ion mass transfer equations (Fick diffusion equations), potential equations (Ohm's law), and electrochemical reaction equations at the solid-liquid interface (Butler Volmer equation) (Zhang et al., 2020). Therefore, the Li-ion diffusion rate can be considered as an important factor affecting the battery performance. Each cathode material has its unique Li-ion transport pathway accompanied by corresponding activation energy (Julien et al., 2014, Manthiram, 2020).

In general, LMO is spinel oxide with high thermodynamic stability and high voltage.

LMO is characterised by the stable crystal structure, and fast Li-ion conductivity due to the three-dimensional Li-ion diffusion pathway, but the lowest theoretical capacity among LFP, LMO, NCA, and NCM due to the highest molecular weight as shown in **Figure 1. 11**. LFP is polyanion oxide with a stable olivine structure, wherein, all oxygens are strongly covalently bonded to P^{5+} to form the $(PO_4)^{3-}$ tetrahedral polyanion thus difficult to extract. LFP also holds a low theoretical capacity, and the electronic conductivity is the poorest among the four main LIBs technologies for EVs, due to LFP containing iron cations with just one oxidation state (2^+ or 3^+ for lithiation/delithiation, respectively), moreover, ionic conductivity is also the lowest due to only one-dimensional Li-ion diffusion pathway. NCA and NCM show the advantages of high theoretical capacity and high operating voltage, and exhibit relatively fast Li-ion conductivity due to the two-dimensional Li-ion diffusion pathway. However, the drawback of NCA and NCM batteries is that cobalt is expensive, scarce, and thermally unstable (Manthiram, 2020, Wang et al., 2019b).

1.1.4. Ni-rich NCM: One of the Most Promising Cathode for EVs

1.1.4.1. Advantage on both Specific Capacity and Operating Voltage for Ni-rich NCM in Comparison with Li/Mn-rich Cathodes

‘Range anxiety’ and ‘Charging time anxiety’ are the main barriers for EVs to compete with internal combustion engine vehicles (Li et al., 2020c, Chakraborty et al., 2022).

Lots of attention has been paid to new cathode materials with higher specific capacities and higher operating voltage. One of them is $\text{LiNi}_{0.5}\text{Mn}_{1.5}\text{O}_4$ spinel. It is a Mn-rich cathode, whose redox potential is around 4.8 V versus Li/Li^+ , but the theoretical capacity is only up to 147 mAh/g (Markevich et al., 2019). And such $\text{LiNi}_{0.5}\text{Mn}_{1.5}\text{O}_4$ battery requires a high-voltage resisting electrolyte (Roth, 2012). Another cathode material is Li-rich NCM the two-phase material of Li_2MnO_3 and LiTMO_2 (TM = Ni, Co, Mn), formally known as $x\text{Li}_2\text{MnO}_3 \cdot (1-x)\text{LiTMO}_2$ with a specific capacity greater than 250 mAh g^{-1} (de Biasi et al., 2019). The featured voltage and capacity profiles of these two cathode materials can be found in **Figure 1. 11**. Li-rich NCM cathodes encounter several problems like voltage fading, short lifespan, etc., which hinder commercial application (Zheng et al., 2017).

In addition, Ni-rich layered oxide $\text{LiNi}_{1-x}\text{M}_x\text{O}_2$ (M= Co or Mn, etc.; $1-x > 0.5$) is deemed as the most promising cathode for EVs because of their high capacity (>200 mAh g^{-1}) above a charge voltage of 4.3 V, relatively low cost, and environmental friendly characteristic due to low cobalt content, as well as better chemical stability in the charged state (Konarov et al., 2017, Wu et al., 2015, Xu et al., 2016).

Typical voltage profiles of NCM layered oxide cathodes of different Ni contents and LiCoO_2 are shown in **Figure 1. 12**. The numbers (111, 523, 622, 811) represent the stoichiometric ratios of Ni: Co: Mn. All NCM compounds exhibit similar charge/discharge profiles (**Figure 1. 12**). Compared with other cathode materials in **Figure 1. 11**, NCM811 appears relatively slow voltage fading and high discharged capacity, which indicates the synergic advantages of specific capacity and operating

voltage for Ni-rich NCM. Furthermore, the operating potential of Ni-rich NCM at 4.3 V (versus Li/Li⁺) is also amicable for conventional electrolytes, for example, LiPF₆/carbonates electrolyte, making it relatively easy to be commercialized based on the existing electrolyte system (Markevich et al., 2019).

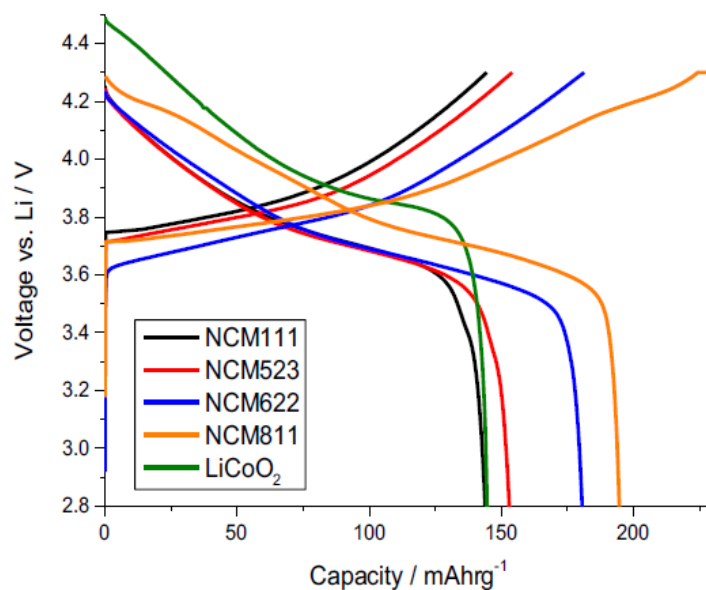


Figure 1. 12. Comparison of charge and discharge curves of NCM cathodes and LiCoO₂ (Markevich et al., 2019).

1.1.4.2. Structural and Chemical Aspects of High-Voltage and High-Capacity Ni-rich NCM

The capacity and voltage advantage of Ni-rich NCM originates from the chemical and structural properties. Ni-rich NCM battery is a new member of the NCM family with higher Ni content, which is also a solid solution of LiNiO₂, LiCoO₂, and LiMnO₂ as shown in **Figure 1. 13. (a)** (Susai et al., 2018). Ni-rich NCM is developed based on the conventional NCM compound, which holds the same structure of LiNi_{1/3}Mn_{1/3}Co_{1/3}O₂ presented in **Figure 1. 13. (b)** (Li et al., 2019), but lattice parameters are different due to

the substitution of cobalt and manganese with nickel to give $\text{LiNi}_{1-x-y}\text{Co}_x\text{Mn}_y\text{O}_2$ ($x+y < 0.5$). The different stoichiometric ratios of Ni, Co, and Mn are the pronounced characteristics distinguishing Ni-rich NCM from conventional NCM.

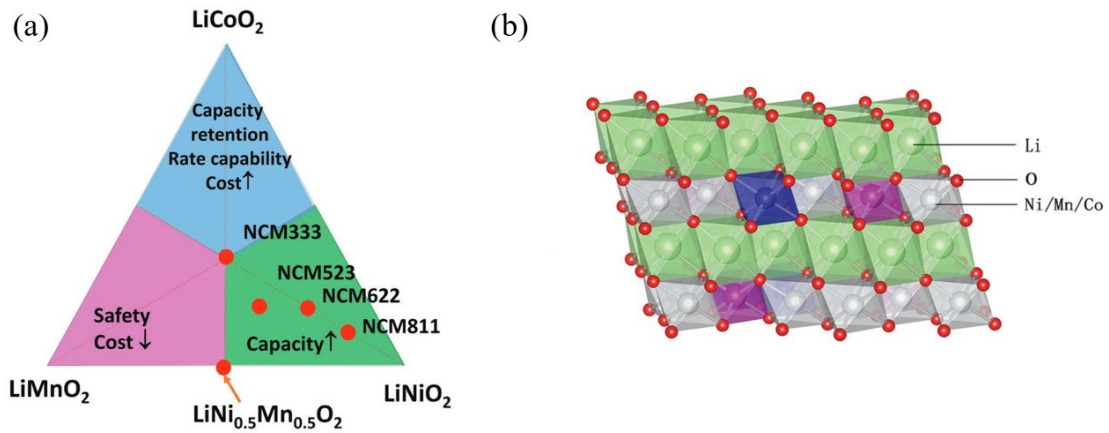


Figure 1. 13. (a) Phase diagram of LiNiO_2 , LiCoO_2 , and LiMnO_2 ; (b) Layered structure of Ni-rich NCM compound (Susai et al., 2018, Li et al., 2020b).

Each transition metal element contributes different features to NCM material (Radin et al., 2017). Firstly, manganese offers excellent chemical stability, as the high-spin $\text{Mn}^{3+/4+}$:eg band lies well above the O^{2-} :2p band (Manthiram, 2017). In comparison with other transition metals in Ni-rich NCM, the valence of Mn is naturally oxidised to 4+ while the valence of Ni is reduced to 2+ in the fully lithiated state. While during deintercalation, nickel and cobalt are oxidised to higher valence states, manganese remains in the tetravalent state. Manganese exhibits electrochemically inert and benefits for the local structure stability. Even in the overcharged state (deeply delithiated state) manganese ion is chemically stable (Radin et al., 2017, Manthiram et al., 2017).

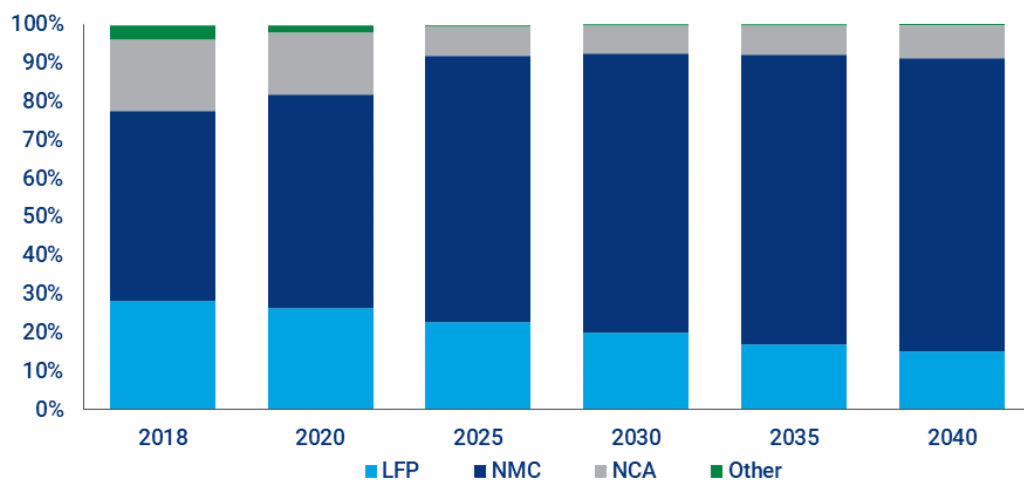
Cobalt improves the rate performance and layered ordering, as the smaller size of cobalt can result in smaller interlayer space of the transition metal (TM) layer, which makes

the lithium layer wider and the lithium ions can migrate more easily. Meanwhile, the substitution of cobalt for nickel in TM slabs can reduce Li/Ni disordering, so a strictly 2D α -NaFeO₂ type layered structure can be obtained (Susai et al., 2018, Rougier et al., 1996).

Nickel is the crucial redox active element in NCM, whose redox couples of Ni^{2+/3+} and Ni^{3+/4+} contribute most to the reversible capacity. Unlike LiCoO₂ where only 50% lithium is utilized due to oxygen release, Ni^{2+/3+} in NCM batteries can be easily oxidised to the +4 state by charging without the release of molecular oxygen in the ternary NCM system, hence a large amount of lithium can be employed, which results in larger reversible specific capacity than that of LiCoO₂. The specific capacity increases along with more nickel content in these materials, up to 240 mAhg⁻¹, which is the limitation of LiNiO₂(LNO) (Markevich et al., 2019, Radin et al., 2017, Susai et al., 2018, Chakraborty et al., 2020).

It is believed that because of the high energy density and continuous technology development, NCM (or NMC) will gradually replace LFP, NCA, and other batteries for EV applications. **Figure 1. 14** shows the predicted share of total LIBs for EVs by battery type from 2018 to 2040 (Mitchell, 2020). Nickel-manganese-cobalt oxide is the increasingly dominant LIB chemistry for EVs. Moreover, the detailed cathode shares in LIB markets based on installed GWh from 2012 to 2030 are shown in **Figure 1. 15** (Celine Buechel, 2021), which shows that the overall trend of the LIB market is the shifting from cobalt-rich to nickel-rich cathodes. In the most recent 2023, the data illustrates that the largest market for LIBs cathodes is occupied by NMC532 and

NMC622 accounting for over 60% of the market share, while NMC811 holds a relatively minor presence, constituting less than 10% of the market. However, projections anticipate a substantial shift by 2030, wherein NMC811 is forecasted to capture nearly 40% of the LIB cathode market. Meanwhile, it is foreseen that NMC811 together with NMC622 will constitute the predominant cathode technologies in the LIB market by that timeframe.



Source: Wood Mackenzie

Figure 1. 14. Share of total LIBs for EVs by battery type from 2018 to 2040 with the prediction (Mitchell, 2020).

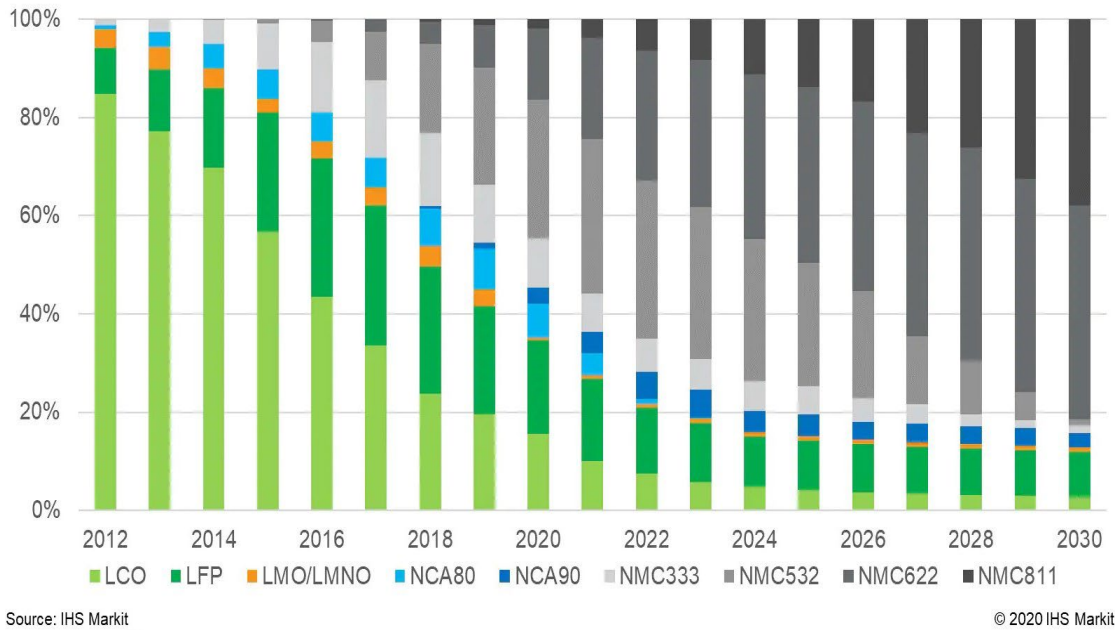


Figure 1. 15. Cathode shares in LIB markets based on installed GWh (Celine Buechel, 2021).

1.2. Significance and Originality of the Thesis

According to the background study, it can be known that LIBs-based EVs have achieved great progress in the road-transport market. As NCM holds the synergistic advantage of higher voltage and higher capacity than that of LFP, NCM LIBs have become the dominant batteries for EVs. However, the current cathode share in LIB markets is mainly occupied by NCM622 and NCM523 rather than NCM811 or higher nickel content NCM. The application of NCM622 and NCM523 would limit the driving range of EVs and accordingly become a problem for EVs to compete with internal combustion engine vehicles in the market. It is therefore important to realise Ni-rich NCM with stoichiometric ratios of $Ni \geq 0.8$ as the dominant cathode materials of LIBs for the next-generation passenger EVs with the expected driving ranges greater than 600 km per

charge, approaching those of internal combustion engine vehicles (Choi et al., 2020). However, the commercialization of these Ni-rich NCM with Ni content $\geq 80\%$ is difficult, because such ultra-high Ni content cathode material has intrinsic drawbacks of (1) performance degradation i.e., voltage and capacity fade and (2) safety risk over the lifespan of the battery (Zhang, 2020). These two drawbacks would become more serious with increasing nickel content in Ni-rich NCM according to the fundamental characteristic of NCM materials on the correlation of performance and safety with Ni content as shown in **Figure 1. 16** (Noh et al., 2013). Batteries with higher Ni content demonstrate higher capacity, poor thermal stability, and lower capacity retention. It is paramount to make innovations to mitigate these problems for ultra-high Ni content NCM.

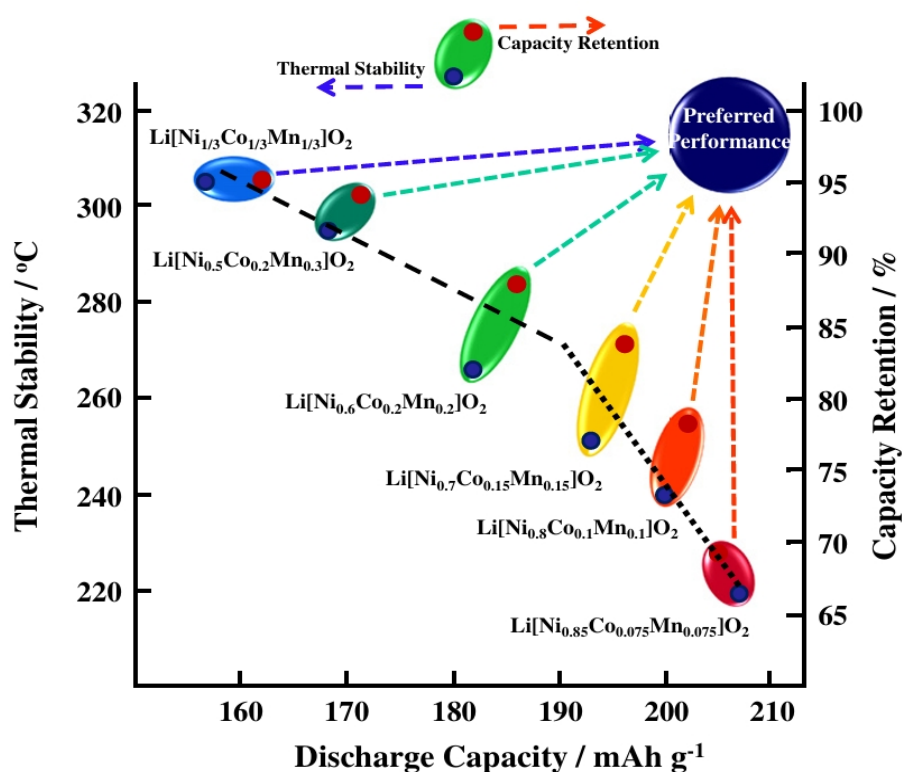


Figure 1. 16. Fundamental characteristics of NCM materials on the correlation of performance and safety with Ni content (Noh et al., 2013).

This thesis will focus on the modification of superior Ni-rich layered oxide cathodes (stoichiometric ratios of $\text{Ni} \geq 0.8$) with novel coating and/or doping strategies to achieve improved electrochemical performances. After the coating and/or doping modification on the cathode material or the precursor with the novel sol/antisolvent method, as well as the combination of radially aligned structure, the performance of Ni-rich NCM with Ni content $\geq 80\%$ has been greatly improved. Key performance improvements include higher initial Coulombic efficiency, better rate capability, improved cycling and thermal stability, and higher energy density.

This thesis delineates a clear objective centred on the development of novel modification strategies to mitigate performance degradation and pull out the full potential of Ni-rich layered oxides (Ni content $\geq 80\%$) as cathodes for advanced LIBs. By doing so, it is envisaged that these meticulously tailored approaches will propel the performance frontiers of next-generation NLO cathodes.

The research was carried out in four stages: (1) the underlying mechanism of Ni-rich NCM electrochemical performance degradation and current modification strategies were studied by abundant pieces of literature review, (2) the innovative and effective modification strategies to mitigate the problems that accelerate Ni-rich NCM (Ni content $\geq 80\%$) electrochemical performance decaying were investigated based on the experimental studies and analysis, (3) the combined modification strategies were pursued to achieve synergistic modification effect and excellent electrochemical

performance of Ni-rich NCM (Ni content $\geq 80\%$), (4) the extreme high Ni content layered oxide cathode i.e. LiNiO_2 was further modified with the developed method.

The outcomes of this thesis will contribute to accelerating the development of high-performance Ni-rich NCM cathodes with stoichiometric ratios of Ni ≥ 0.8 , and relieve the issue of ‘Range anxiety’ and ‘Charging time anxiety’ of EVs. The innovations in the modification strategies for improving the electrochemical performances of Ni-rich layered oxides (Ni content $\geq 80\%$) in this thesis are gathered here.

Firstly, in the work of sol/antisolvent coating with crystalline LiBO_2 for $\text{LiNi}_{0.85}\text{Co}_{0.1}\text{Mn}_{0.05}\text{O}_2$ cathode towards high initial Coulombic efficiency and ultra-stable mechanical integrity, a novel and facile sol/antisolvent coating modification of Ni-rich layered oxide $\text{LiNi}_{0.85}\text{Co}_{0.1}\text{Mn}_{0.05}\text{O}_2$ is developed. The uniform LiBO_2 nano-spherical particles coating together with LiBO_2 nanorods wrapping provide double protection against electrolyte. This simple in-site modification and repairing technology guarantees good mechanical integrity of polycrystalline Ni-rich cathode.

Secondly, in the work of sol/antisolvent combined coating and doping with boron-related materials for $\text{LiNi}_{0.83}\text{Co}_{0.05}\text{Mn}_{0.12}\text{O}_2$ cathode towards high specific capacity and high cycling stability, the combined boron-related coating and doping modification can be achieved by sol/antisolvent coating for the precursor with the further lithiation calcination. The study also shows that the combination of joint coating and doping by

boron-related material, along with the radially aligned structure, has greater advantages over just doping or coating modification. The triple synergistic effect achieves high stability in cycling at both cut-off voltages of 4.3 V and 4.5 V.

Thirdly, in the work of sol/antisolvent with boron treatment for the modification of LiNiO_2 cathode, the sol/antisolvent boron treatment can produce ordered and well-crystallised primary particles of LiNiO_2 , accompanied by the improved discharge capacity and rate capability. The synthesised LiNiO_2 inherits the radially aligned structure of the precursor. The performances of the boron-treated radially structured polycrystalline LiNiO_2 by sol/antisolvent method on the specific capacity and the long-term cycling stability in the voltage range of 2.8-4.3 V and 2.8-4.6 V are better than that of the single crystal LiNiO_2 as reported by other people (Kim et al., 2022). It demonstrates that the benefit from the radially arranged structure of the Ni-rich layered oxide cathodes is also applicable to the extremely high Ni content material of LiNiO_2 .

Chapter 2 Literature Review

This chapter presents a literature review of the underlying mechanism of Ni-rich NCM electrochemical performance degradation and the current modification strategies. To address the performance degradation of Ni-rich NCM, it is important to identify the leading causes. $\text{Li}^+/\text{Ni}^{2+}$ cation mixing, surface structural degradation, side reactions, and microcracks are the four main factors inducing electrochemical performance decay (Li et al., 2020a). Based on the understanding of the four main factors accounting for electrochemical performance decay and the review of the current modification strategies for NLO cathode materials, the design principle of the modification can be elaborated. Inspired by the study in this chapter, innovative modifications of Ni-rich NCM are expected to achieve superior electrochemical performance.

2.1. Four Main Factors Responsible for the Decaying of Ni-Rich NCM

2.1.1. $\text{Li}^+/\text{Ni}^{2+}$ cation mixing

The NCM material $\text{LiNi}_x\text{Co}_y\text{Mn}_z\text{O}_2$, with $x + y + z = 1$ belongs to the hexagonal $\alpha\text{-NaFeO}_2$ ($R\bar{3}m$) structure. In this structure, the O element is located in the intermediate layer between the Li and TM layers (**Figure 2. 1. (a)**) (Sun and Zhao, 2017). First-principles theoretical simulation to calculate the Jahn–Teller (JT) distortion of the TM–O octahedral complex has demonstrated that the multivalence states $\text{Ni}^{2+}/\text{Ni}^{3+}$ and $\text{Co}^{2+}/\text{Co}^{3+}$ coexist in the NCM material from NCM111 to NCM811 (**Figure 2. 1. (b)**)

(Sun and Zhao, 2017). Ni^{2+} (0.69 Å) ion is larger than that of the Ni^{3+} (0.56 Å) ion and has an ionic radius similar to that of Li^+ (0.76 Å) ions, which makes $\text{Li}^+/\text{Ni}^{2+}$ cation mixing easier. $\text{Li}^+/\text{Ni}^{2+}$ cation mixing can result in irreversible capacity degradation and poor rate performance owing to the presence of Ni^{2+} in the Li layer (Xiao et al., 2022). Higher nickel ion content results in more severe mixing and more negative effects on the electrochemical performance of NLO materials.

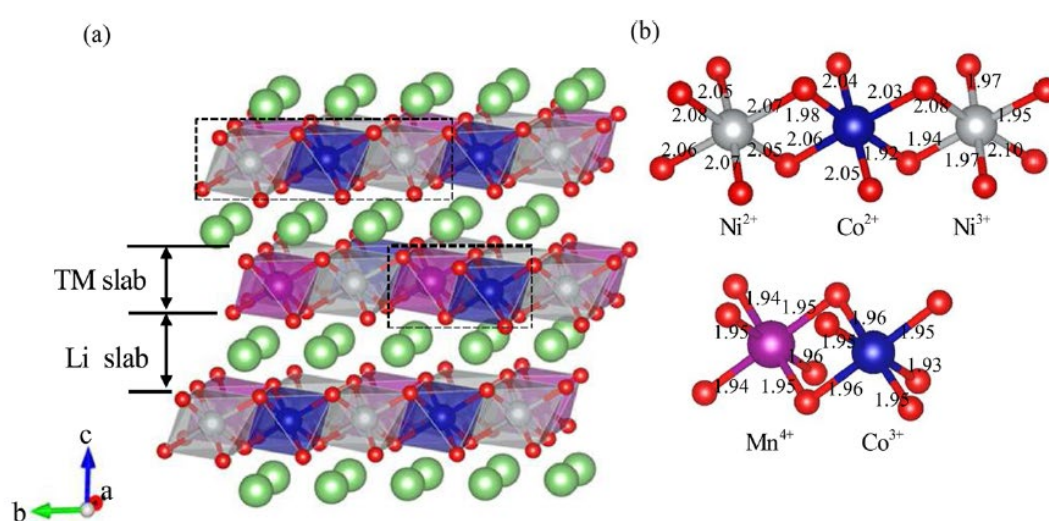


Figure 2. 1. TM-O octahedral complexes in NCM: (a) Ni, Mn, and Co reside at the octahedral site surrounded by six O atoms; (b) Local view of the TM-O octahedral complexes (Sun and Zhao, 2017).

During charging, the Ni^{2+} ions in the Li layer can be oxidised to a high valence state, resulting in a local shortening of the inter-slab distance. This shortening is caused by the smaller Ni^{3+} ion, which can constrain Li insertion during discharge and ultimately lead to some irreversible capacity loss as shown in **Figure 2. 2** (Manthiram et al., 2017). Meanwhile, lithium ions located in the TM layers are also difficult to extract from the crystal lattice, which impedes the Li-ion diffusion and weakens the rate capability (Fu

et al., 2014).

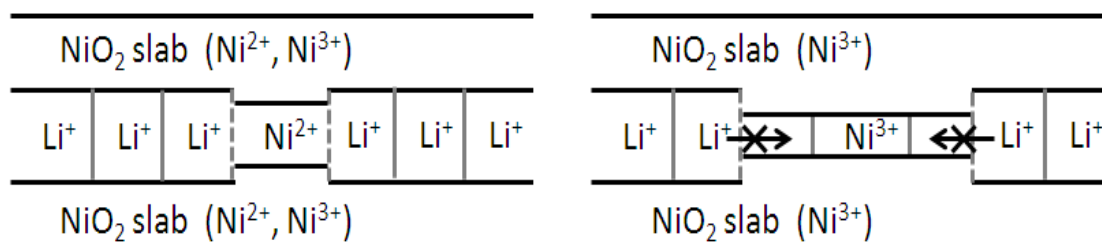


Figure 2. 2. Schematic diagram of local collapse of inter-slab space due to Li⁺/Ni²⁺ cation mixing during charging-discharging (Manthiram et al., 2017).

The degree of Li⁺/Ni²⁺ cation mixing can be measured by using X-ray diffraction (XRD) analysis. Typical XRD patterns of LiNi_{0.8}Co_{0.1}Mn_{0.1}O₂ with different excess amounts of Li are shown in **Figure 2. 3**. The sharp diffraction peaks and clear peak splitting of the (006)/(102) and (108)/(110) pairs indicated a well-crystallised layered structure. The I(003)/I(104) intensity ratio of the XRD data is typically used to show the level of Li⁺/Ni²⁺ cation mixing. A high I(003)/I(104) intensity ratio represents a low degree of Li⁺/Ni²⁺ cation mixing (Wu et al., 2015). Theoretically, less Ni²⁺ implies less Li⁺/Ni²⁺ cation mixing (Wang et al., 2019a). In addition to using I(003)/I(104) intensity ratio of the XRD data to evaluate the degree of Li⁺/Ni²⁺ cation mixing of Ni-rich NCM, a 3D tomographic morphology and elemental mapping information using nano-scale X-ray Absorption Near Edge Structure (nano-XANES) with high spatial resolution was also developed to analyse cation mixing. XANES can show the Ni³⁺ concentration of NCM particles as shown in **Figure 2. 4** (Yang et al., 2019). The red colour represents a high Ni³⁺ percentage. Nano-XANES method can serve as a supplement for analyzing Li⁺/Ni²⁺ cation mixing. In this PhD research, the traditional XRD analysis will be used to evaluate the degree of Li⁺/Ni²⁺ cation mixing of the synthesised Ni-rich cathode

materials.

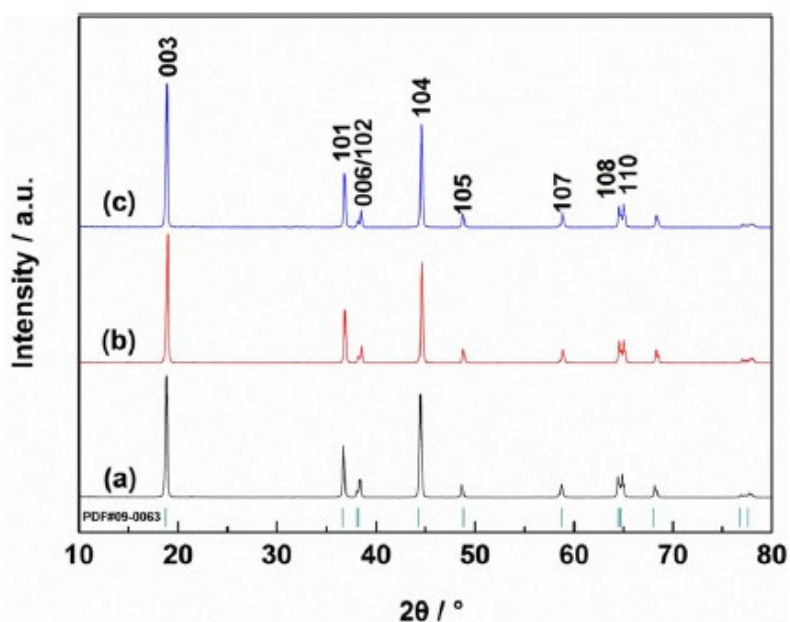


Figure 2. 3. XRD patterns of $\text{LiNi}_{0.8}\text{Co}_{0.1}\text{Mn}_{0.1}\text{O}_2$: (a) with Li excess of 0%, (b) Li excess of 10%, and (c) Li excess of 20% (Wu et al., 2015).

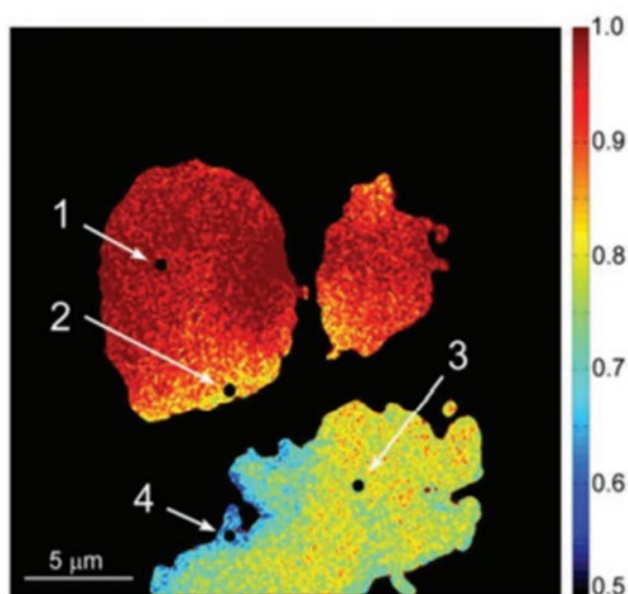
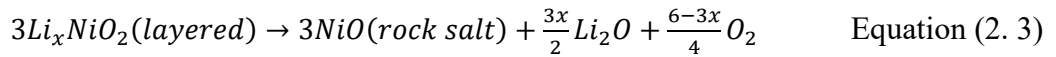
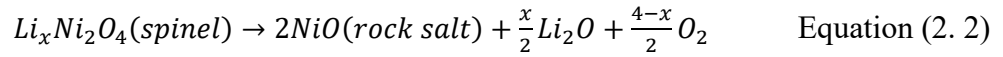
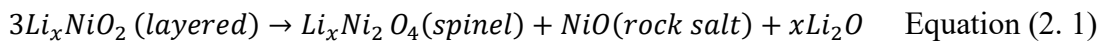


Figure 2. 4. 2D XANES mapping showing the Ni^{3+} concentration of NCM ($\text{LiNi}_{0.8}\text{Co}_{0.1}\text{Mn}_{0.1}\text{O}_2$) particles after cycling. (The colour scheme indicates the percentage of Ni^{3+} : $\text{Ni}^{3+}/(\text{Ni}^{3+} + \text{Ni}^{2+})$) (Yang et al., 2019).

It is worth mentioning that $\text{Li}^+/\text{Ni}^{2+}$ cation mixing is also called Li/Ni disordering. The phenomenon of Li/Ni disordering occurs throughout the lifespan of the NLO battery from the initial active material synthesis to the end of the battery life. Normally, the Li/Ni disordering of NLO can be considered as the thermal decomposition of Li_xNiO_2 , as described by Equation (2. 1) and (2. 2) with the overall reaction of Equation (2. 3) (Zhang, 2020).



Because of its thermodynamically unstable characteristics, Li_xNiO_2 is reduced to a low valence of 2^+ along with Li_2O and O_2 products. Therefore, it would be effective to solve the Li/Ni disordering of NLO by improving its thermodynamic stability. Meanwhile, Li/Ni disordering worsens as the NLO battery gets deeply discharged owing to the production of more Ni^{2+} ions at a large degree-of-discharge (DOD).

Based on the above literature studies, it can be concluded that $\text{Li}^+/\text{Ni}^{2+}$ cation mixing is a crystal structure change phenomenon derived from the unstable layered structure of NLO material. Discovering and eliminating it will be beneficial for reducing the barriers to Li-ion extraction/insertion within the NLO material, leading to the persistently high specific capacity delivered from the NLO material during the electrochemical cycling.

2.1.2. Surface Structural Degradation

When LIB undergoes the charge and discharge cycles, it is common for the layered oxide cathode to experience surface structural degradation. The surface structural degradation of Ni-rich NCM is characterised by a transition from a layered structure ($R\bar{3}m$) to a spinel-like structure ($Fd\bar{3}m$) and rock-salt structure ($Fm\bar{3}m$). This issue becomes more severe at higher temperatures and is directly induced by the migration of TM ions into the Li layer during cycling. The surface structural instability of Ni-rich NCM is closely linked to the transfer of Ni^{2+} ions to the Li^+ sites. In other words, $\text{Li}^+/\text{Ni}^{2+}$ cation mixing induces the nonstoichiometric NCM and surface structural degradation. An illustration of the ordered and disordered structures of layered lithium metal oxides and their structural transformations is shown in **Figure 2. 5** (Liu et al., 2015). The interfacial reactions between the electrolyte and cathode can result in increased formation of Ni^{2+} ions due to the reduction of high-valence Ni^{4+} ions and then the migration to Li layers, causing further surface structural degradation (Yang et al., 2023).

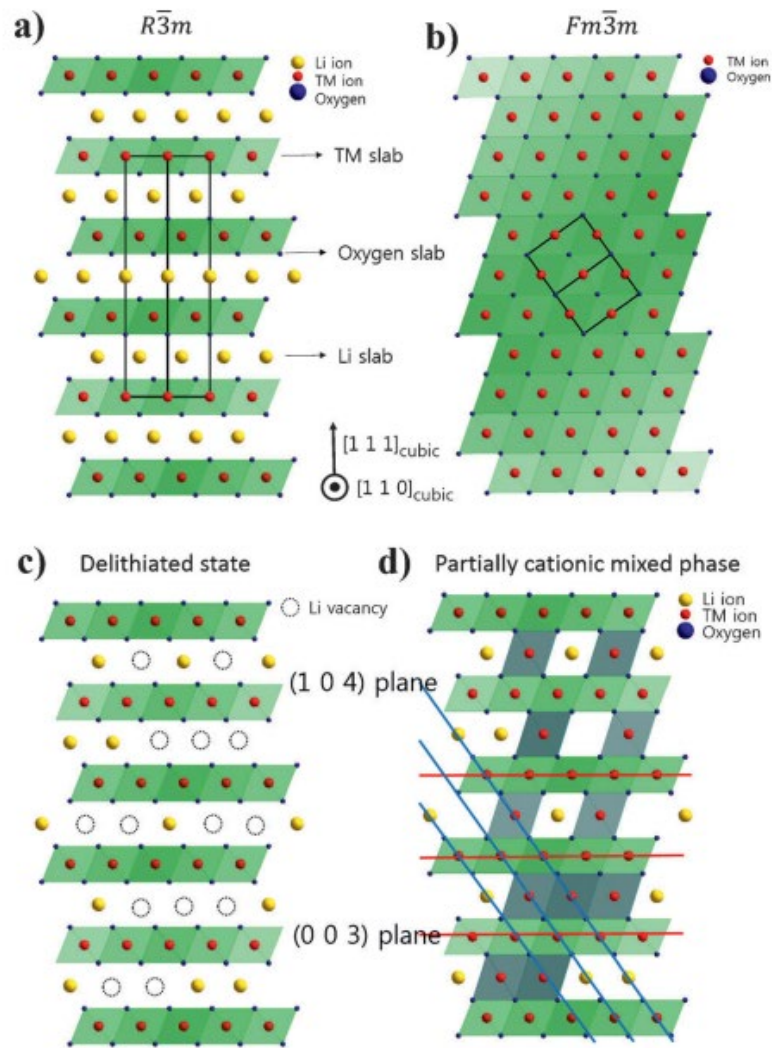


Figure 2. 5. Illustration of structural transformation in layered lithium metal oxides with cation disorder: (a) Well-ordered $R\bar{3}m$ structure; (b) The cation mixing phase with $Fm\bar{3}m$ structure; (c) $R\bar{3}m$ structure with Li vacancies in highly charged state; (d) Partially cation mixed phase with TM ions in Li slab (Liu et al., 2015).

NiO rock-salt phase is ionically insulated, which can result in sluggish Li-ion diffusion kinetics and lead to capacity fading. As the battery cycles, the transformation from layer to spinel/rock salt structure typically begins on the surface of individual Ni-rich NCM particles and gradually spreads inward. The surface structural degradation can result in altered lattice constants and the release of oxygen from the lattice in Ni-rich NCM. This process can cause the generation and expansion of holes and cracks in cathode materials,

accelerate the reaction with the electrolyte, and cause significant performance degradation and safety problems (Zhang et al., 2021a, Tang et al., 2019, Hwang et al., 2014, Yang and Xia, 2016, Gu et al., 2013, Yan et al., 2017).

Figure 2. 6 presents the charge and discharge voltage curves of the NCM811/Li half-cell in the first cycle, along with the corresponding differential capacity plot. The three pairs of oxidation/reduction peaks in the differential capacity plot correspond to phase transitions between H1–M, M–H2, and H2–H3 (Märker et al., 2019). H represents the hexagonal structure and M represents the monoclinic structure. All the phases of H1, M, H2, and H3 belong to $R\bar{3}m$ layered structure.

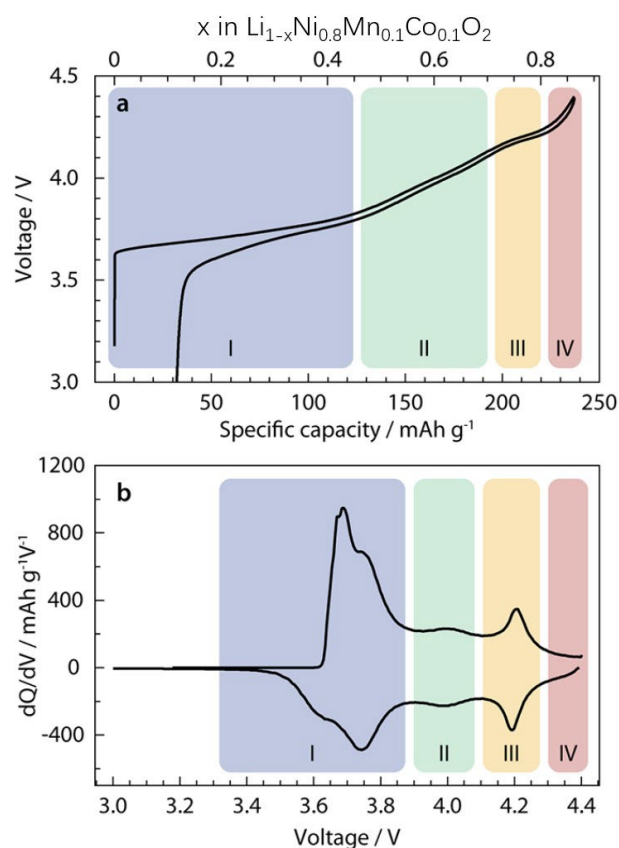


Figure 2. 6. (a) First charge and discharge voltage curves of a NCM811/Li half-cell; and (b) The corresponding differential capacity (dQ/dV) plot (Märker et al., 2019).

For the end-member of NLO, Li_xNiO_2 ($0 \leq x \leq 1$) experiences a symmetry change of rhombohedral structure \rightarrow monoclinic structure \rightarrow rhombohedral structure when lithium is extracted from the host structure with different lithium/vacancy ordering within the lithium layer. The phase change is reversed when Li is inserted into the host structure (Delmas et al., 1999, Arroyo y de Dompablo and Ceder, 2003). A schematic diagram of such phase change with Li/vacancy ordering for Li_xNiO_2 with the identification of different phases is shown in **Figure 2. 7** (Delmas et al., 1999). “Rhombohedral” is not a crystal system, it is replaced by the “Hexagonal” phase, and is labeled by “H”. When lithium is extracted from Li_xNiO_2 ($0 \leq x \leq 1$), it also experiences the reversible sequence of stable phases as follows: H1 (pristine LiNiO_2) \rightarrow M \rightarrow H2 \rightarrow H3 (Bianchini et al., 2019). Comparing **Figure 2. 6** and **Figure 2. 7**, it can be found that the obvious difference is the different degrees of the phase transitions for NCM811 and LiNiO_2 . LiNiO_2 exhibits a stronger degree of phase transition on H2–H3 with a longer transition platform in the charge/discharge curves.

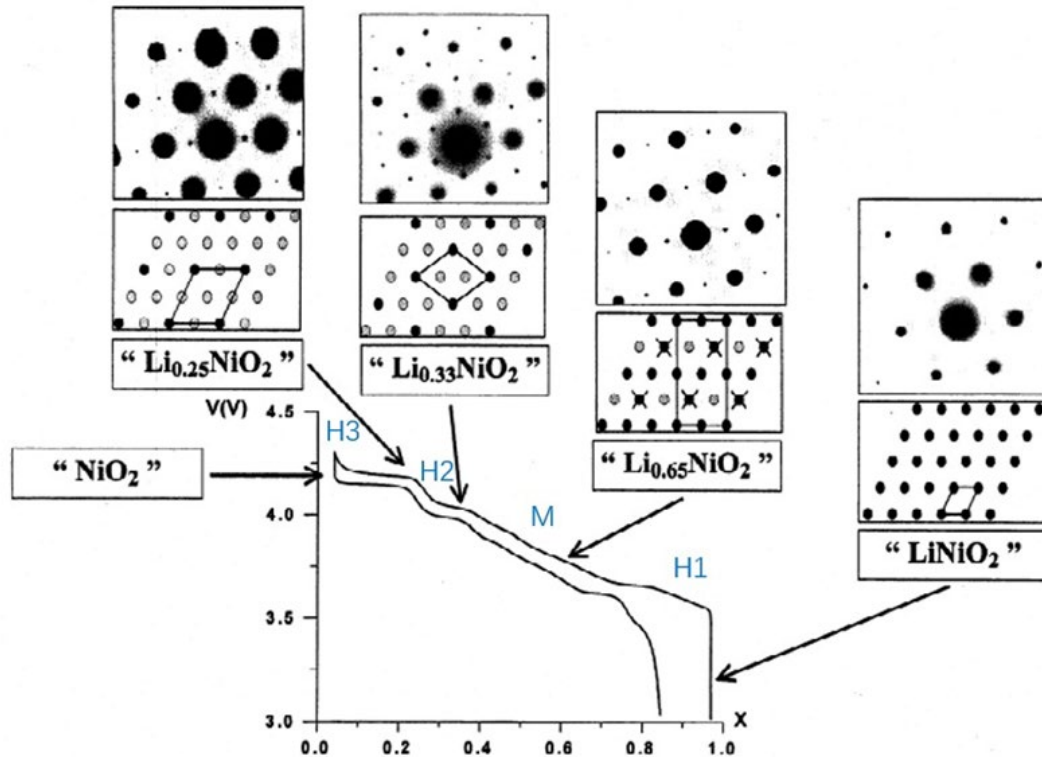


Figure 2. 7. Illustration of the phase change with Li/vacancy ordering for Li_xNiO_2 with identification of different phases (Delmas et al., 1999, Bianchini et al., 2019).

Among the phase transitions of Ni-rich NCM (Ni content $\geq 80\%$) during cycling, the H2–H3 phase transition is detrimental and undesirable, as it can speed up surface structural degradation (Tan et al., 2022). The reason for H2–H3 phase transition accelerating the surface structural degradation of Ni-rich NCM is discussed here. This is mainly because such a phase transition can lead to detrimental anisotropic volume change and anisotropic mechanical strain, which can cause internal microcracks. The microcracks triggered by the H2–H3 phase transition create a fresh surface where structural degradation can easily occur. Meanwhile, surface structural degradation phenomena would develop from the external surface of the particle to the new surface inside (Jamil et al., 2020).

The detrimental volume changes triggered by H2–H3 phase transition have been

demonstrated by Lai et al. through high-resolution synchrotron radiation diffraction by Rietveld refinement with a $R\bar{3}m$ structure model on the investigation of a $\text{LiNi}_{0.85}\text{Co}_{0.10}\text{Mn}_{0.05}\text{O}_2$ cathode material (N85CM) (Lai et al., 2020). The change in the lattice parameters of the N85CM cathode during the first charge-discharge process is shown in **Figure 2. 8** using high-resolution synchrotron radiation diffraction analysis. A significant decrease in the lattice parameter c along with the largest volume shrinkage by phase transition of $\text{H2} \rightarrow \text{H3}$ can be detected. Oxygen release and/or TM migration are considered the main reasons.

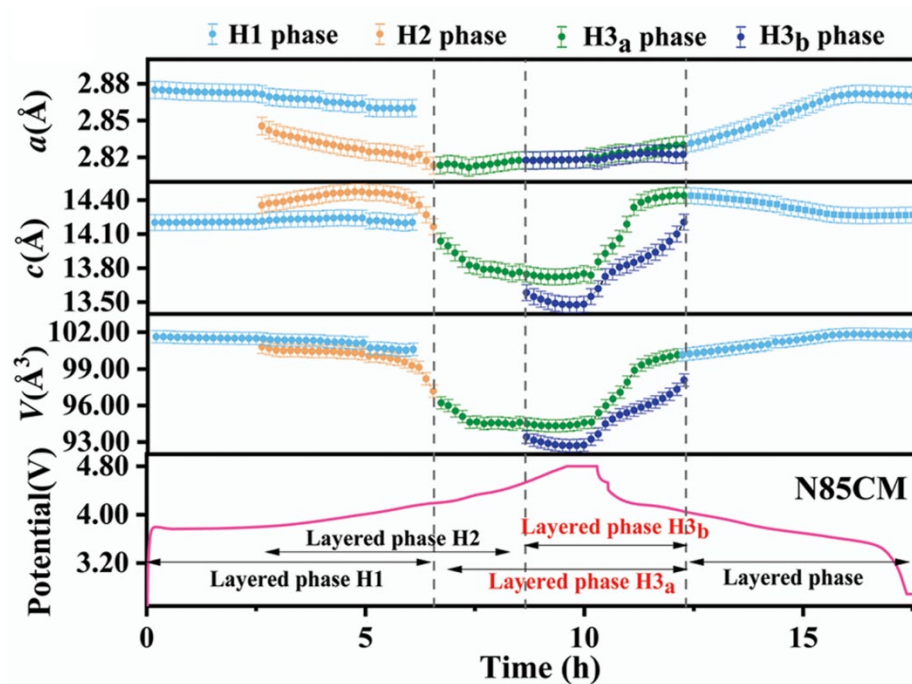


Figure 2. 8. High-resolution synchrotron radiation diffraction analysis of N85CM cathodes during the first cycling process (Lai et al., 2020).

It can be considered that the essence of surface structural degradation (layered-spinel-rock salt structural transformations) of NLO can be equal to $\text{Li}^+/\text{Ni}^{2+}$ cation mixing. The H2-H3 phase transition is a distinctive feature for NLO with Ni content greater than or equal to 80 %, as it cannot be observed for NCM111 and NCM622, as shown in **Figure**

2. 9 (Jung et al., 2017). The fresh internal microcracks associated with the transformation of the H2–H3 (naturally, the accelerated reduction of unstable Ni^{4+} to be Ni^{2+} ions in the new surface) can enhance the degree of structural degradation due to more $\text{Li}^+/\text{Ni}^{2+}$ cation mixing in the new surfaces. Therefore, suppressing the H2–H3 phase transition and improving its reversibility will be beneficial for mitigating the layered-spinel-rock salt structural transition, and accordingly improving the electrochemical performance of Ni-rich NCM with stoichiometric ratios of $\text{Ni} \geq 0.8$.

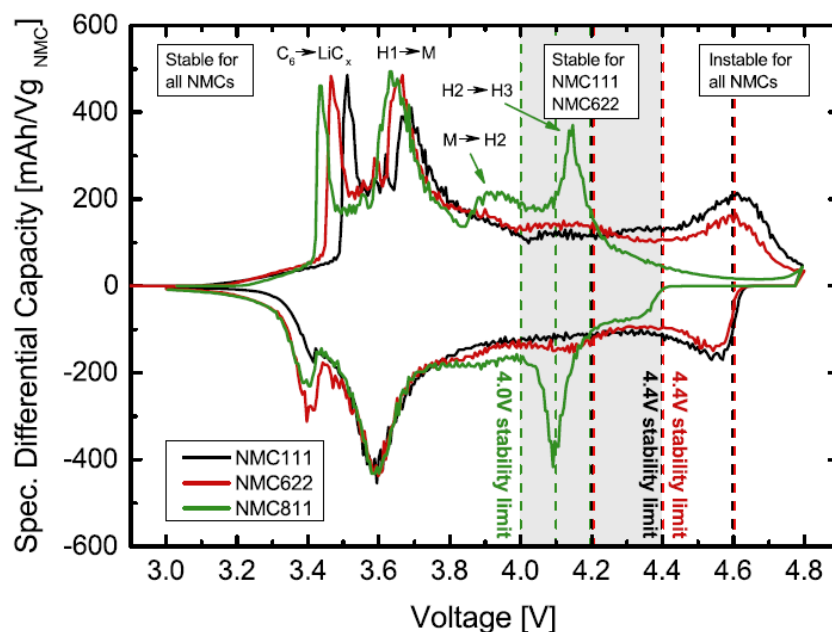


Figure 2. 9. dQ/dV curves of three different NMC/graphite cells recorded at 0.1 C-rate (3rd cycle) (Jung et al., 2017).

The surface structural degradation is also derived from the unstable layered structure of NLO material. Beyond the XRD analysis can be used to determine the existence of structural degradation, transmission electron microscopy (TEM) can also be valuable for identifying the structural changes by observing the changes in the arrangement of atoms in NLO material near the particle surface. In this PhD research, XRD and TEM

analyses will be used to evaluate the effect of the structure degradation on the electrochemical performance of NLO materials and demonstrate the restriction of the surface structural degradation by the proposed strategies.

2.1.3. Side Reactions

In addition to lithium insertion/desorption reactions inside NLO LIBs, there are also many side reactions in NLO cathode materials (Oka et al., 2023). The side reactions can directly influence the electrochemical performance of LIBs, which can be divided into two types: the formation of lithium residue $\text{Li}_2\text{CO}_3/\text{LiOH}$ on the surface of Ni-rich layered oxides before the assembly of the battery and the reactions between the active materials and the electrolytes inside the LIBs. These side reactions can result in a thicker solid electrolyte interface (SEI) film during cycling, along with an increase in the electrochemical polarisation resistance and the concentration polarisation impedance. In particular, at a high operating voltage (over 4.3 V) or high current density, transition metal dissolution reactions can be deepened by acid leaching (Xu et al., 2016).

Specifically, to maintain a layered structure, excessive Li is used to synthesise Ni-rich NCM cathodes, which can easily react with moisture and air. The residual lithium oxide $\text{Li}_2\text{O}/\text{LiOH}$ can absorb moisture and CO_2 at the particle surface under ambient conditions during storage and produce Li_2CO_3 and LiOH , commonly known as residual lithium, as shown in **Figure 2. 10** (Cho et al., 2014). $\text{Li}_2\text{CO}_3/\text{LiOH}$ layer is electrochemically inactive to lithium intercalation/de-intercalation, which is believed to be responsible for the capacity loss of the NCM material (Wu et al., 2014).

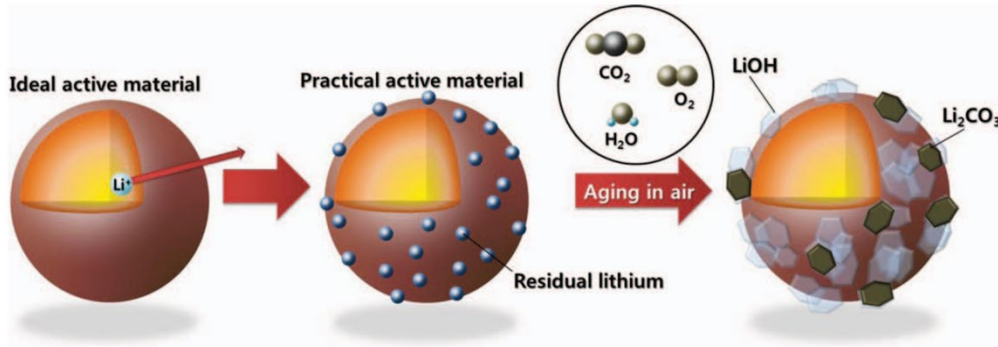
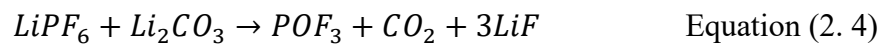


Figure 2. 10. Surface reaction of Ni-rich materials in air (Cho et al., 2014).

Furthermore, Li_2CO_3 can react with the LiPF_6 -based electrolyte solutions, which can seriously deteriorate the cyclic stability, because the gaseous species of Li_2CO_3 can be absorbed on the surface of the active material with a decreased active surface area on the cathode material and gradually aggregate the battery's polarisation (Bi et al., 2016).

The specific reaction pathway is shown below:



On the other hand, the side reactions among the active materials and electrolytes are more complex. Because of the side reactions among the active materials and electrolytes, the electrochemical kinetics and cycling stability of the NLO LIBs will be weakened. Meanwhile, potential safety issues could also occur, leading to the NLO LIBs aging.

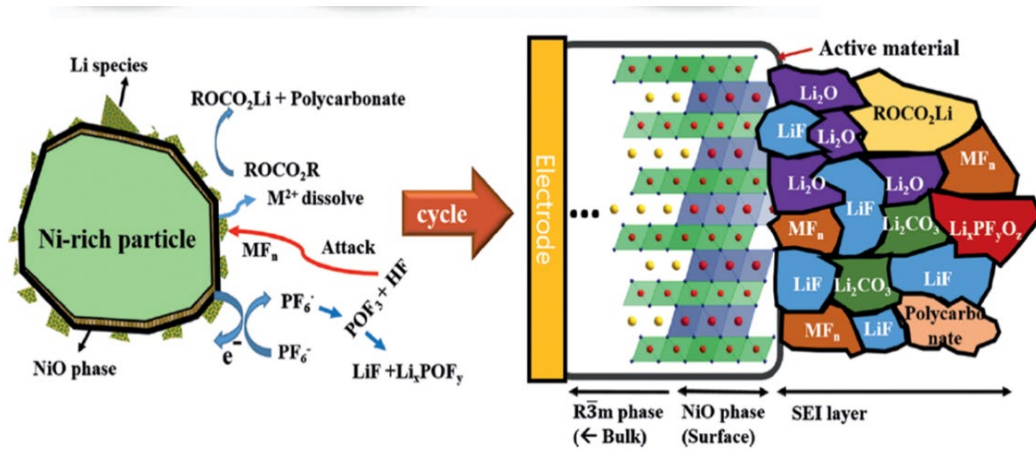
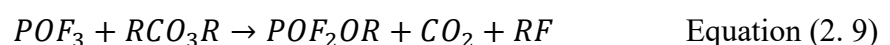
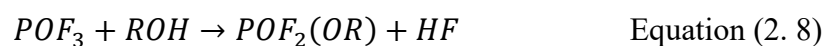
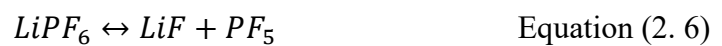
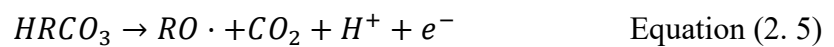


Figure 2. 11. Formation of the SEI layer after cycling of the Ni-rich cathode material in liquid electrolyte (Liu et al., 2015).

An image of the SEI layer due to side reactions between the surface of the Ni-rich material and electrolyte is shown in **Figure 2. 11** (Liu et al., 2015). The inorganic components of LiF, Li₂CO₃, and Li₂O are inactive materials, which would impede the diffusion of Li⁺ ions and influence electrochemical performance. Organic components such as Li_xPF_yO_z and ROCO₂Li are the decomposition products of electrolytes, which are formed based on the proposed oxygen radical mechanism (Guéguen et al., 2016).

The detailed side reactions involving the solvents and LiPF₆ salt based on the oxygen radical mechanism are shown below:(Guéguen et al., 2016)



According to the above reaction equations, it can be known that when the cyclic ethylene carbonate (R = C₂H₃ in Equation (2. 5)) is oxidised, it may produce RO· radicals that

may subsequently (via Equation (2. 7)) hydrolyze the salt and leads to various organofluorine compounds, such as fluoroethylene C₂H₃F. An equilibrium reaction between LiPF₆, LiF, and PF₅ is shown in Equation (2. 6). Alkylfluorophosphate and alkyl difluorophosphate in Equation (2. 8) and Equation (2. 9) can be further produced due to the reaction among POF₃, ROH and carbonate solvents. These organic phosphate products also impede Li-ion intercalation.

Besides the reaction of POF₃ and PF₅ with consumption of ROH can lead to the formation of HF, traces of water can also lead to the formation of HF as shown below:(Seidl et al., 2016)

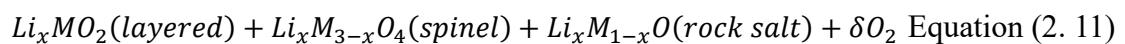
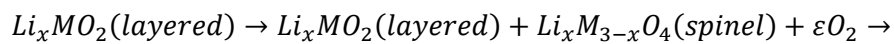


The formation of HF is a major reason for the failure of LIBs during long-term cycling. It is postulated that HF is mainly responsible for the dissolution of the layered NCM electrode material, resulting in capacity attenuation as it can reduce Li⁺ ion insertion sites. Beyond resulting in the loss of positive electrode capacity, the dissolved transition metal ions and their complexes can move into the negative electrode and destroy the SEI, contributing to a further increase in cell impedance and capacity fading (Guéguen et al., 2016, Pouraghajan et al., 2021, Evertz et al., 2016). MF_x (M represents Ni, Co, Mn, etc. other than Li) can also be produced because of the dissolution of NCM materials as by-products on the surface of the NCM particles (Li et al., 2020b).

The SEI layer produced by the side reactions between the surface of Ni-rich materials and electrolytes has both positive and negative effects (Gourdin et al., 2013). For a positive impact, a denser SEI layer would be more effective in preventing the electrode

from undergoing additional reactions with the electrolyte. This is because the electrolyte molecules cannot travel to the active material surface, thus suppressing SEI growth. Because of this protection, the cycling performance and service life of the battery can be greatly improved. For the negative impact, a certain amount of electrolyte and lithium ions is permanently consumed during the irreversible formation of the SEI layer (Pinson and Bazant, 2012). The initial loading capacity was no longer available for Li insertion because of the consumption of Li^+ ions. In particular, for Ni-rich NCM, more metastable Ni^{4+} ions were induced when charging to a high cut-off voltage. The decomposition of electrolytes becomes more serious because of the catalytic activity of Ni^{4+} , the harsh interfacial chemical reaction and TMs dissolution are also deepened (Xue et al., 2020, Li et al., 2017b).

Beyond the SEI formation due to the side reactions from the decomposition of electrolytes and the dissolution of metal elements from the active material, there are also O_2 gas production side reactions inside LIBs. Ni-rich layered oxide cathodes suffer from the detrimental effect of oxygen release, which is triggered by decomposition of the active material (NLO). A simplified decomposition reaction for NLO cathode to produce O_2 is shown below (M represents Ni, Co, Mn, etc.) (Sharifi-Asl et al., 2019).



This equation is consistent with the thermal decomposition of Li_xNiO_2 in Equation (2. 3). The release of oxygen during the charge/discharge process of NLO LIBs proceeds through the following process: when Ni is oxidised to form an extremely unstable Ni^{4+}

species at the extreme delithiation state, the unstable Ni^{4+} species can readily capture electrons from the oxygen atom. Subsequently, because the oxygen atom loses its electrons, the evolution of oxygen gas and the formation of oxygen vacancies are induced. However, more O_2 gas and pores are produced when O is continuously oxidised (Liao and Manthiram, 2015, Yin et al., 2021).

CO_2 and CO also evolve along with the oxygen evolution inside NLO LIBs. The observed CO_2 and CO emissions were mainly due to the chemical reaction of the reactive lattice oxygen with the electrolyte. The cell voltage vs. time. accompanied by the gas evolution analysis of a NCM811-graphite cell over four charge/discharge cycles at 0.2 C and 25°C between 2.6 and 4.8 V is shown in **Figure 2. 12** (Jung et al., 2017). Different types of gases were detected in the NCM811-graphite cell during charge/discharge cycles. Jung et al.'s research also shows that, for NCM111 and NCM622, the oxygen release occurs at roughly 4.7 V vs. Li/Li⁺ at 25 °C, while for NCM811, it occurs at a voltage of 4.3 V vs. Li/Li⁺ at 25 °C, which is much lower than that of NCM111 and NCM622. Therefore, the end-of-charge voltage is constrained for the practical application of NCM811, which affects the achievable specific energy.

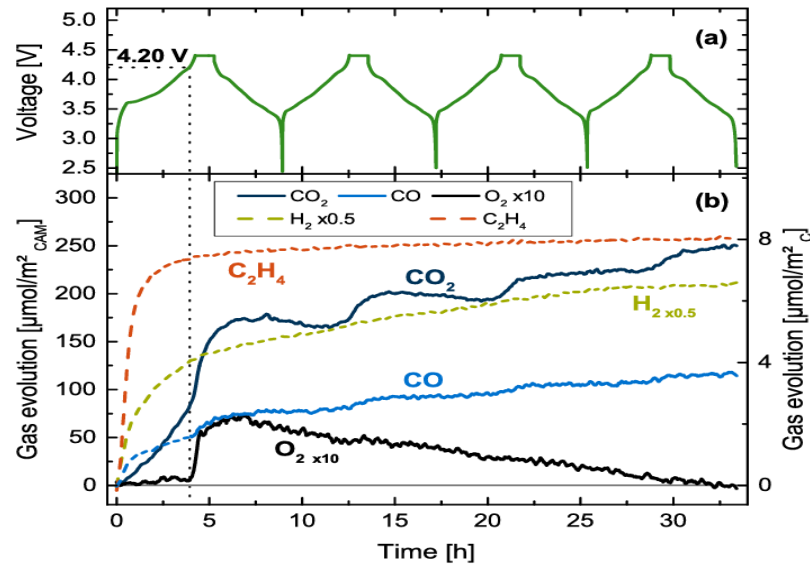


Figure 2. 12. Cell voltage vs. time of a NCM811-graphite cell over four charge/discharge cycles at 0.2 C and 25°C between 2.6 and 4.8 V, in a cell containing 400 μL of 1.5 M LiPF_6 in ethylene carbonate, glass fiber separators and 16.40 mg NCM811 (The corresponding gas analysis is shown below, the dashed lines stem from the graphite electrode) (Jung et al., 2017).

It is worth mentioning that in addition to the capacity fading problem, the oxygen release phenomenon can also result in serious safety problems, especially for NCM with a stoichiometric ratio of $\text{Ni} \geq 0.8$ (Liao and Manthiram, 2015). When the nickel-rich cathode is charged above 4.2 V (high voltage), the released oxygen species (O_2 , O^{2-} , O^-) from the host structure of the cathode material in the highly delithiated states react rapidly with the electrolyte. Not only the structural degradation but also the generation of the cathode-electrolyte interphase layer is believed to be triggered by this reaction. However, this reaction generates a large amount of heat, which triggers serious thermal runaway (Dai et al., 2023). The large amount of O_2 released together with the heat release can be considered as a poor thermal stability characteristic of NLO. Thermal runaway caused by the poor thermal stability of the electrode material is highly likely

to cause the battery explosion, which seriously hinders the development of Ni-rich cathode materials (Song et al., 2023).

For thermal stability comparison, the samples for the different NCM materials with different nickel contents were tested by heating up to 600 °C in the absence of electrolytes by Bak et al. (Bak et al., 2014). The results are shown in **Figure 2. 13**.

Compared with NCM611, NCM811 released a larger amount of oxygen when the charged samples were heated to 600 °C. The temperatures for the substantial O₂ release of different NCM materials coincided well with the onset temperatures of the first phase transition (structural degradation) from the layered phase to the spinel phase. The higher the Ni content, the poorer the thermal stability of the NCM materials.

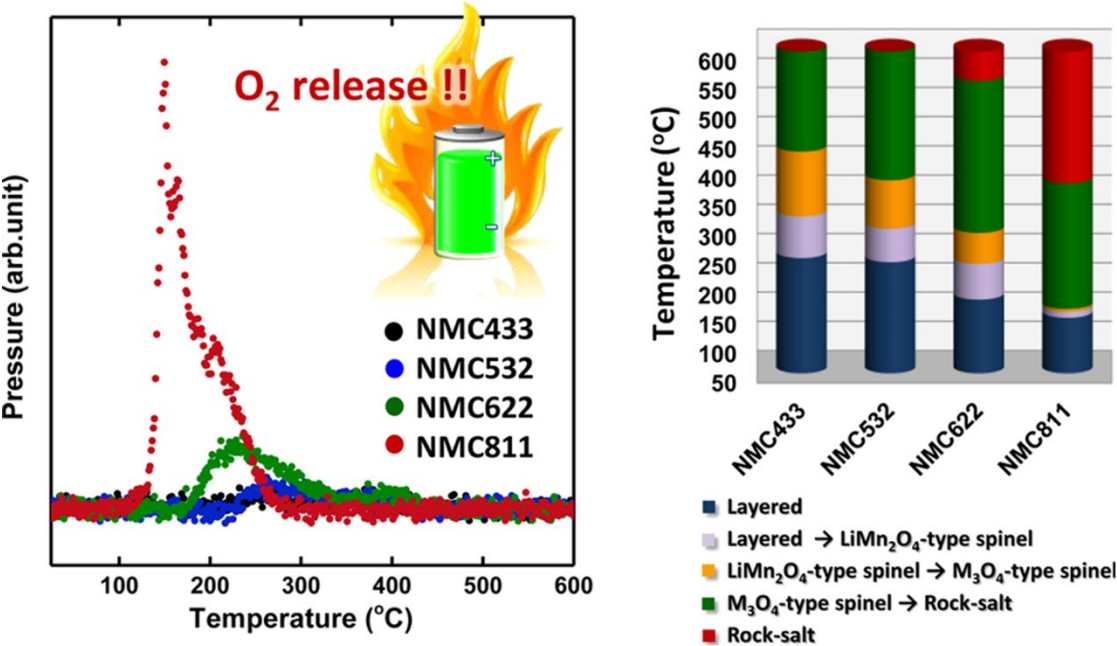


Figure 2. 13. Mass spectroscopy profiles for the oxygen collected simultaneously during the measurement of in situ time-resolved X-ray diffraction and the corresponding temperature region of the phase transitions for NMC samples (Bak et al., 2014).

Through the above literature studies on the side reactions, we can know that the side reactions are complex because involving almost all the components inside LIBs. Not only the SEI layer can be produced along with the increased battery resistance, but the gas release especially for the oxygen release can be triggered, which is very dangerous for the safety of the battery. In particular, the catalytic activity of Ni^{4+} makes the side reaction of NLO ($\text{Ni} \geq 0.8$) more abundant, resulting in more consumption of active Li and Ni by the electrolyte. Separating the contact between Ni^{4+} and the electrolyte turns into predominant to inhibit the side reactions. Considering the side reaction can induce changes in the battery resistance and many kinds of by-products on the surface of the cathode material, carrying out the battery resistance analysis and the SEI components analysis of the produced NLO batteries is important in this PhD research.

2.1.4. Micro-cracks

It has been reported that the formation of microcracks is mainly due to anisotropic changes in the lattice dimension along with lattice volume shrinkage and expansion during Li extraction and insertion, which is very harmful to the long-term capacity of Ni-rich layered cathodes (Liu et al., 2017). Meanwhile, oxygen vacancies are also one of the reasons for microcrack generation. This is because stress can be formed owing to the concentration gradient of oxygen vacancies, and the connection of oxygen vacancies can produce a flawed structure (Yin et al., 2021). The image of microcrack inside the NCM622 sample after 150 charge-discharge cycles is shown in **Figure 2. 14** (Kim et al., 2015). Obviously, the ionic and electronic connectivity of sub-surface primary particles

would be degraded with increased impedance and a sluggish, incomplete electrochemical reaction owing to these microcracks. On the other hand, the electrolyte can further penetrate the interior of the cathode material along the microcracks to create a new SEI layer, resulting in more structural degradation and side reactions, which would be detrimental to the electrochemical performance of the NLO cathode materials.

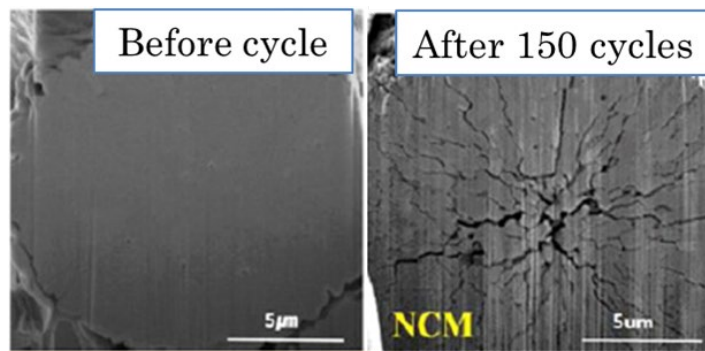


Figure 2. 14. Images of crack inside a NCM622 sample after 150 charge-discharge cycles (Kim et al., 2015).

For the normally used polycrystalline NLO material, nanometre-sized primary particles agglomerate to form micrometer-sized secondary particles. There are many grain boundaries and voids inside NLO, as shown in **Figure 2. 15**. These parts can be considered weak mechanical parts of the material. The inter-granular cracking along the boundaries between primary particles is therefore deemed to be the predominant reason for the structural failure of the polycrystalline NLO materials (Liu et al., 2017).

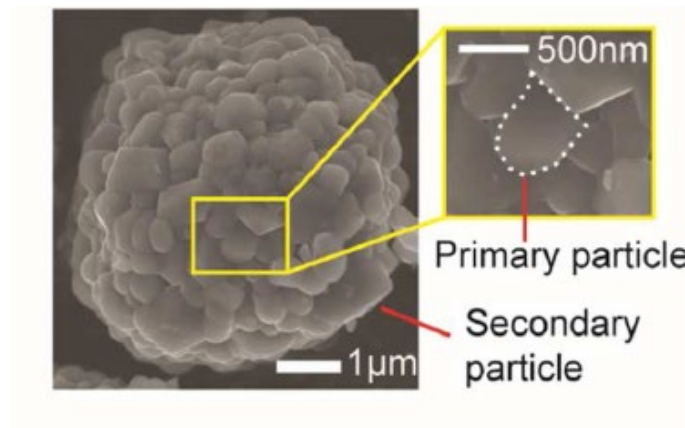


Figure 2. 15. Image of uncycled a NLO primary and secondary particles. The white dashed line delineates the boundary of a primary particle (Liu et al., 2017).

It is suggested that constraining the DOD can mitigate the generation of micro-cracks polycrystalline NLO cathodes as shown in **Figure 2. 16**, wherein, 4.2-2.5 V is 0-100% DOD and 4.05-3.48 V is 10-70% DOD. According to the schematic shown in **Figure 2. 16**, it can be seen that, for the cycle test with a DOD of 0-100%, microcracks can easily be generated in the secondary particles because of the high stress with large shrinkage and expansion of NLO crystal lattices. For the cycle test with a DOD of 10-70%, the generation of microcracks can be reduced because of the small shrinkage and expansion of NLO crystal lattices. The formation of a NiO-like structure on the surface of primary particles can also be restricted with a DOD of 10-70%. However, it is not a good choice for commercialisation because of its decreased energy density (Watanabe et al., 2014).

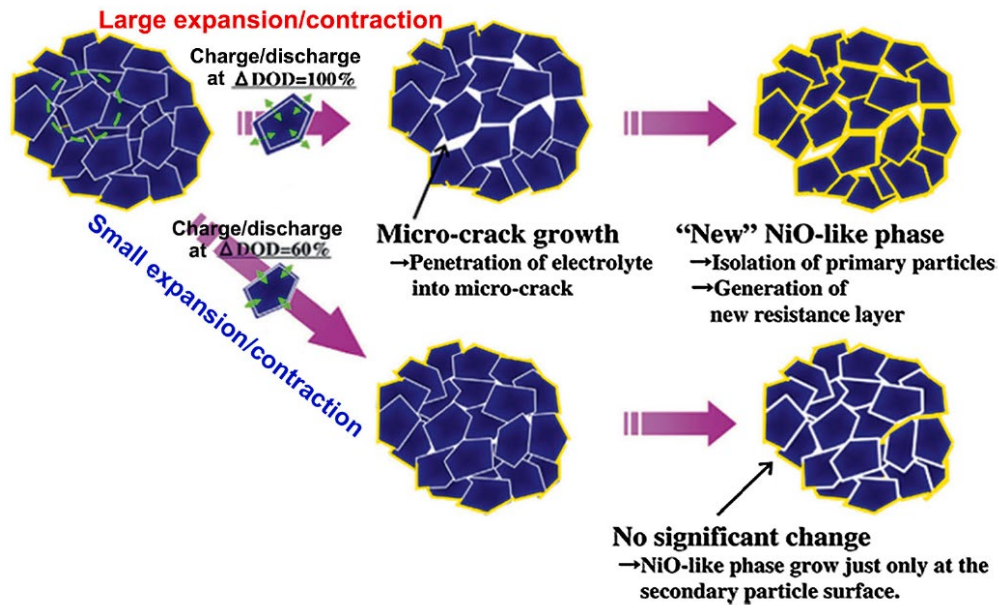


Figure 2. 16. Schematic illustration of micro-crack growth and structural deterioration of a Ni-rich layered oxide cathode ($\text{LiNi}_{0.76}\text{Co}_{0.14}\text{Al}_{0.70}\text{O}_2$) with different DOD cycling (Watanabe et al., 2014).

The formation of microcracks can be considered as a mechanical issue of NLO materials. The mechanical properties calculation of a NLO cathode material ($\text{LiNi}_{0.8}\text{Co}_{0.1}\text{Mn}_{0.1}\text{O}_2$, NCM811) were calculated by Min and Cho et al. using the density functional theory (Min and Cho, 2018). The anisotropic mechanical properties of the NCM811 are shown in **Figure 2. 17**, which shows that NCM811 withstands a greater compression stress than tension stress. The in-plane direction strength was higher than that in the out-of-plane direction for both the tension and compression conditions. Density functional theory calculation also demonstrated that the stability of the entire structure relies on the interaction of the Li, O, and TM layers. When more lithium is extracted from the layered oxide material, the stability of the TM and O layers weakens. The mechanical integrity of NLO can deteriorate without the bonding network of Li–O. Therefore, the mechanical

strength of NLO weakened with the increasing Ni content during electrochemical cycling. This is because there is more extraction of Li at the same voltage for a higher Ni content, along with a larger specific capacity (Min and Cho, 2018).

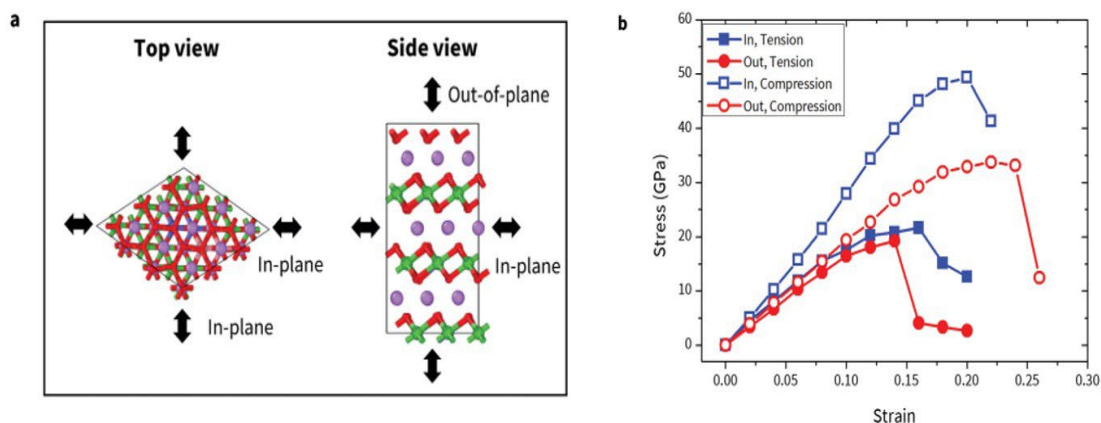


Figure 2. 17. Mechanical property calculation of NCM811 under the boundary condition of tensile and compressive deformation based on density functional theory: (a) Directions where the tensile and compressive deformation is applied for the in-plane and out-of-plane; (b) Stress-strain curves for NCM811 under tensile and compressive deformation in both in- and out-of-plane directions (Min and Cho, 2018).

In summary, to solve the problems of microcracks in NLO cathode materials, approaches that can decrease the anisotropic changes in the lattice dimensions, improve the mechanical strength of the NLO material, and reduce the formation of oxygen vacancies during the charge/discharge process are required. This also implies not only the problems of electrochemistry but also the problems of chemistry and mechanics that need to be solved for NLO cathode materials. Since microcracks can occur in both the inner and outer regions of NLO particles, the milling process for NLO particles to observe the internal microcracks will be required for this PhD research.

Through a comprehensive study of the mechanism of electrochemical performance

degradation of NLO cathodes, it is clear that the four main factors of $\text{Li}^+/\text{Ni}^{2+}$ cation mixing, surface structural degradation, side reactions, and microcracks are intrinsic problems for NLO cathodes. These problems lead to electrochemical performance decay of NLO cathodes and are influenced by the increase of the Ni content in Ni-rich cathodes. To mitigate these four main problems, many modification strategies including surface coating, lattice/bulk doping, and strategies beyond coating/doping, have been proposed to improve the performance of NLO cathode materials, as discussed in Section 2.2.

2.2. Current Modification Strategy

2.2.1. Coating of Ni-rich Cathode Materials for Lithium-ion Batteries

Because of changing the surface chemistry or providing physical protection layers, surface coating has proven effective in improving the electrochemical properties and thermal stability of cathode materials for LIBs. Specifically, the surface coating can prevent direct contact between the cathode material and the electrolyte, and accordingly avoid the decomposition of the electrolyte and mitigate detrimental side reactions. For the NLO cathode, the coating layer can also release the surface layer to spinel/rock salt phase transformations. This is because the interfacial reactions between the high-valence Ni^{4+} ions and the electrolyte to become Ni^{2+} ions can be restrained, along with less Li/Ni disordering. In addition, oxygen removal, particularly in the highly delithiated state, can be mitigated by coating, therefore, the cycle lifetime of NLO cathodes can be enhanced (Chen et al., 2010, Xia et al., 2018b, Nisar et al., 2021).

Ideally, the coating layers should be thin, homogenous, and have superior ionic and electronic conductivities. When a coating material with high ionic and electronic conductivity is used, Li-ion diffusion/electron migration during cycling is enhanced, which improves the rate performance of battery. In addition, a mechanically rigid and stable coating film is ideal because it can mitigate the generated stresses associated with volumetric changes during charging/discharging. Moreover, an easy and scalable coating process is valuable for popularisation. The ideal requirements for the surface coating of cathode materials to address the challenges of current surface coating are shown in **Figure 2. 18** (Nisar et al., 2021).

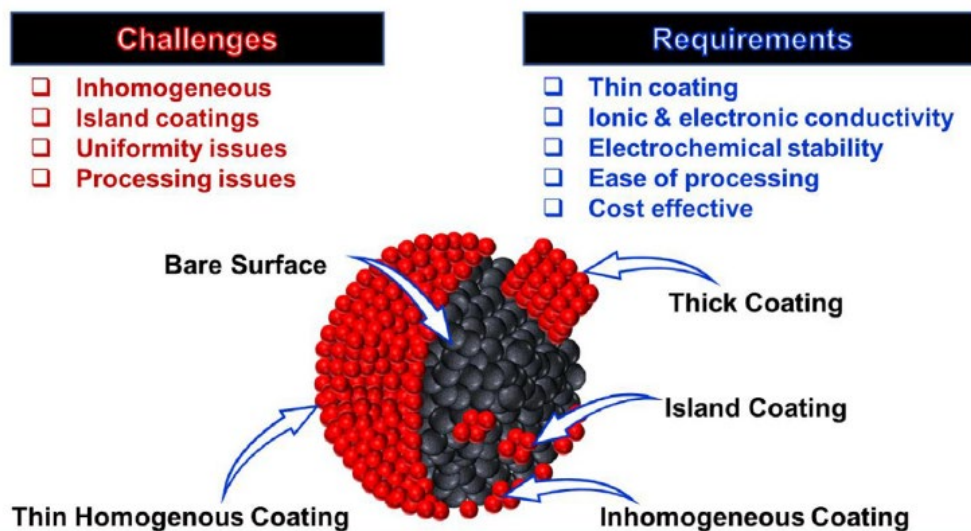


Figure 2. 18. Challenges and requirements of surface coatings for cathode materials (Nisar et al., 2021).

There are four main coating approaches for cathodes: co-precipitation coating, sol-gel coating, dry coating (ball milling), and chemical vapour deposition (CVD) coating, as shown in **Figure 2. 19** (Zuo et al., 2017). Different coating approaches can achieve different electrochemical performances. For co-precipitation coating types (**Figure 2. 19. (a)**), various coating films can be produced on the cathode material, involving both

the monolayer and the multiple layers. However, many process parameters influence the precipitation effect, such as the pH, reaction temperature, and dropping speed of the reagent.

In the sol-gel coating process (**Figure 2. 19. (b)**), deionized water or other solution will be used to disperse the cathode particles in a sol condition, and then the functional solution will be added into the sol to get the gel under certain reaction conditions. After the evaporation of the gel, a coated sample can be obtained. Compared with other coating technologies, the reaction is relatively easy to control, and the chemical uniformity of the coating layer can be guaranteed for a multi-component system. However, concerning the NLO cathode, when water is used to produce the sol solution, the cathode surface structure is destroyed, owing to its significant sensitivity to water.

Dry coating (**Figure 2. 19. (c)**) is a modification technology of mechanical coating by nanoparticles in surface modification equipment. Dry coating has the advantage of relatively low cost and has a small impact on the environment compared with the wet process. However, because of inhomogeneous and island coatings, the dry coating process hinders broad commercial adoptability.

The chemical vapor deposition process is shown in **Figure 2. 19. (d)**. A more uniform coating layer can be obtained through CVD coating, as nucleation and film formation occur simultaneously at high temperatures in the tubular furnace. However, the high-temperature fields are more complicated and costly.

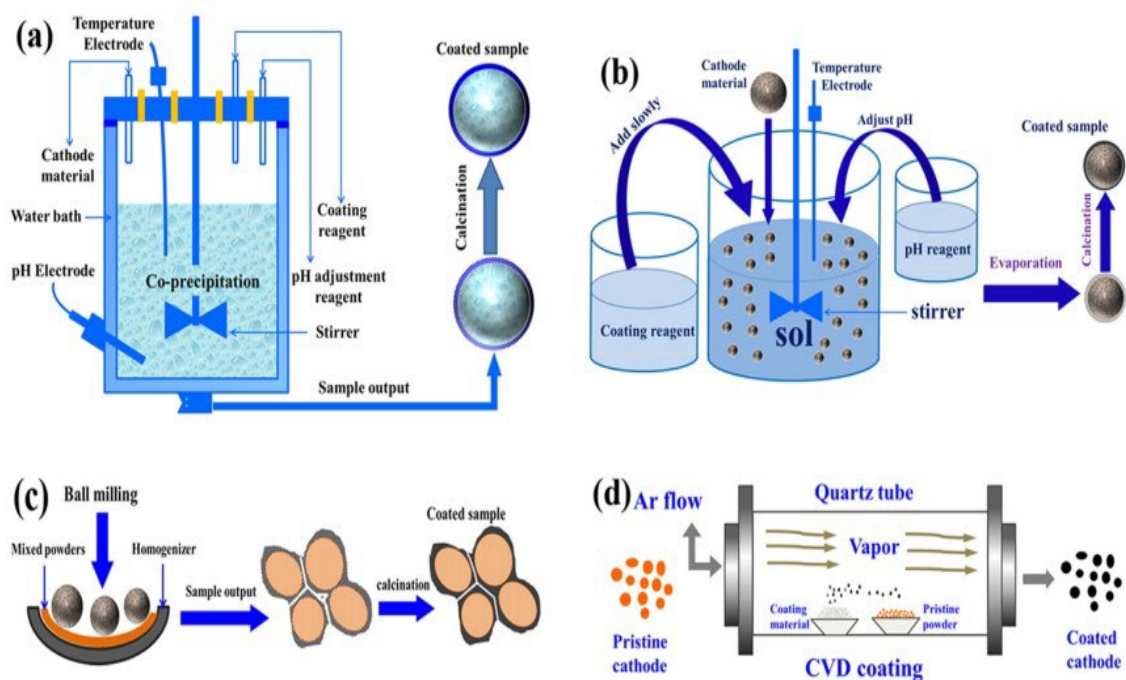


Figure 2. 19. Schematic diagram of four different coating processes:(a) Co-precipitation; (b) Sol-gel; (c) Dry coating; and (d) Chemical vapor deposition (CVD) (Zuo et al., 2017).

According to Ye et al.'s review (Ye et al., 2021), various coating materials are used for the modification of Ni-rich cathode materials, which can be divided into inactive and active coatings. Oxides, fluorides, and phosphates are ascribed to the inactive coatings. Carbon-based materials, electron-conductive polymers, and inorganic Li-ion conductors are active coating. Although a large number of active and inactive coatings have been adopted by researchers to improve the electrochemical performance of different cathode materials. The interactions between the coating materials and the active materials and electrolyte solutions have not yet been clarified completely.

One hot coating direction is the in-situ form of the conductor membrane on the surface of NCM cathode materials by capturing Li residual impurities. Several coating modifications have been reported, such as the $\text{La}_4\text{NiLiO}_8$ coating formed by partially sacrificing Ni ions from the cathode substrate to react with nano- La_2O_3 and LiOH by

the solid-state method, which exhibits good electron and ionic conductivities, and acts as a protector, and can effectively prevent the electrolyte attack of NCM811 (Zhou et al., 2021). Another example is the in-situ form of lithium boron oxide during the cycle progress by the reaction between B_2O_3 and Li-sources from the active materials or electrolyte, lithium boron oxide is a fast ionic conductor material that can not only suppress the side reactions but also promote ion migration (Li et al., 2020a). A more concrete and graphic example is shown in **Figure 2. 20**, which presents a diagram for the in-situ building of a hybrid nano-coating for NCM811 material (Li et al., 2016). Ultrathin hybrid Li_xAlO_2 and $Li_xTi_2O_4$ nanomembranes encapsulated on the surface of NCM811 cathode materials were produced by hydrolysis of titanium isopropoxide and aluminum isopropoxide in NCM811 aqueous solution by consuming the Li-residue on the surface of the NCM811 cathode material. The hybrid nanomembrane-encapsulated NCM811 cathode was effectively stabilised during long-term cycling. These examples give the idea that at the same time by creating the coating protection, the drawbacks of the NLO materials are eliminated.

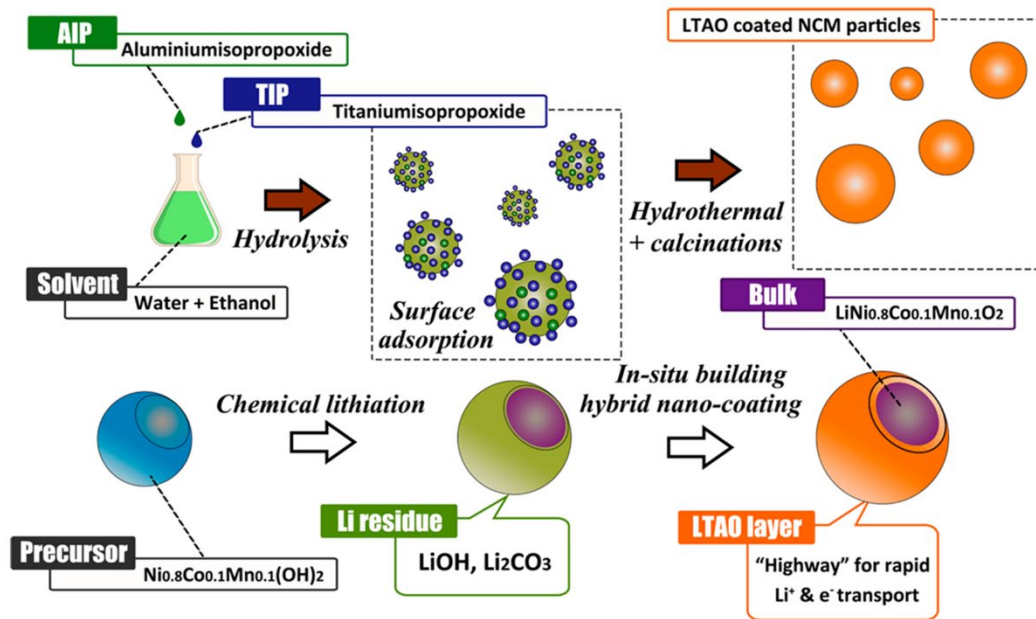


Figure 2. 20. Diagram of the design and synthesis of hybrid nanomembrane-encapsulated NCM cathode materials (Li et al., 2016).

From the literature reviews on coating modification, it becomes evident that the wet coating process offers a distinct advantage in verifying the uniformity of the coating film, thus, the wet coating processes are extensively employed in commercial cathode material manufacturing to protect the cathode materials. However, one challenge is associated with the sensitivity of Ni-rich NCM cathode materials to water, owing to the excessive Li used for Ni-rich NCM cathodes to maintain a layered structure. Therefore, a non-aqueous environment, for example in ethanol, is more suitable for the surface coating of Ni-rich NCM cathodes (Li et al., 2020b, Xia et al., 2018b). These studies open the mind to exploring the utilization of the non-aqueous environment to modify NLO materials in the wet coating process to achieve coating protection in this PhD research.

2.2.2. Doping of Ni-rich Cathode Materials for Lithium-ion Batteries

Doping, also known as cation substitution, has proven to be a promising way to overcome the problem of structural instability of electrode materials, so as to enhance the cycling stability and safety issues of Ni-rich cathode materials. Many dopant ions have been studied to improve the structural stability of Ni-rich materials. Common dopants used for NLO are Al–aluminum, Zr–zirconium, Ti–titanium, B–boron, etc. (Yan et al., 2020). The C/3 cycling test of NCM811 electrodes comprising undoped and doped active materials in coin cells at 45°C was performed by Weigel et al. as shown in **Figure 2. 21** (Weigel et al., 2019). The C/3 cycling test results shown in **Figure 2. 21** were performed from 2.8 V to 4.3 V after 1 cycle at C/15 rate, 2 cycles at C/10, then a rate capability measurement with 3 cycles at C/3, 0.8 C, 1 C, 2 C, 4 C and C/10 (C defined as 180 mAh g⁻¹). Al–aluminum, Ti–titanium, Mg–magnesium, Si–silicon, Zr–zirconium, and Ta–tantalum are the doped elements. Obviously, unlike the undoped NCM811 cathodes (black points) exhibiting relatively fast capacity fading, the capacity fading rate of the doped NCM811 cathodes slows down. In particular, Ta-doped NCM811 exhibited the highest discharge capacity and the best long-term cycling stability. Such improvement is considered to be related to the multiple structural and surface effects associated with (1) the limitation of the *c* parameter contraction at the end of the charging, (2) the increased Li⁺ ion intercalation kinetics, (3) the decreased cation mixing, and (4) the surface stabilisation together with the lowered impedance growth throughout cycling (Weigel et al., 2019).

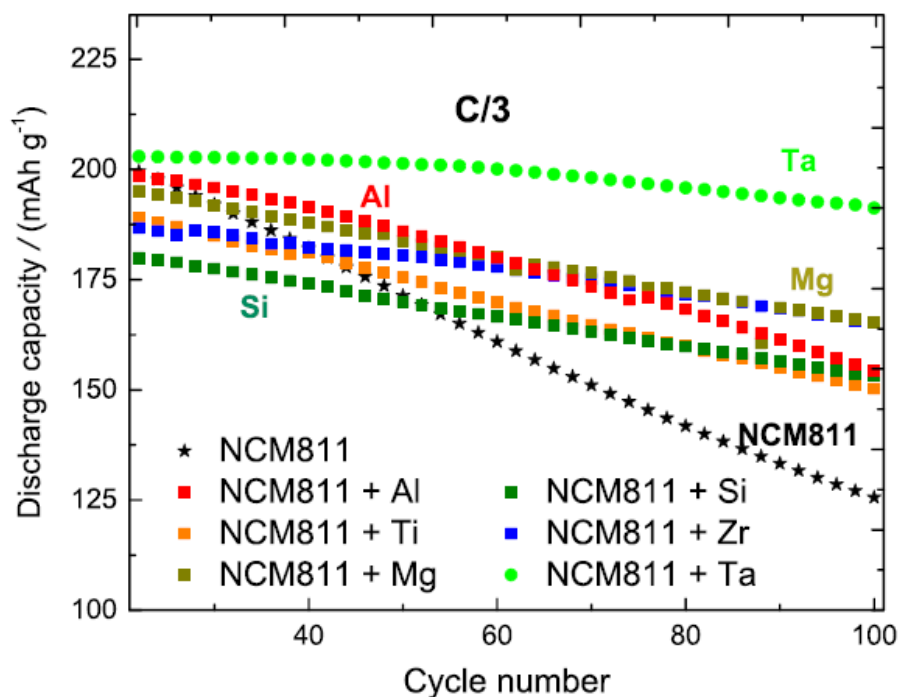


Figure 2. 21. Discharge capacities of NCM811 electrodes comprising undoped and doped active materials, in coin cells at 45°C (Weigel et al., 2019).

Except for the cation substitution, anion substitution strategies, such as F–fluorine, Cl–chlorine, and S–sulfur, have also been reported. However, the number of anions available for substitution is smaller than that of cations (Binder et al., 2018). Cation doping is encouraging and requires further study. Nevertheless, there is no thorough explanation of the mechanism by which each dopant element improves the performance of Ni-rich materials.

Normally, the layered structure of electrodes is not affected by a few dopants, except for the formation of small new phases. To achieve doping/atom substitution, researchers have often used co-calcination, self-combustion, co-precipitation, and solid-state reaction methods (Li et al., 2020b). Cations can be divided into four different valence groups: monovalent, divalent, trivalent, and tetravalent. Among them, monovalent and divalent dopant elements act as pillars to support the structural integrity, which remains

in the Li layers. Trivalent and tetravalent dopants occupy the TM sites. The electrochemical performance can be improved through proper doping with increased lattice spacing, reduced bandgap, and increased electrical conductivity of cathodes (Sharifi-Asl et al., 2019).

To clarify the mechanisms of Al and Mg dopants at the atomic level, first-principles calculations were employed to study the effects of Al and Mg doping on oxygen evolution and structural stability in $\text{Li}_{1-x}(\text{Ni}_{0.8-y}\text{Co}_{0.1}\text{Mn}_{0.1})\text{O}_2$ (x and $y = 0.04$ for Mg and Al doping, respectively) (Min et al., 2017). They investigated the most representative defective states, oxygen vacancies, and cation disordering, by computing the formation energies of each defect for the fully lithiated and delithiated structures. The atomic configuration model used for the calculation is shown in **Figure 2. 22**. The calculation results indicate that Al doping at the Ni site results in the lowest formation energy, which is the most energetically stable. Mg doping preferentially occupies the Li sites. Meanwhile, first-principles calculations provide the theoretical foundations to understand that oxygen evolution can be effectively prevented by doping Al with larger formation energy for the oxygen vacancy defective state than the undoped and Mg-doped samples. The cation-disordered structures in the fully lithiated state can be mitigated by doping Mg with a larger formation energy for the Li/Ni exchange defective state than that of the undoped and Al-doped samples.

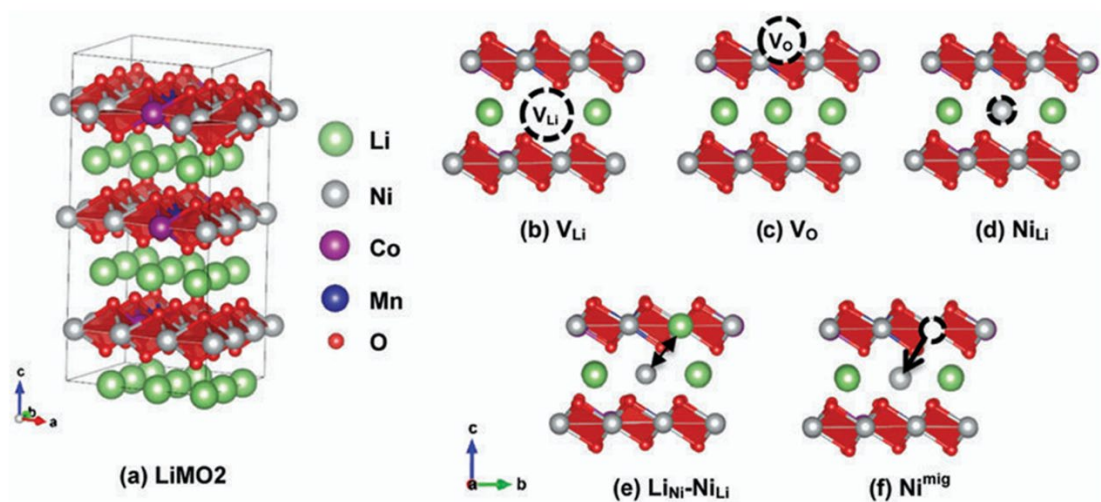


Figure 2. 22. Atomic configurations for the structure of (a) LiMO_2 , where M=transition metals (Ni, Co, and Mn), and the schematic structures for each of the defects, (b) Li vacancies (V_{Li}), (c) oxygen vacancy (V_{O}), (d) excess Ni (Ni_{Li}), (e) Li/Ni exchange ($\text{Li}_{\text{Ni}}-\text{Ni}_{\text{Li}}$), and (f) Ni migration (Ni^{mig}) (Min et al., 2017).

The study on the literature reviews of the doping and coating modifications indicates that doping mainly changes the internal composition of the cathode material, the coating mainly changes the external composition of the cathode material. It is worth noting that, in addition to the different doping elements with distinct modification effects, the doping sites also influence the modification effects, which either stabilise the layered structure or increase the Ni-O bond strength (Zhang, 2020). According to the understanding of the mechanism of Ni-rich NCM electrochemical performance degradation, it is known that the factor of $\text{Li}^+/\text{Ni}^{2+}$ cation mixing causes the nonstoichiometric structure of Ni-rich materials and structure degradation. Beyond the crack generation and capacity fading that can be triggered by the problem of oxygen release, the drawback of oxygen release can also result in serious safety problems, especially for a stoichiometric ratio of $\text{Ni} \geq 0.8$. The weak Ni-O bond is responsible for these problems. To meet the demand for

high-performance batteries for EV applications, it is necessary to explore optimised dopants to stabilise the Li-TM-O host structure of Ni-rich NCM against phase transitions and oxygen release. The binding energy of Ni-O, Co-O, and Mn-O is $391.6 \text{ kJ}\cdot\text{mol}^{-1}$, $368 \text{ kJ}\cdot\text{mol}^{-1}$, and $402 \text{ kJ}\cdot\text{mol}^{-1}$, respectively (Dean, 1978, Chen et al., 2018). B-O binding force is high (B-O bond enthalpy: $809 \text{ kJ}\cdot\text{mol}^{-1}$) (Li et al., 2020a), which is even higher than that of Zr-O ($766 \text{ kJ}\cdot\text{mol}^{-1}$) (Jamil et al., 2020). Boron is a promising choice among the elements available for the doping modification of Ni-rich NCM, which can be the preferred doping element in this PhD research. The B doping sites will be investigated by the analyses of TEM and XRD on the synthesised NLO materials to clarify the B doping effects in the specific experiment.

2.2.3. Beyond Doping and Coating Strategies of Ni-rich Cathode Materials for Lithium-ion Batteries

Beyond the doping and coating strategies for improving the electrochemical performance, different modification strategies have also been proposed, which involve the design of core-shell structure of Ni-rich cathode materials (Wu et al., 2019b, Liu et al., 2021), the design of a full concentration gradient structure (Lim et al., 2016), using a single crystal structure to replace the polycrystalline structure of Ni-rich cathode materials (Deng et al., 2022, Yoon et al., 2023), and refining the primary particles of polycrystalline Ni-rich cathode materials with the radial distribution (Park et al., 2018, Ryu et al., 2020). A schematic of these strategies is presented in **Figure 2. 23**.

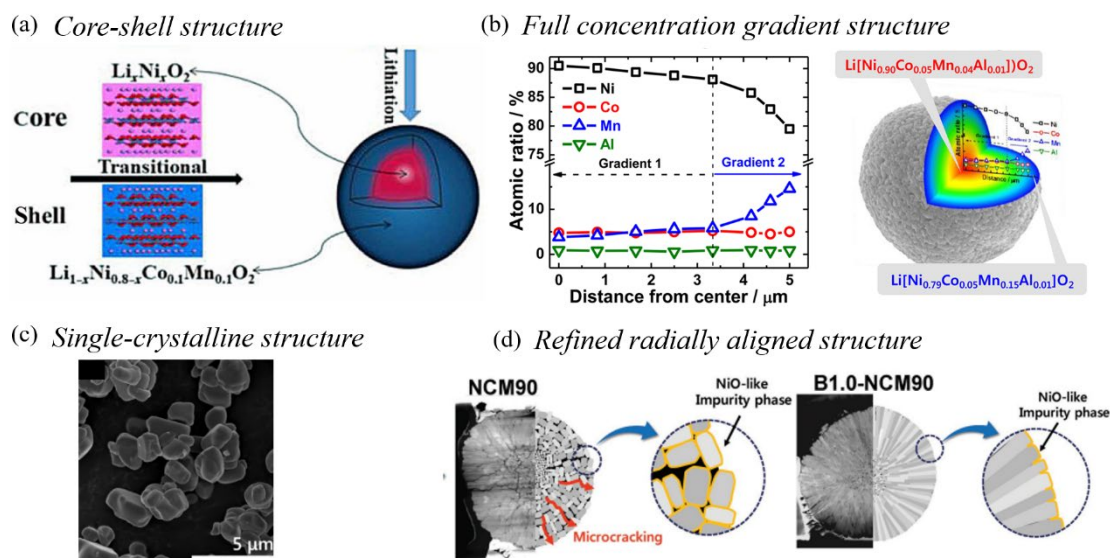


Figure 2. 23. Strategies beyond doping and coating for improving the electrochemical performance of Ni-rich cathode materials: (a) Core-shell structure (Wu et al., 2019b); (b) Full concentration gradient structure (Lim et al., 2016); (c) Single-crystalline structure (Deng et al., 2022); (d) The refined radially aligned structure (Park et al., 2018).

The principles of the above four strategies beyond coating and doping modification are also discussed. The strategies of core-shell structure and full concentration gradient structure aim to create Ni-rich cathode particles with a relatively low Ni content outer layer but an extremely high Ni content inside. Such designs can guarantee a high specific capacity from the inside and cycling stability owing to the protection from the outside layer rich in Co or Mn. However, the corresponding modifications begin with the synthesis of the precursor. The co-precipitation method is mainly adopted to achieve the core-shell structure and full concentration gradient structure by adding a Ni-high aqueous solution into the reactor to form the inside part, followed by the addition of Ni-less aqueous solution to form the outside part. Meanwhile, NaOH solution and ammonia solution acted as the precipitating agent and chelating agent, respectively, during the

entire process.

For the single-crystalline structure strategy, the calcination temperature for obtaining a single-crystal morphology is higher than that of the conventional polycrystalline Ni-rich cathode, which means that more energy will be consumed for calcination. Compared with polycrystalline structures, single-crystalline cathode structures have the advantages of being resistant to mechanical fracturing and tolerance of gas evolution, usually appearing with more stable cycling stability than the polycrystalline Ni-rich cathodes (Ryu et al., 2021, Yang et al., 2023). Owing to the low Li-ion diffusion kinetic inside the single-crystalline cathode material, single-crystal cathodes deliver unsatisfactory performance, especially at high C rates. Reducing the size of single-crystal particles or regulating the surface facets would help to enhance the cathode kinetics and cycling stability (Ran et al., 2022, Kim et al., 2022).

In contrast to the randomly oriented primary particles that form the conventional spherical secondary particles of a Ni-rich cathode, the refined radially particles in the strategy of the refined radially aligned structure are composed of the radially aligned primary particles. The refined structure can shorten the Li-ion diffusion pathways, reduce the aggregation of stress, and dissipate strain energy along the interparticle boundaries during cycling as shown in **Figure 2. 24** (Lee et al., 2019, Ryu et al., 2020). The refined structure has many advantages, which can improve Li-ion diffusion kinetic and achieve better mechanical integrity. It is reported that adding dopants like B, Al, W, and Ta can realise the radially aligned structure of Ni-rich cathode materials, probably owing to the lower surface energy of the (003) facet as the preferential faceting to be

elongated (Sun et al., 2020, Kim et al., 2020). Another viable approach to control the morphology of the Ni-rich cathode materials is to adjust the reaction parameters for synthesising the precursor. Research has shown that a co-precipitation process with an optimised high $\text{NH}_3 \cdot \text{H}_2\text{O}$ concentration and high stirring speed can produce a precursor with a radially aligned structure without dopants (Xu et al., 2019).

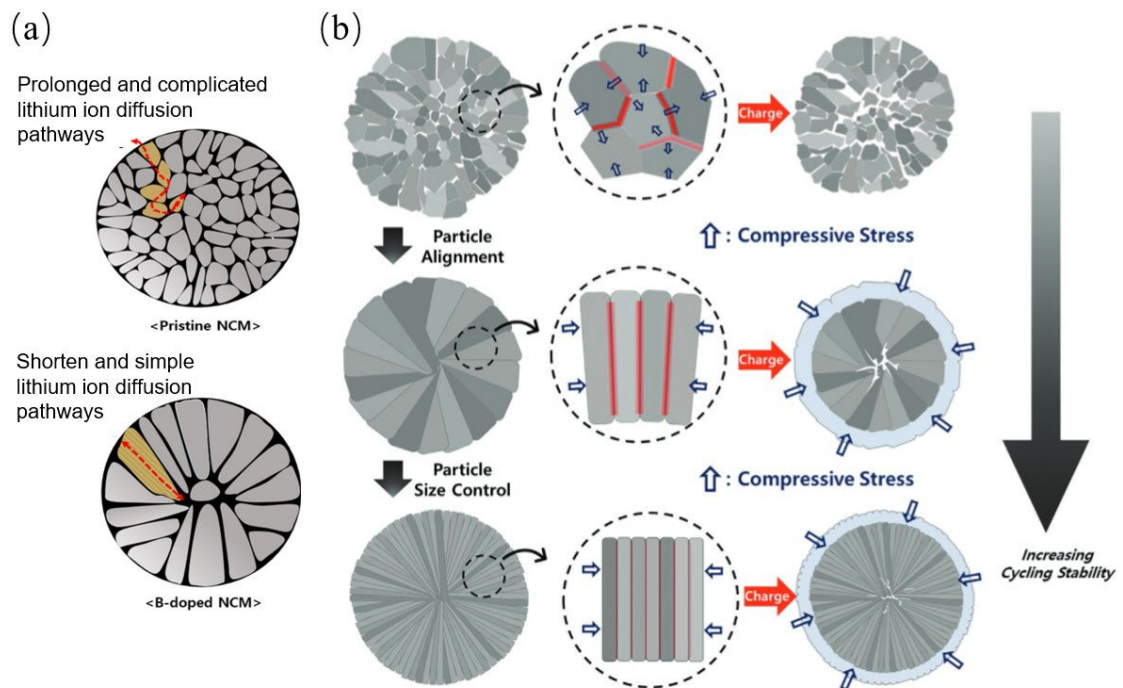


Figure 2. 24. (a) Li-ion diffusion pathways inside the randomly orientated primary particles and the radially aligned primary particles (Lee et al., 2019); (b) Differences in the local stress concentration and stress distribution among the secondary particles consisting of randomly oriented, radially oriented, and size-refined radially oriented particles (Ryu et al., 2020).

In summary, the literature review of the performance degradation mechanism of NLO cathode materials and the current modification strategies helps to understand the problems of NLO cathode materials, answers the question of why the modification is necessary for NLO cathode materials, and instructs the analysis about the modification of NLO cathode materials using the different characterisation tools. The purpose of the modification strategies becomes clear: to strengthen the internal structure, establish a protective layer between the electrode and electrolyte, reduce microcrack occurrence, and ultimately improve the cycling performance, rate capability, and safety issues of NLO cathode materials for LIBs. For NLO ($\text{Ni} \geq 0.8$) cathode materials, the side reaction between the active material surface and the electrolyte is the most detrimental and fatal drawback. A uniform surface protection layer on the NLO cathode materials can be placed as the premier solution. Among the current modification strategies, it is preferable to use wet coating modification, that is co-precipitation coating and sol-gel coating, to build a uniform protection layer. However, some drawbacks to the current wet coatings, such as the complicated process parameters in the co-precipitation strategy and the high-temperature evaporation necessary for the sol-gel strategy, require innovations. The aqueous environment should also be avoided because of the sensitivity of NLO cathode materials to water. To address these problems, a novel wet coating, named sol/antisolvent coating, was developed in this thesis based on the thinking of “like dissolves like”. Considering the multiple modifications may result in better effects, a modification from the novel wet coating method along with the combined doping and coating treatment and the radially aligned structure was proposed.

Chapter 3 Materials and Equipment

This chapter describes the materials and experimental equipment used to modify Ni-rich cathode materials and prepare coin cells. The coin cell assembly process, electrochemical property test equipment, and material characterisation instruments are also listed.

3.1. Materials and Experimental Equipment

Table 3. 1 presents the materials and reagents used in this study. Ni-rich NCM with stoichiometric ratios of $\text{Ni} \geq 0.8$ is the object of modification to achieve superior NLO cathodes. Ni content of cathode materials and precursors used in this study was greater than 80%. $\text{LiNi}_{0.85}\text{Co}_{0.1}\text{Mn}_{0.05}\text{O}_2$ from Ningbo Rongbay New Energy Technology Co., Ltd was used as the cathode material. $\text{Ni}_{0.83}\text{Co}_{0.05}\text{Mn}_{0.12}(\text{OH})_2$ and $\text{Ni}(\text{OH})_2$ were obtained from Zhejiang Huayou Cobalt Co., Ltd., and Hebei Guifa Alloy Wear-Resistant Materials Co. Ltd., respectively. $\text{LiOH}\cdot\text{H}_2\text{O}$ was used as the Li source. Carbon black (Super P®), polyvinylidene fluoride (PVDF), and N-methyl pyrrolidone (NMP) were used as the conductive agent, binder, and solvent to be mixed with the NLO powders to prepare the electrode slurry. Lithium metaborate (LiBO_2) was a coating material used to modify Ni-rich cathode materials. Boron oxide (B_2O_3) was used to realise boron-related coating/doping of Ni-rich cathode material. Ethanol ($\text{C}_2\text{H}_5\text{OH}$) and tetrahydrofuran ($\text{C}_4\text{H}_8\text{O}$) were solvents with different functions used in the modification process.

Table 3. 1. Materials and reagents used in the study.

No.	Material	Manufacturer	Application
1	$\text{LiNi}_{0.85}\text{Co}_{0.1}\text{Mn}_{0.05}\text{O}_2$	Ningbo Ronbay New Energy Technology Co., Ltd.	Cathode material to be modified.
2	$\text{Ni}_{0.83}\text{Co}_{0.05}\text{Mn}_{0.12}(\text{OH})_2$	Zhejiang Huayou Cobalt Co., Ltd.	Precursor to be modified.
3	$\text{Ni}(\text{OH})_2$	Hebei Guifa Alloy Wear-Resistant Materials Co. Ltd.	Precursor to be modified.
4	$\text{LiOH}\cdot\text{H}_2\text{O}$	Aladdin (Purity: 98%)	Lithium source for lithiation calcination.
5	Carbon black (Super P®)	Alfa Aesar (Purity: 99+%)	Conductive agent for preparing electrode slurry.
6	Polyvinylidene fluoride (PVDF)	Kynar (HSV 900)	Binder for preparing electrode slurry.
7	N-methyl pyrrolidone (NMP)	Aladdin (Purity: 99.9%)	Solvent for preparing electrode slurry.
8	Lithium metaborate (LiBO_2)	Aladdin (Purity: 99.9%)	Coating material for modification.
9	Boron oxide (B_2O_3)	Aladdin (Purity: 99.9%)	Boron-related coating/doping modification.
10	Ethanol ($\text{C}_2\text{H}_5\text{OH}$)	Aladdin (Purity: 99.8±%)	Dispersion medium for modification process.
11	Tetrahydrofuran ($\text{C}_4\text{H}_8\text{O}$)	Aladdin (Purity: 99.9±%)	Antisolvent for modification process.

Figure 3. 1, **Figure 3. 2**, and **Figure 3. 3** show the primary experimental equipment, including the BEQ horizontal high-temperature tubular furnace (**Figure 3. 1**), WZM 1.5 L double-tank ball mill machine (**Figure 3. 2**), and MBRAUN UNI-lab glove box workstation (**Figure 3. 3**). The tubular furnace was mainly used for the calcination process to synthesise superior Ni-rich cathode materials. The ball mill machine was used to evenly mix the lithium source and the precursor of the cathode active materials. The coin cell assembly and disassembly were performed in the glove box filled with protective argon gas, with O₂ and H₂O concentrations of less than 0.5 ppm. In addition to the large equipment, some relatively small equipment are not shown. They are also indispensable in applications, such as multi-point magnetic stirrers, automatic film applicators, electrode sheet punching machines, laboratory tablet compressors, hydraulic crimpers, and blast drying ovens. These relatively small pieces of equipment were used to stir the electrode slurry, coat the electrode slurry onto aluminum foil, punch the electrode sheet, compress the electrode sheet, seal the coin cell, dry the materials, and evaporate the organic solvents. All of these play important roles in the transformation of raw materials into finished cells.



Figure 3. 1. BEQ horizontal high-temperature tubular furnace.



Figure 3. 2. WZM 1.5 L double-tank ball mill machine.



Figure 3. 3. MBRAUN UNI-lab glove box workstation.

3.2. Electrochemical Property Test Equipment and Material Characterisation Instruments

In this study, the coin cells were used for testing the electrochemical properties of NLO materials. A schematic diagram of the coin cell assembly showing each component is presented in **Figure 3. 4**. The coin cell was composed of a positive case, cathode, separator, anode, spacer, spring, and negative case. After the components were assembled in sequence, as depicted in **Figure 3. 4**, the appropriate amount of electrolyte was added to the cell, then the cell was sealed on a hydraulic crimper to produce the

final coin cell battery. The cathode slurry was coated onto the aluminum foil and dried to form the cathode. The separator was a monolayer or multilayer microporous membrane obtained from Celgard®. A pure lithium disk was used as the anode. The addition of a spacer and spring closely packed the coin cell.

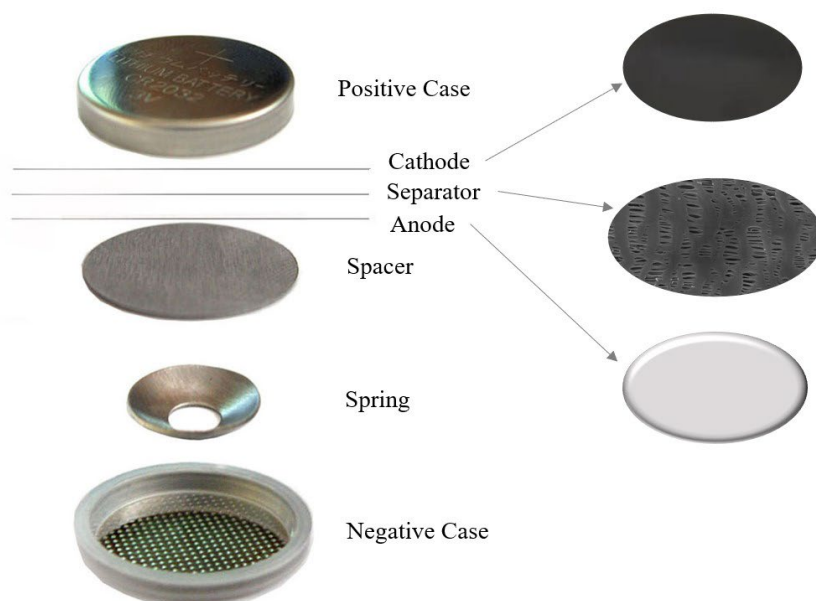


Figure 3. 4. Coin cell assembly showing each component.

Solartron Analytical 1400 cell test station and Wuhan LAND cell test system were used to analyse the electrochemical properties of the coin cells. The corresponding test stations are shown in **Figure 3. 5** and **Figure 3. 6**, separately. Cyclic voltammetry measurement (CV) and electrochemical impedance spectroscopy (EIS) of the coin cell batteries were performed using a Solartron Analytical workstation. Galvanostatic cycling with potential limitation (GCPL) measurements were completed in the LAND cell test system, which involves long-term cycling tests, rate capability tests, different cut-off voltage tests, and different current density tests. The LAND cell test system can

also make the coin cell battery in the delithiated state for further thermal stability evaluation. To minimise the impact of atmospheric fluctuations, these two electrochemical property test systems were kept in a separate battery testing room with controlled temperature and humidity levels.



Figure 3. 5. Solartron Analytical 1400 cell test station.

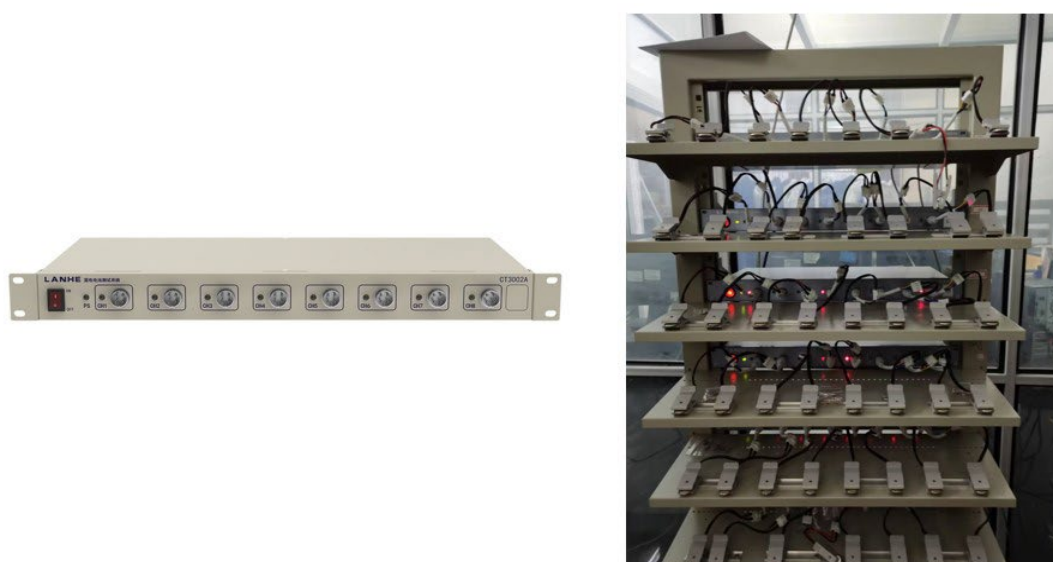


Figure 3. 6. Wuhan LAND cell test system: left is the LANHE CT3002A system with 8 channels; right is the real test image.

The names and brands of the material characterisation instruments used in this study are listed in **Table 3. 2.** Main material characterisation instruments used in this study.. The pictures of material characterisation instruments are not shown here, as they can be obtained by contacting the dealers. The purpose of each material characterisation instrument is summarised. SEM is used to observe the microscopic morphology of the material. TEM is used to identify the morphology of the nano-sized coating layer and the phase transitions of the material. SEM/EDS is used to analyse the element distribution of the material. TEM/EDS is used to determine the element composition by semi-quantitative estimation. XRD is used to identify the material's crystalline structure. AFM is used to present the 3D image of the material and calculate Young's modulus. FIB-SEM is used to observe the microstructure of the cross-section of the material. XPS is used to analyse the chemical state of the material surface. ICP-OES is used for qualifying the dissolved elements from the material. DSC-TG is used to observe the dehydration and decomposition of material. DSC 3 is used to measure phase transition and heat flow from the material. FTIR is used to determine the existence of a particular substance. Some of these characterisation instruments are complementary to obtaining the structural and functional information for the material. A thorough understanding of the material can be realised using multiple characterisation technologies. The specific applications of each characterisation instrument are elaborated in detail in the subsequent sections. Thanks to these characterisation technologies, the mechanism of each modification on NLO cathode materials can be clarified.

Table 3. 2. Main material characterisation instruments used in this study.

No.	Characterisation Method	Instrument
1	Scanning electron microscope (SEM)	Hitachi S4800
2	Transmission electron microscope (TEM)	JEOL JEM2100
3	Scanning electron microscopy with energy dispersive X-ray spectroscopy (SEM/EDS)	FEI Quanta FEG 250
4	Transmission electron microscope equipped with energy dispersive X-ray spectroscopy (TEM/EDS)	ThermoFisher Talos F200x
5	X-ray diffraction (XRD)	Bruker D8 DISCOVER
6	Atomic force microscope (AFM)	VEECO Dimension 3100
7	Focused ion beam scanning electron microscope (FIB-SEM)	Carl Zeiss Auriga
8	X-ray photoelectron spectroscopy (XPS)	Shimadzu Krotos AXIS Supra
9	Inductively coupled plasma optical emission spectrometer (ICP-OES)	SPECTRO ARCOS
10	Differential scanning calorimetry and thermogravimetric analyser (DSC-TG)	NETZSCH STA 449F3
11	Thermal analysis system (DSC 3)	Mettler Toledo
12	Fourier transform infrared spectrometer (FTIR)	Thermo Nicolet 6700

Chapter 4 Sol/Antisolvent Coating with Crystalline LiBO₂ for LiNi_{0.85}Co_{0.1}Mn_{0.05}O₂ Cathode Towards High Initial Coulombic Efficiency and Ultra-stable Mechanical Integrity

This chapter reports the novel and facile sol/antisolvent coating modification of LiNi_{0.85}Co_{0.1}Mn_{0.05}O₂ (NCM). Ethanol was used to disperse the nano-sized LiBO₂ to form the sol, and tetrahydrofuran (THF) was used as an antisolvent to prepare a cluster of nanoparticles to be coated on the surface of NCM. The coating thickness could be tuned by varying the amount of THF added. The LiBO₂ nanorod deposition was formed over the crack of the NCM cathode, likely acting as a patch to repair the original defect of the intrinsic crack. The uniform LiBO₂ nano-spherical particles coating together with LiBO₂ nanorods wrapping provided double protection against electrolytes. This simple in-site modification and repair technology guarantees a high initial Coulombic efficiency of 90.3% at 0.2 C between 2.8 and 4.3 V vs Li⁺/Li, superior rate capability, enhanced fast charge property at 3 C, and good mechanical integrity of the polycrystalline Ni-rich cathode. The work described in this chapter has been published in 2022.

4.1. Introduction

As mentioned in Chapter 1, Ni-rich layered oxides (NLO) (Ni ≥ 80%) are promising

cathode materials for high-energy LIBs for EVs. However, their practical application is difficult because of the effects of the four main problems, including $\text{Li}^+/\text{Ni}^{2+}$ cation mixing, surface structural degradation, side reactions, and microcracks, which have been introduced in Chapter 2. Among these four problems, the problem of microcracks is very harmful to the long-term capacity of NLO cathodes, as it increases cell impedance and accelerates side reactions. The anisotropic shrinkage and expansion of the primary particles from the H2→H3 phase transition are responsible for the intergranular cracking (Yin et al., 2021). On the other hand, intragranular cracks can be ascribed to bond dissociation or structural instability, which is not only a mechanical failure but also a problem of structural degradation (Min and Cho, 2018, Yin et al., 2021). Both single-crystalline NLO (SC-NLO) and polycrystalline NLO (PC-NLO) can suffer microcracks (Ryu et al., 2021), but SC-NLO exhibits relatively high mechanical integrity compared with PC-NLO (Payandeh et al., 2021). For PC-NLO, intergranular cracking has been demonstrated to be a critical mechanism for cycling degradation because of the existence of grain boundaries and voids inside the primary particles as the mechanically weak part of the material (Liu et al., 2017), which is also mentioned in Chapter 2. In particular, under fast (dis)charging conditions, the degree of cracking becomes significant. The cracks not only gathered at the centre of the PC-NLO but also developed to the secondary particle surface with the increase in current density (Xia et al., 2018a). Therefore, it is a great challenge to mitigate the prominent problem of intergranular microcracks in PC-NLO during cycling at fast (dis)charging. The purpose of this study is to alleviate the formation of microcracks and synergistically improve the

electrochemical properties of polycrystalline Ni-rich cathode materials.

Surface coating is a fundamental and effective method for modifying cathode materials with reduced microcracks. In particular, the surface coating acted as a protective passivation film with high stability. The coating layer plays a role in preventing direct contact between the cathode material and electrolyte, and to a certain extent, avoids the attack from the electrolyte and diminishes the potentially harmful side reactions related to structural stability. For instance, metal ion dissolution results from HF erosion (Yan et al., 2020). The surface phase transformations of the NLO cathode can also be released under the protection of the coating layer owing to the slow interfacial reaction between high-valence Ni^{4+} ions and the electrolyte with fewer Ni^{2+} ions (Xia et al., 2018b). Among these coating materials, LiBO_2 modification of cathode materials is abundant because of its high Li-ion conductivity and deformability, even for application in all-solid-state lithium batteries (Li et al., 2020a, Du et al., 2019, Zhang et al., 2019c). To the best of our knowledge, there are two predominant methods adopted for coating LiBO_2 : the dry coating method with ball milling and a solution method based on the chemical reaction between H_3BO_3 and $\text{LiOH}\cdot\text{H}_2\text{O}$ or residual lithium species (LiOH or Li_2CO_3) on NLO (Li et al., 2020a, Lim et al., 2014, Du et al., 2019). In comparison to the dry coating of typical inhomogeneous and islanded characteristics, it is easy to confirm the uniformity of the coating film using the wet chemical coating of the solution method (Nisar et al., 2021). However, the conventional solution method normally requires a complex synthesis process with a high temperature and a long coating time (Zuo et al., 2017). Therefore, a new wet-coating method must be developed.

An antisolvent precipitation method has attracted our attention, which presents the unique advantage of an easy process in which ethanol is used as an antisolvent with poor solubility to realise lithium-containing oxide precipitation on $\text{LiNi}_{0.5}\text{Co}_{0.2}\text{Mn}_{0.3}\text{O}_2$ and $\text{LiNi}_{0.8}\text{Co}_{0.1}\text{Mn}_{0.1}\text{O}_2$ in a completely dissolved lithium-containing oxide aqueous solution (Hashigami et al., 2019b, Hashigami et al., 2018, Hashigami et al., 2019a). Antisolvent precipitation is a key process that can be realised at room temperature. However, considering the sensitivity of water to NLO with metallic element leaching, as well as the possibility of surface structure destruction because of excessive Li existence to maintain a layered structure (Xia et al., 2018b, Zuo et al., 2017). The aqueous environment should be avoided. It was reported that the sol system can guarantee a uniform coating reagent distribution with the help of chelating agents such as citric acid (Zuo et al., 2017), or dispersion of coating precursors such as metallo-organic compounds in ethanol or methanol (Li et al., 2016, Huy et al., 1996). Herein, the integration of the sol system and the antisolvent effect without the chemical reaction process is envisaged for the coating. This is a purely physical process involving nanoparticle dispersion and aggregation. A schematic of the strategy for sol/antisolvent LiBO_2 coating of the active material is shown in **Figure 4. 1**. The key steps include forming a nano- LiBO_2 sol in an organic medium with a commercial LiBO_2 powder and utilising the antisolvent effect of other organic media to accomplish LiBO_2 nanoparticle aggregation and its deposition on active materials. With further antisolvent treatment and high-speed rotation, LiBO_2 nanoparticles can be transformed into nanorods and wrapped on the outermost surface after coating with smaller nano- LiBO_2 . Post-

calcination in an oxygen atmosphere was performed to obtain the final LiBO_2 -coated NCM. The protection mechanism of the LiBO_2 nanoparticle coating was achieved by hindering electrolyte penetration into NLO, restricting TM ion dissolution, and protecting against attack from HF.

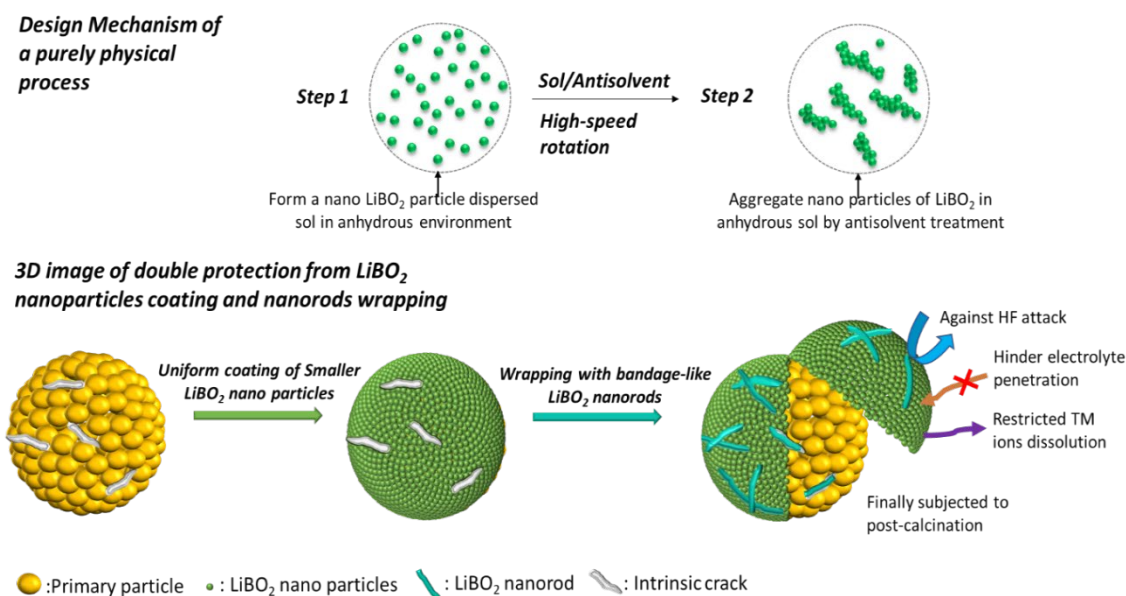


Figure 4. 1. Design mechanism of the sol/antisolvent method in anhydrous environment for coating.

Such a sol/antisolvent wet coating is fast and convenient, with a coating time of only 35 min. PC-NLO coated by salmon-roe-like nano LiBO_2 particles was developed using this method. The final synthesised LiBO_2 -coated NCM has a three-layer structure with a thin NiO-like rock-salt phase layer existing between the LiBO_2 coating layer and the NCM bulk of the layered structure, which exhibits enhanced Li-ion diffusion characteristic and improved rate capability. The fast-charging property is improved with higher capacity retention and restricted microcracks, according to the cathode cross-section observations. In addition, the ICE developed from 78.65% for pristine NCM to a very high ICE value of 90.3% after LiBO_2 coating at 0.2 C. Moreover, the bandage-like

LiBO₂ nanorods can deposit over the crack, likely acting as a patch to repair the intrinsic defect before battery operation. Owing to the additional blocking from the LiBO₂ nanorods, the penetration of the electrolyte into the interior of the electrode along the intrinsic cracks can be further mitigated. The side reactions could also be alleviated to a large extent. It is expected that such a facile sol/antisolvent wet coating can result in good mechanical integrity of the PC-NLO during cycling.

4.2. Experimental Section

4.2.1. Pristine NCM and LiBO₂ powders

The pristine NCM sample is LiNi_{0.85}Co_{0.1}Mn_{0.05}O₂, a kind of PC-NLO obtained from Ningbo Ronbay New Energy Technology Co., Ltd (Ronbay). HELOS (H3938) & OASISDRY/L, R3 laser particle size analyser was used to evaluate the particle size distribution of the NCM. The result is shown in **Figure 4. 2** with the volume mean diameter (VMD) of 11 μm. The D₁₀, D₅₀, and D₉₀ were 4.71 μm, 10.07 μm, and 18.62 μm respectively. Anhydrous LiBO₂ powder as the coating material was purchased from Aladdin, Shanghai. To understand the thermal properties of the pristine NCM and LiBO₂ powders, differential scanning calorimetry (DSC) and thermogravimetric (TG) analysis were performed using a simultaneous thermal analyser NETZSCH STA 449F3 in an argon atmosphere.

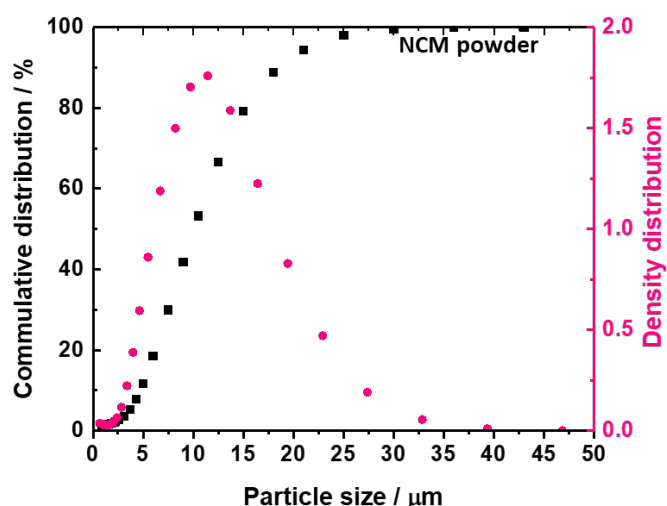


Figure 4. 2. Particle size distribution of $\text{LiNi}_{0.85}\text{Co}_{0.1}\text{Mn}_{0.05}\text{O}_2$ (NCM) powders.

4.2.2. Synthesis of LiBO_2 -coated NCM by Sol/Antisolvent Wet Coating

LiBO_2 -coated NCM was synthesised by combining sol/antisolvent wet coating of NCM with nano- LiBO_2 . A schematic of the actual experimental operation is shown in **Figure 4. 3**. First, the NCM powder was mixed with a LiBO_2 ethanol sol solution. THF was chosen as the antisolvent with a very low polarity (dielectric constant of 7.52) compared to that of ethanol (dielectric constant of 24.6) (Society, 2022). LiBO_2 coating is fulfilled by making the aggregation of nano- LiBO_2 deposits on the surface of NCM with THF antisolvent effect. The nano- LiBO_2 dispersed ethanol sol was produced using anhydrous alcohol to disperse the LiBO_2 particles with the assistance of an ultrasonic instrument. The selection of THF as an antisolvent is not just only based on the consideration of the large polarity difference between ethanol and THF, the properties of relatively inert, high volatility, and good wettability of THF are also the advantages to be chosen as the antisolvent. Due to inertia, the undesired detriment to the performance of cathode

material during the mixing can be averted. Because of its high volatility, THF can be easily removed after drying in a blast drying oven. With the help of good wettability, not only is the outer surface of the primary particles of Ni-rich cathode material covered by LiBO_2 nanoparticles, but the gaps between the primary particles can also be adhered by some LiBO_2 nanoparticles. The gaps between the primary particles are the mechanical weak part of the material, involving grain boundaries and voids, the deposition of LiBO_2 nanoparticles on gaps ensures better protection against electrolyte attack.

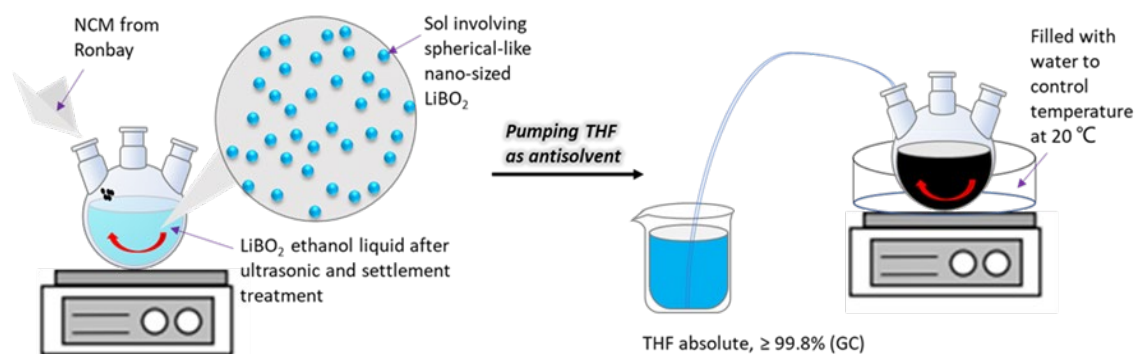


Figure 4. 3. Schematic diagram of combined sol/antisolvent wet coating NCM with nano- LiBO_2 : First, NCM powder was mixed in LiBO_2 ethanol sol, followed by pumping THF as an antisolvent for depositing LiBO_2 on the NCM surface.

The detailed experimental procedure is as follows. To prepare LiBO_2 -coated NCM, 2 g NCM powder was weighed for each coating modification. To produce the LiBO_2 ethanol sol, 0.083 g LiBO_2 (mass ratio for LiBO_2/NCM was 4:96) was added to 60 mL of anhydrous alcohol with ultrasonic treatment for 9 h at a frequency of 53 kHz. After settlement for 3.5 days, the sol was obtained for the follow-up wet coating. The sol showed no obvious “Tyndall effect” at bright environment but a very clear “Tyndall

effect” in a dark environment with laser beam irradiation (**Figure 4. 4**). The 50 mL upper clear liquid from the two beakers (i.e. LiBO₂ ethanol sol) was put into a three-neck flask. 2 g NCM powder was added to the sol and stirred at 800 rpm for 10 min. After mixing the NCM powders in the sol, the sol turned black. THF was pumped into the black liquid using a peristaltic pump to coat LiBO₂ onto the surface of the NCM. The entire process was performed in a three-neck flask maintained at 20 °C in a water bath with continuous magnetic stirring. After full consumption of THF, the black liquid was vacuum filtered to collect the produced LiBO₂-adhered NCM powder. The powder was then placed in a blast drying oven at 50 °C and dried overnight. The dried powder was transferred into a tubular furnace and heated at 500 °C for 8 h in an oxygen atmosphere to enhance the mechanical properties of the coating film. The final LiBO₂-coated NCM was synthesised via calcination.

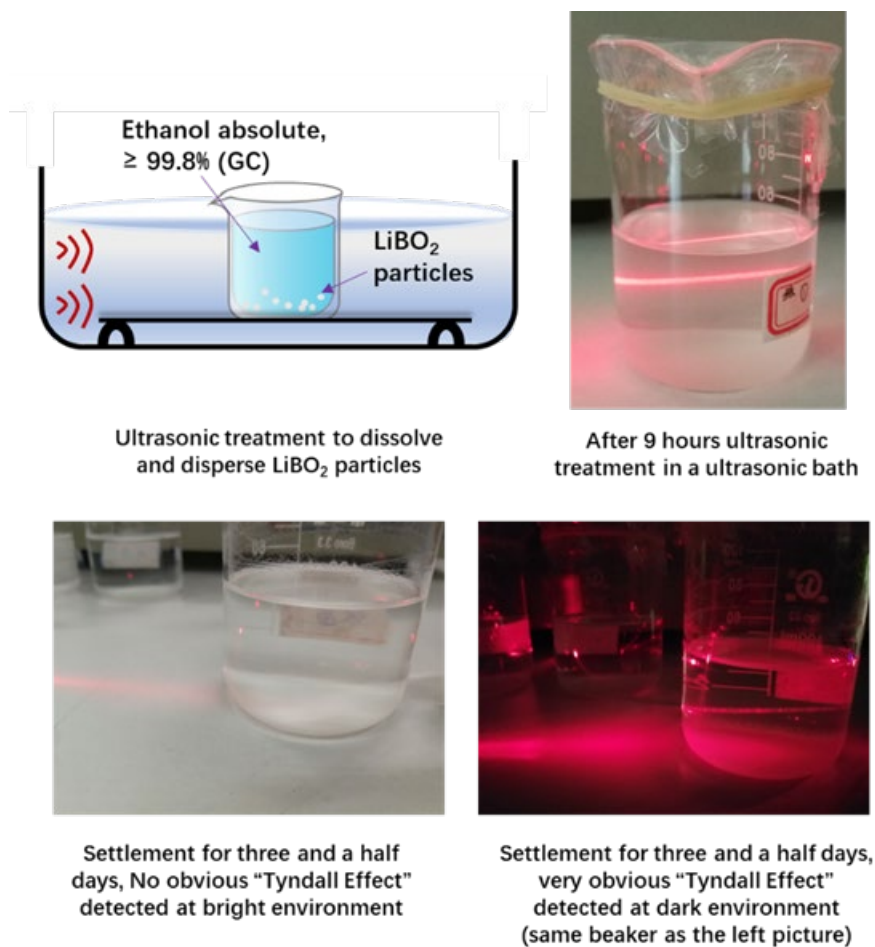


Figure 4. 4. Pictures of "Tyndall effect" of prepared LiBO₂ ethanol sol.

To control the different coating thicknesses, two different addition dosages of 70 ml and 35 ml THF were applied, which corresponded to pumping times of 35 min and 17.5 min at a flow rate of 2 ml/min through the peristaltic pump. The modified samples with 35-min and 17.5-min THF treatment were named 1b-NCM and 2b-NCM, respectively, where b represents LiBO₂. As a supplement, the antisolvent effect of THF was verified using a laser beam, where the scattering light intensity became strong after pouring THF into the LiBO₂ ethanol sol (**Figure 4. 5**).

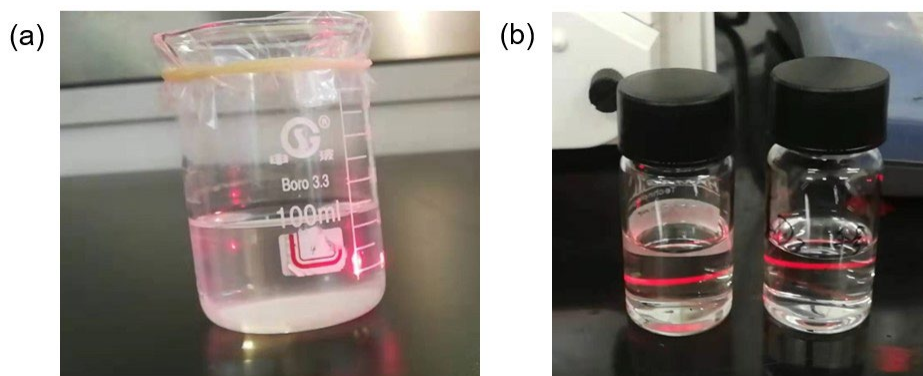


Figure 4. 5. (a) No clear scattering of light on the irradiation of laser beam in sol after settlement for three and a half days; (b) Stronger scattering of light through the colloidal particles after adding THF into the upper LiBO_2 ethanol sol.

4.2.3. Materials Characterisation

ICP-OES (SPECTRO ARCOS) analysis was performed to confirm the elementary composition of the NCM sample. The morphologies and microstructures of NCM and LiBO_2 -coated NCM were analysed using scanning electron microscope (SEM, S4800, Hitachi) and transmission electron microscope (TEM, JEM2100, JEOL). Elemental analysis was performed using scanning electron microscopy with energy dispersive X-ray spectroscopy (SEM/EDS, FEI Quanta FEG 250). The crystalline structure was tested by high-performance X-ray diffraction (XRD, D8 DISCOVER, Bruker) from 10° to 80° at a scan rate of $1^\circ/\text{min}$. The obtained XRD data were analysed using the Rietveld refinement program in the General Structure Analysis System (GSAS) software package. Atomic Force Microscope (AFM, Dimension 3100, Veeco) was used to probe the 3D geometric features and mechanical properties of the materials. The cross-section of the cathode materials was examined using focused ion beam (FIB)-SEM (Auriga, Carl Zeiss). To investigate the composition characteristics of solid electrolyte interphase (SEI)

formation, X-ray photoelectron spectroscopy (XPS, Krotos AXIS Supra, Shimadzu) was performed on the surface of the cathode.

4.2.4. Electrochemical Tests

The electrochemical performances of the NCM and LiBO₂-coated NCM materials were investigated through galvanostatic cycling with potential limitation (GCPL) measurements between 2.8-4.3 V (vs. Li/Li⁺) at different current densities (1 C = 200 mA g⁻¹) at room temperature using a LAND cell test system in a 2032 coin-type half cell. The cell was mainly composed of cathode electrodes, lithium metal foil as the anode, Celgard 2400 separator, and an electrolyte of 1M LiPF₆ in a volume ratio of 3:7 ethylene carbonate (EC)/dimethyl carbonate (DMC). The slurry for preparing the cathode electrode was prepared by magnetic mixing of the active material, Super P conductor, and PVDF binder in a mass ratio of 8:1:1 in N-methyl pyrrolidone (NMP) solvent. The slurry was subsequently coated onto an Al foil, dried in a blast drying oven at 80 °C for 12 h, and then punched and pressed into circle electrodes with a diameter of 14 mm. The as-prepared cathode electrode was incorporated into a coin-type cell filled with 80 μL electrolyte in an argon-filled glove box (O₂ < 0.5 ppm; H₂O < 0.5 ppm, MBRAUN UniLab). The mass loading of active material was approximately 5 mg cm⁻². After completion of the cell assembly, the coin-type cells were placed in a battery testing room for 24 h before the electrochemical test. Cyclic voltammetry (CV) measurements and electrochemical impedance spectroscopy (EIS) tests over the frequency range of 0.1 MHz to 0.01 Hz between 2.8-4.3 V (vs. Li/Li⁺) at 0.1 mV/s plus

the varied scan rates were conducted on an electrochemical workstation (Solartron Analytical). Li-ion diffusion coefficient and resistance of different coin cells with the NCM cathode and LiBO₂-coated NCM cathode were studied.

4.3. Results and Discussion

4.3.1. Successful Synthesising of LiBO₂-coated NCM by Sol/Antisolvent Wet Coating

LiBO₂ is an ionic compound with high polarity, based on the principle of “like dissolves like”, the weaker the polarity of the solution, the lower the solubility of LiBO₂. The solubility of crystalline LiBO₂ in water is 2.57 g/100 g (20 °C), whereas, for ethanol, the solubility is very poor. It was even reported that crystalline lithium borate powder is insoluble in alcohol (Agency, 1980, Kipper, 2007). Ethanol has a relatively low polarity with a dielectric constant of 24.6, compared with water with a high dielectric constant of 78.54 (20 °C) (Society, 2022). Due to the poor solubility of LiBO₂ in the ethanol solution, the LiBO₂ sol dispersed in ethanol can be prepared (**Figure 4. 4**).

Although the LiBO₂ ethanol sol has been produced, it is essential to determine whether the following antisolvent treatment is effective in transferring the nanoparticles onto the NCM surface. SEM was first performed to characterise the microstructures of the pristine NCM, 1b-NCM, and 2b-NCM samples, and the results are shown in **Figure 4.**

6. Figure 4. 6. (a) illustrates the SEM image of the pristine NCM, wherein some small particles are detected depositing along the grain boundaries, which should be the lithium residues. Compared with NCM particles with a mean diameter of 11 μm, the amount of

lithium residue is small. The sol/antisolvent coating modification and post-calcination did not remove the existence of the lithium residues from NCM. This is mainly because the post-calcination temperature is only 500 °C, which is much lower than the thermal decomposition temperature of LiOH (starting at 800 °C with the reaction $\text{LiOH} \rightarrow \text{Li}_2\text{O} + \text{H}_2\text{O}$) and Li_2CO_3 (starting at 730 °C with the reaction $\text{Li}_2\text{CO}_3 \rightarrow \text{Li}_2\text{O} + \text{CO}_2$). It is difficult to reduce the lithium residues by post-calcination at 500 °C. Because of the small amount of lithium residues and the small impact of the modification treatment on the lithium residues, it is reasonable to compare the pristine sample with the modified sample subjected to the post-calcination process.

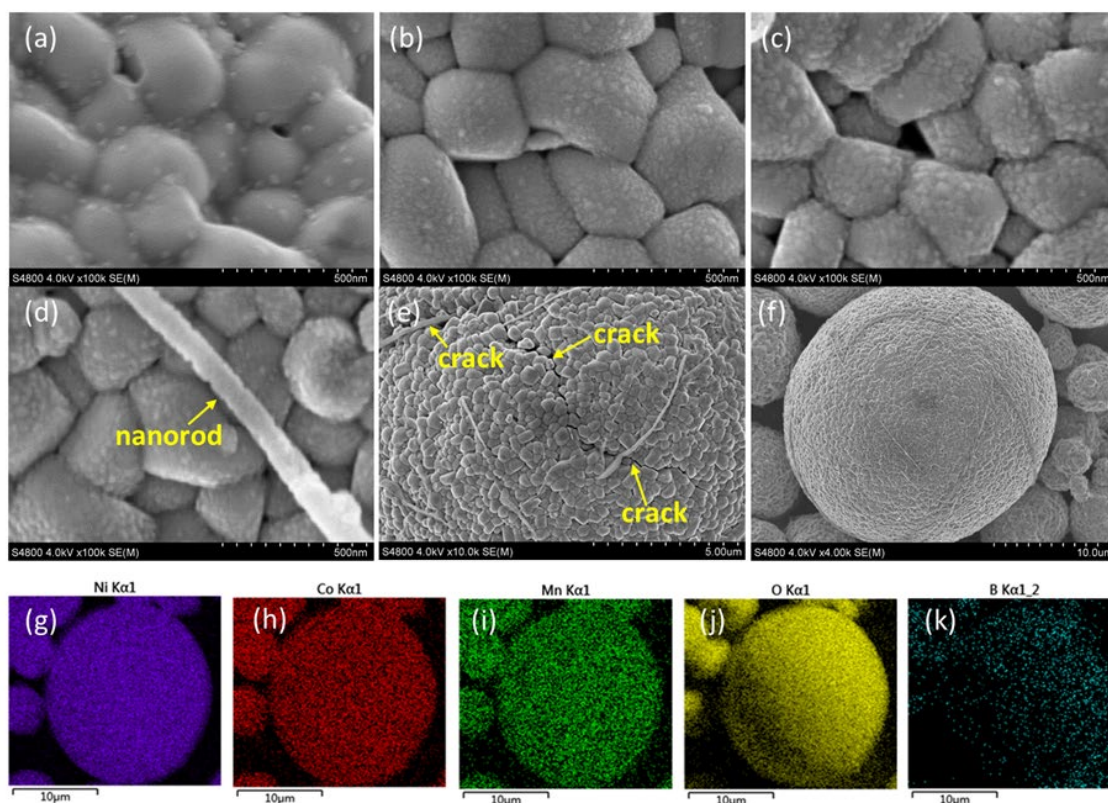


Figure 4. 6. SEM images: (a) pristine NCM, (b) 1b-NCM, (c) 2b-NCM, (d-f) bandage-like nanorod wrapping the outmost layer of 1b-NCM; and EDS mapping of Ni, Co, Mn, O and B elements: (g-k) 1b-NCM.

Figure 4. 6. SEM images: (a) pristine NCM, (b) 1b-NCM, (c) 2b-NCM, (d-f) bandage-like nanorod wrapping the outmost layer of 1b-NCM; and EDS mapping of Ni, Co, Mn, O and B elements: (g-k) 1b-NCM. show SEM images of 1b-NCM and 2b-NCM, respectively. Both surfaces are intensively covered by nano-sized particles, which are completely different from pristine NCM. Compared to 2b-NCM treated with 35 ml of THF, 1b-NCM was subjected to a double dose of 70 ml THF. Nano-particle coating film of 1b-NCM (**Figure 4. 6. (b)**) appears to be more compact than that of 2b-NCM (**Figure 4. 6. (c)**). Moreover, abundant small nano LiBO_2 particles were formed to gather together with nanorods adhering to the outermost layer of NCM for 1b-NCM (**Figure 4. 6. (d)**). The high magnification image shown in **Figure 4. 7** indicates that the nanorod is composed of the aggregation of smaller LiBO_2 nanoparticles. According to this Figure, the tiny LiBO_2 nanoparticles gather to form the nanorod which can be easily identified on the end face of the large nanorod and the enlarged image of the small nanorod. These nanorods likely acted as bandages to wrap the NCM secondary particles, including the defect region of the cracks (**Figure 4. 6. (e)** and **(f)**). It can be seen that the LiBO_2 nanorods blocked the opening of the intrinsic cracks of the material to some degree, which mitigated the penetration of the electrolyte. EDS mapping was further conducted for 1b-NCM, as shown in **Figure 4. 6. (g-k)**, where the element boron was detected on the surface of observed secondary particles. The distribution of boron was comparatively uniform, indicating a homogeneous layer of the nano- LiBO_2 coating.

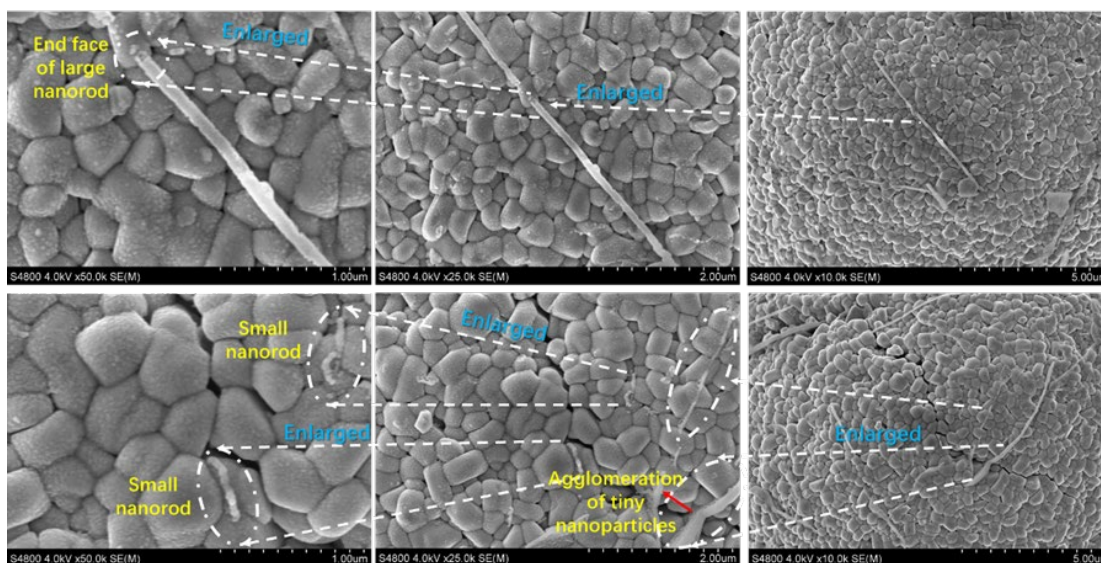


Figure 4. 7. SEM images of enlarged nanorods comprising tiny LiBO_2 nanoparticle aggregates.

The uniformity of the surface coating film of 2b-NCM was poor, corresponding to the shorter time of the antisolvent process with less THF consumption. For 2b-NCM, LiBO_2 ethanol sol was obtained from the residual liquid in the 100 ml cylinder beakers after the consumption of 1b-NCM, possibly involving some LiBO_2 particles from the bottom of the cylinder beakers. Some amorphous LiBO_2 lumps were also found on the surface of 2b-NCM. Considering the coarse coating film of 2b-NCM, severe variation would occur in the electrochemical performance test. The electrochemical properties comparison before and after sol/antisolvent wet coating modification will focus on the pristine NCM and 1b-NCM. In the following description, unless otherwise specified, the LiBO_2 -coated NCM refers to the 1b-NCM samples.

Referring to **Figure 4. 6**, the size of the LiBO_2 particles is much smaller than that of the NCM primary particle which has a length larger than 500 nm. With the help of the antisolvent effect, NCM acts as nucleation in the sol to adsorb a large amount of smaller

nano LiBO_2 particles, accompanied by nanorod formation from nanoparticle aggregation under high-speed rotation conditions. The principle of sol/antisolvent wet coating can be ascribed to the poor solubility of ethanol and the antisolvent effect of THF on LiBO_2 , as well as the highly driven force from the surface energy reduction of nanoparticles. After the formation of the nanorods with further antisolvent effects, the LiBO_2 nanorods can be thrown onto the cathode material surface under the action of centrifugal force originating from high-speed rotation. Cracks are the deficient part of the cathode material, and it is easy for LiBO_2 nanorods to adhere to cracks that have a very high surface energy. Meanwhile, there is more friction between the nanorod and the cracked part than other smooth parts of the cathode material, which can effectively fix the nanorod and reduce slippage. Therefore, LiBO_2 nanorods can be deposited over cracks.

It is worth mentioning that the nanosized lamella-shaped coating film was also successfully synthesised using the LiBO_2 ethanol sol after being placed for over 15 days in such a sol/antisolvent wet coating method. As shown in the SEM image in **Figure 4.8**, NCM is intensively covered by nanosized lamella, which is of LiBO_2 , completely different from the spherical-like nano- LiBO_2 coating. This demonstrates that such a sol/antisolvent wet coating can realise the multi-morphology coating modification. Because the sol/antisolvent wet coating process is almost complete in a nonaqueous environment, it is beneficial for NCM coating modification. Furthermore, in contrast to the evaporation treatment of the organic solution to obtain the final coated material in sol/gel coating (Zuo et al., 2017), vacuum filtration is adopted in this novel

sol/antisolvent to obtain the coated product, which makes the wet coating process more environmentally friendly.

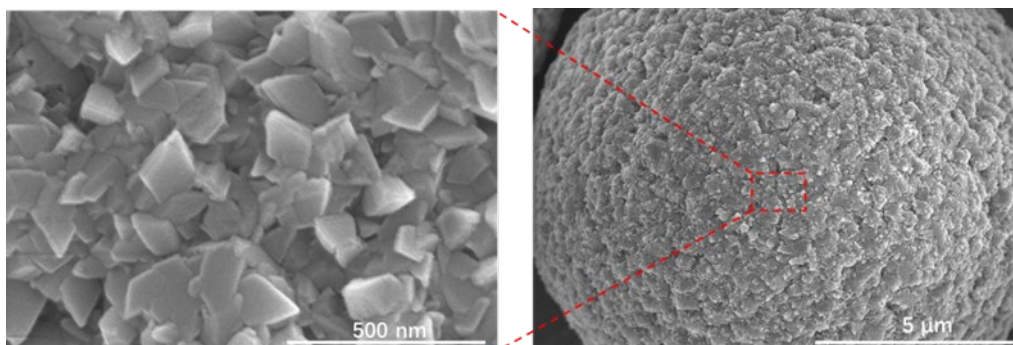


Figure 4. 8. Lamella-shaped coating in sol/antisolvent method by using LiBO_2 ethanol sol placed for over fifteen days.

4.3.2. XRD, TEM, and AFM Tests

Various techniques were employed to analyse the pristine NCM and LiBO_2 -coated NCM. It has been suggested that Li/Ni disordering tends to increase significantly with increasing annealing temperature (Hinuma et al., 2007). The influence of post-calcination after wet-coating at 500 °C for 8 h on Li/Ni disordering was analysed by XRD analysis. In practice, $I(003)/I(104)$ intensity ratios of XRD data can be used to show the level of Li/Ni disordering. A high $I(003)/I(104)$ intensity ratio indicates a low degree of Li/Ni disordering (Wu et al., 2015). XRD patterns of NCM and LiBO_2 -coated NCM are shown in **Figure 4. 9**. The peaks of both original and modified materials were well-indexed based on the layered hexagonal $\alpha\text{-NaFeO}_2$ structure with a space group of $R\bar{3}m$. For NCM, the $I(003)/I(104)$ intensity ratio is 1.913, while the value of LiBO_2 -coated NCM decreases after post-calcination treatment, but it is still as high as 1.878, which is larger than 1.2, suggesting that cation mixing is very low (Ren et al., 2020).

Meanwhile, the splitting of (006)/(102) was also clear and was inserted as an enlarged diffraction peak. These data indicate that LiBO₂-coated NCM maintained a well-layered structure. However, no feature peaks of crystal LiBO₂ are detected, mainly because of the trace amount. Furthermore, the crystal structure parameters of NCM and LiBO₂-coated NCM were calculated using the Rietveld refinement method, as shown in **Table 4. 1**. The results show that lattice parameters *a* and *c* of LiBO₂-coated NCM are both larger than those of NCM. All *c/a* ratios were higher than 4.9, suggesting high cation ordering in all the samples (Sun et al., 2019). The variation in the lattice parameters of the material can be ascribed to the increased Li⁺/Ni²⁺ cation mixing owing to the post-calcination treatment. Because Li⁺ has a larger ion radius of 0.076 nm than Ni²⁺ with an ion radius of 0.069 nm, TMO₂ inter-slab thickness can be increased after the Ni site is replaced by Li, where TM represents transition-metal (Lei et al., 2019).

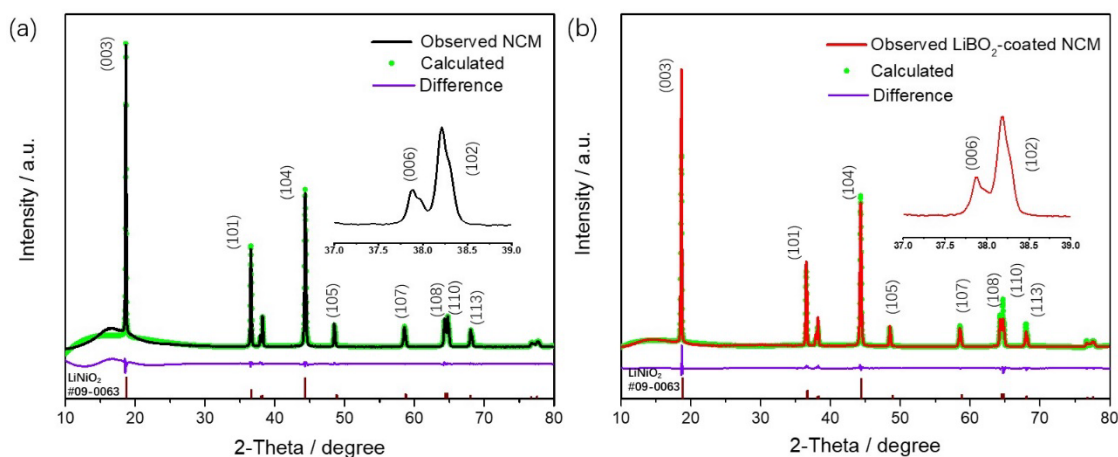


Figure 4. 9. XRD patterns and Rietveld refinement results of samples: (a) pristine NCM; (b) LiBO₂-coated NCM.

Table 4. 1. Crystal structure parameters of original NCM and LiBO₂-coated NCM

Sample	a (Å)	c (Å)	c/a	R_{wp} (%)	R_p (%)
NCM	2.8733	14.2073	4.945	9.92	6.34
LiBO ₂ -coated NCM	2.8771	14.2163	4.941	9.12	6.16

To clarify the detailed morphology and structure of the nano-LiBO₂ coating, TEM was performed to characterise the pristine NCM and LiBO₂-coated NCM. Since the TEM test is limited to samples with thickness of less than 1 μm , while the VMD of the original NCM was 11 μm , powders of active materials were smashed using a hydraulic tablet press machine for the TEM test. The result is shown in **Figure 4. 10**. The multi-dimensional atom arrangements are not completely exhibited because the particle has a reasonable thickness in the TEM test. Two sets of lattice fringes were identified for each species. **Figure 4. 10** (a) illustrates a high-resolution transmission electron microscopy (HRTEM) image of pristine NCM. The lattice spacings of 0.4791 nm and 0.202 nm are in good agreement with (003) and (104) interplanar spacings of hexagonal NCM layered structure ($R\bar{3}m$). No coating material was observed for pristine NCM. In contrast, for the LiBO₂-coated NCM, as shown in **Figure 4. 10** (b), many spherical particles adhered to the surface of the NCM bulk. The coating particles looked like salmon roe piling up tightly, some of which were marked by pink dotted circles. The interplanar distances in the two orientations of the coated nanoparticles were measured to be 0.215 and 0.204 nm, respectively. In addition to glass-LiBO₂, lithium metaborate also has a crystal system of α -LiBO₂ and γ -LiBO₂ (Lei et al., 2009). The raw LiBO₂ powder was also confirmed to be a typical crystalline LiBO₂ sample rather than glass-LiBO₂, as no

exothermic peak for the glass transition was detected in the DSC curve (Figure 4. 11.

(b)) (Wu et al., 2019c).

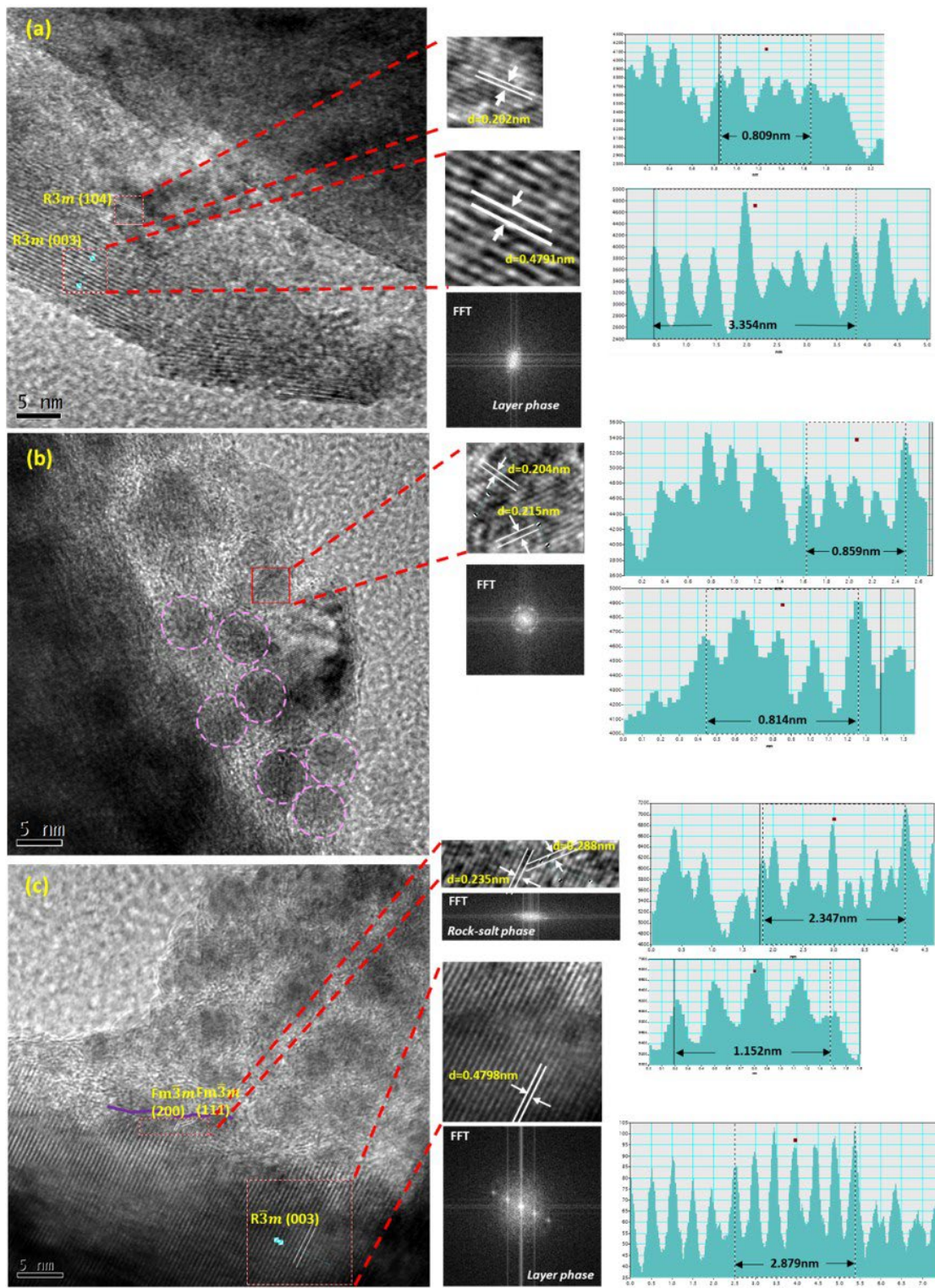


Figure 4. 10. HRTEM images and corresponding FFT patterns for (a) pristine NCM; (b) and (c) LiBO₂-coated NCM.

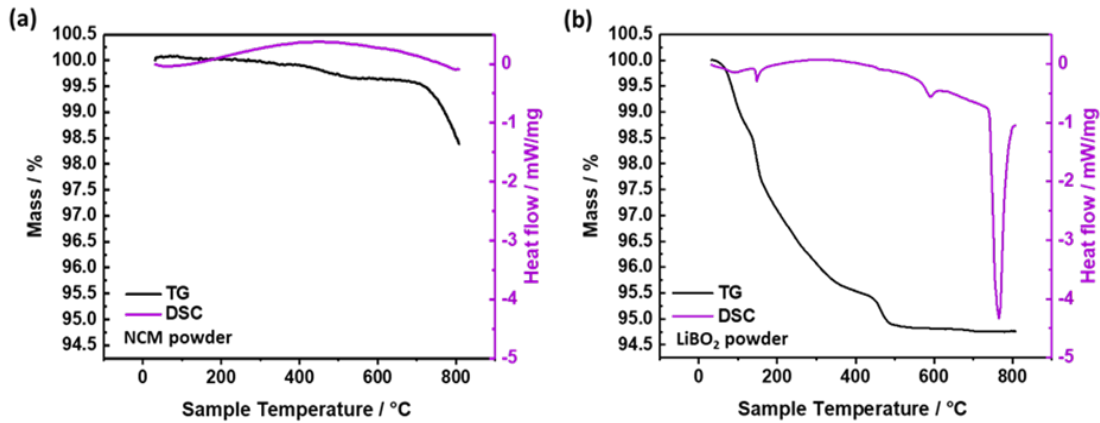


Figure 4. 11. TG-DSC curves of samples at 30-820 °C at a heating rate of 10 °C/min in an argon atmosphere: (a) NCM powder and (b) LiBO₂ powder.

Another HRTEM image of LiBO₂-coated NCM is presented in **Figure 4. 10.** (c), in which the lattice spacing of 0.4798 nm is defined for the (003) plane of NCM bulk, while NiO-like rock-salt phase (*Fm $\bar{3}m$*) with interplanar spacings of 0.235 and 0.288 nm with an angle of 120° for (200) and (111) planes were also observed between the top of the bulk layered phase and LiBO₂ coating. Such a new rock-salt phase is clearer with nearly 2.5 nm thickness shown in the enlarged HRTEM image in **Figure 4. 12.** Ni cations were transferred from the original transition metal layer to the Li layer. The boundary line between the rock-salt phase and LiBO₂ coating is indicated by a purple curve. It is generally considered that the NiO-like rock salt phase layer can act as a pillar to stabilise the original layered structure and prevent further structural transformation during the charge/discharge process (Zheng et al., 2017). The thermal stability decreases with an increasing Ni content of NCM materials (Noh et al., 2013). The formation of the NiO-like rocksalt can be ascribed to the thermal decomposition process of NLO because of the post-calcination, which is equal to the Li/Ni disordering from the viewpoint of chemistry based on Equation (4. 1):(Zhang, 2020)

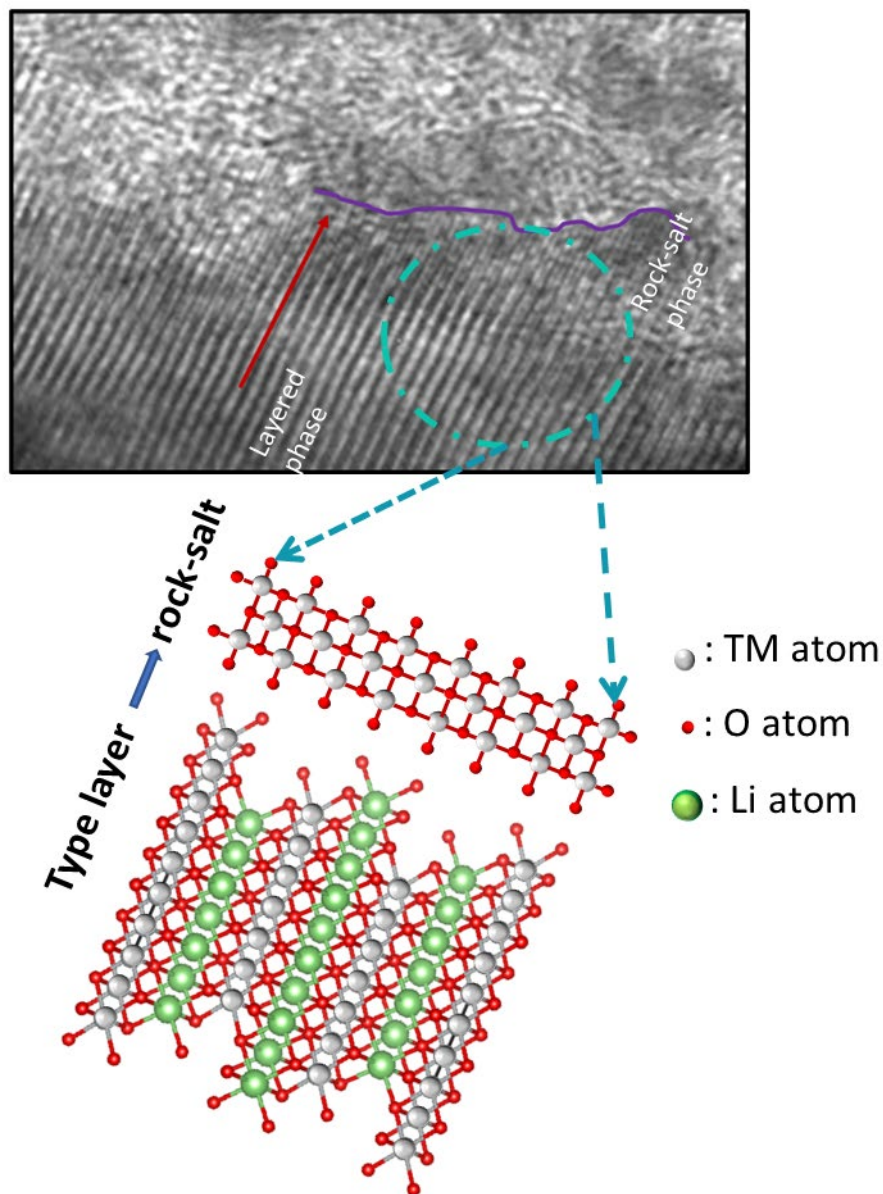
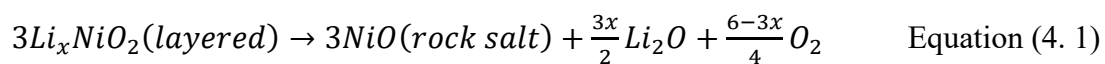


Figure 4. 12. The enlarged HRTEM image of LiBO₂-coated NCM shows the phase transformation from the layered phase into the rock-salt phase with a purple curve indicating the boundary between the rock-salt phase and the LiBO₂ coating.

The phase transformation to the rock-salt phase can also be detected in LiBO₂-coated NCM according to the enlarged diffraction peaks of selected regions in the XRD patterns

of pristine NCM and LiBO₂-coated NCM (**Figure 4. 13**). In this figure, it is clear that the peaks after modification shift to the left tending to (111) face and (220) face of NiO (Kong et al., 2019), indicating the phase transformation. The formation of the rock-salt phase can be considered as one reason for the variation in Li/Ni disordering after the sol/antisolvent wet coating modification. Based on the above TEM and XRD analyses, a three-layer structure composed of an inner NCM with a layered structure, an interlayer with a very thin rock-salt structure, and an outer coating of the crystalline LiBO₂ layer can be confirmed for LiBO₂-coated NCM.

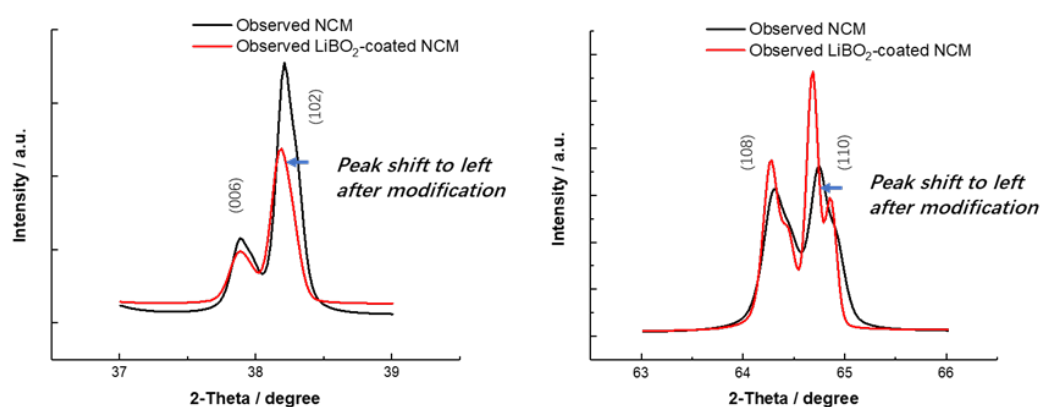


Figure 4. 13. Selected regions of the XRD patterns of the pristine NCM and LiBO₂-coated NCM are shown in **Figure 4. 9**.

AFM was used to analyse the mechanical properties and geometric morphology of the pristine NCM and LiBO₂-coated NCM. The 2b-NCM sample obtained with a shorter time and smaller dosage of THF for the antisolvent process was also analysed to better illustrate the coating function of the LiBO₂ nanoparticles. AFM images are shown in

Figure 4. 14.

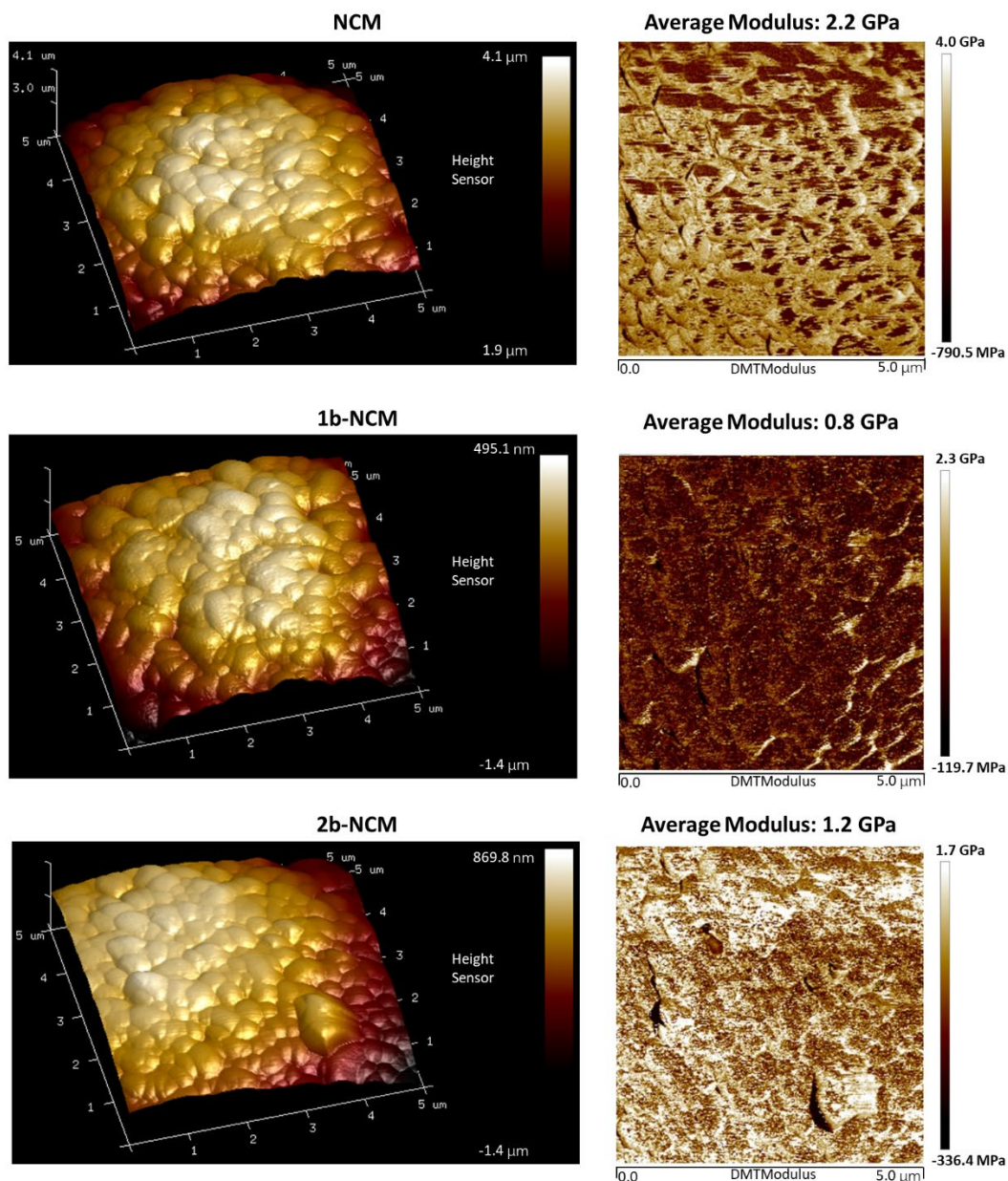


Figure 4. 14. AFM images and mechanical properties of the surface of NCM, 1b-NCM, and 2b-NCM by AFM.

In contrast to the clean surface of the NCM primary particles, very small LiBO_2 particles were detected on the entire surface of 1b-NCM. The average modulus of NCM was 2.2 GPa which was the highest among the three samples. Although 1b-NCM exhibited the lowest average modulus with the value of 0.8 GPa, 2b-NCM showed an average

modulus of 1.2 GPa, which is the middle level among the three samples. The results demonstrate that the LiBO₂ coating made the stiff surface of NCM soft, which would be beneficial for releasing the stress initiated by charge/discharge cycling. Hence, crack formation after cycling was mitigated after the sol/antisolvent wet coating of LiBO₂. Moreover, together with the elastic modulus, the surface roughness parameters R_q (root-mean-square roughness) and maximum height difference H_d were also analysed and summarised in **Table 4. 2**. After coating with small nano-sized LiBO₂ particles, the surface roughness was reduced to R_q of 263 nm and 224 nm for 1b-NCM and 2b-NCM, respectively, while R_q of NCM is 323 nm. H_d of 1b-NCM was also decreased. Owing to the low surface roughness, the contact gaps among the solid materials can be diminished, and the material homogeneity is enhanced. Hence, the uniformity of the electric net inside the cathode can be improved accordingly. The deposition of nano-LiBO₂ on the grain boundary of NCM is considered a beneficial factor for reducing the surface roughness.

Table 4. 2. Surface morphology and mechanical parameters of NCM, 1b-NCM, and 2b-NCM by AFM

Parameter	NCM	1b-NCM	2b-NCM
Elastic Modulus / GPa	2.2	0.8	1.2
R_q / nm	323	263	224
H_d / μm	2.2	1.8951	2.2698

The Young's modulus of NCM811, α -LiBO₂, and γ -LiBO₂ are presented in **Table 4. 3** according to other studies with values of approximately 220, 51, and 312 GPa, respectively (Lim et al., 2018, Basalaev et al., 2019). Compared with α -LiBO₂, the

Young's modulus of γ -LiBO₂ was approximately six times higher even higher than that of NCM811. It can be concluded that the coated LiBO₂ particles are mainly α -LiBO₂ with a low Young's modulus, which can effectively decrease the surface stiffness of the cathode. However, the different elastic modulus between 1b-NCM and 2b-NCM can be reasonably ascribed to the different thicknesses of the coating films. 2b-NCM exhibits a higher value implying a thinner coating in comparison with 1b-NCM. Therefore, the thickness of the coating film could be adjusted by changing the amount of antisolvent used in this novel wet coating process. In combination with the convenient adjustment of coating thickness and the discussion of the principle of sol/antisolvent wet coating, the four main advantages of sol/antisolvent wet coating are summarised in **Table 4. 4**; that is the aqueous environment is avoided, coatings with different morphologies are available, no high-temperature evaporation occurs, and changing the antisolvent dosage can tune the coating thickness.

Table 4. 3. Young's modulus of NCM811, α -LiBO₂ and γ - LiBO₂

Material	Young's modulus /GPa
NCM811	~220 (Lim et al., 2018)
α -LiBO ₂	~51 (Basalaev et al., 2019)
γ -LiBO ₂	~312 (Basalaev et al., 2019)

Table 4. 4. List of advantages of sol/antisolvent wet coating

Advantage	Description
① Non-aqueous environment	Ethanol/THF solution without water;
② Multi-morphology coating available	Spherical-like/lamella-shaped coating;
③ No evaporation of organic solution	Vacuum filtration to obtain coated sample;
④ Convenient adjustment of coating thickness	Changing antisolvent dosage.

An FTIR test was performed to further identify the coating film. The FTIR absorption spectra of LiBO₂, NCM and LiBO₂-coated NCM is shown in **Figure 4. 15**. According to Li Lei etc.'s paper (Lei et al., 2009), such LiBO₂ sample mainly appears the absorption peaks of α -LiBO₂ highlighted with the red wavenumbers. Meanwhile, there are also some absorption spectra consistent with the signals of γ -LiBO₂ with the wavenumbers labelled in black for the LiBO₂ sample. After comparison, it is apparent that the LiBO₂-coated NCM reveals the signal of the main FTIR absorption peak of α -LiBO₂ at appropriately 1170 cm⁻¹, which does not appear for NCM. The other relatively distinct absorption peak for LiBO₂-coated NCM at appropriately 896 cm⁻¹ is also detected in good agreement with the absorption peak of γ -LiBO₂, which is different from that of NCM. In addition, an XRD test was performed on the LiBO₂ sample, indicating the coexistence of α -LiBO₂ and γ -LiBO₂, as shown in **Figure 4. 16**, whereas the signal intensity of γ -LiBO₂ was much lower than that of α -LiBO₂. These results imply that the coating film of LiBO₂ consists of mixed phases of α -LiBO₂ and γ -LiBO₂. After coating modification, the surface mechanical properties changed from stiff to soft, mainly owing

to α -LiBO₂. The lattice distances of 0.215 and 0.204 nm in the coating film are shown in **Figure 4. 10.** (b) can be assigned to (020) and (021) lattice planes, respectively, of α -LiBO₂.

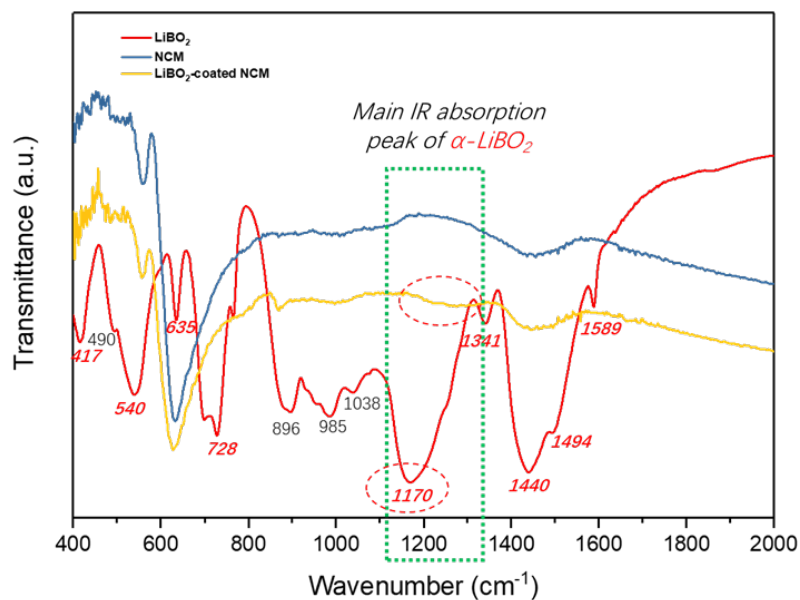


Figure 4. 15. FTIR absorption spectra of LiBO₂, NCM, and LiBO₂-coated NCM.

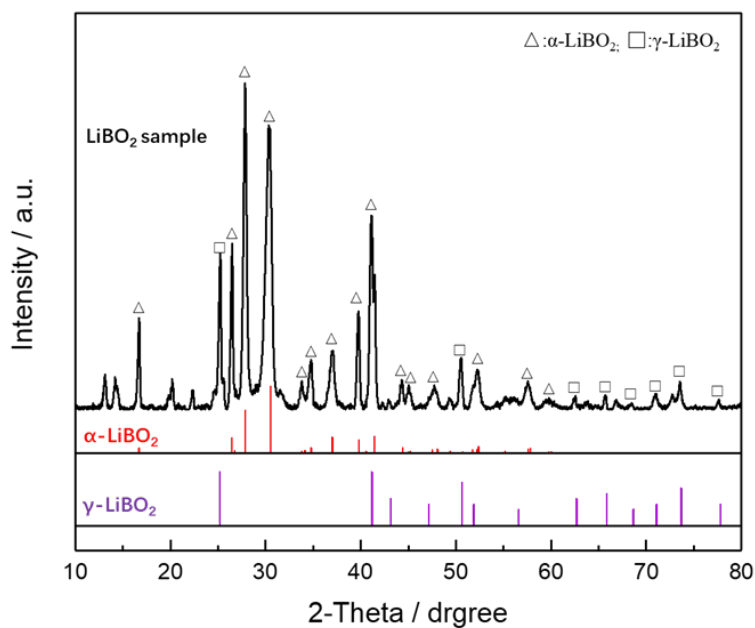


Figure 4. 16. XRD pattern of the LiBO₂ sample.

In summary, although after sol/antisolvent LiBO₂ coating, Li/Ni disordering increases to a certain degree, the crystallinity of LiBO₂-coated NCM does not suffer a serious impact but still maintains good cation ordering. Based on the AFM results, the morphology was improved with a lower surface roughness. Thus, the electric net can be enhanced. Meanwhile, the surface of the cathode material becomes soft, which is expected to mitigate microcrack formation during cycling.

4.3.3. Improved Rate Capability and High Current Cycling Performance after LiBO₂ Coating with Electrochemical Study

Salmon-roe-like LiBO₂ nanoparticles are covered onto the surface of NCM through the sol/antisolvent wet coating process. The modification effects on the electrochemical performance were studied by GCPL measurements by comparing the NCM and LiBO₂-coated NCM samples. First, the rate performances of pristine NCM and LiBO₂-coated NCM were measured in the voltage range of 2.8-4.3 V (vs. Li/Li⁺). For the LiBO₂-coated NCM, the test was slightly different. The first five cycles at 0.1 C were changed to 0.2 C (i.e. initial 10 cycles at 0.2 C), and the current density returned directly to 0.2 C after 3 C, all others were the same (**Figure 4. 17. (a)**). Such adjustments were performed based on the detection of some deep capacity diving for LiBO₂-coated NCM at a small current density of 0.1 C (10 mA g⁻¹), particularly for thicker coating along with THF antisolvent treatment of 1 and 2 h, dominantly ascribed to the low electron conductivity of α -LiBO₂ and γ -LiBO₂. The theoretical calculation of α - and γ -phase

LiBO₂ crystals were reported with wide-gap dielectrics band gaps $E_g(\alpha)=7.6$ eV and $E_g(\gamma)=10.4$ eV, much wider than E_g of a delithiated NCM811 (less than 2.0 eV) (Basalaev et al., 2019, Lim et al., 2018). A comparison of the discharge capacities between NCM and LiBO₂-coated NCM at different current densities is shown in **Figure 4. 17. (a)**, both NCM and LiBO₂-coated NCM exhibit lower specific capacity along with increased current density. Nevertheless, unlike the rapid capacity decline for NCM, the capacity variation of LiBO₂-coated NCM is not significant, which implies that LiBO₂ coating modification of the cathode can effectively improve the rate capability of the NCM/Li half-coin cell.

Figure 4. 17. (b) shows the cycling performance at 3 C (3 C= 600 mA g⁻¹) for NCM and LiBO₂-coated NCM. A long activation process (ten cycles at 0.2 C) was applied to the LiBO₂-coated NCM cathode to ensure good electrochemical kinetics for long-term cycling tests. In detail, both NCM and LiBO₂-coated NCM were first activated at 0.2 C for 10 cycles, followed by every 5 cycles of 0.5 C, 1 C, and 2 C cycles, then finally cycled at 3 C for a total of 100 cycles. Although some capacity fluctuation appears for LiBO₂-coated NCM at the initial 0.2 C, the cycling performance at the following 3 C high current density was noticeably improved. Not only does the initial specific capacity develop from 123.3 mAh g⁻¹ to 148.4 mAh g⁻¹ during the first discharge cycle, and the 3 C cycling stability strengthened with capacity retention increasing from 68.37% to 76.55% after the whole 75 cycles at 3 C.

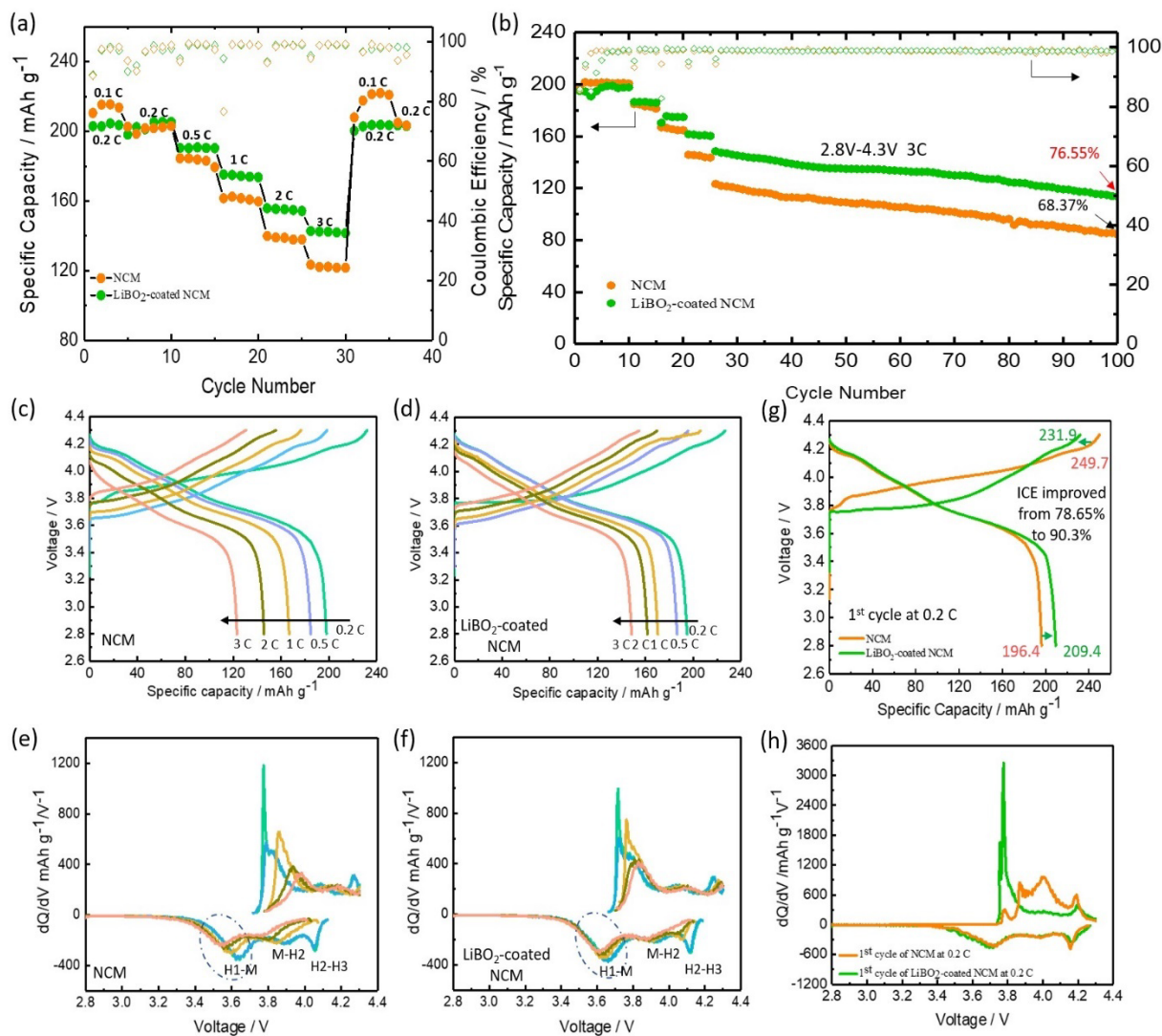


Figure 4. 17. Detailed electrochemical performance test data of NCM and LiBO₂-coated NCM:(a) Rate performances; (b) Cycling performances at 3 C between 2.8-4.3 V; (c and d) First cycle charge/discharge profiles from panel b at 0.2, 0.5, 1, 2, and 3 C, respectively; (e and f) dQ dV⁻¹ curves at selected cycles of 1st and 5th cycle at 2 C, 1st, 33rd and 55th cycle at 3 C; (g and h) First cycle charge-discharge characteristic curves showing improvement of ICE, and the corresponding dQ dV⁻¹ curves.

An in-depth evaluation of the GCPL data was performed to explore the reasons for improved electrochemical performance. The charge/discharge voltage profiles of the first cycle of NCM and LiBO₂-coated NCM at 0.2, 0.5, 1, 2, and 3 C in the 3 C cycling test are shown in **Figure 4. 17.** (c and d). The smaller polarisation and overpotential are responsible for the improved rate capability owing to the LiBO₂ coating. **Figure 4. 17.** (e and f) illustrate the dQ dV⁻¹ curves at 3 C cycling test involving 1st cycle and 5th cycle at 2 C, 1st cycle, 33rd cycle and 55th cycle at 3 C. We identified three pairs of redox peaks coinciding with the phase transitions of the hexagonal phase to the monoclinic phase (H1–M), monoclinic phase to the hexagonal phase (M–H2), and hexagonal phase to the hexagonal phase (H2–H3) (Zhang et al., 2019a). Compared with NCM, LiBO₂-coated NCM maintains better reversibility of the peak for the H1–M phase transition, marked by dotted circles. Potential differences in the H1–M phase transition between the oxidation and reduction peaks for the 1st cycle at 2 C, the 1st cycle at 3 C, and the 55th cycle at 3 C were calculated. For NCM, the potential differences are 0.134 V, 0.261 V, and 0.422 V, respectively, whereas for LiBO₂-coated NCM, the corresponding potential difference of the H1–M peak is much smaller, with values of 0.051 V, 0.116 V, and 0.210 V.

Coulombic efficiency (CE) is an important index for estimating the cycling life of LIBs (Xiao et al., 2020). The initial Coulombic efficiency (ICE) provides fundamental information regarding the electrochemical process (Ha et al., 2021). Referring to the tests of rate performance and 3 C cycling, it was found that all ICEs of LiBO₂-coated NCM at the initial 0.2 C are higher than that of NCM. A LiBO₂-coated NCM sample in

the 1 C cycling test (**Figure 4. 18**) reveals the highest ICE value of 90.30% at 0.2 C versus that of NCM with a value of 78.65%. It is a superior ICE value for NLO compounds at 0.2 C within the voltage range of 2.8-4.3 V. A comparison of ICE with other coating modifications is presented in **Table 4. 5**. It can be found that such crystalline LiBO₂ coating stands out among other studies, the ICE value is higher than other test cases even at smaller current density or higher cut-off voltage for the first cycle. The corresponding 1st cycle charge-discharge characteristic curves at 0.2 C of two samples are shown in **Figure 4. 17. (g)**. The charge capacity of pristine NCM was 249.7 mAh g⁻¹ in the first cycle. It decreases to 231.9 mAh g⁻¹ for LiBO₂-coated NCM, which means that the total number of Li ions departing from the cathode decreased after LiBO₂ coating. In contrast, the discharge capacity of the first cycle at 0.2 C increases from 196.4 mAh g⁻¹ for NCM to 209.4 mAh g⁻¹ for LiBO₂-coated NCM, which indicates that the total number of Li ions back to the cathode increased (Xiao et al., 2020).

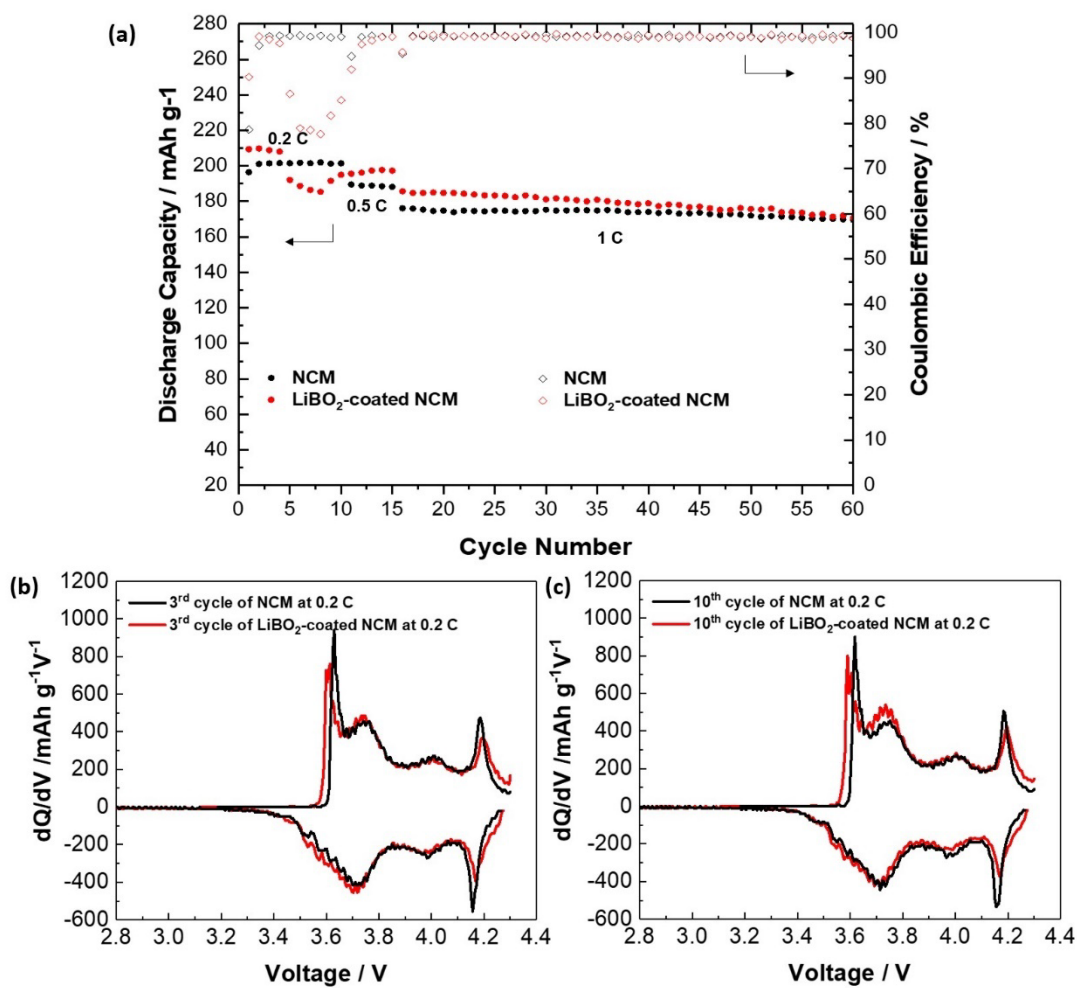


Figure 4. 18. (a) Cycling performances of NCM and LiBO₂-coated NCM within the voltage range of 2.8-4.3 V at 1 C; (b and c) dQ dV⁻¹ curves at selected cycles of 3rd cycle and 10th cycle at 0.2 C (Black is NCM, red is LiBO₂-coated NCM).

Table 4. 5. Improvement of initial Coulombic efficiency of NLO by coating

Coating materials	Cathode materials	Initial Coulombic efficiency	References
Mixed α - and γ - LiBO ₂	LiNi _{0.85} Co _{0.1} Mn _{0.05} O ₂	ICE increased to 90.3% at 0.2 C (40 mA g ⁻¹) in the voltage range of 2.8-4.3 V	This work
Li ₃ PO ₄	LiNi _{0.8} Co _{0.1} Mn _{0.1} O ₂	ICE increased to 81.2% at 0.2 C (40 mA g ⁻¹) between 3.0 and 4.3 V	(Fan et al., 2019)
Graphene-Li ₃ PO ₄	LiNi _{0.8} Co _{0.1} Mn _{0.1} O ₂	ICE increased to 82.7% at 0.2 C (40 mA g ⁻¹) between 3.0 and 4.3 V	(Fan et al., 2019)
Li ₃ PO ₄	LiNi _{0.85} Co _{0.1} Mn _{0.05} O ₂	ICE increased to 89.1% at 0.1 C (20 mA g ⁻¹) between 2.8 and 4.3 V	(Fang et al., 2021)
Li ₂ O-2B ₂ O ₃	LiNi _{0.8} Co _{0.1} Mn _{0.1} O ₂	ICE increased to 88.83% at 0.1 C (18 mA g ⁻¹) in the voltage range of 2.8-4.3 V	(Zhang et al., 2019b)
Al ₂ O ₃	LiNi _{0.8} Co _{0.1} Mn _{0.1} O ₂	ICE increased to 88.02% at 0.1 C (18 mA g ⁻¹) in the voltage range of 2.8-4.3 V	(Zhang et al., 2019b)
ZrO ₂	LiNi _{0.8} Co _{0.1} Mn _{0.1} O ₂	ICE increased to 88.04% at 0.1 C (18 mA g ⁻¹) in the voltage range of 2.8-4.3 V	(Zhang et al., 2019b)
La ₂ Ni _{0.5} Li _{0.5} O ₄	LiNi _{0.8} Co _{0.1} Mn _{0.1} O ₂	ICE increased to 83.9% and 84.6% respectively at 0.2 C (40 mA g ⁻¹) in the voltage range of 2.75-4.3 V and 2.75-4.5 V	(Wu et al., 2019a)

Based on the study by Kasnatscheew et al. (Kasnatscheew et al., 2016a), the specific capacity loss in the first cycle can be categorised into two types: irreversible, which is related to the structural changes of NCM occupying a small part of the capacity loss,

and reversible, which is caused by the kinetic limitations and can be recovered through continued cut-off voltage loading. Herein, both the irreversible and reversible capacity losses decreased after the sol/antisolvent LiBO₂ coating modification, which boosted the ICE. The enhanced lithiation reaction kinetics are responsible for the decrease in reversible capacity loss because of the increased Li-ion diffusion coefficient owing to the high ion conductivity of both α -LiBO₂ and γ -LiBO₂. Recent research has reported that the lithium ionic conductivity of α -LiBO₂ is on the order of 10^{-6} Scm⁻¹, and that of γ -LiBO₂ is on the order of 10^{-5} ~ 10^{-6} Scm⁻¹ (Hirose et al., 2019). These values are much higher than the lithium ionic conductivity of NCM on the order of 10^{-8} ~ 10^{-9} Scm⁻¹ (Heenan et al., 2020, Amin and Chiang, 2016). The decline in irreversible capacity loss can be ascribed to the coating layer of crystalline LiBO₂ as well as the already existing rock-salt phase after LiBO₂ coating, as detected in the TEM image. Therefore, the LiBO₂ coating serves as a barrier against contact with the electrolyte to mitigate the reduction of unstable Ni⁴⁺ to Ni²⁺ ions, thus alleviating Li⁺/Ni²⁺ cation mixing (Gauthier et al., 2015). Meanwhile, the already existing rock-salt phase before cycling can further reduce the rate of the forward reaction in Equation (4. 1) in the view of thermodynamics. Thus, the irreversible capacity loss associated with structural changes can be reduced during the first cycle. In addition, compared with LiBO₂-coated NCM, the decomposition of the electrolyte is more serious for NCM because of the catalytic activity of Ni⁴⁺ without coating protection (Xue et al., 2020). After LiBO₂ coating, the harsh interfacial chemical reaction and transition metal dissolution were alleviated. When the consumption of Li

ions for side reactions decreases, more Li ions can return to the cathode with a higher ICE.

In addition, the voltage plateaus of the 1st cycle charge/discharge curve of the two samples are completely different. In **Figure 4. 17. (g)** a longer first voltage plateau near 3.8 V is distinguished for LiBO₂-coated NCM. The corresponding dQ dV⁻¹ curve clearly shows that the first phase transition (corresponding to H1→M at 3.78 V) turns into a stronger and sharper peak presented in **Figure 4. 17. (h)**, which indicates that more abundant Li ions have been extracted from the LiBO₂-coated NCM at the stage of H1→M phase transition. Meanwhile, the second phase transition of M→H2 at 4.0 V becomes very weak. The last phase transition of H2→H3 was transferred to a slightly higher voltage (4.2 V) with a lower peak intensity. However, after the initial 0.2 C cycling, LiBO₂-coated NCM exhibited typical differential capacity analysis (dQ dV⁻¹) curves, similar to the pristine NCM, as shown in **Figure 4. 18. (b and c)**.

Some other distinctions can be observed in these two figures(**Figure 4. 17. (g and h)**), wherein the voltage for H1→M phase transition becomes lower with a broader voltage range. The same phenomenon can be detected in **Figure 4. 18. (b and c)**. H2→H3 phase transition was consistently depressed in these graphs. As we know, the mechanical strain, which is initiated by the detrimental anisotropic volume change mainly due to H2–H3 phase transition in the highly charged state, would lead to internal microcracks (Lai et al., 2020). The suppression of H2–H3 phase transition after crystalline LiBO₂ coating can be considered favourable for improving the electrochemical performance. Considering the rock-salt phase NiO layer in LiBO₂-coated NCM, the bulk layered

structure must occupy excessive Li ions. It is suspected that extracting Li ions to a stoichiometric ratio of 0.2 ~ 0.4 would become comparatively more difficult than the pristine NCM (Liu et al., 2015). The higher voltage detected for H2–H3 phase transition of the LiBO₂-coated NCM during the charging process can probably demonstrate such an argument. Furthermore, the larger capacity contributed by H1–M phase transition suggests that the crystalline LiBO₂ coating facilitates phase transition to the monoclinic (M phase) metastable phase.

Generally, during the discharging of the cell at a high current density, the discharge voltage declines to a great degree compared to the open-circuit voltage owing to an overvoltage. The overvoltage is equal to the product of the internal cell resistance and current (Kasnatscheew et al., 2016a, Kasnatscheew et al., 2016b). The lower the discharge voltage, the lower the discharge capacity. For the rate performance, the Li-ion diffusion rate is deemed as the determining factor because the Li-ion diffusion rate becomes much slower than the electron migration with the increase in current density (Liu et al., 2018). Compared with bulk NCM, both α -LiBO₂ and γ -LiBO₂ are fast Li-ion conductors, which can help improve the Li-ion diffusion rate of the cathode and accordingly improve the rate performance of the material. Meanwhile, the soft LiBO₂ nanoparticle coating together with the bandage-like LiBO₂ nanorod deposition can mitigate the disruption of the electron pathway. The broken electron pathway is initiated by battery operation and the already existing intrinsic crack defects of the cathode material. Such a modification with double protection from nanoparticle coating and nanorods wrapping can provide a better continuous electric net, which is also helpful in

achieving excellent rate performance. The enhanced structural integrity after cycling was demonstrated by follow-up FIB-SEM analysis.

The improved lithium diffusion is further confirmed by CV analysis at varied scan rates from 0.1-0.5 mV s⁻¹ in the voltage range of 2.8-4.3 V based on the Randles-Sevcik equation as follows:(Tian et al., 2015, Viji et al., 2016)

$$\frac{I_p}{m} = 0.4463F \left(\frac{F}{RT} \right)^{1/2} C \nu^{1/2} A_e D_{Li^+}^{1/2} \quad \text{Equation (4. 2)}$$

Where I_p is the peak current (A), m is the mass of active material, R is gas constant, F is Faraday constant, T is the absolute temperature (298.15 K), Li^+ concentration C is determined referring to one Li^+ occupying on average unit cell (Tian et al., 2015), thereof, $1.635 \times 10^{-2} \text{ mol cm}^{-3}$ for NCM with unit cell volume of 101.58 \AA^3 , $1.630 \times 10^{-2} \text{ mol cm}^{-3}$ for $LiBO_2$ -coated NCM with unit cell volume of 101.91 \AA^3 based on the cell refinements, ν is scan rate (V s^{-1}), A_e is the electroactive area ($1.99 \times 10^2 \text{ cm}^2 \text{ g}^{-1}$ for NCM, $2.60 \times 10^2 \text{ cm}^2 \text{ g}^{-1}$ for $LiBO_2$ -coated NCM). CV curves of NCM and $LiBO_2$ -coated NCM are shown in **Figure 4. 19** (a) and (b). Li-ion diffusion coefficient D_{Li^+} can be derived from the fitted slopes of data by plotting I_p versus square root of scan rate (**Figure 4. 19.** (c)). For NCM, Li-ion diffusion coefficient D_{Li^+} at the oxidation peak is calculated to be $4.808 \times 10^{-11} \text{ cm}^2 \text{ s}^{-1}$ (Li-extraction from active material), and D_{Li^+} at the reduction peak is $2.088 \times 10^{-11} \text{ cm}^2 \text{ s}^{-1}$ (Li-insertion to active material). For $LiBO_2$ -coated NCM, both Li-extraction and Li-insertion D_{Li^+} were higher with the values of $1.303 \times 10^{-10} \text{ cm}^2 \text{ s}^{-1}$ and $6.458 \times 10^{-11} \text{ cm}^2 \text{ s}^{-1}$ respectively. **Table 4. 6** gathers the Li-ion diffusion coefficients of NCM and $LiBO_2$ -coated NCM using the Randles-Sevcik

equation. This result confirms that the superior electrochemical performance at high current density can be partly ascribed to the improved Li-ion diffusion coefficient after the crystalline LiBO₂ coating through sol/antisolvent treatment.

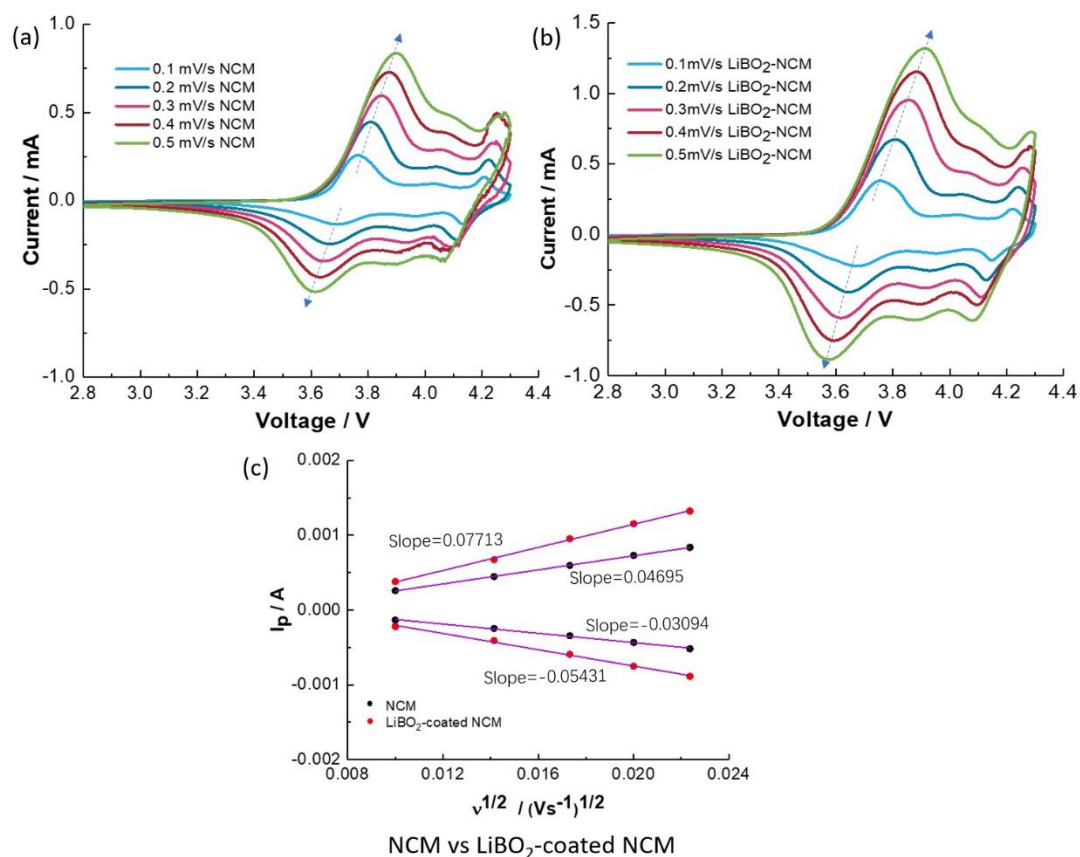


Figure 4. 19. CV curves of (a) NCM, (b)LiBO₂-coated NCM at varied scan rates within the voltage range of 2.8-4.3 V; (c) Corresponding plots for I_p vs $v^{1/2}$.

Table 4. 6. Li-ion diffusion coefficients of NCM and LiBO₂-coated NCM by Randles-Sevcik equation

$D_{Li^+} / \text{cm}^2 \text{ s}^{-1}$	Li-extraction	Li-insertion
NCM	4.808×10^{-11}	2.088×10^{-11}
LiBO ₂ -coated NCM	1.303×10^{-10}	6.458×10^{-11}

4.3.4. Comparison of SEI Chemical Composition and Micro-cracks of NCM and LiBO₂-coated NCM after Cycling

To understand the passivation effect of crystalline LiBO₂, the SEI layer (also called as cathode-electrolyte interphase CEI) on the cathode surface was characterised by XPS. Both NCM and LiBO₂-coated NCM were analysed before and after 3 C cycling. All the spectra were corrected by referencing the C 1s line to 284.8 eV. The wide scans of NCM and LiBO₂-coated NCM cathode electrodes are shown in **Figure 4. 20**. The wide scan spectra indicate that both samples are covered by CEI layers after 3 C cycling, which is mainly produced by oxidative decomposition of electrolyte with strong peaks of O 1s at a binding energy of 532.1 eV (**Figure 4. 20. (a)**) and 531.7 eV (**Figure 4. 20. (b)**) (Liu et al., 2020, Zhang et al., 2018a). Meanwhile, the peaks of C 1s and F 1s are weakened after 3 C cycling at the binding energy of 284.5 eV and 688.5 eV, respectively (Liu et al., 2020). Hence, electrolyte decomposition was the main component of the CEI layers in both samples.

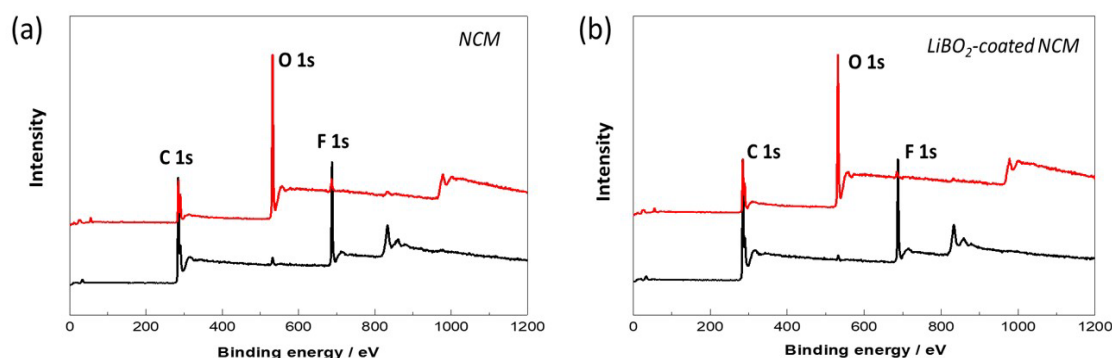


Figure 4. 20. XPS survey scan of (a) NCM, (b) LiBO₂-coated NCM (the black line represents uncycled samples, the red line represents samples after 3 C cycling).

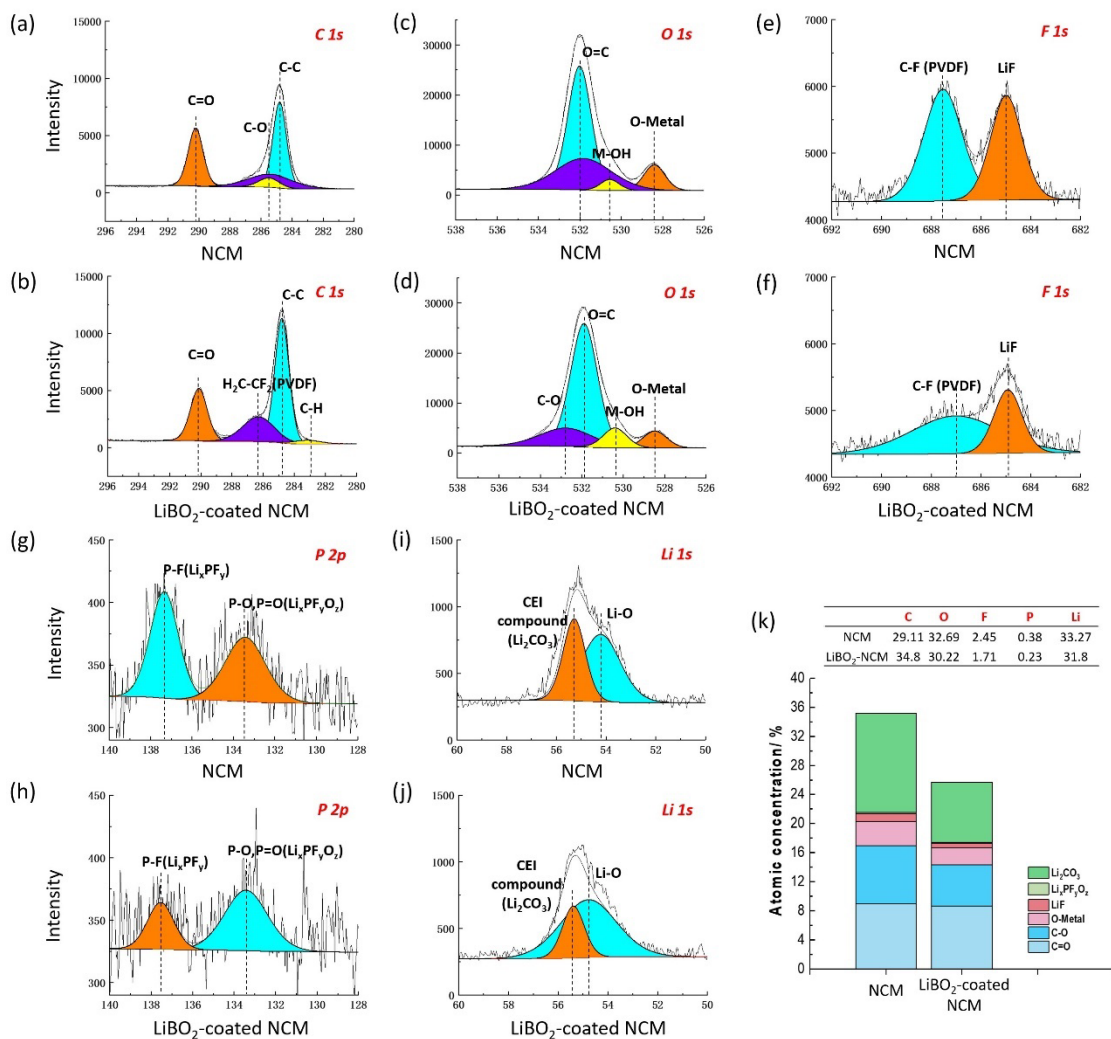


Figure 4. 21. XPS spectra of samples after 3 C cycling: (a, c) C 1s, O 1s of NCM; (b, d) C 1s, O 1s of LiBO₂-coated NCM; (e, g, and i) F 1s, P 2p and Li 1s of NCM; (f, h and j) F 1s, P 2p and Li 1s of LiBO₂-coated NCM; (k) The chemical composition ratio for CEI species in the interfacial layers (the atomic concentrations of C, O, F, P, and Li for different samples are listed).

The individual element XPS spectrum after 3 C cycling was fitted with sub-peaks and assigned to the chemical states shown in **Figure 4. 21**. In C 1s spectra (**Figure 4. 21**. (a) and (b)), electrolyte decomposition with C=O (290.3, and 290.1 eV), C-O (285.5 eV) were identified (Liu et al., 2020). Compared with NCM, the electrolyte decomposition deposition on the cathode surface of LiBO₂-coated NCM was reduced with the

emergence of the $\text{H}_2\text{C}-\text{CF}_2$ peak (286.3 eV) and weakened peak intensity of the $\text{C}=\text{O}$ bond (Schulz et al., 2018). This was confirmed by the O 1s spectra, where NCM (**Figure 4. 21. (c)**) presents a higher intensity of the $\text{O}=\text{C}$ peak with binding energy at 532.0 eV than that of LiBO_2 -coated NCM (**Figure 4. 21. (d)**) at 531.9 eV. Some C-O from electrolyte decomposition (532.8 eV, **Figure 4. 21. (d)**) was detected for LiBO_2 -coated NCM (Liu et al., 2020). The other two subpeaks of O 1s spectra can be assigned to M-OH (530.5, and 530.4 eV) and O-metal (528.4, and 528.5 eV) (Liu et al., 2020, Zhang et al., 2018a). Obviously, the intensity of the O-metal peak for LiBO_2 -coated NCM was lower, implying less active metal element dissolution and less Li_2O formation.

F 1s, P 2p, Li 1s XPS spectra of corresponding samples are shown in **Figure 4. 21. (e-j)**. As shown in **Figure 4. 21. (e)** and **(f)**, the peaks of C-F (687.6, and 687.0 eV) correspond to PVDF, the peak at (685.0, and 684.9eV) is assigned to LiF (Liu et al., 2020), wherein LiF peak intensity is much lower for LiBO_2 -coated NCM. In P 2p spectra (**Figure 4. 21. (g)** and **(h)**), P-F (137.3, and 137.5 eV) and P-O, P=O chemical bonds (133.5, and 133.4 eV) conform to the feature peaks of Li_xPF_y and $\text{Li}_x\text{PO}_y\text{F}_z$ (Schulz et al., 2018, Huang et al., 2019). Li 1s spectra are shown in **Figure 4. 21. (i)** and **(j)**, the peaks at higher binding energy (55.3, and 55.4 eV) are related to Li_2CO_3 . The lower binding energy (54.2, and 54.8 eV) is in agreement with the Li-O chemical bond, which is ascribed to the active material of the NCM cathode electrode, for LiBO_2 -coated NCM it should be assigned to Li-O of LiBO_2 with a broad peak (Schulz et al., 2018, Zhang et al., 2018b).

A ratio analysis of the main components of the CEI layer after 3 C cycling for NCM and LiBO₂-coated NCM was performed. The C=O and C-O species are organic compounds, while Li₂CO₃, Li_xPF_yO_z, LiF, and O-metal are the dominant inorganic constituents.

Figure 4. 21. (k) presents the chemical composition ratio of the CEI layer in the interfacial layer of NCM and LiBO₂-coated NCM derived from XPS analysis. The detected CEI chemical composition ratio of the interface layer on NCM is higher than that of LiBO₂-coated NCM, which demonstrates that less electrolyte decomposition occurs after the crystalline LiBO₂ coating modification and less accumulation of organic/inorganic interfacial species deposited on the cathode after being subjected to the high current density cycling with the crystalline LiBO₂ coating. It is concluded that the nanocrystalline LiBO₂ coating acts as a protective layer against attack from the electrolyte and mitigates side reactions between the active material and electrolyte.

To analyse the microcrack formation inside the Ni-rich cathode material, FIB-SEM analysis was performed to observe the cross-section of the cathode electrode after cycling. Cross-sectional SEM images of the NCM and LiBO₂-coated NCM samples after 1 C and 3 C cycling are shown in **Figure 4. 22**. Both samples appear to crack along the boundary of the primary particles, but the densities of the intergranular cracks of the two types of samples are completely different. For the LiBO₂-coated NCM, the crack is mainly restricted in the centre of secondary particles. While for NCM, the crack propagated from the centre to the surface of the secondary particles, especially after 3 C cycling, and the crack became more serious in contrast to that of LiBO₂-coated NCM (more clearly in the magnified images). Therefore, the LiBO₂ coating could effectively

restrict the development of cracking after cycling even at a high current density.

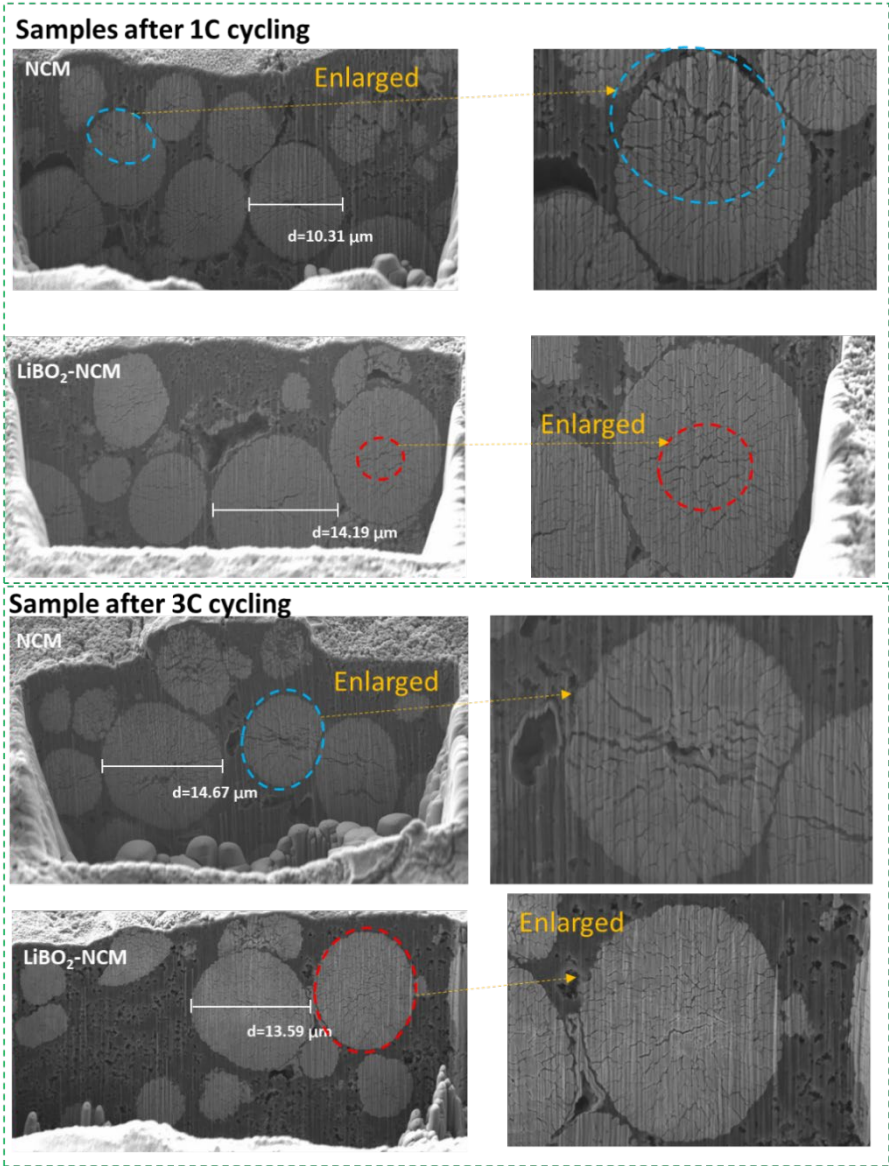


Figure 4. 22. FIB-SEM characterisation of cathode electrodes made by NCM and LiBO_2 -coated NCM after cycling

Based on comprehensive investigations of the electrochemical and mechanical properties, five main reasons are considered responsible for the fewer microcracks after LiBO_2 coating. First, because of the soft mainly $\alpha\text{-LiBO}_2$ coating, the particle stiffness can be reduced, which is beneficial for releasing stress and strain initiated in the process of Li-ion extraction/insertion of active material, thereby reducing crack formation (Liu

et al., 2021). The depressed H2–H3 phase transition after the crystalline LiBO₂ coating can be considered as the second reason, which plays an active role in alleviating secondary particle structure cracking, as noticeable microcracking occurs in the voltage regions above 4.0 V together with the lattice unit cell volume change that coincided with the H2–H3 phase transition (Zhang, 2020). Third, α -LiBO₂ and γ -LiBO₂ can absorb CO₂ at room temperature (Román-Tejeda and Pfeiffer, 2012). Although the CO₂ absorption is not considerably high, the crystalline LiBO₂ coating can positively alleviate the impact of gas evolution during cycling. Fourth, the three-layer structure together with the cracks blocked by the LiBO₂ nanorods provides strong protection against the attack from the electrolyte. The element loss from the cathode material initiated by side reactions between the NCM and the electrolyte can be effectively prohibited. Because the stability of the entire structure relies on the interaction of the Li, O, and TM layers, the limited element loss during cycling makes the layered oxide material more stable and inhibits crack formation after cycling (Min and Cho, 2018). Finally, the cracking degree is normally considered to be positively correlated with the charging/discharge rate, mainly because of the enhanced mismatch between the local ionic and electronic conductivities (Xia et al., 2018a). In the case of the LiBO₂-coated NCM, α -LiBO₂ and γ -LiBO₂ increased the Li-ion diffusion coefficient and decreased the electronic conductivity. Under the synergistic effects of the modified ion and electron conductivity, the microcracks induced by the high current density can be alleviated.

Additionally, because the polycrystalline Ni-rich cathode material has plentiful primary particles to form a near-spherical secondary particle, the structural compactness of the

secondary particles with a larger size is poorer than that of particles with a small size. Regardless of the stage before the battery operation or during battery operation, the large-sized polycrystalline Ni-rich cathode material is more prone to cracking. Prior to battery operation, the large-sized polycrystalline Ni-rich cathode material can easily crack under external shocks in the ball-milling process and fracturing process, which are the steps of the cathode material synthesis process. Meanwhile, during battery operation, the primary particles of large-sized polycrystalline material would suffer more inconsistent shrinkage and expansion during Li-ion extraction and insertion because of the longer Li-ion diffusion pathway in its charging/discharging cycle. It is therefore considered that the buffering protection from soft LiBO₂ nanoparticle coating and nanorod wrapping against cracking would be more pronounced for a polycrystalline material with a larger size than that with a small size.

4.4. Conclusion

A fast and convenient sol/antisolvent wet coating was developed to achieve nano-LiBO₂ coating of NLO in an anhydrous environment. The synthesised LiBO₂-coated NCM has a three-layer structure with a thin NiO-like rock-salt phase layer that exists between the LiBO₂ coating and NCM bulk. Owing to the α - and γ -mixed LiBO₂ coating modification, the modified battery exhibited a high ICE and a better fast charging ability with improved rate performance and 3 C cycling stability. The improved battery performance can be ascribed to the smaller polarisation, strengthened electrochemical reversibility of the H1–M phase transition and depressed H2–H3 phase transition, and enhanced Li-ion

diffusion coefficient of the electrode. The protection of the crystalline LiBO_2 coating was demonstrated by the reduced accumulation of organic/inorganic interfacial species deposits after cycling. The predominant problem of microcracks during the cycling of PC-NLO was also effectively alleviated by such a sol/antisolvent nano- LiBO_2 coating. In summary, the hypothesis of nanoparticle dispersion and aggregation for wet coatings is feasible. In addition to LiBO_2 , it is also worth studying other coating materials with sol/antisolvent methods to further improve NLO.

Chapter 5 Sol/Antisolvent Combined Coating and Doping with Boron-related Materials for $\text{LiNi}_{0.83}\text{Co}_{0.05}\text{Mn}_{0.12}\text{O}_2$ Cathode Towards High Capacity and High Cycling Stability

This chapter reports the sol/antisolvent treatment of the precursor of Ni-rich cathode material and the subsequent lithiation calcination to obtain a superior Ni-rich cathode material with combined boron-related doping and coating, along with an intrinsic daisy-like structure. Complete smooth and dense boron-related coating and near-surface doping can be achieved by Daisy-Ni83-Bmiddle which inherits the daisy-like structure from the precursor and can achieve superior long-term cycling, excellent rate performance, and strengthened thermal stability.

5.1. Introduction

Ni-rich layered oxides $\text{LiNi}_x\text{Co}_y\text{Mn}_{1-x-y}\text{O}_2$ and $\text{LiNi}_x\text{Co}_y\text{Al}_z\text{O}_2$ (NCM and NCA, $x \geq 0.8$) are regarded as the most promising cathodes for electric vehicles (EVs) because of their high capacities, high working potentials and relatively low costs (Zhang, 2020). The higher the nickel content, the higher capacity it can deliver, as nickel is the crucial redox active element in NCM and NCA with the $\text{Ni}^{2+}/3+$ and $\text{Ni}^{3+}/4+$ redox couples contributing primarily to the reversible capacity (Markevich et al., 2019). However, compared to traditional layered ternary oxides with low Ni content, the higher Ni content in NCM

and NCA leads to poorer cycling stability, weaker rate capability, and inferior thermal stability. These disadvantages limit the life span of batteries and impact their application in EVs (Bak et al., 2014, Wolfman et al., 2022). More serious Li/Ni disordering, structural degradation, parasitic reactions, and microcracks are identified as the main factors that accelerate the electrochemical and thermal instability of NLO ($\text{Ni} \geq 80\%$). To promote the use of NLO ($\text{Ni} \geq 80\%$) as excellent cathode materials, many strategies have been proposed to address their relatively quick degradation during cycling. Coating, which alters surface chemistry or provides physical protection layers, is the most fundamental strategy. Coating can be classified into two categories: inactive and active coatings. The inactive coatings such as oxides, fluorides, and phosphates can mainly act as passive layers against side reactions between the cathode and electrolyte. Active coatings, on the other hand, offer dual benefits, which not only can act as a protection layer to improve the surface structural stability of the cathode material but can also accelerate the charge transfer between the cathode material and electrolyte with enhanced rate capability because of superior electron conductivity and/or superior Li-ion conductivity, such as carbon-based coating materials (Ye et al., 2021, Guan et al., 2020). For high-energy density lithium-ion battery cathode materials such as NLO ($\text{Ni} \geq 80\%$), active coatings are considered ideal for modification (Nisar et al., 2021). For instance, dual-conductive coating layers composed of the Li-ion conductor Li_3PO_4 and the electronic conductor polypyrrole (PPy) have been developed by Chen et al. to improve both the cyclability and C-rate performance of $\text{LiNi}_{0.8}\text{Co}_{0.1}\text{Mn}_{0.1}\text{O}_2$ (Chen et al., 2017). Doping, another effective and commonly used strategy, improves the

structural stability of NLO ($\text{Ni} \geq 80\%$), making it more stable and resistant to phase transitions and oxygen release. There are two types of doping: cationic (dopants like Al, Ti, Si, Mg, and Fe, etc.) and anionic (dopants like F, Cl, and S, etc.) (Weigel et al., 2019, Binder et al., 2018). With proper lattice/bulk doping, the electrochemical properties can be enhanced owing to the increased lattice spacings, reduced bandgap, and increased electrical conductivity (Sharifi-Asl et al., 2019). Furthermore, doping strengthens the TM-O bond (TM = transition metal) within the Li-TM-O host structure, making it more stable and resistant to phase transitions and oxygen release. This results in slower capacity fading and better thermal stability (Min et al., 2017).

Although the above-mentioned modification strategies are often categorised separately, their combination is crucial for enhancing the internal and external structures of the cathode material, leading to superior electrochemical performance (Yan et al., 2020). This is because their combination has multifunctional effects (Ahaliabadeh et al., 2022). Ni-rich NCM and NCA ($\text{Ni} \geq 80\%$) with core-shell or concentration gradient structure offer promising avenues for research. Usually, the core-shell structure features a high-capacity Ni-rich core surrounded by a Ni-poor shell that enhances the structural and thermal stability (Wang et al., 2022, Wu et al., 2019b). Some shells can be composed of a spinel phase or rock-salt phase, improving the particle rigidity and stability during harsh electrochemical testing (Kim et al., 2018, Kalluri et al., 2020). The concentration gradient structure within NLO ensures that all internal regions are electrochemically active with varying transition metal (TM) concentrations. Mn-rich or Co-rich surfaces can maintain structural integrity and reduce strain during cycling (Lim et al., 2016, Liu

et al., 2021). Finally, the refined microstructure of Ni-rich NCM or NCA ($\text{Ni} \geq 80\%$) represents another novel approach. Doping with boron and aluminum can conceive the refined microstructure (Sun et al., 2020). In the refined structure, the primary particles are elongated and aligned in a radial orientation, unlike conventional polycrystalline Ni-rich layered oxides with randomly oriented primary particles. The refined morphology can reduce the aggregation of stress and dissipate the strain energy along the interparticle boundaries during cycling. The stress mitigation effect becomes more pronounced with narrower radially aligned primary particles (Ryu et al., 2020).

The objective of this investigation was to attain the highest level of performance from NLO ($\text{Ni} \geq 80\%$) materials by harnessing the advantages of their refined microstructure and the concurrent impact of coating and doping. It is important to note that we did not incorporate dopants with the intention of establishing a radially aligned arrangement of primary particles, but rather to adopt a precursor with a refined structure. The cathode material can inherit such a radially aligned structure after lithiation under the appropriate calcination conditions. Generally, boron-containing oxides (B_2O_3 , $\text{Li}_2\text{O} \cdot 2\text{B}_2\text{O}_3$, Li_3BO_3 , and LiBO_2), which are the hot coating agents for the modification of cathode materials, are considered good ion-conductors with high chemical stability (Yan et al., 2020, Yoon et al., 2021, Li et al., 2022, Lv et al., 2022). Boron is also a highly effective dopant for improving the structure and thermal stability of Li-TM-O host structure. This is primarily due to B-O binding energy is 809 kJ mol^{-1} , significantly exceeding those of Ni-O ($319.6 \text{ kJ mol}^{-1}$), Co-O (368 kJ mol^{-1}), Mn-O (402 kJ mol^{-1}), and Al-O (512 kJ mol^{-1}) of Ni-rich NCM or NCA (Park et al., 2018, Jeong et al., 2020). Therefore, it is

reasonable to consider that a high-capacity and high-stability NLO ($\text{Ni} \geq 80\%$) cathode can be achieved through combined coating and doping with boron-related oxides or boron-related lithium salts based on the intrinsic radially aligned microstructure. In this study, we used a unique NLO precursor ($\text{Ni}_{0.83}\text{Co}_{0.05}\text{Mn}_{0.12}(\text{OH})_2$) with a "daisy-like" cross-section for lithiation and modification. The outer regions of this precursor exhibit a remarkably radially aligned arrangement, resembling daisy petals, while the central region, resembling the pistil, comprises tightly packed, very small particles. To achieve the combined boron-related coating and doping modification, small amounts of B_2O_3 were added homogeneously on the surface of the specific hydroxide precursor by sol/antisolvent treatment before the lithiation process, which was developed in our previous study (Zhang et al., 2022). This approach ensures the lithiated oxide inherits the tailored structure and achieves the desired combined boron-based modification. To the best of our knowledge, previous research has only focused on separative boron-related coating modification or separative boron-related doping modification (Chen et al., 2021, Lv et al., 2022, Xia et al., 2022, Park et al., 2018, Amalraj et al., 2021). Despite some research reports on simultaneous boron-related coating and doping modification, the intrinsic refined microstructure of a radially aligned arrangement has not been studied together (Xie et al., 2019, Li et al., 2022).

The synthesised Ni-rich cathode material exhibits excellent electrochemical performance and thermal stability due to the "three-in-one" effect. Daisy-Ni83-Bthin and Daisy-Ni83-Bmiddle can deliver superior discharge capacity of 208.8 mAh g^{-1} and 209.1 mAh g^{-1} at 0.2 C , together with the discharge capacity of 223.7 mAh g^{-1} and 222.1

mAh g⁻¹ at 0.1 C between 2.8-4.3 V, and more outstanding discharge capacity of 233.2 mAh g⁻¹ and 230.4 mAh g⁻¹ at 0.1 C between 2.8-4.5 V. Meanwhile, Daisy-Ni83-Bthin and Daisy-Ni83-Bmiddle demonstrated improved cycling stability compared with the pristine Daisy-Ni83. However, the modification mechanisms of Daisy-Ni83-Bthin and Daisy-Ni83-Bmiddle differ slightly. Especially for Daisy-Ni83-Bmiddle, it achieves exceptional capacity retentions over 90% after 100 cycles at various current rates (3 C, 1 C, 0.5 C, 0.2 C) between 2.8-4.3 V and 0.2 C between 2.8-4.5 V, which are also higher than that of pristine Daisy-Ni83 in all the evaluation scenarios. This superior performance was attributed to the combined boron-related coating and doping achieved in Daisy-Ni83-Bmiddle. While, Daisy-Ni83-Bthin primarily undergoes boron doping modification and lacks the complete protective coating layer, leading to weaker resistance against high current density and high cut-off voltage. Furthermore, the search for the optimal lithiation calcination condition reveals four factors for achieving the ideal specific capacity in specially structured Ni-rich cathode materials: a highly ordered layered structure, clean surface without obvious lithium residues, reduced gaps among primary particles, and daisy-like radially refined structure.

5.2. Experimental Section

5.2.1. Ni-rich LiNi_{0.83}Co_{0.05}Mn_{0.12}O₂ Cathode Material (Daisy-Ni83) Preparation

To exploit the distinct advantage of the refined microstructure, we use the hydroxide precursor Ni_{0.83}Co_{0.05}Mn_{0.12}(OH)₂ in itself holding a tailored microstructure obtained

from Huayou Cobalt company. Scanning electron microscopy (SEM, S4800, Hitachi) was used to analyse the morphology. **Figure 5. 1** shows SEM morphologies of the precursor $\text{Ni}_{0.83}\text{Co}_{0.05}\text{Mn}_{0.12}(\text{OH})_2$. The precursor holds a spherical shape with interwoven lamellar primary particles (**Figure 5. 1. (a and b)**). SEM images of the cross-section of the precursor at different magnifications are shown in **Figure 5. 1. (d, e, and f)**, which looks like a daisy as shown in **Figure 5. 1. (c)**. Large lamellar particles with a length of approximately $1\ \mu\text{m}$ were arranged radially; meanwhile, many small nanoparticles with a length of approximately $50\ \text{nm}$ filled up the core of the precursor.

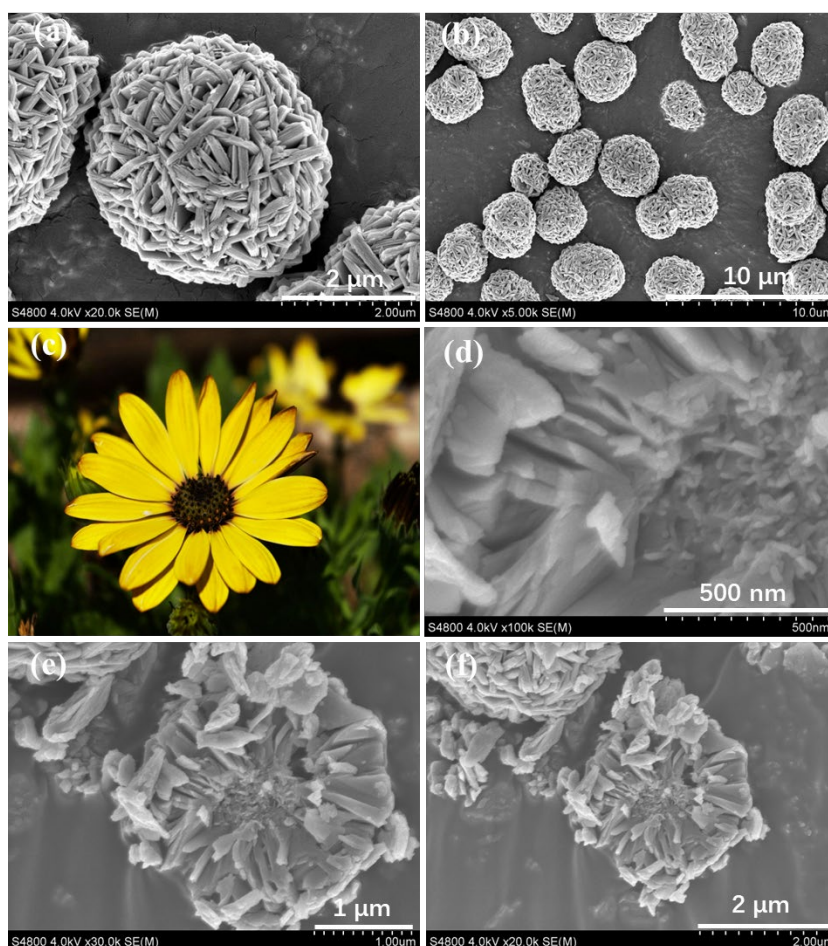


Figure 5. 1. SEM morphologies of the precursor $\text{Ni}_{0.83}\text{Co}_{0.05}\text{Mn}_{0.12}(\text{OH})_2$: (a and b) spherical-shape precursor, (c) a picture of daisy, (d, e, and f) cross-section images of precursor at different magnifications.

X-ray diffraction test (XRD, D8 ADVANCE, Bruker) was performed on the precursor powder to identify the crystalline structure. The test result is shown in **Figure 5. 2**, which demonstrates that the precursor is pure β -Ni(OH)₂ phase having a hexagonal-layered structure (Li et al., 2011, Yin et al., 2019).

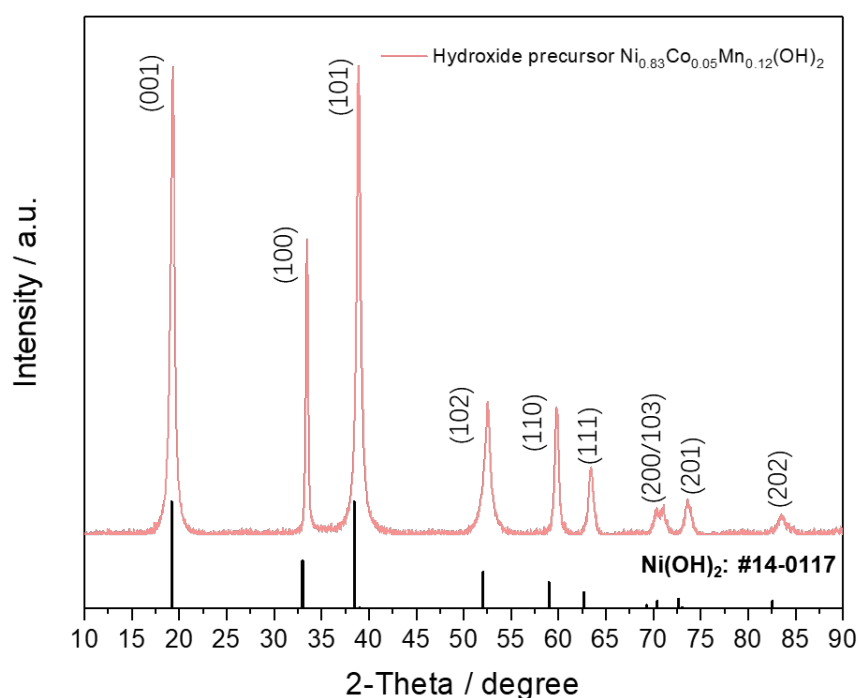


Figure 5. 2. XRD spectrum of the hydroxide precursor Ni_{0.83}Co_{0.05}Mn_{0.12}(OH)₂.

It is commonly acknowledged that, the more the Ni content, the optimal calcination temperature for lithiation shifts to the lower value. It is basically due to the presence of unstable Ni³⁺ at a higher temperature, which would lead to serious Li⁺/Ni²⁺ cation mixing and the deterioration of electrochemical properties (Butt et al., 2022). However, too low a calcination temperature will cause poor structural crystallinity of the material (Zheng et al., 2018). To prepare high-capacity Ni-rich cathode material, the calcination temperature for Ni_{0.83}Co_{0.05}Mn_{0.12}(OH)₂ with mixed exceeded LiOH·H₂O was varied

from 720 °C to 810 °C for 13 h in oxygen atmosphere for comparison. Before being subjected to the final calcination temperature in the lithiation process, the sintered materials were kept at 500 °C for 5 h to make the profound melt of the lithium source. The ramping rate was 3 °C/min for heating and is natural cooling in an oxygen atmosphere. Among those different calcination processes, the one that can guarantee high discharge capacity ($\geq 200 \text{ mAh g}^{-1}$) when charged to 4.3 V will be confirmed as the optimal calcination condition. The synthesised high-capacity cathode material from the optimal calcination condition will be named “Daisy-Ni83”. The same lithiation calcination condition will be used for the following combined boron-related coating and doping-treated cathode materials.

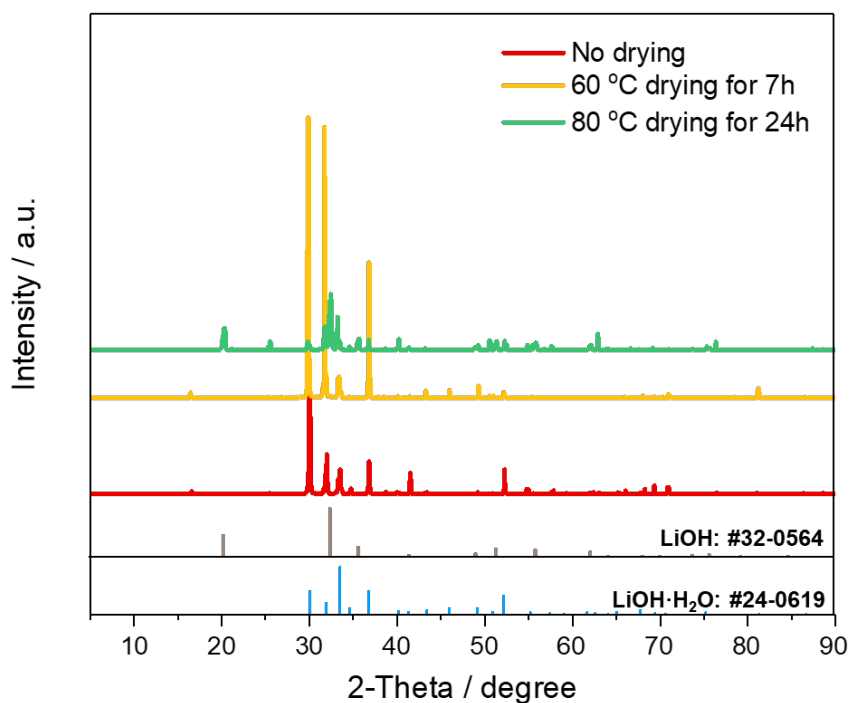


Figure 5. 3. XRD patterns of LiOH·H₂O after different drying treatments.

It should be noted that lithium hydroxide monohydrate ($\text{LiOH}\cdot\text{H}_2\text{O}$) can easily absorb moisture when exposed to the air. $\text{LiOH}\cdot\text{H}_2\text{O}$ was dried before mixing with the precursor. However, a high drying temperature and long drying time could remove the crystal water from $\text{LiOH}\cdot\text{H}_2\text{O}$ by changing the lithium salt to LiOH (Wolfman et al., 2022). In this case, the molar weight of the lithium source becomes larger than the designed one. To avoid such conditions, XRD tests were performed on 7 g $\text{LiOH}\cdot\text{H}_2\text{O}$ samples before and after different drying cycles. According to **Figure 5. 3**: XRD patterns of $\text{LiOH}\cdot\text{H}_2\text{O}$ upon different drying treatments, the sample appears pure $\text{LiOH}\cdot\text{H}_2\text{O}$ phase before drying, while the sample dried at 80 °C for 24 h changes into the LiOH phase with the coexistence of $\text{LiOH}\cdot\text{H}_2\text{O}$ phase. The XRD pattern of the sample drying at 60 °C for 7 h was almost the same as the sample before the drying and fitted well with the $\text{LiOH}\cdot\text{H}_2\text{O}$ diffraction code of JCPDS 24-0619. Therefore, it is appropriate to select the drying treatment at 60 °C for 7 h to remove the moisture from the lithium source for lithiation.

5.2.2. Synthesis of Boron-related Coating and Doping Modified Ni-rich $\text{LiNi}_{0.83}\text{Co}_{0.05}\text{Mn}_{0.12}\text{O}_2$ Cathode Material with Intrinsic Radially Aligned Microstructure

B_2O_3 purchased from Aladdin Shanghai was chosen as the boron source to modify Daisy-Ni83. For the XRD test, the B_2O_3 particles were milled and pulverized using ethanol during grinding. The XRD spectrum (**Figure 5. 4**) demonstrates that it is a completely amorphous material with broad humps consistent with the B_2O_3 diffraction code of JCPDS 06-0297 (Shuai et al., 2017).

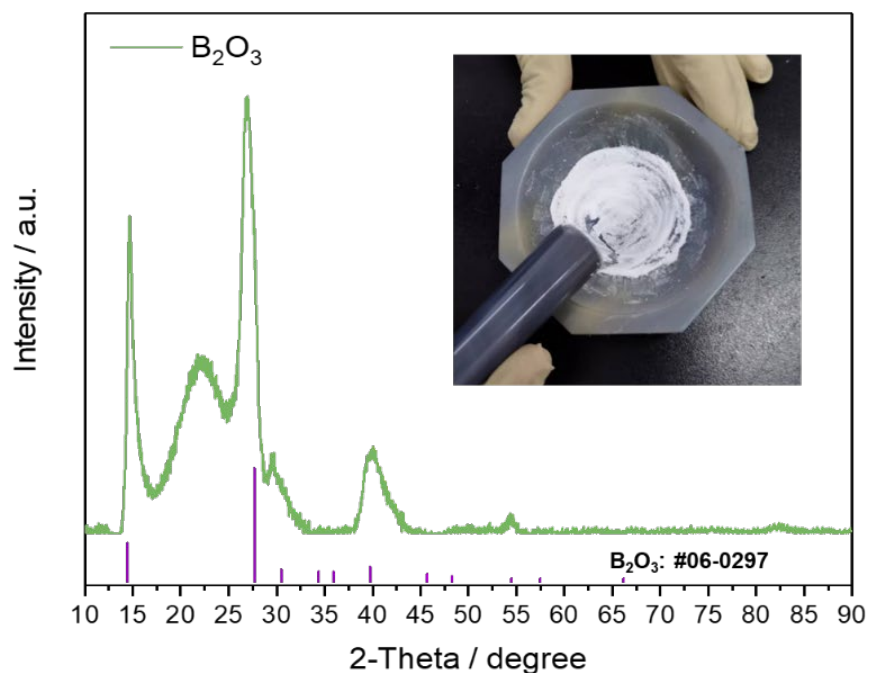


Figure 5. 4. XRD pattern of B_2O_3 after milling.

A schematic diagram of the synthesis of the boron-related coating and doping-modified $LiNi_{0.83}Co_{0.05}Mn_{0.12}O_2$ based on the intrinsic refined microstructure of the daisy-like cross-section is shown in **Figure 5. 5**. First, a B_2O_3 coating is achieved on the precursor by a sol/antisolvent coating. The process is similar to the coating of $LiBO_2$ onto the cathode material that we have done previously (Zhang et al., 2022). B_2O_3 -coated $Ni_{0.83}Co_{0.05}Mn_{0.12}(OH)_2$ was further calcinated with the dried lithium source to obtain the final modified cathode materials.

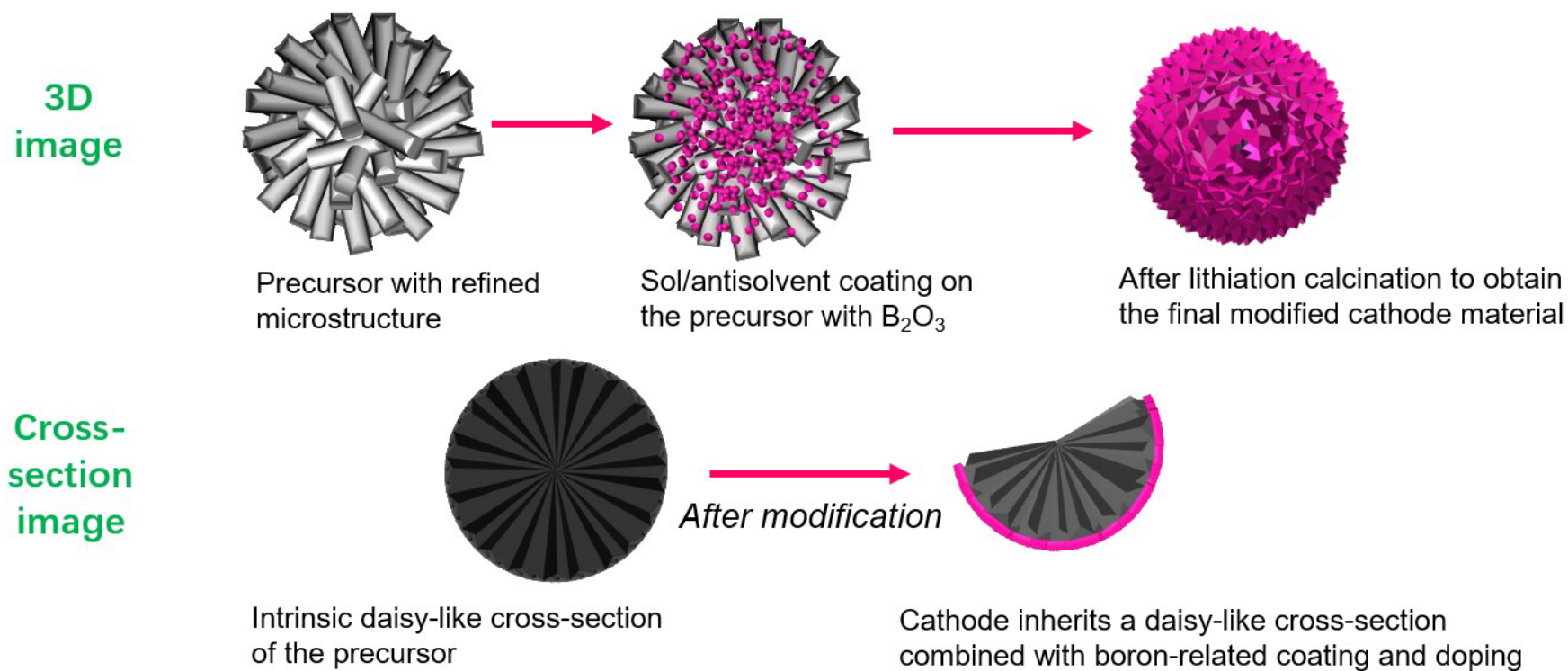


Figure 5. 5. Schematic diagram of the synthesis of the combined boron-related coating and doping-modified $LiNi_{0.83}Co_{0.05}Mn_{0.12}O_2$ based on the intrinsic refined microstructure of daisy-like cross-section.

In the detail of synthesising boron-related coating and doping modified Ni-rich $\text{LiNi}_{0.83}\text{Co}_{0.05}\text{Mn}_{0.12}\text{O}_2$ cathode material with the intrinsic refined microstructure, 2 g precursor with daisy-like cross-section image as shown in **Figure 5. 1** was poured into 50 ml B_2O_3 ethanol sol and was stirred at 800 rpm with a magnetic stirrer for 10 min. Then 35 ml tetrahydrofuran (THF) was used as the antisolvent with using the peristaltic pump to control the feeding speed at 2 ml/minute. The sol/antisolvent coating was limited to 17.5 min. A three-neck flask was used to coat the precursors with B_2O_3 . The three-neck flask was maintained at 20 °C in a water bath with continuous magnetic stirring.

To compare the effects of different amounts of B_2O_3 on the cathode material, we prepared the ethanol sols containing different doses of B_2O_3 . The mole mass ratios of boron to precursor $\text{Ni}_{0.83}\text{Co}_{0.05}\text{Mn}_{0.12}(\text{OH})_2$ were varied to be 0.05, 0.075, and 0.1. Based on the 2 g precursor, the masses of B_2O_3 added to 60 ml anhydrous alcohol were 0.0377, 0.0566, and 0.0755 g, respectively. After completing the B_2O_3 coating of the precursor, the solid particles were collected by vacuum filtration. The powder was dried in a blast drying oven at 50 °C overnight. The subsequent lithiation calcination process was the same as the process for Daisy-Ni83. The synthesised cathode materials would inherit the daisy-like cross-section combined with boron-related coating and doping. They were named Daisy-Ni83-Bthin, Daisy-Ni83-Bmiddle, and Daisy-Ni83-Bthick based on the treatment from different B_2O_3 ethanol sols with B_2O_3 contents of 0.0377 g, 0.0566 g, and 0.0755 g, respectively. An interesting phenomenon is the production of B_2O_3 ethanol sol (**Figure 5. 6**) is much quicker than LiBO_2 ethanol sol, which needs only 100

min rather than 9 h for dispersing B_2O_3 in 60 ml anhydrous alcohol with ultrasonic treatment. Furthermore, the B_2O_3 ethanol sol can be used after deposition of only one day more efficiently than the $LiBO_2$ ethanol sol which requires over three days for deposition.



Figure 5. 6. Transparent B_2O_3 ethanol sol with the light scattering by laser beam.

5.2.3. Electrochemical and Thermal Stability Tests of Daisy-Ni83, Daisy-Ni83-Bthin, Daisy-Ni83-Bmiddle, and Daisy-Ni83-Bthick

For electrochemical tests, different cathode materials were mixed with a Super P conductor and PVDF binder at a mass ratio of 8:1:1 in N-methyl pyrrolidone (NMP). The slurry was coated onto an Al foil and dried in a blast drying oven at 80 °C for 5 h. The electrode plate was then punched and pressed with 10 MPa into 14 mm diameter circle electrodes for weighting. Afterward, the circled electrode plates were put in an

oven at 80 °C another 12 h. Then the positive electrode was then assembled with a Celgard M825 separator, lithium metal anode, spacer, spring, positive and negative cases, and 100 μL electrolyte into a 2032 coin-type half cell. The electrolyte was composed by the volume ratio of 3:7 ethylene carbonate (EC)/dimethyl carbonate (DMC) with 1 M LiPF_6 . The electrolyte amount of 100 μL was higher than that used with 80 μL electrolyte for the first work, considering that a higher electrolyte amount favors long-time cycling due to the inevitable electrolyte decomposition in longer cycle tests (Chen et al., 2019). The coin-cell assembly was completed in an argon-filled glove box with O_2 less than 0.5 ppm and H_2O less than 0.5 ppm (MBRAUN UniLab). The mass of active material was approximately 6–8 mg. Various electrochemical testing machines and methods have been used for these coin cells. First, galvanostatic cycling with potential limitation (GCPL) measurements at different current densities ($1\text{ C} = 200\text{ mA g}^{-1}$) in the voltage range of 2.8 to 4.3 V (vs Li/Li^+) using a LAND cell test system at room temperature. The purpose of such GCPL testing was to investigate the cycling stabilities and rate performances of the different cells. Second, electrochemical impedance spectroscopy (EIS) tests over the frequency range of 0.1 MHz to 0.01 Hz were conducted for coin cells to investigate the electrolyte resistance (R_s) and charge transfer resistance (R_{CT}) for each coin cell. EIS tests were performed by an electrochemical workstation (Solartron Analytical).

Thermal stability was analysed using a differential scanning calorimeter (DSC 3, Mettler Toledo). Normally, delithiated cathode materials are used for the thermal stability test (Kim et al., 2019, Wang et al., 2021). For obtaining the delithiated cathode

materials, the coin cells were firstly fully cycled 3 times at 0.2 C in the voltage range of 2.8 to 4.4 V and then charged to 4.3 V at 0.1 C and stopped. The charged cells were then disassembled in an argon-filled glove box. The positive electrode was removed from the cell and rinsed in dimethyl carbonate (DMC) for 3 h, and dried in a glove box for another 3 h. Subsequently, the cathode material was scraped from the aluminum foil, collected, and stored in a bottle in the glove box. The cathode powder in the bottle was then transferred to an aluminum crucible and sealed using a Mettler Toledo press in a glove box. The sealed crucible with cathode material was investigated by DSC 3 in a nitrogen atmosphere from 30 to 400 °C at a rate of 1 °C/min to obtain the DSC data.

5.2.4. Material Composition and Microstructure Characterisation of Daisy-Ni83, Daisy-Ni83-Bthin, Daisy-Ni83-Bmiddle, and Daisy-Ni83-Bthick

ICP-OES (SPECTRO ARCOS) analysis was carried out to confirm the elementary compositions of the synthesised Ni-rich cathode materials. The phase states of the synthesised Daisy-Ni83, Daisy-Ni83-Bthin, Daisy-Ni83-Bmiddle, and Daisy-Ni83-Bthick were identified by XRD (D8 ADVANCE, Bruker). The morphologies and microstructures of the Ni-rich cathode materials were observed using scanning electron microscope (SEM, S4800, Hitachi). A transmission electron microscope (TEM) equipped with energy dispersive X-ray spectroscopy (Talos F200x, ThermoFisher) was adopted to obtain high-resolution images of Daisy-Ni83, Daisy-Ni83-Bthin, Daisy-Ni83-Bmiddle and Daisy-Ni83-Bthick, as well as the cathode electrolyte interphase

(CEI) film after cycling. Scanning electron microscopy with energy dispersive X-ray spectroscopy (SEM/EDS, FEI Quanta FEG 250) was also used to perform the elemental mapping. X-ray photoelectron spectroscopy (XPS, Krotos AXIS Supra, Shimadzu) was used to analyse the boron compounds in the cathode material powders and the compositional characteristics of the CEI films on different cathodes.

5.3. Results and Discussion

5.3.1. Four Factors Determining the Optimal Lithiation Calcination Condition for Daisy-Ni83

The high discharge capacity, equal to or larger than 200 mAh g⁻¹ when charged to 4.3 V based on the electrochemical test, is deemed as the index to determine the optimal lithiation calcination condition for Daisy-Ni83. **Figure 5. 7** shows the 1 C cycling performances of LiNi_{0.83}Co_{0.05}Mn_{0.12}O₂ cathode materials synthesised at 720, 750, and 780 °C with 5% mole excess LiOH·H₂O in the voltage range of 2.8-4.3 V. The 1 C cycling performances was tested with an activation process with 10 cycles at 0.2 C and followed by 5 cycles at 0.5 C before the long 1 C cycling with a total of 165 cycles in the voltage range of 2.8-4.3 V. The molar ratio of precursor to LiOH·H₂O was initially determined as 1:1.05, considering the evaporation of lithium source at high temperatures and the possibly severe Li/Ni disordering arising from the lack of lithium (Yu et al., 2020). The results show that the discharge capacity declines at 0.2 C as the calcination temperature is reduced, wherein the red, blue, and yellow point represents the LiNi_{0.83}Co_{0.05}Mn_{0.12}O₂ cathode material synthesised at 780 °C, 750 °C, and 720 °C,

respectively. Obviously, the long-term cycling at 1 C experiences quick capacity fading for all samples, especially after the 90th cycle as shown in **Figure 5. 7**.

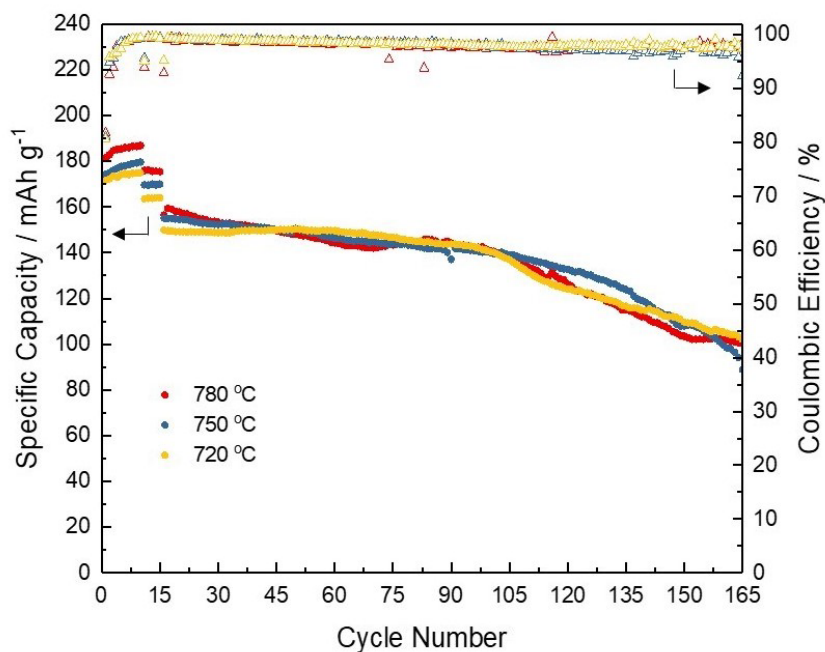


Figure 5. 7. 1 C cycling performances of $\text{LiNi}_{0.83}\text{Co}_{0.05}\text{Mn}_{0.12}\text{O}_2$ cathode materials synthesised at 720, 750, and 780 °C with 5% mole excess $\text{LiOH}\cdot\text{H}_2\text{O}$ between 2.8-4.3 V.

The detailed maximum discharge capacity of each sample at 0.2, 0.5, and 1 C in the voltage range of 2.8 to 4.3 V synthesised at different calcination temperatures with 5% mole excess lithium source is listed in **Table 5. 1**. The discharge capacity of $\text{LiNi}_{0.83}\text{Co}_{0.05}\text{Mn}_{0.12}\text{O}_2$ cathode material synthesised at 780 °C with 5% mole excess $\text{LiOH}\cdot\text{H}_2\text{O}$ appears relatively higher than those synthesised at 750 °C and 720 °C at different current densities. However, the discharge capacity of 186.9 mAh g^{-1} at 0.2 C between 2.8-4.3 V is not high enough.

Table 5. 1. Maximum discharge capacity of each cathode material at 0.2, 0.5, and 1 C in the voltage range of 2.8 to 4.3 V synthesised at different calcination temperatures with 5% mole excess LiOH·H₂O.

Temperature Discharge Capacity (mAh g ⁻¹)	720 °C	750 °C	780 °C
	0.2 C	175	179.7
0.5 C	164.1	170	176.2
1 C	150.3	155.1	159.4

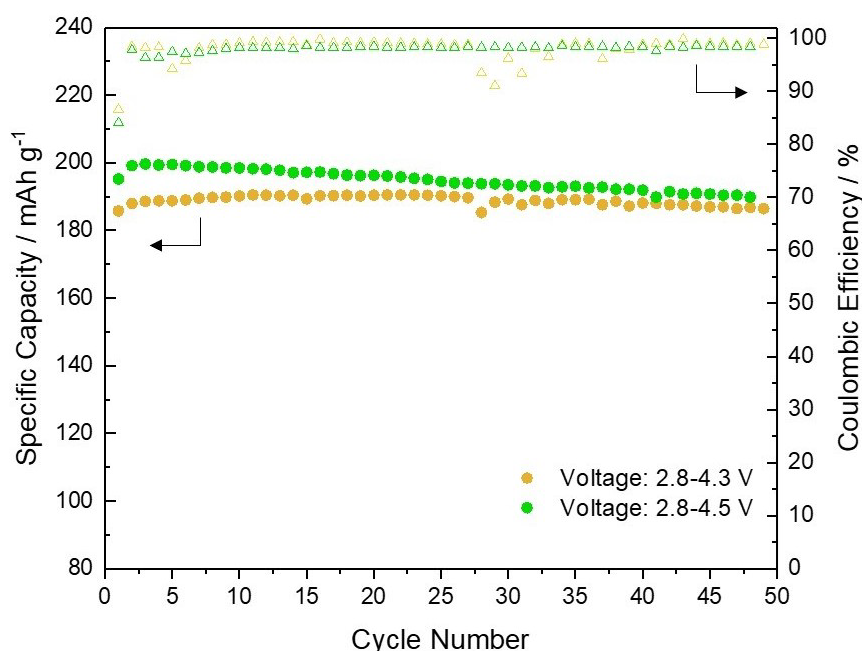


Figure 5. 8. 0.2 C cycling performances of LiNi_{0.83}Co_{0.05}Mn_{0.12}O₂ cathode material synthesised at 780 °C with 5% mole excess LiOH·H₂O in the voltage range of 2.8-4.3 V and 2.8-4.5 V.

A higher discharge capacity of 190.5 mAh g⁻¹ at 0.2 C between 2.8-4.3 V is found during 0.2 C cycling of LiNi_{0.83}Co_{0.05}Mn_{0.12}O₂ cathode materials synthesised at 780 °C with 5% mole excess LiOH·H₂O as shown in **Figure 5. 8**. The discharge capacity can reach 199.7

mAh g⁻¹ at 0.2 C with the cut-off voltage at 4.5 V, but such capacity is still not ideal (Konarov et al., 2017). To improve the specific capacity of the Ni-rich cathode material until it reaches an index equal to or larger than 200 mAh g⁻¹ when charged to 4.3 V, the reasons for the relatively low capacity need to be determined.

SEM and XRD tests were performed to investigate the factors associated with relatively low specific capacity. **Figure 5. 9** shows the SEM images of the surface of the original Ni_{0.83}Co_{0.05}Mn_{0.12}(OH)₂ precursor and LiNi_{0.83}Co_{0.05}Mn_{0.12}O₂ cathode materials synthesised at different temperatures from 720 °C to 780 °C with 5% mole excess LiOH·H₂O. It can be seen that the primary particles on the outside surface of LiNi_{0.83}Co_{0.05}Mn_{0.12}O₂ cathode material are distributed more densely after changing the calcination temperature from 720 °C to 780 °C as shown in **Figure 5. 9.** (b1), (c1), and (d1). This is because the size of primary particles increases owing to the better fusion of primary particles at higher calcination temperatures. Meanwhile, abundant small particles adhere to the surface of the cathode materials, especially at lower calcination temperatures, which should be the lithium residues (Zhang et al., 2022). These lithium residues make the surface of the cathode material appear dirty, as shown in **Figure 5. 9.** (b1) and (c1). The existence of abundant lithium residues can be considered a reason for the low specific capacities. The generation of lithium residues can increase the interface impedance of cathode materials and lead to irreversible capacity loss during the first cycle (Su et al., 2021).

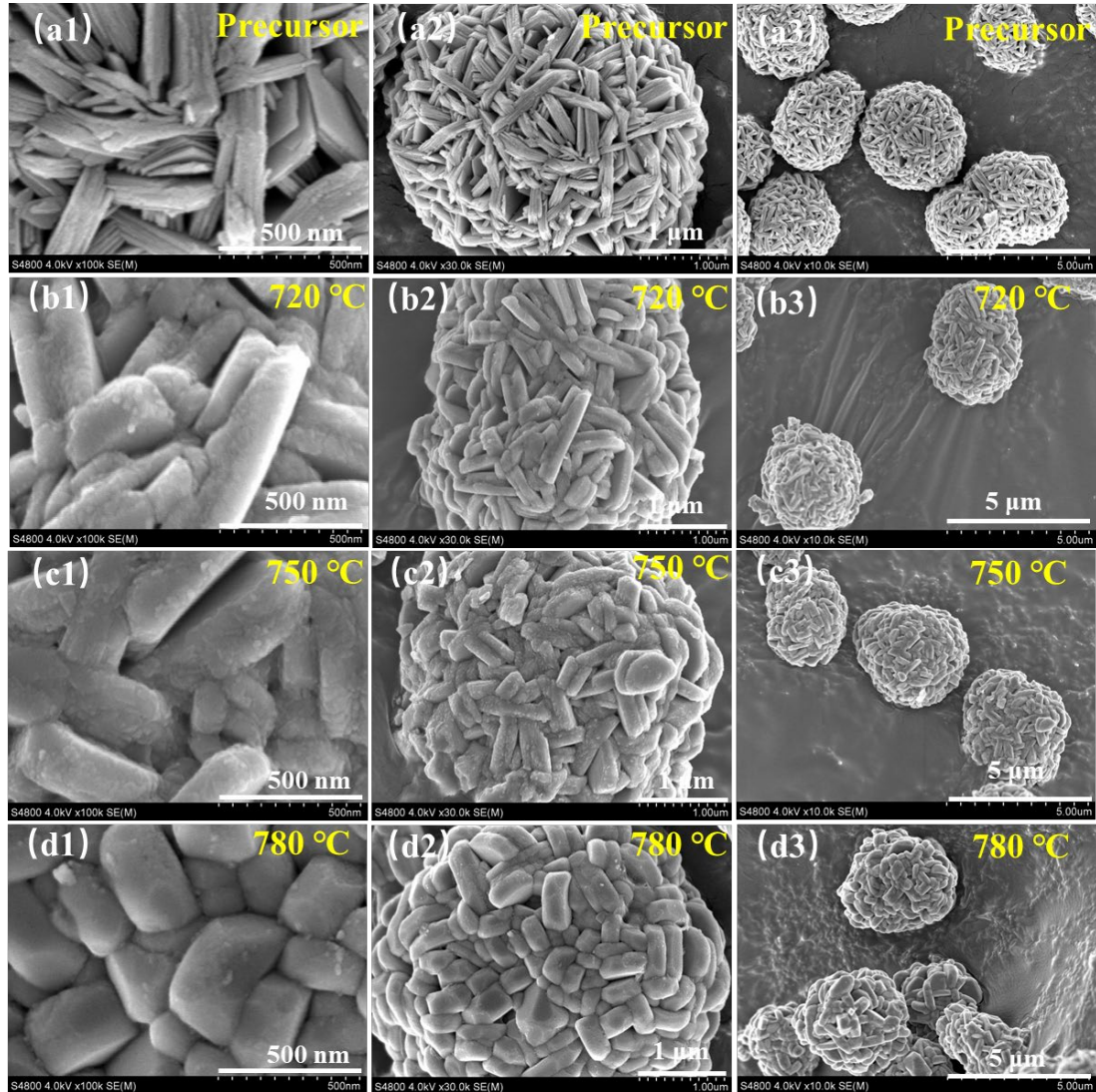


Figure 5. 9. SEM images on the surface of the original $\text{Ni}_{0.83}\text{Co}_{0.05}\text{Mn}_{0.12}(\text{OH})_2$ precursor and $\text{LiNi}_{0.83}\text{Co}_{0.05}\text{Mn}_{0.12}\text{O}_2$ cathode materials synthesised at different temperatures with 5% mole excess $\text{LiOH}\cdot\text{H}_2\text{O}$: (a1-a3) precursor, (b1-b3) cathode material synthesised at 720 °C, (c1-c3) cathode material synthesised at 750 °C, (d1-d3) cathode material synthesised at 780 °C.

Figure 5. 10 shows the cross-section SEM images of the original $\text{Ni}_{0.83}\text{Co}_{0.05}\text{Mn}_{0.12}(\text{OH})_2$ precursor and $\text{LiNi}_{0.83}\text{Co}_{0.05}\text{Mn}_{0.12}\text{O}_2$ cathode materials synthesised at different temperatures with 5% mole excess $\text{LiOH}\cdot\text{H}_2\text{O}$, it is clear that the grain size of primary particles gets increases from 720 °C to 780 °C (**Figure 5. 10.** (b1), (c1), and (d1)). There are large gaps between the primary particles for samples synthesised at 720 °C (**Figure 5. 10.** (b1) and (b2)), whereas gaps can hardly be found for samples synthesised at higher calcination temperatures, such as at 780 °C (**Figure 5. 10.** (d1) and (d2)). It is reasonable to consider that the gaps between primary particles of samples synthesised at low temperature is another factor accounting for the low specific capacity, similar to the sample synthesised at 720 °C. Because the gaps can be filled after the fusion of primary particles at higher calcination temperatures, the drawback of gaps between the primary particles can be mitigated. Theoretically, the minimised gaps between the primary particles can enhance the conductivity of the cathode material, and the corresponding specific capacity can be improved. In addition, as shown in **Figure 5. 10.** (a1), (b1), (c1), and (d1), 720 °C, 750 °C, or 780 °C, daisy-like structure was not destroyed. A higher calcination temperature corresponds to a larger petal structure. The distribution of primary particles with radially aligned arrangements resembling petals of daisies originating from precursor, was inherited for all samples.

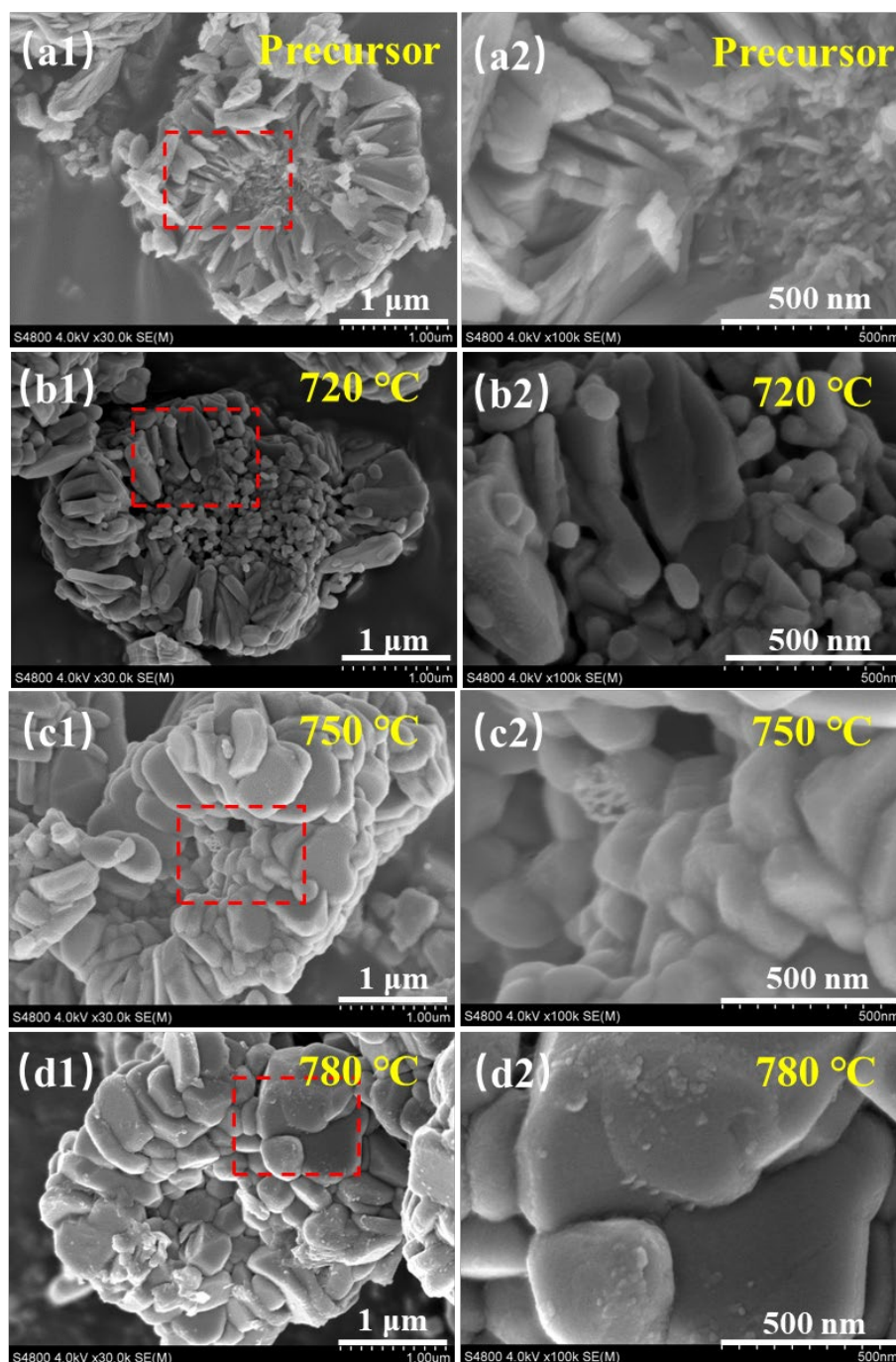


Figure 5. 10. SEM images on the cross-section of the original $\text{Ni}_{0.83}\text{Co}_{0.05}\text{Mn}_{0.12}(\text{OH})_2$ precursor and $\text{LiNi}_{0.83}\text{Co}_{0.05}\text{Mn}_{0.12}\text{O}_2$ cathode materials synthesised at different temperatures with 5% mole excess $\text{LiOH}\cdot\text{H}_2\text{O}$: (a1-a2) precursor, (b1-b2) cathode materials synthesised at 720 °C, (c1-c2) cathode materials synthesised at 750 °C, (d1-d2) cathode materials synthesised at 780 °C (the red dashed boxes on the left are magnified as shown on the right).

XRD results of $\text{LiNi}_{0.83}\text{Co}_{0.05}\text{Mn}_{0.12}\text{O}_2$ cathode materials synthesised at 720 °C, 750 °C, and 780 °C with 5% mole excess $\text{LiOH}\cdot\text{H}_2\text{O}$ are shown in **Figure 5. 11**. The XRD patterns of different samples match well with the standard pattern of $R\bar{3}m$ LiNiO_2 (JCPDS No.09-0063). The main characteristic peaks are marked in this XRD spectrum. Generally, the Li/Ni disordered distribution is considered to be one of the main reasons for the capacity decrease of Ni-rich layered oxide (Wu et al., 2015). The ratio of $I(003)/I(004)$ can act as the index to indicate the degree of Li/Ni disordering. The higher the ratio, the more well-defined is the layered structure of the material. The values of $I(003)/I(004)$ for $\text{LiNi}_{0.83}\text{Co}_{0.05}\text{Mn}_{0.12}\text{O}_2$ cathode materials synthesised at 720, 750, and 780 °C with 5% mole excess $\text{LiOH}\cdot\text{H}_2\text{O}$ are listed in **Table 5. 2**. Compared with the sample synthesised at 780 °C, the values of $I(003)/I(004)$ for samples synthesised at 720 °C and 750 °C are lower, which means the higher calcination temperature of 780 °C gives the material better crystallinity than those synthesized at 720 °C and 750 °C. However, a calcination temperature that is too high will affect the crystallinity. This is because a temperature that is too high can destroy the Li/Ni ordering owing to the inevitable loss of Li and O (Zhang, 2020, Wang et al., 2017).

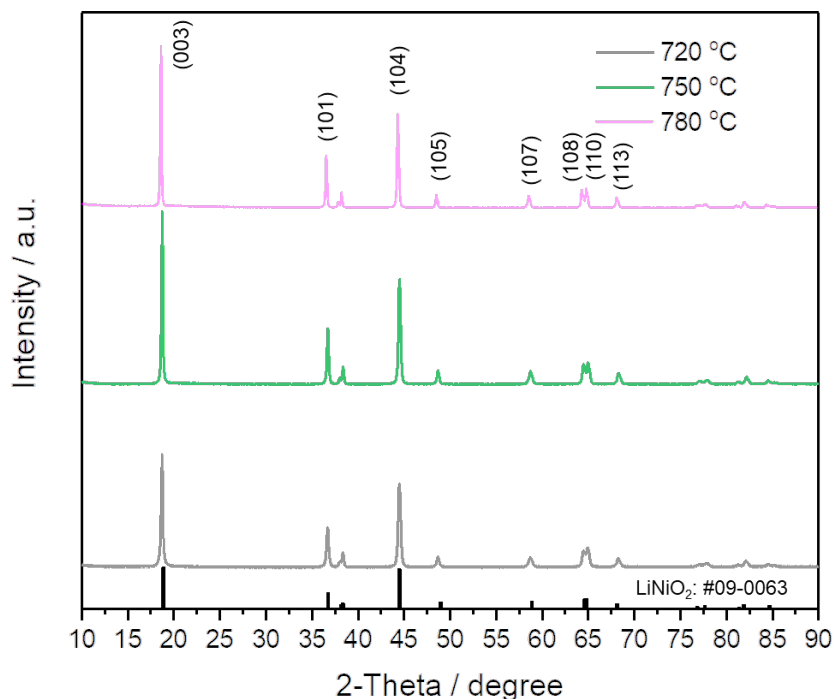


Figure 5. 11. XRD patterns of $\text{LiNi}_{0.83}\text{Co}_{0.05}\text{Mn}_{0.12}\text{O}_2$ cathode materials synthesised at different temperatures with 5% mole excess $\text{LiOH}\cdot\text{H}_2\text{O}$. the gray line represents 720 °C, the green line represents 750 °C, and the purple line represents 780 °C.

Table 5. 2. $I(003)/I(104)$ intensity ratios of XRD data to indicate the degree of Li/Ni disordering for $\text{LiNi}_{0.83}\text{Co}_{0.05}\text{Mn}_{0.12}\text{O}_2$ cathode materials synthesised at 720 °C, 750 °C and 780 °C with 5% mole excess $\text{LiOH}\cdot\text{H}_2\text{O}$.

Sample	720 °C	750 °C	780 °C
$I(003)/I(104)$	1.2872	1.5405	1.6233

To determine the upper limit temperature for synthesising such specially structured polycrystalline cathode material, the calcination temperature of 810 °C with 5% mole excess $\text{LiOH}\cdot\text{H}_2\text{O}$ was also studied. XRD and SEM analysis of the cathode material

810 °C with 5% mole excess $\text{LiOH}\cdot\text{H}_2\text{O}$ were performed. **Figure 5. 12** shows the corresponding XRD and SEM results, which shows that the sample synthesised at 810 °C fits well with the $R\bar{3}m$ LiNiO_2 structure. But the ratio of $I(003)/I(004)$ is extremely low with only 1.0825 less than 1.2, indicating that the temperature of 810 °C is not appropriate for sintering such precursors, owing to severe cationic disordering (Ren et al., 2020). Compared with the particles synthesised at 780 °C, as shown in **Figure 5. 9** (d1), the primary particle size at 810 °C calcination condition becomes larger with the same scalebar of 500 nm, even some single crystals with lengths over 1 μm can be found, which are marked by the white dotted circles in the inserted SEM image of **Figure 5. 12**. Considering such poor Li/Ni ordering and the tendency of single crystal growth, the reversible specific capacity would be low, and no electrochemical test was performed for such an 810 °C sample.

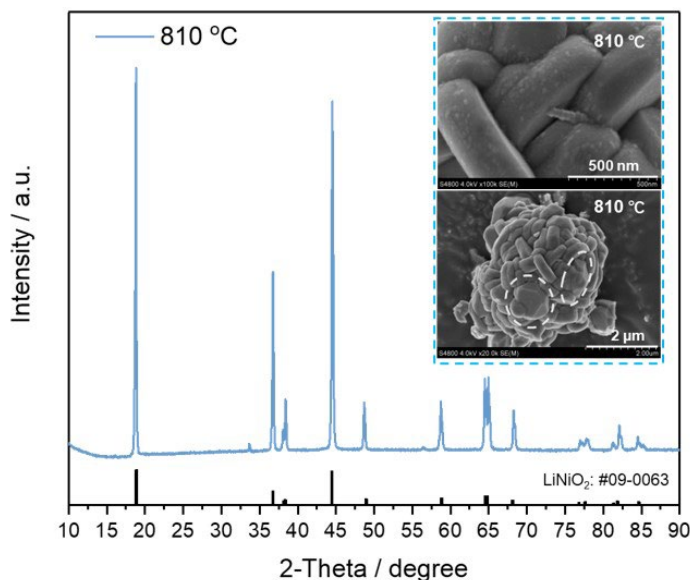


Figure 5. 12. XRD patterns of $\text{LiNi}_{0.83}\text{Co}_{0.05}\text{Mn}_{0.12}\text{O}_2$ cathode material synthesised at 810 °C with 5% mole excess $\text{LiOH}\cdot\text{H}_2\text{O}$ (SEM images of such cathode material are inserted).

From the above comprehensive analysis, it can be confirmed that without destroying the daisy-like structure, the problems of large amounts of lithium residues, gaps between primary particles, and Li/Ni disordered distribution of cathode materials are the main reasons for the relatively low capacity. It is reasonable to think a slight decrease in the amount of lithium source and an appropriate increase in the calcination temperature can effectively eliminate the aforementioned problems. The lithiation calcination conditions were adjusted to a calcination temperature of 800 °C along with 2% mole excess LiOH·H₂O. 50 cycles charging/discharging performances of LiNi_{0.83}Co_{0.05}Mn_{0.12}O₂ cathode material synthesised at 800 °C with 2% mole excess LiOH·H₂O at the current density of 0.2 C within the voltage range of 2.8-4.3 V and 2.8-4.5 V is shown in **Figure 5. 13**. It indicates that different from LiNi_{0.83}Co_{0.05}Mn_{0.12}O₂ cathode materials synthesised at 780 °C with 5% mole excess LiOH·H₂O, as shown in **Figure 5. 8**, LiNi_{0.83}Co_{0.05}Mn_{0.12}O₂ cathode material synthesised at 800 °C with 2% mole excess LiOH·H₂O delivers higher capacities, the discharge capacity can reach 198.5 mAh g⁻¹ at the current density of 0.2 C in the potential range of 2.8-4.3 V, and reach 214.9 mAh g⁻¹ for 0.2 C at 4.5 V. These values can reach the ideal capacities for Ni-rich layered oxides of appropriately 200 mAh g⁻¹ up to 4.3 V (Konarov et al., 2017). The corresponding LiNi_{0.83}Co_{0.05}Mn_{0.12}O₂ cathode material synthesised at 800 °C with 2% mole excess LiOH·H₂O was therefore named Daisy-Ni83.

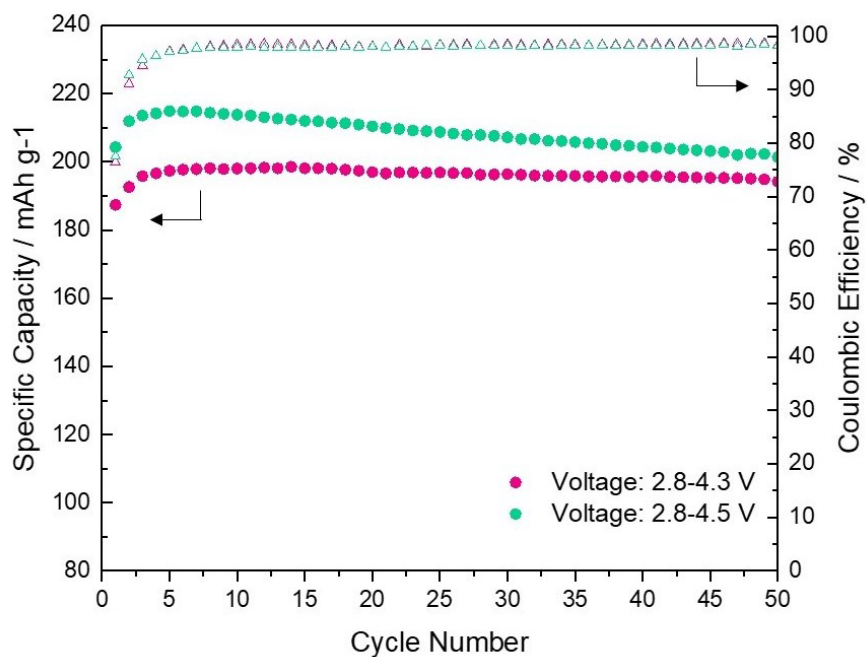


Figure 5. 13. 0.2 C cycling performances of $\text{LiNi}_{0.83}\text{Co}_{0.05}\text{Mn}_{0.12}\text{O}_2$ cathode material synthesised at 800 °C with 2% mole excess $\text{LiOH}\cdot\text{H}_2\text{O}$ (Daisy-Ni83) in the voltage range of 2.8-4.3 V and 2.8-4.5 V.

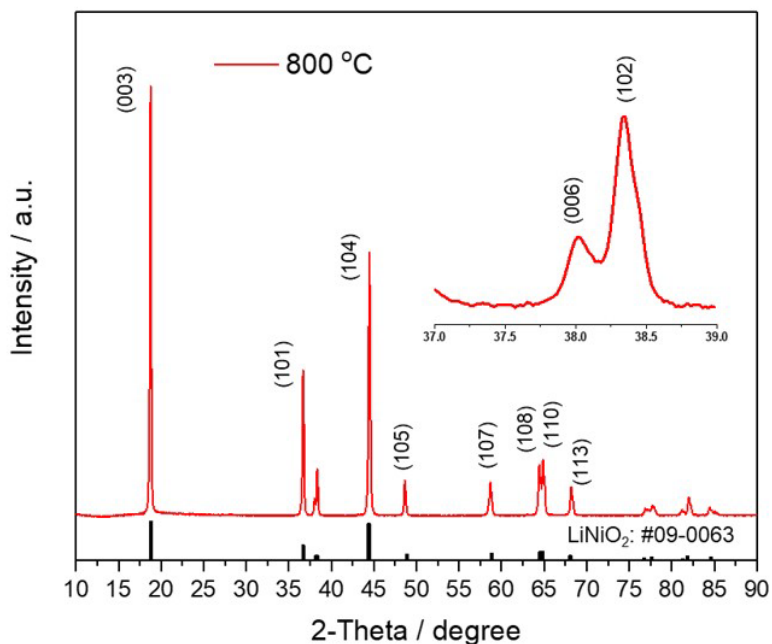


Figure 5. 14. XRD patterns of $\text{LiNi}_{0.83}\text{Co}_{0.05}\text{Mn}_{0.12}\text{O}_2$ cathode material synthesised at 800 °C with 2% mole excess $\text{LiOH}\cdot\text{H}_2\text{O}$ (Daisy-Ni83).

The XRD analysis of Daisy-Ni83 is shown in **Figure 5. 14**. The XRD spectrum demonstrated that Daisy-Ni83 fitted well with the standard pattern of $R\bar{3}m$ LiNiO₂ (JCPDS No.09-0063). The I(003)/I(104) intensity ratio is 1.5394 larger than 1.2, and the clear separation of adjacent peaks of (006)/(102) and (108)/(110) can be observed, confirming that Daisy-Ni83 has a well ordered layered structure with a high degree of crystallinity.

SEM images on the surface and cross-sections at different angles and magnifications for Daisy-Ni83 are shown in **Figure 5. 15**. In contrast to the appearance of large amounts of lithium residues on the surface of cathode materials synthesised at 720, 750, and 780 °C with 5% mole excess LiOH·H₂O, as shown in **Figure 5. 9**, the lithium residue was greatly reduced for Daisy-Ni83, which appeared as a clean surface (**Figure 5. 15. (a1-a4)**). Meanwhile, the overall gaps among primary particles are further reduced owing to the developed particle fusion when comparing **Figure 5. 15. (a1)** of cathode material synthesised at 800 °C and **Figure 5. 9. (d1)** cathode material synthesised at 780 °C. For Daisy-Ni83, no matter the cutaway images with an oblique angle (**Figure 5. 15. (b1-b4)**), or cross-section images of a plane perpendicular to the secondary particle (**Figure 5. 15. (c1-c4)**), the arrangement of primary particles keeps a good radical distribution, liking the blooming flower. Overall, the characteristics of good crystallinity, less amount of lithium residues, improved particle fusion, and the daisy-like cross-section structure inherited from the precursor enabled Daisy-Ni83 to achieve the ideal specific capacity. The relevant lithiation calcination conditions were determined to be optimal for synthesising Ni-rich cathode materials.

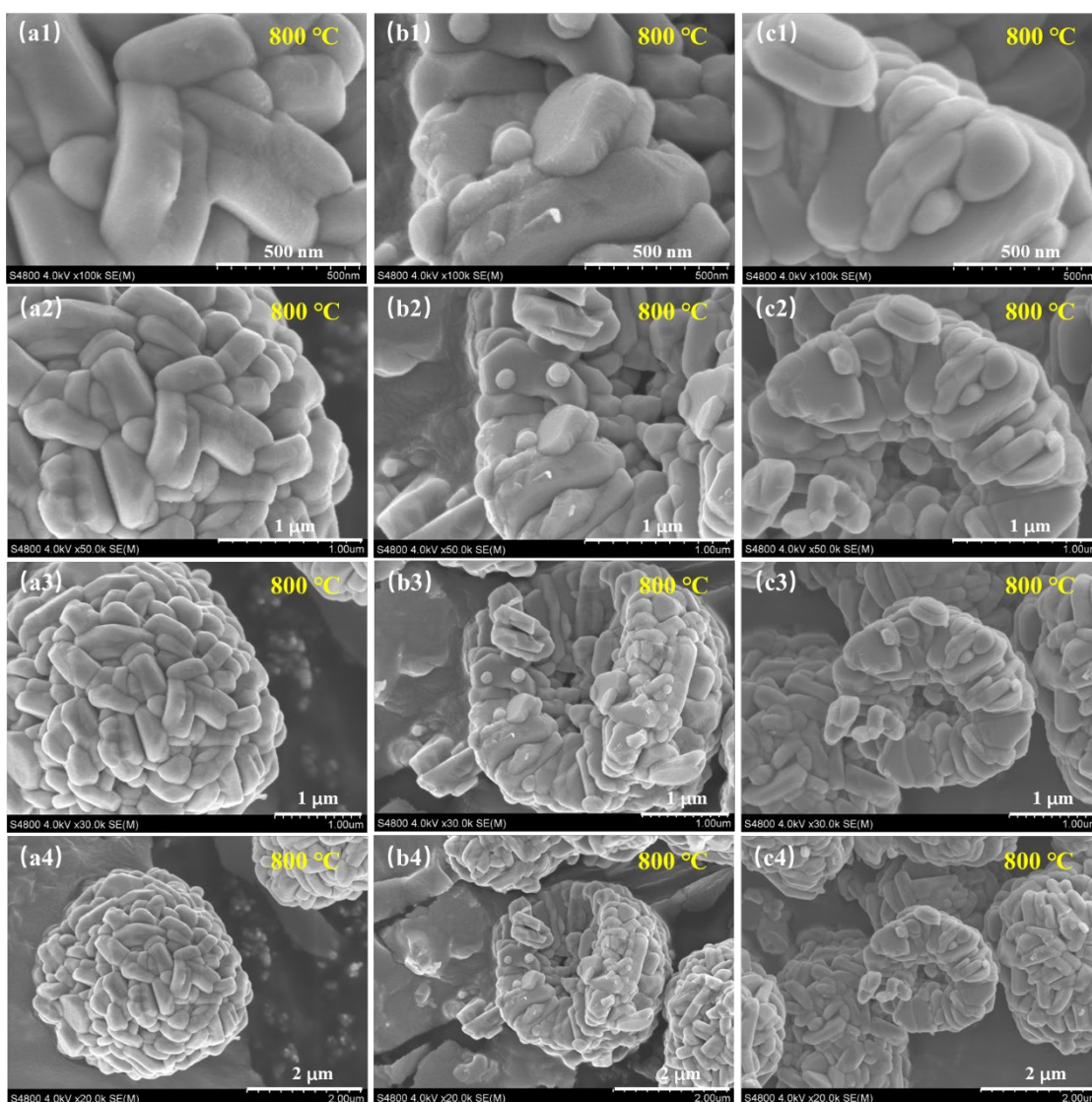


Figure 5. 15. SEM images of $\text{LiNi}_{0.83}\text{Co}_{0.05}\text{Mn}_{0.12}\text{O}_2$ cathode material synthesised at $800\text{ }^\circ\text{C}$ with 2% mole excess $\text{LiOH}\cdot\text{H}_2\text{O}$ (Daisy-Ni83): (a1-a4) surface images at different magnifications, (b1-b4) cutaway images with an oblique angle, (c1-c4) cross-section images of a plane perpendicular to the sphere.

The longer 0.2 C cycling within the voltage ranges of 2.8-4.3 V and 2.8-4.5 V of Daisy-Ni83 are further studied. The results are shown in **Figure 5. 16**. The first 10 cycles at 0.2 C can be regarded as the activation process. For the cycling voltage between 2.8-4.3 V, it delivers the discharge capacity of 198.1 mAh g^{-1} at the 11th cycle, after 50 cycles, Daisy-Ni83 exhibits 193.8 mAh g^{-1} with a capacity retention of 97.83% versus the 11th

cycle. The radial arrangement of the primary particles played a significant role in realising the good capacity retention of Daisy-Ni83. That is because, compared with the randomly oriented primary particles suffering localized stress concentration during galvanostatic cycling and the complicated and twisted Li-ion diffusion pathway, such a daisy-like arrangement of primary particles is beneficial for stress release, and the Li-ion diffusion pathway is simple along the radial direction. Therefore, materials with daisy-like refined microstructure can achieve good delithiation/lithiation reversibility (Park et al., 2018, Lee et al., 2019).

Nevertheless, when it reaches the 79th cycle within the voltage range of 2.8-4.3 V as shown in **Figure 5. 16**, it appears to fluctuate, and the Coulombic efficiency drops from 99.02% to 94.36%, then to 90.53% without overcharge from the 78th cycle to the 79th cycle, then the 80th cycle. Meanwhile, the obvious polarisation with voltage drop appears after the 78th cycle as inserted in **Figure 5. 16**, which suggests degradation of the cathode (Xin et al., 2022), despite the internal short circuit at the 88th cycle stopping the observation on the performance of the cathode material. For the voltage window at 2.8-4.5 V, the continuous charge/discharge process was realized for each cycle from the first cycle to the 150th cycle. However, the material appears a relatively quicker capacity fading rate than that with the cut-off voltage of 4.3 V, with a capacity retention of 93.21% from the specific capacity of 213.6 mAh g⁻¹ at the 11th cycle to the specific capacity of 199.1 mAh g⁻¹ after 50 cycles. After the 140th cycle, the capacity fading rate accelerates, evidenced by a steeper slope. Finally, at the last 150th cycle, it delivered a discharge capacity as low as 165.6 mAh g⁻¹, and the capacity retention dropped to 77.53% after

150 cycles at 0.2 C in the voltage range of 2.8-4.5 V.

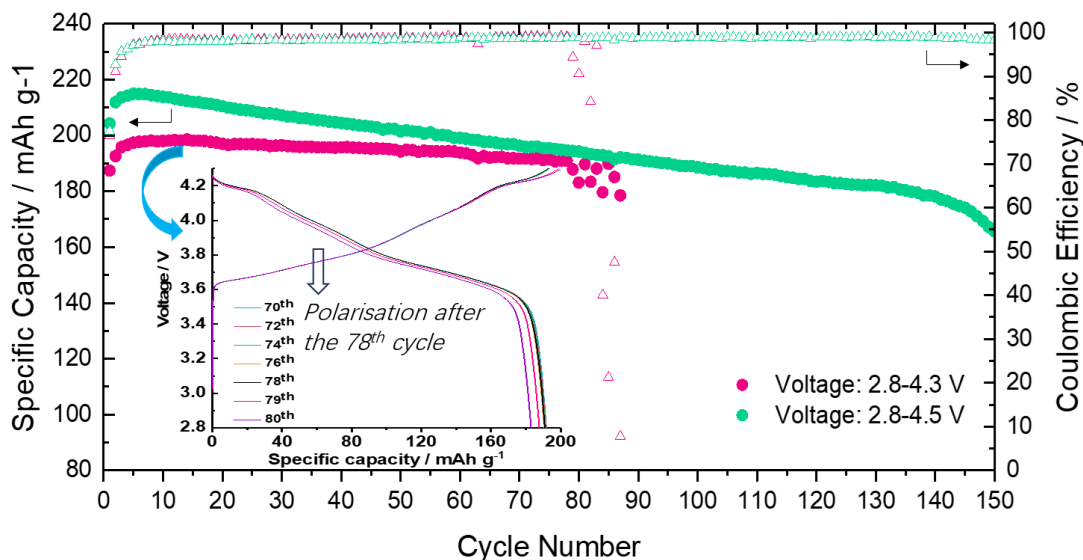


Figure 5. 16. 0.2 C longer cycling performances of $\text{LiNi}_{0.83}\text{Co}_{0.05}\text{Mn}_{0.12}\text{O}_2$ synthesised at 800 °C with 2% mole excess $\text{LiOH}\cdot\text{H}_2\text{O}$ (Daisy-Ni83) in the voltage range of 2.8-4.3 V and 2.8-4.5 V (Charge/discharge curves within 2.8-4.3 V are inserted).

Overall, the four factors of good crystallinity with ordered layered structure, clean surface without obvious lithium residues, reduced gaps among primary particles, and daisy-like radial refined structure were demonstrated to effectively guarantee a high discharge capacity and good capacity retentions over 50 cycles. However, for the longer cycling at 0.2 C, the material exhibits unstable charge/discharge performances, characterized by either declined Coulombic efficiencies accompanied by obvious polarisation or a more rapid capacity fading rate. This implies that depending only on the radially distributed microstructure is not sufficient to guarantee the long-term cycling stability for such Ni-rich cathode materials. We believe protections from coating and/or doping are necessary for Daisy-Ni83 to alleviate the Coulombic efficiency decline and/or capacity fading, which originate from the high surface reactivity with the

electrolyte and the mechanical degradation of the cathode particles during long-term charge/discharge cycling (Li et al., 2020c, Zhao et al., 2022b).

5.3.2. Greatly Developed Cycling Stability at Different Cut-off Voltages at 4.3 V and 4.5 V after the Treatment of the Combined Boron-related Coating and Doping with Intrinsic Radially Aligned Microstructure

For the cycling stability study, four types of test conditions at different current rates of 1 C, 0.5 C, 0.2 C within the voltage range of 2.8-4.3 V and 0.2 C within the voltage range of 2.8-4.5 V are launched for the samples of Daisy-Ni83, Daisy-Ni83-Bthin, Daisy-Ni83-Bmiddle, and Daisy-Ni83-Bthick. The cycling test results are shown in **Figure 5. 17**, the red point represents the data of Daisy-Ni83, the yellow point represents the data of Daisy-Ni83-Bthin, the blue point represents the data of Daisy-Ni83-Bmiddle, and the green point corresponds to the data of Daisy-Ni83-Bthick. Thereinto, 1 C cycling performances between 2.8-4.3 V with the initial 10 cycles activation at 0.2 C, followed by 5 cycles at 0.5 C, and the subsequent 150 cycles at 1 C are shown in **Figure 5. 17. (a)**. The performances over 200 cycles at 0.5 C with the initial ten activation cycles at 0.1 C between 2.8-4.3 V are shown in **Figure 5. 17. (b)**. For 0.2 C cycling, two voltage ranges of 2.8-4.3 V and 2.8-4.5 V are tested. The **Figure 5. 17. (c)** shows 150-cycles performances at 0.2 C with the initial 10 cycles activation at 0.1 C with a cut-off voltage of 4.3 V, and **Figure 5. 17. (d)** shows 150-cycles performances at 0.2 C with the initial 10 cycles activation at 0.1 C with a cut-off voltage of 4.5 V.

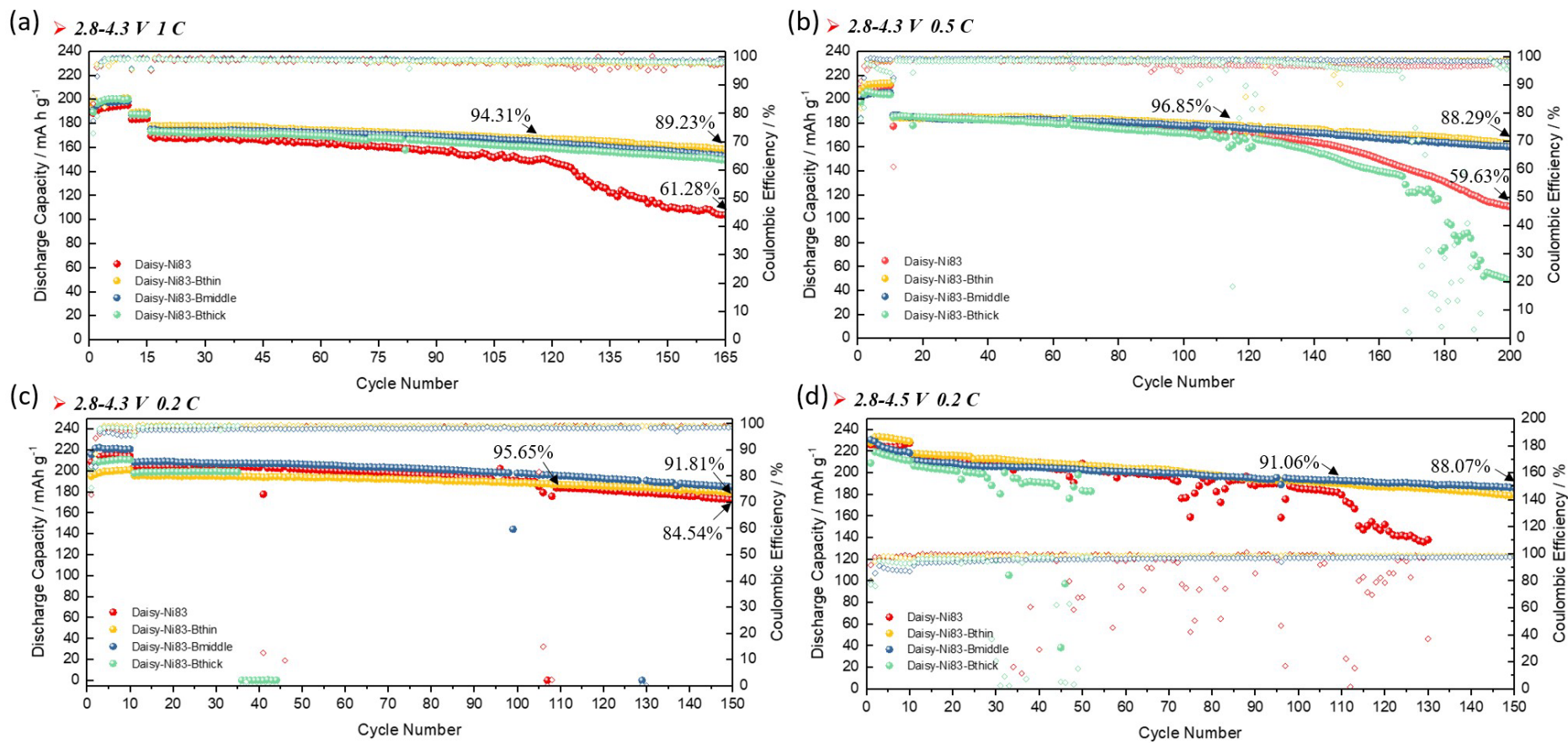


Figure 5. 17. Cycling performance comparison of Daisy-Ni83, Daisy-Ni83-Bthin, Daisy-Ni83-Bmiddle, and Daisy-Ni83-Bthick: (a) 1 C cycling between 2.8-4.3 V; (b) 0.5 C cycling between 2.8-4.3 V; (c) 0.2 C cycling between 2.8-4.3 V; (d) 0.2 C cycling between 2.8-4.5 V.

During 1 C cycling (**Figure 5. 17. (a)**), the initial specific capacity of Daisy-Ni83 is 169.4 mAh g⁻¹ at 1 C, but the capacity decays to 103.8 mAh/g after the full 165 cycles. The capacity retention was calculated to be 61.28 % for Daisy-Ni83 from the initial cycle to the 165th cycle at 1 C. Daisy-Ni83-Bthin achieved a capacity retention of 89.23 % after the full cycling, delivering a specific capacity of 177.4 mAh g⁻¹ in the 1st cycle and 158.3 mAh g⁻¹ in the last 165th cycle. The corresponding capacity retentions for Daisy-Ni83-Bmiddle and Daisy-Ni83-Bthick were 87.15 % and 86.2 %, respectively. Compared with Daisy-Ni83, the three modified cathode materials exhibited better capacity retention for 150 cycles at 1 C between 2.8-4.3 V. Meanwhile, the capacity retention after 100 cycles at 1 C reached 94.31% and 94.29% for Daisy-Ni83-Bthin and Daisy-Ni83-Bmiddle, respectively, a high level compared with other person's report about 89.9% capacity retention after Zr and B-related multiple doping and coating (Feng et al., 2020) and also higher than 87.78% capacity retention for Daisy-Ni83. The capacity retention of 100 cycles at 1 C for Daisy-Ni83-Bthick was relatively lower than that of the other two modified samples, with a value of 92.38%. These data imply that 1 C cycling performance with a cut-off voltage of 4.3 V can be effectively improved by the designed modifications.

In 0.5 C cycling (**Figure 5. 17. (b)**), the specific capacity of the 1st cycle at 0.5 C for Daisy-Ni83, Daisy-Ni83-Bthin, Daisy-Ni83-Bmiddle, and Daisy-Ni83-Bthick is 185.8 mAh g⁻¹, 184.4 mAh g⁻¹, 186.6 mAh g⁻¹, and 184.9 mAh g⁻¹, separately. When it comes to the 200th cycle, the specific capacity of each sample changes to 110.8 mAh g⁻¹, 162.8 mAh g⁻¹, 160.2 mAh g⁻¹, and 54.9 mAh g⁻¹, separately. Not like Daisy-Ni83 and Daisy-

Ni83-Bthick exhibiting quick capacity fading after the full charging/discharging test at the current rate of 0.5 C, both Daisy-Ni83-Bthin and Daisy-Ni83-Bmiddle keep excellent capacity retention of 88.29% and 85.85% after the full 200 cycles, which are much higher than that of Daisy-Ni83 with the capacity retention of 59.63% and Daisy-Ni83-Bthick with the capacity retention of 29.69%. The result indicates that both Daisy-Ni83-Bthin and Daisy-Ni83-Bmiddle can be effective against capacity fading in case of more cycle numbers and longer cycle time.

The same phenomenon occurs in the 0.2 C galvanostatic cycling between 2.8-4.3 V as shown in **Figure 5. 17. (c)**, where both Daisy-Ni83-Bthin and Daisy-Ni83-Bmiddle perform better modification effects. The capacity retention of the full 150 cycles at 0.2 C with the initial 10 cycles activation at 0.1 C develops from 84.54% for Daisy-Ni83 to 91.81% and 88.8% for Daisy-Ni83-Bthin and Daisy-Ni83-Bmiddle, respectively. The specific capacity of the 1st cycle at 0.2 C between 2.8-4.3 V is 203.8 mAh g⁻¹, 195.3 mAh g⁻¹, 208 mAh g⁻¹, and 197.8 mAh g⁻¹ for Daisy-Ni83, Daisy-Ni83-Bthin, Daisy-Ni83-Bmiddle, and Daisy-Ni83-Bthick, separately. The specific capacity at the last cycle at 0.2 C between 2.8-4.3 V is 172.3 mAh g⁻¹, 179.3 mAh g⁻¹, 184.7 mAh g⁻¹, and 0 mAh g⁻¹ for each sample.

In 0.2 C cycling with the cut-off voltage of 4.5 V (**Figure 5. 17. (d)**), the capacity retention for the full 150 cycles can be greatly enhanced from 0% for Daisy-Ni83 to 82.71% and 88.07% for Daisy-Ni83-Bthin and Daisy-Ni83-Bmiddle, respectively. The capacity retention of Daisy-Ni83-Bmiddle reached 91.06% after 100 cycles at 0.2 C in the high voltage range of 2.8-4.5 V, which is a high value compared with other reports

on the cycling performance of Ni-rich cathode material by co-doping (the relevant capacity retention is only 87.68%) (Zhang et al., 2021b).

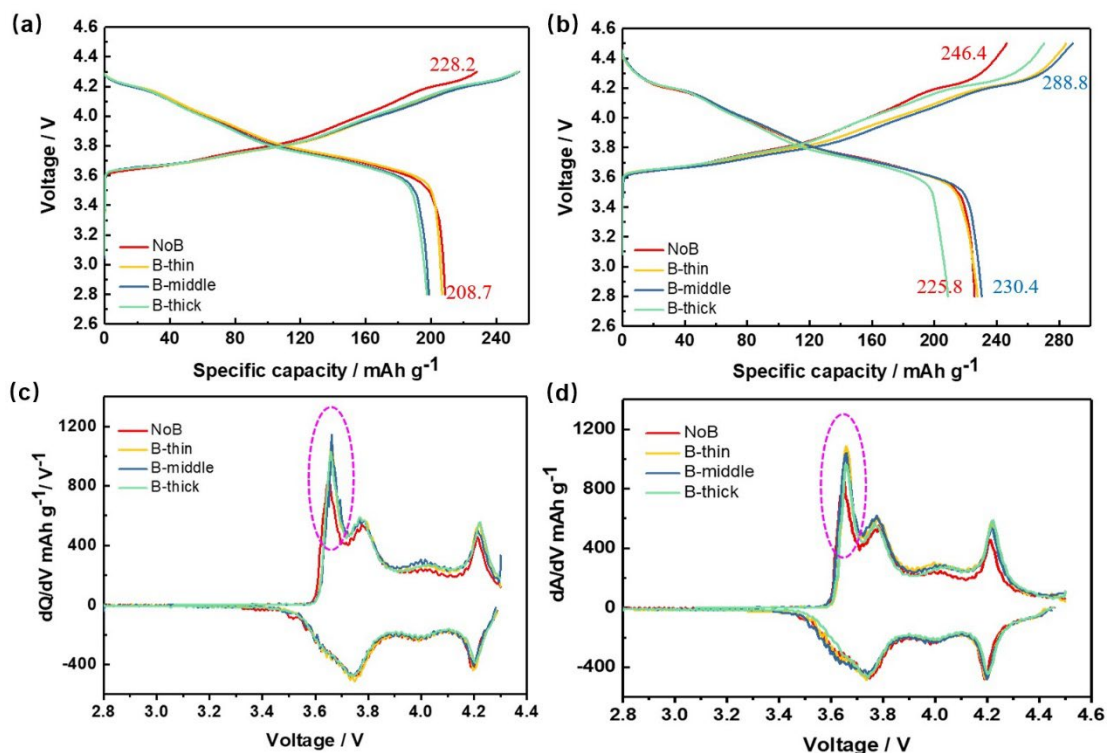


Figure 5. 18. First cycle electrochemical curves comparison for Daisy-Ni83, Daisy-Ni83-Bthin, Daisy-Ni83-Bmiddle, and Daisy-Ni83-Bthick: (a and b) charge/discharge profiles at 0.1 C for the cut-off voltage at 4.3 V and 4.5 V, respectively; (c and d) the corresponding dQ/dV curves at 0.1 C for the cut-off voltage at 4.3 V and 4.5 V, respectively.

Analysis of the first cycle is important for the battery. **Figure 5. 18** compares the electrochemical curves of samples at 0.1 C in 2.8-4.3 V and 2.8-4.5 V at the first cycle from **Figure 5. 17.** (b) and (d). The soared capacity for charging by Daisy-Ni83-Bthin, Daisy-Ni83-Bmiddle, and Daisy-Ni83-Bthick than that of Daisy-Ni83 can be found in **Figure 5. 18.** (a and b). The corresponding dQ/dV curves are shown in **Figure 5. 18.** (c

and d). The delithiation/lithiation reaction of Ni-rich cathode material undergoes several phase transitions matching with three pairs of redox peaks, first from an initial hexagonal phase (H1) to a monoclinic phase (M), then to the second hexagonal phase (H2), and the third hexagonal phase (H3) during charging, and they reverse during discharging (Yang et al., 2023). According to **Figure 5. 18.** (c) and (d), it can be observed that the peak intensities at each phase transition of the modified samples are greater than those of the pristine Daisy-Ni83, especially for the stage of H1 \rightarrow M phase transitions, which are marked by the dotted cycles. This result indicates that sufficient phase transition reactions occurred after modification, which promoted the release of more abundant lithium ions in the first cycle. Meanwhile, Daisy-Ni83-Bmiddle can achieve a specific capacity of 230.4 mAh g⁻¹ at the first cycle at 0.1 C during discharging in 2.8-4.5 V, and Daisy-Ni83-Bthin can achieve a higher specific capacity of 233.2 mAh g⁻¹ at the 3rd cycle in ten cycles activation at 0.1 C between 2.8-4.5 V. The initial high specific capacity provides the foundation for the high specific capacity in the following cycles. To the best of our knowledge, these very high specific capacity values of Ni-rich cathode materials are rarely reported for the Ni content of approximately 80%, which approach 240 mAh g⁻¹ for LiNiO₂.

To better display the variation in the specific capacity before and after modification with Daisy-Ni83, **Table 5. 3** lists the summary of the 1st cycle, 100th cycle, and last cycle discharge capacities for the different current density cycling between 2.8-4.3 V and 2.8-4.5 V. For simplification, the sample name of Daisy-Ni83, Daisy-Ni83-Bthin, Daisy-Ni83-Bmiddle, and Daisy-Ni83-Bthick are labeled as NoB, B-thin, B-middle, and B-thick, respectively. All in all, for the 1st cycle at the different current rates between 2.8-4.3 V and 2.8-4.5 V, all samples deliver almost similar capacity, which means the adding inactive boron-related material does not cut down the electrochemical activity of the material at the initial step of cycling. Nevertheless, the different added amounts of boron-related material would have different effects on the cycling stability, as it has been reported that the excess boron doping can block the Li-ion diffusion pathways and/or enhance the cation disordering (Lee et al., 2019, Roitzheim et al., 2021).

Table 5. 3. Summary of 1st cycle, 100th cycle, and last cycle discharge capacity for different current density cycling in 2.8-4.3 V and 2.8-4.5 V (Initial 10 cycles performance at 0.1 C is also shown.)

	Discharge capacity / mAh g⁻¹ 1 C cycling @ 2.8-4.3 V			Discharge capacity / mAh g⁻¹ 0.5 C cycling @ 2.8-4.3 V		
Sample	1 st cycle (11 th cycle)	100 th cycle (115 th cycle)	150 th cycle (165 th cycle)	1 st cycle (11 th cycle)	100 th cycle (110 th cycle)	190 th cycle (200 th cycle)
NoB	169.4	148.7	103.8	185.8	173.8	110.8
B-thin	177.4	167.3	158.3	184.4	178.6	162.8
B-middle	175.1	165.1	152.6	186.6	176.8	160.2
B-thick	173.2	160	149.3	184.9	169	54.9
	Discharge capacity / mAh g⁻¹ 0.2 C cycling @ 2.8-4.3 V			Discharge capacity / mAh g⁻¹ 0.2 C cycling @ 2.8-4.5 V		
Sample	1 st cycle (11 th cycle)	100 th cycle (110 th cycle)	140 th cycle (150 th cycle)	1 st cycle (11 th cycle)	100 th cycle (110 th cycle)	140 th cycle (150 th cycle)
NoB	203.8	183.6	172.3	215.6	179.4	0
B-thin	195.3	186.8	179.3	217.5	189.9	179.9
B-middle	208	195.2	184.7	211.3	192.4	186.1
B-thick	197.8	0	0	206.4	0	0
	Discharge capacity / mAh g⁻¹ 0.1 C cycling @ 2.8-4.3 V			Discharge capacity / mAh g⁻¹ 0.1 C cycling @ 2.8-4.5 V		
Sample	1 st cycle/ 10 th cycle (activation for 0.5 C cycling)	1 st cycle/ 10 th cycle (activation for 0.2 C cycling)		1 st cycle (activation for 0.2 C cycling)	10 th cycle (activation for 0.2 C cycling)	
NoB	208.7/211.4	208.4/213.9		225.8	227.2	
B-thin	206.9/213.3	194.8/200.8		227.7	229 (233.2_3 th cycle)	
B-middle	198.8/205.5	215.5/220.8		230.4	218.3	
B-thick	197.5/203.7	201.7/210.7		208.8	211.2	

To better show the modification differences among Daisy-Ni83-Bthin, Daisy-Ni83-Bmiddle, and Daisy-Ni83-Bthick, the histogram of capacity retentions of full cycles, and 100 cycles at 1 C, 0.5 C, 0.2 C in 2.8-4.3 V and at 0.2 C in 2.8-4.5 V of all samples referring to **Table 5. 3** is shown in **Figure 5. 19**. For the full long-term cycling under each test condition (**Figure 5. 19. (a-d)**), both Daisy-Ni83-Bthin and Daisy-Ni83-Bmiddle exhibited good modification effects. For the 100 cycles performance (**Figure 5. 19. (e-h)**), only Daisy-Ni83-Bmiddle can achieve all the capacity retention above 90% and higher than that of Daisy-Ni83 in all evaluation scenarios. The capacity retention for the full cycling of Daisy-Ni83-Bmiddle is 2.80%, 2.44%, and 3.01% lower than Daisy-Ni83-Bthin in 2.8-4.3 V at the current rate of 1 C, 0.5 C, and 0.2 C. This difference was relatively small. The capacity retention for full cycling of Daisy-Ni83-Bmiddle is 5.36% higher than Daisy-Ni83-Bthin in 2.8-4.5 V at the current rate of 0.2 C. Considering the requirement of high voltage and high capacity to obtain high energy density, it can be said that Daisy-Ni83-Bmiddle has better comprehensive properties than Daisy-Ni83-Bthin to cope with harsh application conditions of high operating voltage. We will focus on the analysis of Daisy-Ni83-Bmiddle in subsequent study.

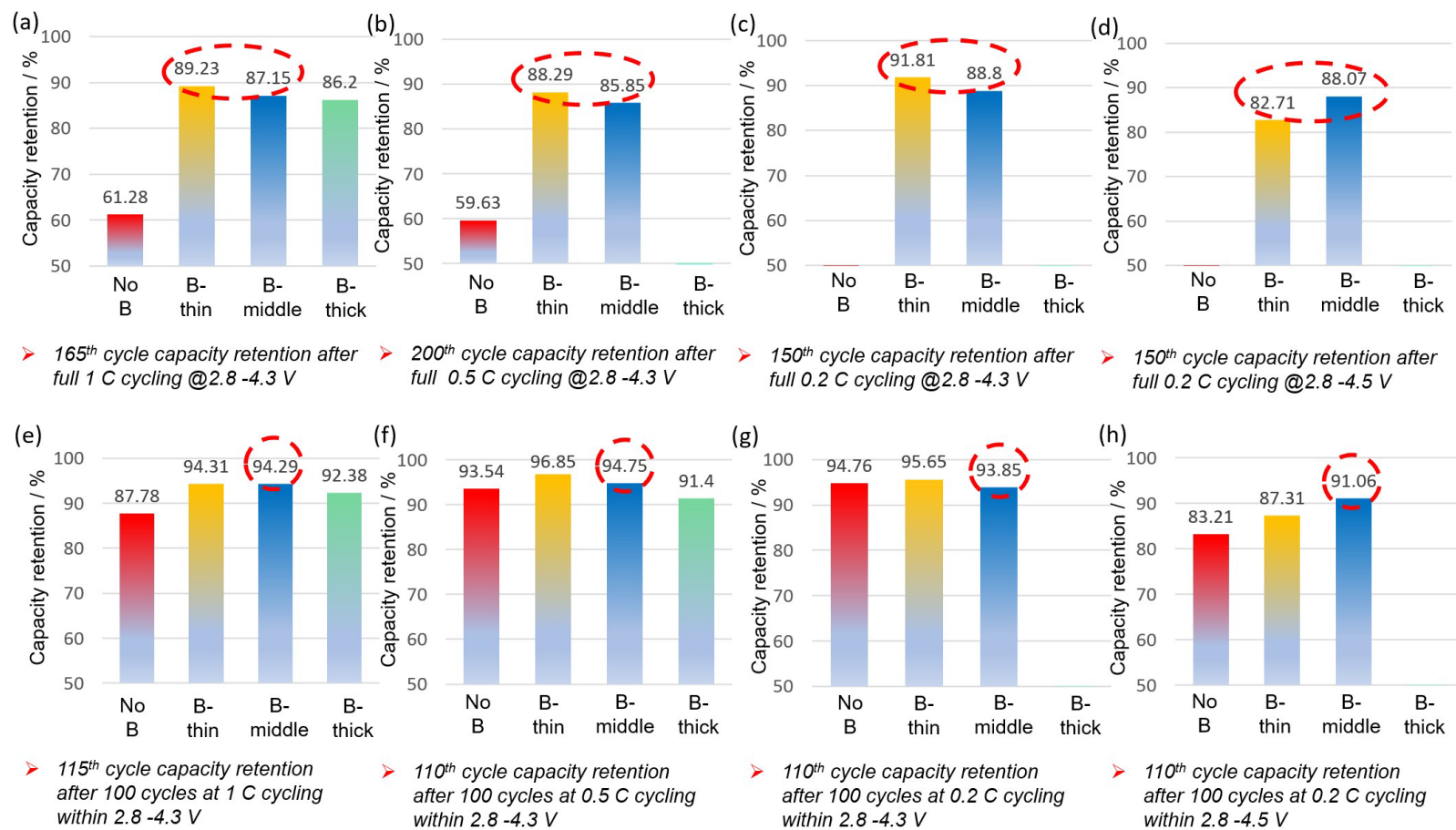


Figure 5. 19. The histogram of capacity retention for Daisy-Ni83, Daisy-Ni83-Bthin, Daisy-Ni83-Bmiddle, and Daisy-Ni83-Bthick: (a-d) full cycles capacity retention at 1 C, 0.5 C, 0.2 C in 2.8-4.3 V and at 0.2 C in 2.8-4.5 V, respectively; (e-h) 100 cycles capacity retention at 1 C, 0.5 C, 0.2 C in 2.8-4.3 V and at 0.2 C in 2.8-4.5 V, respectively.

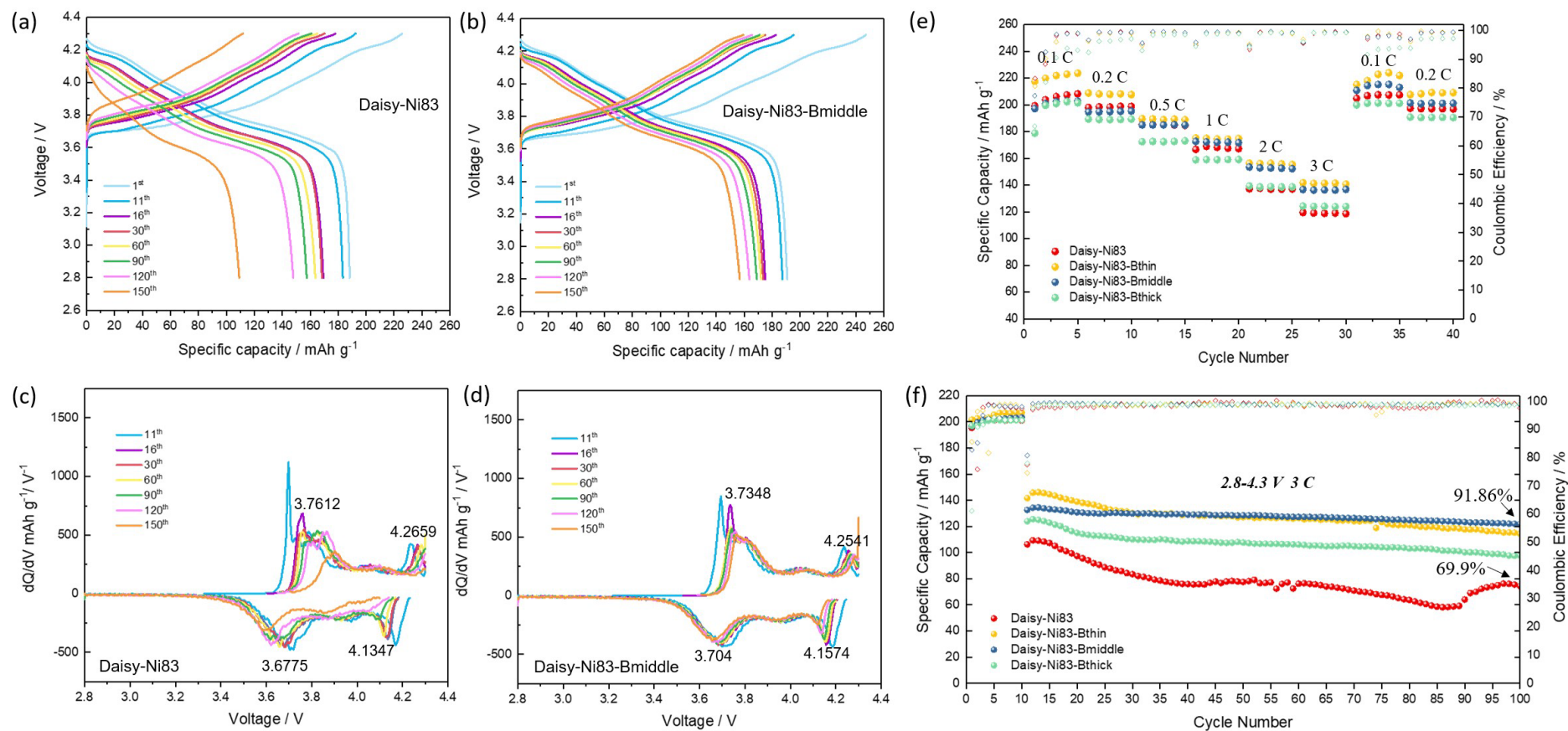


Figure 5. 20. (a, b) Charge/discharge profiles of Daisy-Ni83 and Daisy-Ni83-Bmiddle for 1 C cycling between 2.8-4.3 V from **Figure 5. 17**. (a) involving the 1st cycle at 0.2 C, 11th cycle at 0.5 C, and 16th, 30th, 60th, 90th, 120th, 150th cycle at 1 C. (c, d) Corresponding dQ dV⁻¹ curves of Daisy-Ni83 and Daisy-Ni83-Bmiddle for 1 C cycling between 2.8-4.3 V. (e) Rate performances of all samples between 2.8-4.3 V. (f) 3 C cycling performances of all samples in the voltage range of 2.8-4.3 V.

The charge/discharge profiles of Daisy-Ni83 and Daisy-Ni83-Bmiddle for 1 C cycling between 2.8-4.3 V from cycling performance comparison of **Figure 5. 17.** (a) are shown in **Figure 5. 20.** (a, b). Compared with the large voltage drop that emerged at Daisy-Ni83 (**Figure 5. 20.** (a)) during 1 C cycling, the voltage drop was distinctly depressed at Daisy-Ni83-Bmiddle (**Figure 5. 20.** (b)). The corresponding dQ/dV^{-1} curves of 1 C cycling between 2.8-4.3 V are shown in **Figure 5. 20.** (c, d). It can be seen that no matter H1–M phase transition or H2–H3 phase transition, Daisy-Ni83(**Figure 5. 20.** (c)) suffers seriously from polarisation with poor reversibility. In contrast, as shown in **Figure 5. 20.** (d), the shift of oxidation peaks to higher voltage can be effectively suppressed, and the reduction peaks moving to lower voltage is also depressed by Daisy-Ni83-Bmiddle during 1 C cycling. The voltages for the 1st cycle at 1 C (i.e. the 16th cycle of full 1 C cycling) of redox peaks corresponding to H1–M and H2–H3 phase transitions are marked out. The relevant oxidation-reduction voltage difference of Daisy-Ni83-Bmiddle is 0.0308 V and 0.0967 V smaller than that of Daisy-Ni83, with the value of 0.0837 V and 0.1312 V for the phase transitions. The good reversibility of the phase transitions during the charging/discharging process is an important factor accounting for the superior electrochemical reversibility of Daisy-Ni83-Bmiddle.

Furthermore, the rate performances and high current density cycling were investigated. **Figure 5. 20.** (e) and (f) represent the rate performances of all samples of Daisy-Ni83, Daisy-Ni83-Bthin, Daisy-Ni83-Bmiddle, and Daisy-Ni83-Bthick between 2.8-4.3 V and the corresponding 3 C cycling performances in the voltage range of 2.8-4.3 V, separately. As shown in **Figure 5. 20.** (e), the rate performance is measured every 5

cycles at different current rates of 0.1 C, 0.2 C, 0.5 C, 1 C, 2 C, 3 C, and then back to 0.1 C and 0.2 C. Obviously, Daisy-Ni83-Bthin and Daisy-Ni83-Bmiddle performance better rate performance than Daisy-Ni83. When the current density reaches 3 C, the pristine Daisy-Ni83 delivers the discharge capacity of 119.5 mAh g⁻¹, while Daisy-Ni83-Bthin and Daisy-Ni83-Bmiddle can reach 141.7 mAh g⁻¹ and 136.7 mAh g⁻¹, individually. When the current density returned to 0.1 C, both Daisy-Ni83-Bthin and Daisy-Ni83-Bmiddle exhibited a higher specific capacity of 215.2 mAh g⁻¹ and 210.8 mAh g⁻¹ than that of Daisy-Ni83 with 204.9 mAh g⁻¹. Although Daisy-Ni83-Bthin appears a marginally higher specific capacity than Daisy-Ni83-Bmiddle at a high current rate, the cycling stability of Daisy-Ni83-Bthin at 3 C was not ideal compared with Daisy-Ni83-Bmiddle. The capacity retention of Daisy-Ni83-Bthin for 3 C cycling with 100 cycles is 80.73%, higher than that of Daisy-Ni83 with a capacity retention of 69.9%, but lower than that of Daisy-Ni83-Bmiddle with a capacity retention of 91.86%. Daisy-Ni83-Bthick exhibits the weakest modification effect, with a capacity retention of 78.77%. To better demonstrate the modification effect of Daisy-Ni83-Bmiddle for cycling under a high current rate, only the capacity retentions of Daisy-Ni83 and Daisy-Ni83-Bmiddle are presented in **Figure 5. 20. (f)**. Contrasted to the quick capacity decay and capacity fluctuation of Daisy-Ni83 at 3 C cycling, Daisy-Ni83-Bmiddle displayed excellent cycling stability with much slower capacity decay. The delivered discharge capacity at the end 100th cycle at 3 C is greatly enhanced from 74.3 mAh g⁻¹ for Daisy-Ni83 to 121.8 mAh g⁻¹ for Daisy-Ni83-Bmiddle.

To highlight the benefit of the integration of boron-related coating and doping together with the intrinsic daisy-like structure for strengthening the electrochemical performance of Ni-rich cathode material, the modified results by Daisy-Ni83-Bthin and Daisy-Ni83-Bmiddle were compared with those of other Ni-rich cathode materials. The comparison is gathered in **Table 5. 4**. The initial capacity and capacity retention data under the test conditions are listed.

In summary, regardless of whether the modification with single doping treatment by boron or other multielements (Amalraj et al., 2021, Roitzheim et al., 2021, Zhang et al., 2021b), or the single coating treatment of B₂O₃ or LiBO₂/B₂O₃ hybrid material (Chen et al., 2021, Su et al., 2022), the combination treatment of doping and coating (Feng et al., 2020), or structure adjustment to form a radially oriented structure by boron doping (Park et al., 2018, Lee et al., 2019), Daisy-Ni83-Bthin and Daisy-Ni83-Bmiddle exhibit more stable cycling performances at a cut-off voltage of 4.3 V. Even at a higher cut-off voltage (4.5 V), superior performance was achieved by Daisy-Ni83-Bmiddle. Meanwhile, the initial discharge capacities of Daisy-Ni83-Bthin and Daisy-Ni83-Bmiddle were also relatively high, indicating their superior competitiveness as excellent Ni-rich cathode materials.

Table 5. 4. Electrochemical performance comparison between this work and other people's reports.

<i>Electrodes</i>	<i>Modification</i>	<i>Rate (mA/g)</i>	<i>Initial Capacity (mAh/g)</i>	<i>Capacity Retention</i>	<i>References</i>
<u>Daisy-Ni83</u>	Combined boron-related coating and doping	200 (2.8-4.3 V)	177.4/175.1	<u>94.31%/94.29%</u> (100 cycles)	Daisy-Ni83-Bthin/ Daisy-Ni83-Bmiddle (this work)
$LiNi_{0.8}Co_{0.1}Mn_{0.1}O_2$	Zirconium and boron co-doping and lithium zirconium coating	200 (3.0-4.3 V)	≈180	89.9% (100 cycles)	(Feng et al., 2020)
$LiNi_{0.85}Co_{0.10}Mn_{0.05}O_2$	Boron doping	200 (3.0-4.3 V)	≈180	94% (100 cycles)	(Amalraj et al., 2021)
<u>Daisy-Ni83</u>	Combined boron-related coating and doping	100 (2.8-4.3 V)	184.4/186.6	<u>96.85%/94.75%</u> (100 cycles) <u>88.29%/85.85%</u> (200 cycles)	Daisy-Ni83-Bthin/ Daisy-Ni83-Bmiddle (this work)
$LiNi_{0.8}Co_{0.1}Mn_{0.1}O_2$	Boron doping	80 (3.0-4.3 V)	≈170	87% (120 cycles)	(Roitzheim et al., 2021)
$LiNi_{0.84}Co_{0.10}Mn_{0.06}O_2$	Boron doping to form radially oriented structure	100 (3.0-4.3 V)	≈187	93.1% (50 cycles)	(Lee et al., 2019)
$LiNi_{0.90}Co_{0.05}Mn_{0.05}O_2$	Boron doping to form radially oriented structure	90 (2.7-4.3 V)	unknown	91% (100 cycles)	(Park et al., 2018)
<u>Daisy-Ni83</u>	Combined boron-related coating and doping	40 (2.8-4.3 V)	195.3/208	<u>95.65%/93.85%</u> (100 cycles)	Daisy-Ni83-Bthin/ Daisy-Ni83-Bmiddle (this work)
$LiNi_{0.87}Co_{0.10}Al_{0.03}O_2$	B ₂ O ₃ coating	40 (2.8-4.3 V)	184	86% (100 cycles)	(Chen et al., 2021)
$LiNi_{0.8}Co_{0.1}Mn_{0.1}O_2$	LiBO ₂ /B ₂ O ₃ hybrid coating	40 (2.75-4.3 V)	185.8	95.7% (100 cycles)	(Su et al., 2022)
<u>Daisy-Ni83</u>	Combined boron-related coating and doping	40 (2.8-4.5 V)	217.5/211.3	<u>87.31%/91.06%</u> (100 cycles)	Daisy-Ni83-Bthin/ Daisy-Ni83-Bmiddle (this work)
$LiNi_{0.8}Co_{0.1}Mn_{0.1}O_2$	Doping with sodium and bromine	36 (3.0-4.5 V)	≈210	87.68% (100 cycles)	(Zhang et al., 2021b)

EIS is further studied. The sum of the internal resistances decreased after modification. Table inserted in **Figure 5. 21.** (a) displays the detailed resistance. The electrolyte resistances (R_s) in each coin cell are similar about 1 Ω , while the charge transfer resistance (R_{CT}) on the surface of the cathode material becomes lower from 69.72 Ω for the pristine Daisy-Ni83, to 50.15 Ω for Daisy-Ni83-Bthin, to 32.1 Ω for Daisy-Ni83-Bmiddle, and to 54.46 Ω for Daisy-Ni83-Bthick. To sum up the above analysis, it can be seen that the modification causes the charge transfer resistance of the cathode material to decline, which can be considered as the direct reason for promoting delithiation phase transition reactions, resulting in increased capacity in the charging process. Daisy-Ni83-Bmiddle had the lowest internal resistance, coinciding with the highest charge capacities in the first cycles, as shown in **Figure 5. 18.**

The Warburg impedance can be represented by the low-frequency region of the Nyquist plot related to Li-ion diffusion (Luo et al., 2018). As shown in the EIS test in **Figure 5. 21.** (a), the phase angles of the oblique lines are not 45° but tend to be 90°, which indicates the Warburg impedances of tested samples are consistent with the case of the finite diffusion model under reflective boundary conditions (Lazanas and Prodromidis, 2023). Equation (5. 1) is used to calculate Li-ion diffusion coefficient D_{Li^+} :

$$D_{Li^+} = \frac{R^2 T^2}{2A^2 n^4 F^4 C_{Li}^2 \sigma^2} \quad \text{Equation (5. 1)}$$

Where R is the gas constant, T is the absolute temperature (298.15 K), A is the surface area of electrode (1.5394 cm^2), n is the number of electrons per molecule during the redox process, F is the Faraday constant, C_{Li} is the concentration of lithium ion in electrode ($10^{-3} mol cm^{-3}$), and σ is the Warburg factor. The slope of the plot for Z' vs

$\omega^{-1/2}$ is σ , the corresponding relationship lines between Z' and $\omega^{-1/2}$ for all samples are shown in **Figure 5. 21. (b)** by selecting the tail data from the Nyquist plots. The calculated Li-ion diffusion coefficients for each sample are illustrated in **Figure 5. 21. (c)**. For Daisy-Ni83, D_{Li^+} is calculated to be $8.19 \times 10^{-13} \text{ cm}^2 \text{ s}^{-1}$. For Daisy-Ni83-Bthin, Daisy-Ni83-Bmiddle, and Daisy-Ni83-Bthick, D_{Li^+} are higher with the value of $3.51 \times 10^{-12} \text{ cm}^2 \text{ s}^{-1}$, $4.61 \times 10^{-12} \text{ cm}^2 \text{ s}^{-1}$, and $3.5 \times 10^{-12} \text{ cm}^2 \text{ s}^{-1}$, respectively. This modification can indeed enhance the Li-ion diffusion rate, which plays a positive role in improving the rate performance.

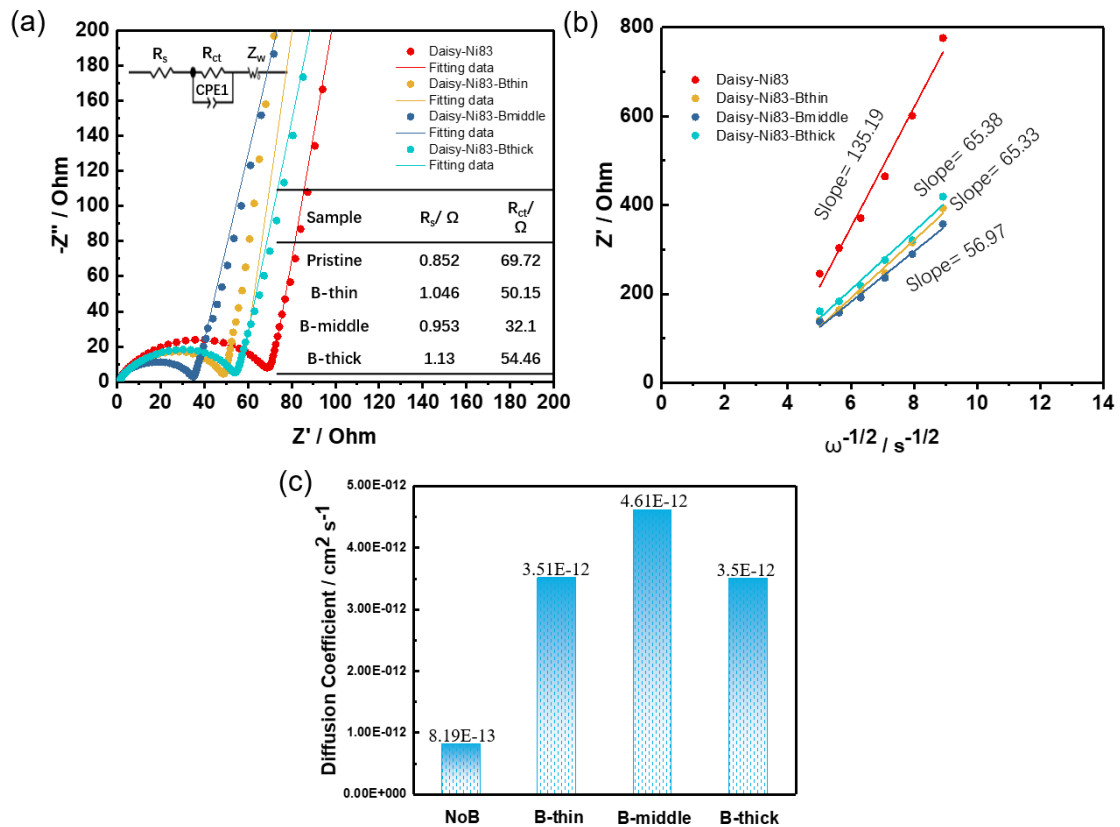


Figure 5. 21. (a) EIS test results of Daisy-Ni83, Daisy-Ni83-Bthin, Daisy-Ni83-Bmiddle, and Daisy-Ni83-Bthick with Nyquist plots and fitting data; (b) Warburg plot used to calculate Li-ion diffusion coefficient; (c) the corresponding diffusion coefficients of Li-ion in each cathode material.

Commonly, a high state of charge (SOC) is believed to be detrimental to the weakening of the electrochemical performance of Ni-rich cathode materials owing to the potential boost in oxygen release and $\text{Li}^+/\text{Ni}^{2+}$ cation mixing (Yang et al., 2023). Combining all the electrochemical analyses for all the samples, we can conclude that the capacity fading during long-term cycling of Daisy-Ni83 can be significantly mitigated by Daisy-Ni83-Bthin and Daisy-Ni83-Bmiddle, even at a high SOC, corresponding to the high charge capacity in the first cycle. The long-term cycling data for each cathode material at different current rates and cut-off voltages are summarised here. On the whole, the capacity retention of full 165 cycles at 1 C cycling with initial 10 cycles at 0.2 C and 5 cycles at 0.5 C in 2.8-4.3 V develops from 61.28% for Daisy-Ni83 to 89.23% for Daisy-Ni83-Bthin and 87.15% for Daisy-Ni83-Bmiddle. The capacity retention of full 200 cycles at 0.5 C cycling with initial 10 cycles at 0.1 C in 2.8-4.3 V develops from 59.63% for Daisy-Ni83 to 88.29% for Daisy-Ni83-Bthin and 85.85% for Daisy-Ni83-Bmiddle. The capacity retention of full 150 cycles at 0.2 C cycling with initial 10 cycles at 0.1 C in 2.8-4.3 V develops from 84.54% for Daisy-Ni83 to 91.81% for Daisy-Ni83-Bthin and 88.8% for Daisy-Ni83-Bmiddle. The capacity retention of full 100 cycles at 3 C cycling with initial 10 cycles at 0.1 C in 2.8-4.3 V develops from 69.9% for Daisy-Ni83 to 80.73% for Daisy-Ni83-Bthin and 91.86% for Daisy-Ni83-Bmiddle. Additionally, at the higher cut-off voltage, the capacity retention of the full 150 cycles at 0.2 C with initial 10 cycles at 0.1 C in 2.8-4.5 V develops from the complete failure with 0% for Daisy-Ni83 to 82.71% for Daisy-Ni83-Bthin and 88.07% for Daisy-Ni83-Bmiddle.

Daisy-Ni83-Bthin and Daisy-Ni83-Bmiddle should have achieved the designed coating

and doping modification to provide effective protection for long-term cycling. In the case of a larger current and higher operating voltage, Daisy-Ni83-Bmiddle is more excellent than Daisy-Ni83-Bthin with better cycling stabilities. There must be some modification differences between Daisy-Ni83-Bthin and Daisy-Ni83-Bmiddle, which will be revealed using various characterisation methods. The negative effect of Daisy-Ni83-Bthick on long-term cycling under most test conditions is also discussed.

5.3.3. Modification Mechanism of Daisy-Ni83-Bthin and Daisy-Ni83-Bmiddle with the Analysis of ICP-OES, XRD, SEM-EDS, TEM, and XPS

The mole ratio of Li, Ni, Co, Mn, and B of Daisy-Ni83, Daisy-Ni83-Bthin, Daisy-Ni83-Bmiddle, and Daisy-Ni83-Bthick are tested based on the analysis of ICP-OES. The data are presented in **Table 5. 5**. For Daisy-Ni83, the mole ratio of Li, Ni, Co, Mn, and B is 1.05: 0.829: 0.0489: 0.118: 0.00432. The molecular formula of Daisy-Ni83 is $\text{Li}_{1.05}\text{Ni}_{0.829}\text{Co}_{0.049}\text{Mn}_{0.118}\text{B}_{0.004}\text{O}_2$. According to the rounding rule, a 0.004-mole ratio of boron in Daisy-Ni83 can be rounded to a 0.00-mole ratio, which is negligible. For Daisy-Ni83-Bthin, the mole ratio is 1.03: 0.821: 0.0482: 0.117: 0.0136 for Li: Ni: Co: Mn: B. For Daisy-Ni83-Bmiddle, the mole ratio is 1.02: 0.819: 0.0481: 0.116: 0.0170 for Li: Ni: Co: Mn: B. In the case of Daisy-Ni83-Bthick, the mole ratio of B suddenly decreased to 0.0103, and the corresponding mole ratio was 1: 0.824: 0.0484: 0.118: 0.0103 for Li: Ni: Co: Mn: B. These ICP-OES data imply that the modification makes boron participates in the formation of the active material. There are three possible existence

forms either in the form of boron-related doping or in the form of boron-related coating, or in the form of combined boron-related doping and coating. The following characterisations SEM and TEM, will address this question. Other characterisation methods including X-ray diffraction (XRD) and X-ray photoelectron spectroscopy (XPS), will be used to clarify the modification mechanism of the greatly developed cycling stability by Daisy-Ni83-Bthin and Daisy-Ni83-Bmiddle.

Table 5. 5. ICP-OES analysis of Daisy-Ni83, Daisy-Ni83-Bthin, Daisy-Ni83-Bmiddle, and Daisy-Ni83-Bthick.

Active material	Elementary composition [mol]				
	Li	Ni	Co	Mn	B
Daisy-Ni83	1.05	0.829	0.0487	0.118	0.00432 (negligible)
Daisy-Ni83-Bthin	1.03	0.821	0.0482	0.117	0.0136
Daisy-Ni83-Bmiddle	1.02	0.819	0.0481	0.116	0.0170
Daisy-Ni83-Bthick	1	0.824	0.0484	0.118	0.0103

Figure 5. 22 shows the SEM images of different precursors and the corresponding cathode material of Daisy-Ni83 (a1-a6), Daisy-Ni83-Bthin (b1-b6), Daisy-Ni83-Bmiddle (c1-c6), and Daisy-Ni83-Bthick (d1-d6) at different magnifications. Before the sol/antisolvent B₂O₃ coating, the gaps between the lamella-shaped structures with the same orientation as the primary particles of the precursor can be clearly identified in **Figure 5. 22.** (a1). After the pristine precursor was subjected to the sol/antisolvent B₂O₃ coating with different ethanol sols with different B₂O₃ concentrations, the gaps between the lamella-shaped structure with the same orientation of primary particles of the precursor were filled, as shown in **Figure 5. 22.** (b1), (c1), and (d1), which corresponds to the precursor of Daisy-Ni83-Bthin, Daisy-Ni83-Bmiddle, and Daisy-Ni83-Bthick.

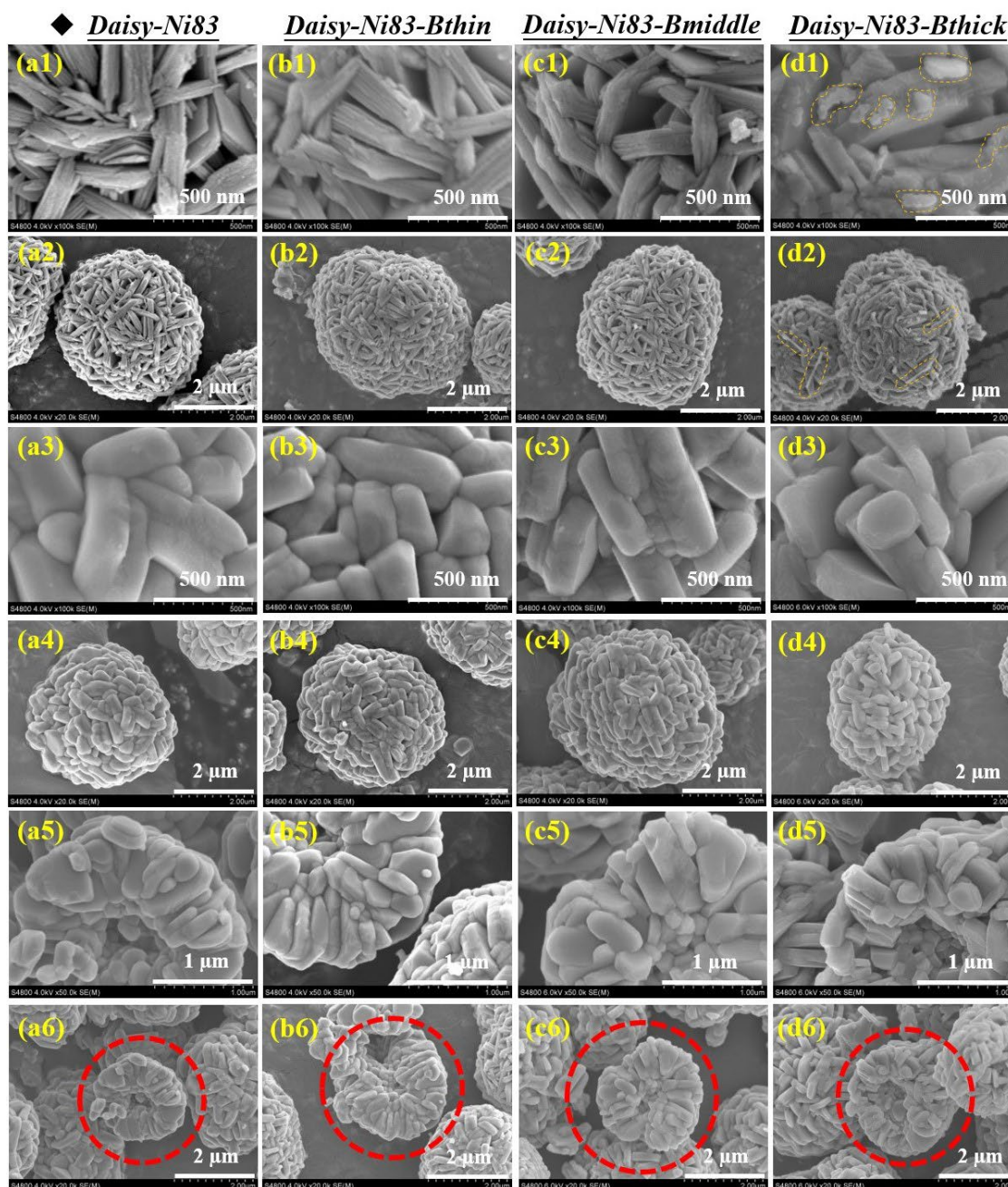


Figure 5. 22. SEM images of different precursors and the corresponding cathode material of Daisy-Ni83(a1-a6), Daisy-Ni83-Bthin(b1-b6), Daisy-Ni83-Bmiddle(c1-c6), and Daisy-Ni83-Bthick(d1-d6) at different magnifications. (The large-sized B_2O_3 particles on the precursor of Daisy-Ni83-Bthick are circled by the yellow dotted lines.)

Meanwhile, the boundaries between the lamella-shaped structures of each primary particle of the precursor became more blurred from Daisy-Ni83-Bthin to Daisy-Ni83-Bmiddle, then to Daisy-Ni83-Bthick, accompanied by an increase in the B_2O_3 concentration in the sol. In particular, the precursor of Daisy-Ni83-Bthick (**Figure 5. 22. (d1)**), not only the gaps between lamella-shaped structures of each primary particle are filled with small nano-sized B_2O_3 , but the boundaries between different primary particles are also covered by relatively larger B_2O_3 particles, which are circled by the yellow dotted lines. An enlarged SEM image of the Daisy-Ni83-Bthick precursor is shown in **Figure 5. 23**. Obviously, such a large slender strip of material enlarged at the right side is composed of many nearly 80 nm-sized B_2O_3 particles.

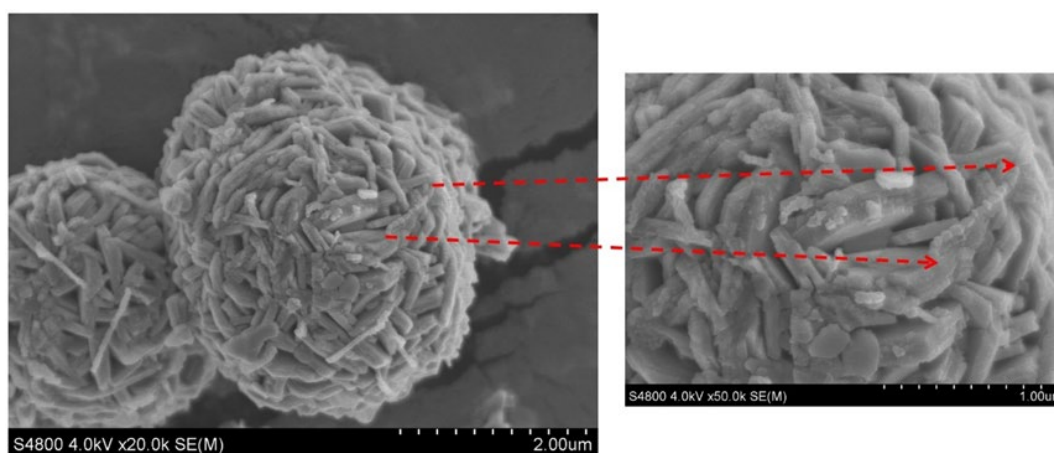


Figure 5. 23. Enlarged SEM image of the precursor of Daisy-Ni83-Bthick.

Theoretically, accompanied by an increase in the amount of B_2O_3 in the ethanol sol, the amount of B_2O_3 coating on the precursor should increase, resulting in an increased mole ratio of boron and a decreased mole ratio of lithium in the cathode material. This is because the increased addition of boron induced more lithium sources to be consumed

after the reaction with B_2O_3 , resulting in a variation in the composition. ICP-OES analysis of Daisy-Ni83, Daisy-Ni83-Bthin, Daisy-Ni83-Bmiddle, and Daisy-Ni83-Bthick shown in **Table 5. 5** is broadly consistent with this idea. The mole ratio of Li gradually decreases from 1.05 for Daisy-Ni83, to 1.03 for Daisy-Ni83-Bthin, then to 1.02 for Daisy-Ni83-Bmiddle, and finally to 1 for Daisy-Ni83-Bthick.

The mole ratio of boron increases from 0.00432 (negligible) for Daisy-Ni83, to 0.0136 for Daisy-Ni83-Bthin, to 0.0170 for Daisy-Ni83-Bmiddle, and finally back to 0.0103 for Daisy-Ni83-Bthick. The sudden decrease in the amount of boron in Daisy-Ni83-Bthick can be ascribed to the larger amount of large-sized B_2O_3 particles adhered to the precursor of Daisy-Ni83-Bthick, which is different from Daisy-Ni83-Bthin and Daisy-Ni83-Bmiddle. Compared to the small-sized B_2O_3 particles, the adhesion of the large-sized B_2O_3 particles onto the precursor of Daisy-Ni83-Bmiddle was relatively weak, as shown in the enlarged SEM image in **Figure 5. 23**. Large-sized B_2O_3 particles protrude from the precursor of Daisy-Ni83-Bthick, and some even have a length longer than 1 μm which can be easily removed by rubbing in the ball mill machine during the process of mixing with a lithium source.

The appearance of large-sized B_2O_3 particles on the precursor of Daisy-Ni83-Bthick is ascribed to the ethanol sol containing the insufficiently dispersed large-scale nanosized B_2O_3 particles, owing to the large amount of added B_2O_3 in ethanol with the limited time of ultrasonic treatment. The large nanosized B_2O_3 particles further gathered together at high-speed rotation, resulting in isolated and long linear-shaped adhesions. Although more lithium sources are consumed by a greater amount of B_2O_3 during the calcination

process for synthesising Daisy-Ni83-Bthick, some of the formed lithium-boron oxides are separated from the active material owing to the stripping of the large-sized B_2O_3 particles during the ball milling process. The separated lithium-boron oxides did not participate in modifying the active material and did not appear in the Daisy-Ni83-Bthick sample for the ICP-OES test; therefore, the larger amount of boron was not detected. Meanwhile, the mole ratio of Ni is higher for Daisy-Ni83-Bthick than Daisy-Ni83-Bthin and Daisy-Ni83-Bmiddle, but lower than Daisy-Ni83 also indicates only small amounts of B_2O_3 taking part in the modification in Daisy-Ni83-Bthick, large amounts of B_2O_3 are wasted due to the insufficient ultrasonic treating time for high concentrated B_2O_3 ethanol sol. The boron-related coating on the precursor was recognised by subsequent SEM-EDS analysis.

The surface distinctions on the precursors of Daisy-Ni83, Daisy-Ni83-Bthin, Daisy-Ni83-Bmiddle, and Daisy-Ni83-Bthick can be identified in **Figure 5. 22.** (a1)-(d1) and (a2)-(d2), but the SEM surface images (**Figure 5. 22.** (a3)-(d3) and (a4)-(d4)) and cross-section images (**Figure 5. 22.** (a5)-(d5) and (a6)-(d6)) of each cathode material in **Figure 5. 22** look similar at different magnifications. Nevertheless, it can be confirmed that all cathode materials maintain a daisy-like radial refined structure, as shown in **Figure 5. 22.** (a6), (b6), (c6), and (d6) marked by the red dotted lines, which indicates that the modified cathode materials of Daisy-Ni83-Bthin, Daisy-Ni83-Bmiddle, and Daisy-Ni83-Bthick all can inherit the intrinsic radially aligned microstructure from the precursor.

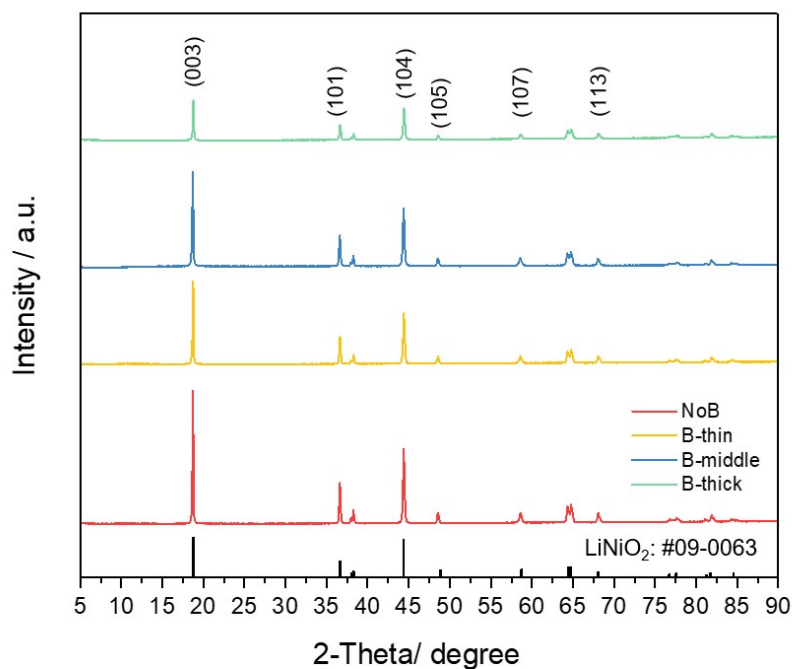


Figure 5. 24. XRD diffraction patterns of cathode material of Daisy-Ni83, Daisy-Ni83-Bthin, Daisy-Ni83-Bmiddle, and Daisy-Ni83-Bthick with high power Bruker D8 ADVANCE.

Table 5. 6. The intensity ratio of $I(003)/I(104)$ for each active material

Active material	$I(003)/I(104)$
Daisy-Ni83	1.5601
Daisy-Ni83-Bthin	1.4537
Daisy-Ni83-Bmiddle	1.5831
Daisy-Ni83-Bthick	1.2324

Figure 5. 24 shows the XRD diffraction patterns of cathode material of Daisy-Ni83, Daisy-Ni83-Bthin, Daisy-Ni83-Bmiddle, and Daisy-Ni83-Bthick with high power Bruker D8 ADVANCE. All the samples can match well with the standard pattern of

$R\bar{3}m$ LiNiO_2 (JCPDS No.09-0063). The corresponding intensity ratios $I(003)/I(104)$ for each active material are listed in **Table 5. 6**. The intensity ratio of the (003) peak to the (104) peak could be used as an indicator of the degree of cation mixing. Among these four active materials, the intensity ratio $I(003)/I(104)$ of Daisy-Ni83-Bthick is the lowest at nearly 1.2, which means that this material has relatively serious cation mixing compared with the other three materials (Ren et al., 2020). The poor Li/Ni ordering was responsible for the negative effect of Daisy-Ni83-Bthick on long-term cycling under most test conditions. The relatively high intensity ratios of $I(003)/I(104)$ for Daisy-Ni83-Bthin and Daisy-Ni83-Bmiddle which are larger than 1.2, are favourable factors for excellent long-term cycling stability under most test conditions. The poor Li/Ni ordering of Daisy-Ni83-Bthick can be ascribed to the presence of higher amounts of B_2O_3 on the precursor, which can consume more lithium and make the lithium source relatively lean for lithiation of the precursor itself.

Figure 5. 25 presents magnifications of selected 2-Theta regions from **Figure 5. 24**. It indicates that, compared with the pristine Daisy-Ni83 (NoB), Daisy-Ni83-Bthin (B-thin), and the sample Daisy-Ni83-Bthick (B-thick)) samples, the peaks slightly shifted to higher angles due to the shrinking of the unit cell by the small boron ions substituting the larger metal ions at the TM layer (Roitzheim et al., 2021). While the sample Daisy-Ni83-Bmiddle shows peaks slightly shifting to lower angles, indicating that the unit cell volume is expanded by B doping at the interstitial sites of the packed oxygen in the TM and lithium layers (Roitzheim et al., 2021, Chen et al., 2018). Regardless of whether B is doped at the Ni site or at the interstitial site, the XRD data imply that the designed

modification can achieve boron doping in the cathode material. However, the number of borons participating in the doping modification and the number of borons participating in the coating modification for each sample could not be determined. The XRD analysis demonstrates that the boron-related sol/antisolvent treatment does not destroy the Li/Ni ordering of Daisy-Ni83-Bthin and Daisy-Ni83-Bmiddle but weakens the Li/Ni ordering of Daisy-Ni83-Bthick.

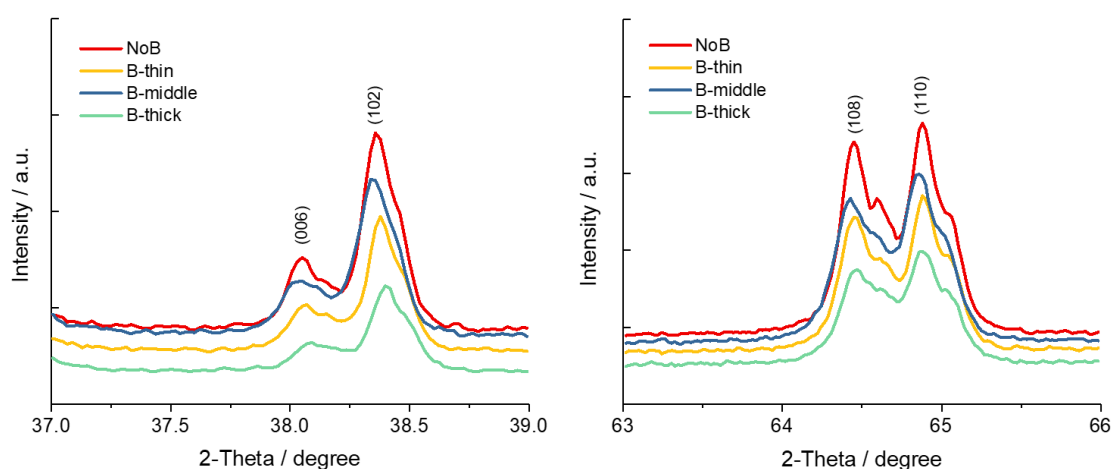


Figure 5. 25. Amplifications of selected 2-Theta regions from **Figure 5. 24**.

Figure 5. 26 illustrates EDS mapping of O, Ni, Mn, Co, and B elements for Daisy-Ni83-Bthin precursor (B-thin precursor), Daisy-Ni83-Bthin cathode material, and Daisy-Ni83-Bmiddle cathode material. For the top row of the B-thin precursor, five elements, O, Ni, Mn, Co, and B were identified on the surface of each secondary particle of the B-thin precursor, and these elements were uniformly distributed to shape each secondary particle of the B-thin precursor. Because boron is a light element and its mole ratio is also the lowest among O, Ni, Mn, Co, and B elements, the signal intensity of boron is not as high as that of other elements. EDS mapping of the B-thin precursor

demonstrates that the precursor can achieve a uniform coating of nano B_2O_3 particles even with the lowest B_2O_3 concentration in ethanol sol for synthesising Daisy-Ni83-Bthin by sol/antisolvent treatment. However, in the element mapping of the cathode material of Daisy-Ni83-Bthin, as shown in the middle row, O, Ni, Mn, and Co can be identified on the surface of each secondary particle of Daisy-Ni83-Bthin, whereas the B element does not show up to outline the shape of each secondary particle. In the bottom row of the cathode material Daisy-Ni83-Bmiddle, the signal intensity of boron on the surface is clear, which can visualise the shape of each secondary particle matching the O, Ni, Mn, and Co element mappings. B signal on the left bottom of the particle is relatively weak because there is a certain angle for the high-energy electron beam irradiating the surface of the particle, and the left bottom area is shaded from the projected side of the spherical-like powder. Based on the EDS mapping and XRD results, it can be speculated that the coated nano B_2O_3 particles on the precursor dominantly participated in the doping modification of Daisy-Ni83-Bthin. For Daisy-Ni83-Bmiddle, the coated nano B_2O_3 particles on the precursor participate in both doping and coating because of the relatively higher B_2O_3 concentration in the ethanol sol for Daisy-Ni83-Bmiddle than for Daisy-Ni83-Bthin.

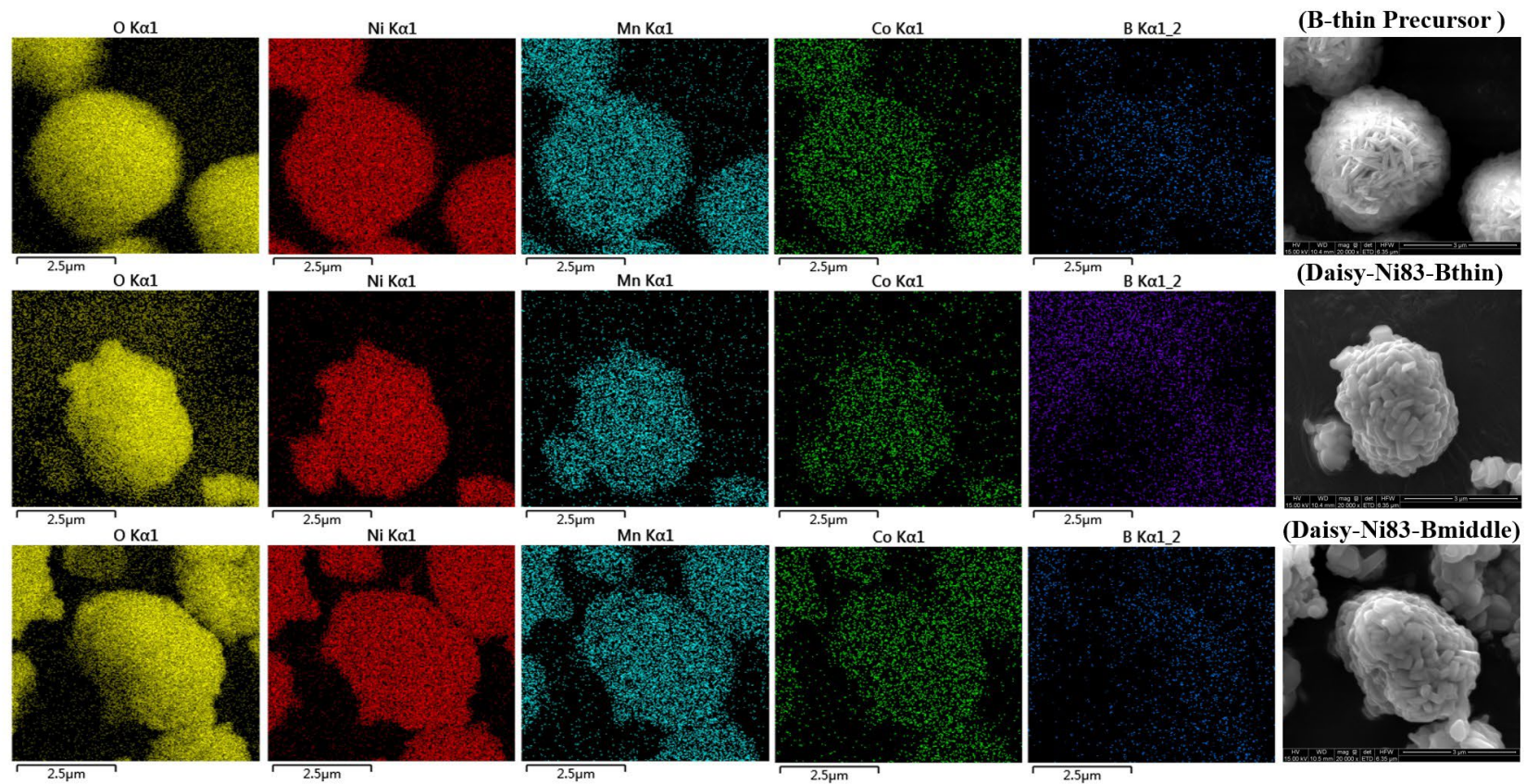


Figure 5. 26. EDS mapping of O, Ni, Mn, Co, and B elements for B-thin precursor, Daisy-Ni83-Bthin, and Daisy-Ni83-Bmiddle.

The speculation that Daisy-Ni83-Bthin is mainly subjected to boron doping, and Daisy-Ni83-Bmiddle is subjected to both boron-related whole surface coating and doping is further confirmed by TEM analysis. **Figure 5. 27** presents TEM images of the cathode materials Daisy-Ni83 and Daisy-Ni83-Bthin with high resolution. In **Figure 5. 27.** (a1), the left image is a spherical secondary particle of Daisy-Ni83, and the right image is the corresponding enlarged image of the green-circled part on the left. The selected area electron diffraction (SAED) pattern is shown inside. 0.4708 nm spacing for (003) planes, 0.2003 nm spacing for (104) planes, and 0.2486 nm spacing for (101) planes match well with the standard XRD pattern of $R\bar{3}m$ LiNiO₂ (JCPDS No.09-0063). Another TEM image of Daisy-Ni83 is shown in **Figure 5. 27.** (a2), a very clear atomic arrangement can be visualised on the right of **Figure 5. 27.** (a2), the distance of the lattice fringes is measured to be 0.4715 nm consistent with the (003) interplanar spacing of $R\bar{3}m$ LiNiO₂. Therefore, the good crystallinity of the secondary particles of pristine Daisy-Ni83 was confirmed.

For comparison, **Figure 5. 27.** (b1 and b2) show the TEM images of Daisy-Ni83-Bthin. The SAED pattern along with high-resolution TEM images of the green circled part of the Daisy-Ni83-Bthin particle are presented. In the SAED pattern of **Figure 5. 27.** (b2), (104), (101), and (113) crystalline planes are identified. Meanwhile, a halo feature appears in the centre of the SAED pattern, indicating the existence of an amorphous material (Roslova et al., 2023). The amorphous material is the coating layer, and a clear border between the bulk of the active material and amorphous material can be discerned. However, only this local protruding part which is cycled by the green line appears as

the coating layer for Daisy-Ni83-Bthin, which cannot be found in other locations along the edges of the particles, as shown in **Figure 5. 27.** (b1). The further amplified image labelled with “2” presents an image of gradual disappearance of the coating layer. This observation indicates that Daisy-Ni83-Bthin possesses only a partial coating on the surface of the spherical secondary particles. The coating is very local and does not completely wrap the secondary particles.

For Daisy-Ni83-Bmiddle, the complete and uniform coating of spherical secondary particles can be detected by TEM analysis. **Figure 5. 28** presents the TEM image of the cathode material of Daisy-Ni83-Bmiddle. A spherical secondary particle of Daisy-Ni83-Bmiddle is shown in **Figure 5. 28.** (a). The picture on the right in **Figure 5. 28.** (a) is the magnified image of the green circled part of the Daisy-Ni83-Bmiddle particle, a very uniform coating layer with the thickness about 10 nm can be distinguished. After observing the full circle of the secondary particle, all areas of the secondary particle surface appeared as a coating. The representative areas are labelled with “I”, “II”, and “III” in **Figure 5. 28.** (a) and the corresponding enlarged TEM images are shown in **Figure 5. 28.** (b, c, and d). In these enlarged figures, the thicknesses of the coating layers at different positions are indicated by blue dotted lines. For the area of “I”, the thickness of 16.3 nm, 15.5 nm, and 14.6 nm are measured for the coating layer. For the area of “II”, the coating thickness of 7.4 nm and 8.4 nm are measured. The coating thickness of 12.8 nm, 7.8 nm, and 11.2 nm are measured for the area “III”. The coating layer was continuous with an average thickness of 11.75 nm based on the eight measured positions, as shown in **Figure 5. 28.** This observation indicates that the coating layer is relatively

uniform and complete for the spherical secondary particles of Daisy-Ni83-Bmiddle, which is different from the gradually disappearing coating layer of Daisy-Ni83-Bthin, as shown in **Figure 5. 27.** (b1) and (b2). Meanwhile, the complete coating layer of Daisy-Ni83-Bmiddle was very smooth and dense, as shown in the magnified TEM images with a scale bar of 10 nm.

In the high-resolution TEM (HRTEM) images of **Figure 5. 28.** (a), (b), (c), and (d), the interplanar spacings of 0.2036 nm, 0.4763 nm (or 0.4789 nm), and 0.2435 nm match well with the (104), (003), and (101) crystal planes of $R\bar{3}m$ LiNiO₂. The interplanar spacing of the (003) plane is shown in **Figure 5. 28.** (b), the two measured interplanar distances (0.4763 nm and 0.4789 nm) are larger than the d-spacing of 0.4715 nm for the (003) plane for the pristine Daisy-Ni83, as shown in **Figure 5. 27.** (a2). This means that lattice expansion of the material occurs after the combined boron-related doping and coating of Daisy-Ni83-Bmiddle. The TEM observation of Daisy-Ni83-Bmiddle is consistent with the XRD results, both indicate the volume expansion of the unit cell of Daisy-Ni83-Bmiddle, in contrast to the pristine Daisy-Ni83 (Liu et al., 2023, Huang et al., 2020).

Such coating modifications can also be found in other secondary particle surfaces in Daisy-Ni83-Bmiddle. EDS mapping and TEM observations indicated that Daisy-Ni83-Bmiddle achieved combined boron-related doping and coating, and the coating was complete and relatively uniform on the secondary particle. Daisy-Ni83-Bthin also achieves boron-related doping and coating, but the coating is incomplete and very local on the particle surface. Therefore, compared with Daisy-Ni83-Bthin, Daisy-Ni83-

Bmiddle exhibits better cycling stability at high cut-off voltage and high current density.

The excellent electrochemical performance of Daisy-Ni83-Bmiddle under harsh conditions of high cut-off voltage and high current density can be ascribed to the smooth, dense, and complete coating layer, which provides stronger protection than the incomplete coating of Daisy-Ni83-Bthin against side reactions between the cathode material surface and the electrolyte.

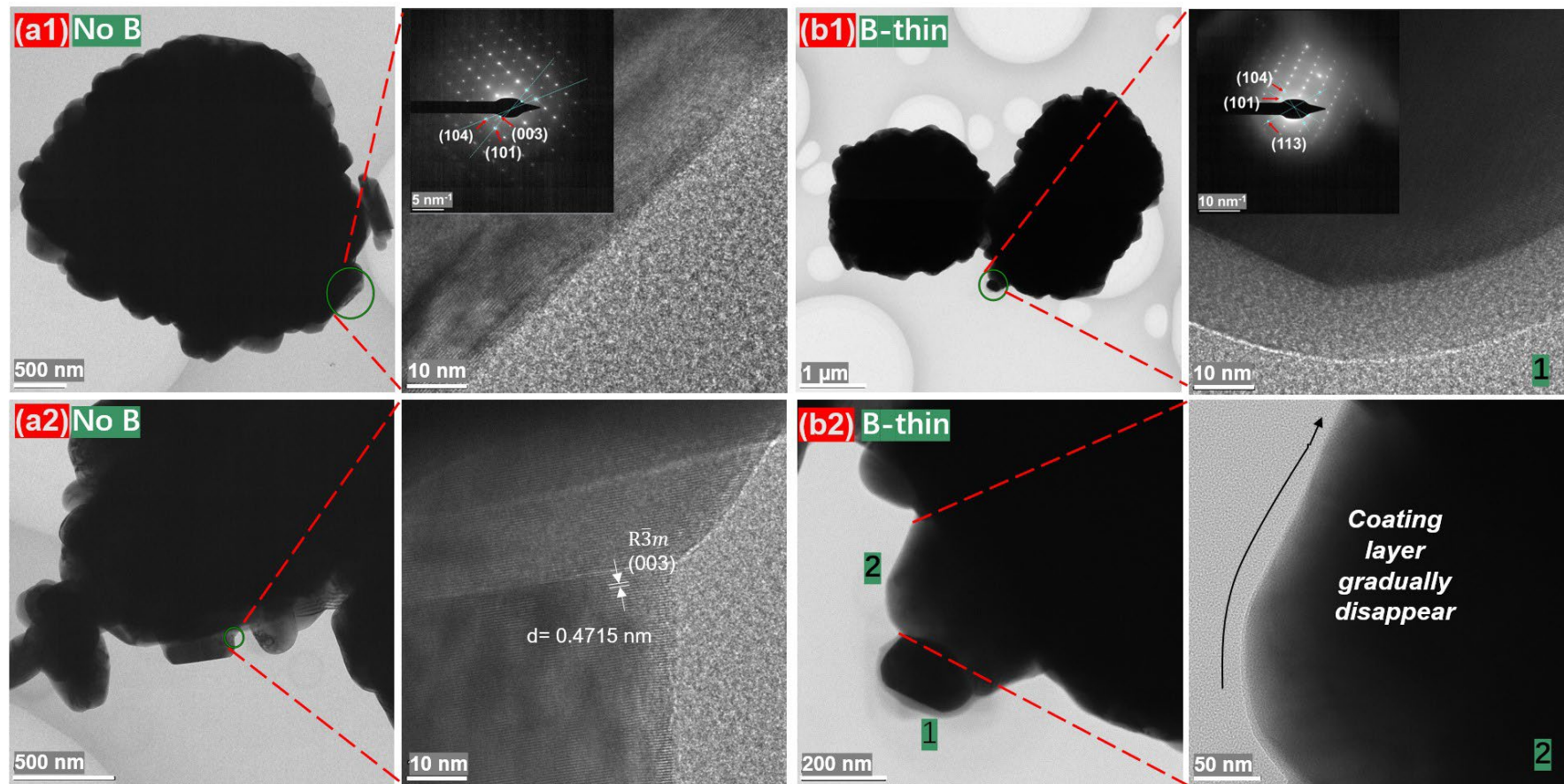


Figure 5. 27. TEM images of cathode material: (a1 and a2) Daisy-Ni83; (b1 and b2) Daisy-Ni83-Bthin, panel b2 is the enlarged image from the area in the green circled part shown in panel b1.

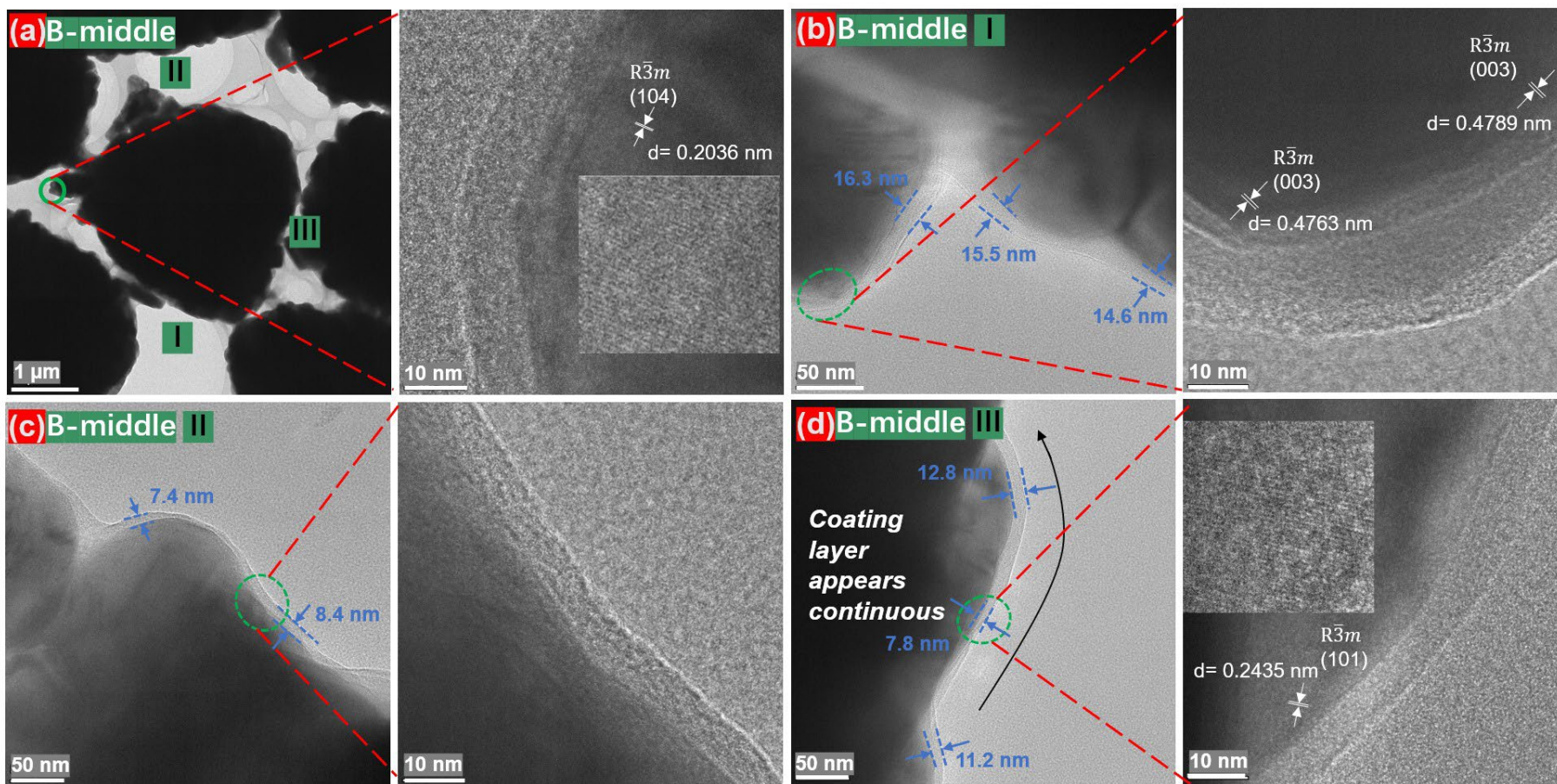


Figure 5. 28. TEM images of cathode material of Daisy-Ni83-Bmiddle: (a) the spherical secondary particle of Daisy-Ni83-Bmiddle with high-resolution TEM image; (b, c, and d) enlarged images for the local areas indicated as “I”, “II”, and “III” of the spherical particle in panel (a).

The EDS analysis equipped in the TEM machine was performed on the coating layer and the near-surface area for the cathode material of Daisy-Ni83-Bthin, which are shown in **Figure 5. 29**. The area inside the coating layer (left image in **Figure 5. 29**), the atomic fraction of B is as high as 21.71%, which means that the coating layer is composed of boron-related material. For the near-surface area as shown on the right-hand side of **Figure 5. 29**, the atomic fraction of B is detected to be 5.97%, and the corresponding mole percentage of B in the sum of Ni, Co, Mn, and B is calculated to be 9.9% much higher than that the ICP-OES result of 1.36% shown in **Table 5. 5**. This indicates that boron doping mainly occurred in the near-surface area of the secondary particles. This point of view is further confirmed by the EDS mapping analysis of the entire secondary particle of Daisy-Ni83-Bthin, as shown in **Figure 5. 30**. For the micron-level survey, EDS can be used to measure a depth of more than 300 nm below the surface. The corresponding signal acquisition of the entire secondary particle of Daisy-Ni83-Bthin costs about 30 min, the atomic fraction of B is 0.18% for the secondary particle and much lower than the B atomic fraction of 5.94% in the near-surface area. Meanwhile, the B signal in the EDS element mapping does not appear because of the very low atomic fraction. It is worth noting that the phenomenon of B atom doping mainly in the surface region of the cathode material, has also been reported by other researchers for the modification of the NCA(LiNi_{0.8}Co_{0.15}Al_{0.05}O₂) cathode (Chen et al., 2018).

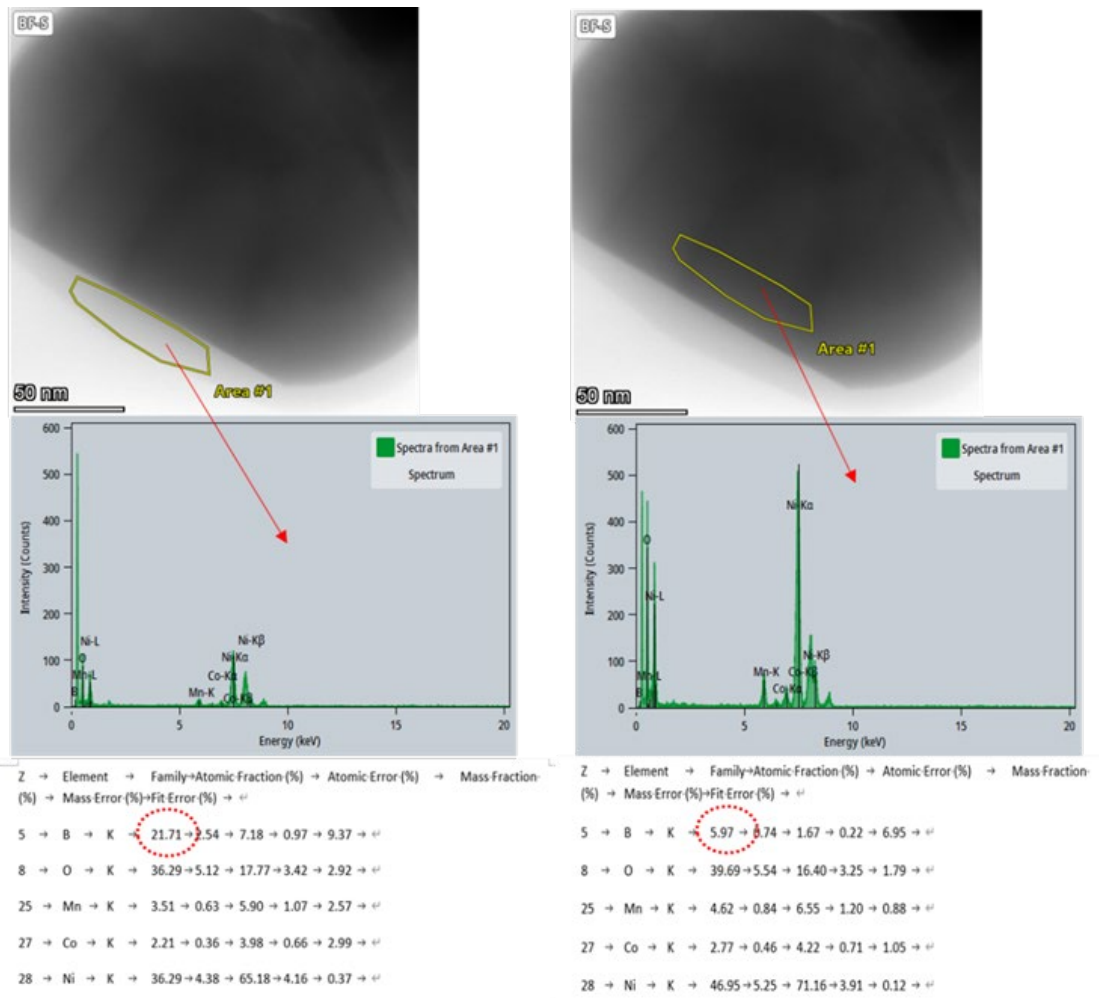
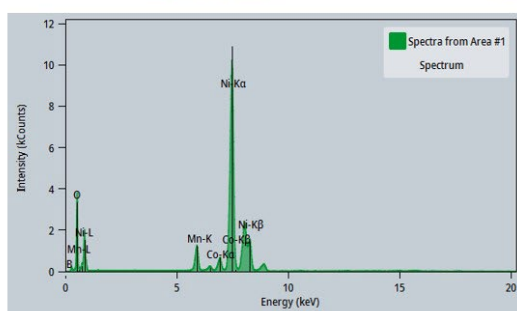
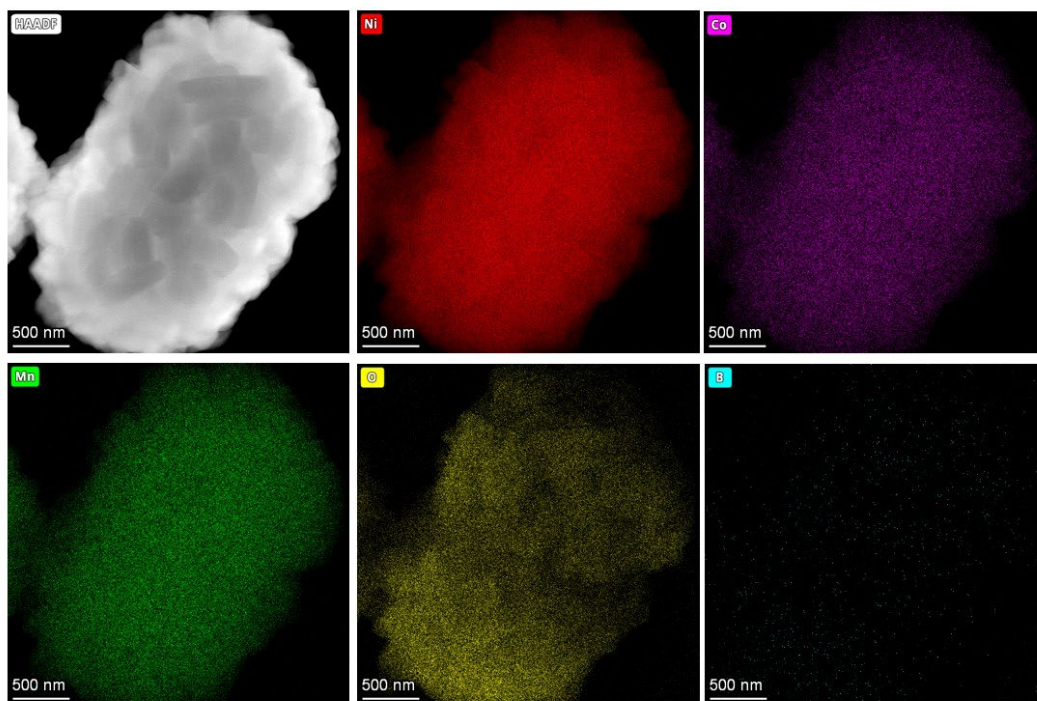


Figure 5. 29. EDS analysis on the coating layer and the near-surface area for cathode material of Daisy-Ni83-Bthin (The analysis area is at position “1” marketed in **Figure 5. 27.** (b2)).



Z	Element	Family	Atomic-Fraction(%)	Atomic-Error(%)
5	B	K	0.18	0.04
8	O	K	25.51	4.50
25	Mn	K	6.52	1.18
27	Co	K	3.82	0.64
28	Ni	K	63.98	4.76

Figure 5. 30. EDS compositional maps of the Ni, Co, Mn, O, and B elements for a secondary particle of Daisy-Ni83-Bthin from **Figure 5. 27.** (b1).

For the boron-related coating layer, the mole ratios of B: O in the TEM-EDS survey were found to be 21.71:36.29 equal to 0.598, matching with the composition of LiBO_2 rather than Li_3BO_3 . The coating material was the glass amorphous LiBO_2 . XPS results (**Figure 5. 31**) about the B 1s peaks in the XPS spectra of different cathode material powders further confirm this conclusion. There was no obvious B 1s XPS peak for Daisy-Ni83 (**Figure 5. 31.** (a)). Meanwhile, B 1s XPS peaks appeared in Daisy-Ni83-Bthin (**Figure 5. 31.** (b)), Daisy-Ni83-Bmiddle (**Figure 5. 31.** (c)), and Daisy-Ni83-

Bthick (**Figure 5. 31. (d)**) at around 192 eV, corresponding to the B-O bonding of LiBO_2 (Hu et al., 2017). Glass amorphous LiBO_2 is a faster ion conductor, which is beneficial for the rate performance (Zhao et al., 2022a).

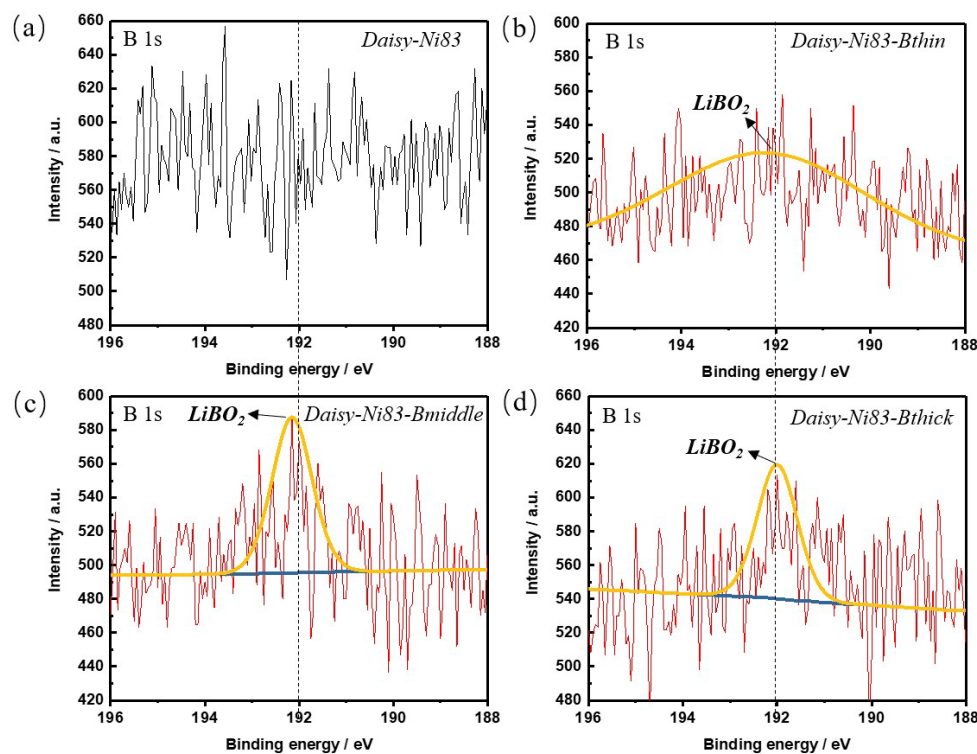


Figure 5. 31. B 1s peaks at XPS spectrum of cathode material powders: (a) Daisy-Ni83; (b) Daisy-Ni83-Bthin; (c) Daisy-Ni83-Bmiddle; and (d) Daisy-Ni83-Bthick.

The particles of Daisy-Ni83 and Daisy-Ni83-Bmiddle after a total of 150 cycles at 1 C with the initial 10 cycles at 0.2 C and 5 cycles at 0.5 C between 2.8-4.3 V were observed by TEM, with images shown in **Figure 5. 32. (a1-a4)** and **(b1-b4)**, respectively. A secondary particle of the cycled Daisy-Ni83 without modification is shown in **Figure 5. 32. (a1)**. Another secondary particle of the cycled Daisy-Ni83-Bmiddle with a complete coating is shown in **Figure 5. 32. (b1)**. According to **Figure 5. 32. (a2)** with a scale bar

of 100 nm, the CEI on the cycled Daisy-Ni83 is obvious along the surface, which looks incompact different from the LiBO_2 coating layer. Such an incompact CEI can hardly be found on the surface of the cycled Daisy-Ni83-Bmiddle with the same scale bar of 100 nm, as shown in **Figure 5. 32.** (b2). A few carbon blacks with ellipsoidal shapes adhering to the coating layer of the cycled Daisy-Ni83-Bmiddle can be found (Zhao et al., 2019, Galimberti et al., 2020). The thickness of the CEI on cycled Daisy-Ni83 reached 25 nm, as shown in **Figure 5. 32.** (a3) almost reach the thickness of LiBO_2 coating layer on the cycled Daisy-Ni83-Bmiddle shown in **Figure 5. 32.** (b3). In contrast to the dense and smooth coating layer in **Figure 5. 32.** (b3), the inhomogeneous characteristic of the CEI on the cycled Daisy-Ni83 in **Figure 5. 32.** (a3) appeared to be more prominent with further magnification. The further magnified TEM images of cycled Daisy-Ni83 and Daisy-Ni83-Bmiddle are observed. In contrast to the thick and inhomogeneous CEI of Daisy-Ni83, as shown in **Figure 5. 32.** (a4), a layer with a thickness of less than 5 nm and relatively even CEI deposits on the outside of the coating layer of Daisy-Ni83-Bmiddle can be detected in **Figure 5. 32.** (b4). Overall, the CEI of cycled Daisy-Ni83-Bmiddle is much smaller and flatter than that of cycled Daisy-Ni83, which indicates that the side reactions were greatly suppressed by Daisy-Ni83-Bmiddle, leading to better cycling performance.

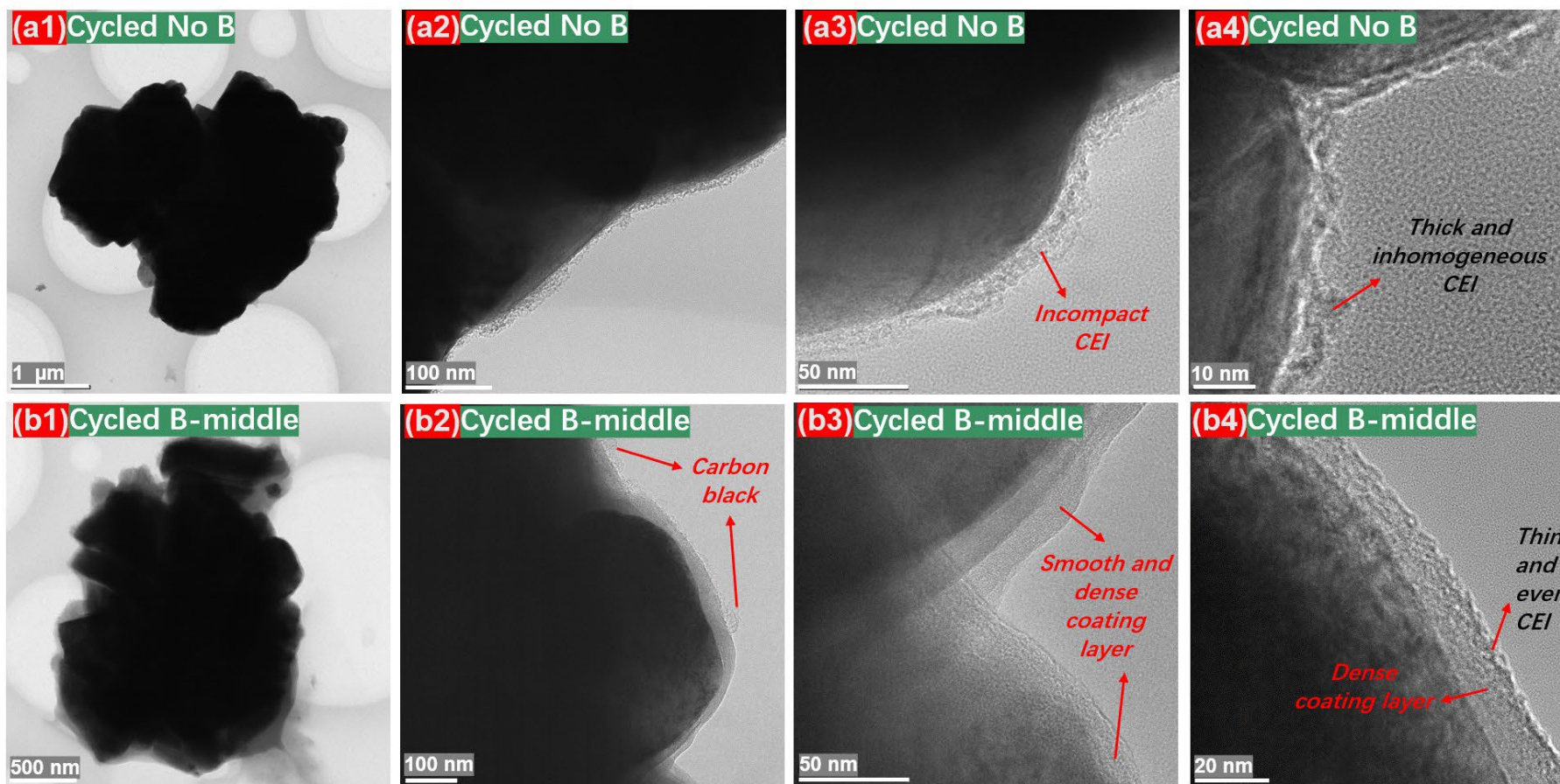


Figure 5. 32. TEM images of Daisy-Ni83 and Daisy-Ni83-Bmiddle particles at different magnifications after the total 150 cycles at 1 C with the initial 10 cycles at 0.2 C and 5 cycles at 0.5 C between 2.8-4.3 V: (a1-a4) Daisy-Ni83 and (b1-b4) Daisy-Ni83-Bmiddle with complete coating.

It is known that CEI is mainly initiated by side reactions between the electrolyte and the surface of Ni-rich materials, along with the decomposition of electrolytes and the dissolution of transition metals (Fang et al., 2021, Liu et al., 2015). The suppressed side reactions of Daisy-Ni83-Bmiddle were further confirmed by XPS analysis. The results are shown in **Figure 5. 33**.

In C 1s spectra (**Figure 5. 33**. (a) and (b)), electrolyte decomposition with C=O, C-O-C, and C-OH (289.7 eV, 287.6 eV, and 285.8 eV) can be confirmed (Schulz et al., 2018). The other two subpeaks at 291.3 eV and 284.8 eV are assigned to C-F of PVDF and C-C of carbon black (Andersson et al., 2002). Compared with the cycled Daisy-Ni83 electrode, the cycled Daisy-Ni83-Bmiddle electrode appears to have higher signals C-F of PVDF and C-C of carbon black along with other lower C 1s signals originating from electrolyte decomposition, which means that less decomposition of the electrolyte occurs for Daisy-Ni83-Bmiddle. P 2p spectra (**Figure 5. 33**. (c) and (g)) also verify such an idea with stronger signals of P-O, P=O chemical bonds for Daisy-Ni83 at 135.1 eV than Daisy-Ni83-Bmiddle at 134.8 eV (Schulz et al., 2018).

More amount of NiF₂/LiF is detected in F 1s spectra with higher peak intensity for Daisy-Ni83 at 685.9 eV (**Figure 5. 33**. (b)) than Daisy-Ni83-Bmiddle at 685.7 eV (**Figure 5. 33**. (f)) (Li et al., 2020d). The restrained interface side reactions of Daisy-Ni83-Bmiddle are also reflected by the Ni 2p spectra, where the peak intensity of NiF₂ for Daisy-Ni83-Bmiddle at 857.9 eV (**Figure 5. 33**. (h)) is weaker than that of Daisy-Ni83 at 858.8 eV (**Figure 5. 33**. (d)) (Zhu et al., 2022, Li et al., 2017a). Ni is the main redox-active element for delivering capacity during cycling; hence, less Ni dissolution

guarantees the excellent electrochemical performance of Daisy-Ni83-Bmiddle (Markevich et al., 2019).

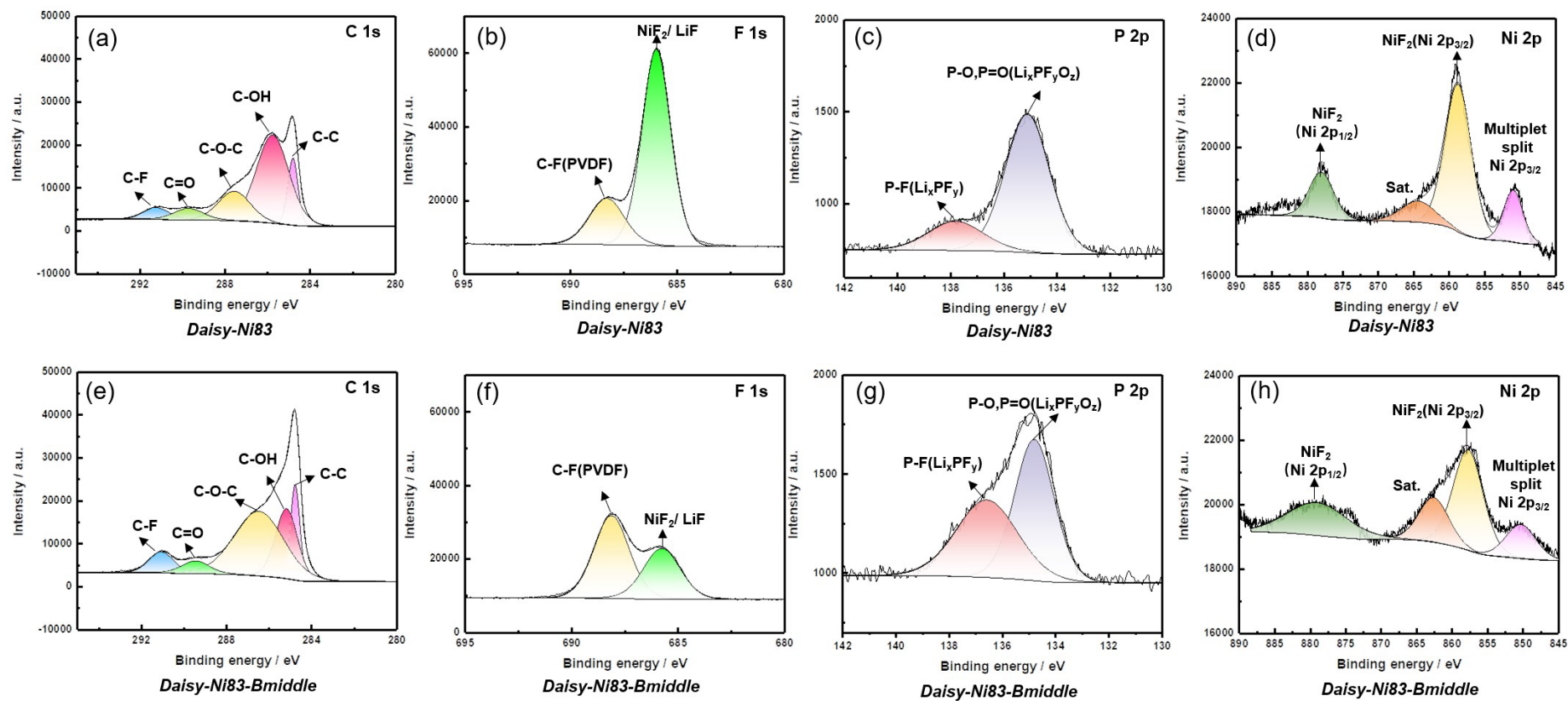


Figure 5. 33. XPS C 1s, F 1s, P 2p, and Ni 2p spectra of the cathode electrode after 150 cycles at 1 C with the initial 10 cycles at 0.2 C and 5 cycles at 0.5 C between 2.8-4.3 V: (a-d) Daisy-Ni83 and (e-h) Daisy-Ni83-Bmiddle.

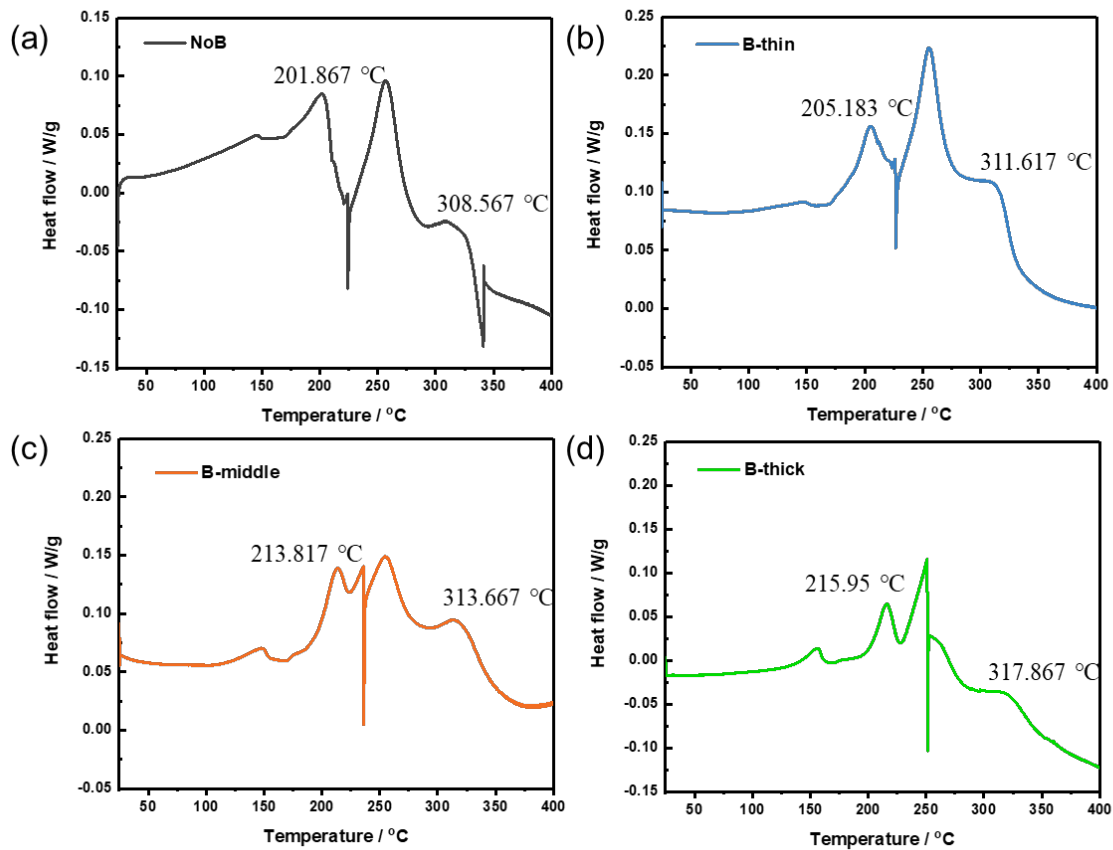


Figure 5. 34. DSC curves of the cathode powders in fully delithiated states at a scanning rate of 1°C/min in nitrogen atmosphere: (a) Daisy-Ni83(NoB), (b) Daisy-Ni83-Bthin(B-thin), (c) Daisy-Ni83-Bmiddle (B-middle), and (d) Daisy-Ni83-Bthick(B-thick).

Figure 5. 34 presents the DSC curves of the cathode powders of Daisy-Ni83, Daisy-Ni83-Bthin, Daisy-Ni83-Bmiddle, and Daisy-Ni83-Bthick at fully delithiated states with the scanning rate of 1°C/min from 30 °C to 400 °C at the nitrogen atmosphere. During the DSC test of NCM811 reported by Wang et al. (Wang et al., 2021), the first exothermic peak occurs at approximately 200-250 °C corresponding to the structural change from layered phase ($R\bar{3}m$) to spinel phase I (LiMn_2O_4 -type), the second exothermic peak at approximately 300 °C corresponds to the structural change from layered phase ($R\bar{3}m$) to spinel phase II (Mn_3O_4 -type). The heat release for structural

change from the layered phase to spinel phase I was much higher than that for spinel phase II. The test results for our samples conform to this feature. The difference is that there is an endothermic peak between 200-250 °C in **Figure 5. 34.** (a), (b), (c), and (d) due to the melting of PVDF (Huang et al., 2016). The starting temperatures for the transition from the layered phase to spinel phase I and from the layered phase to spinel phase II are marked in **Figure 5. 34.** (a), (b), (c), and (d), which are 201.9 °C/308.6 °C, 205.2 °C/311.6 °C, 213.8 °C/313.7 °C, and 216 °C/317.9 °C separately for Daisy-Ni83, Daisy-Ni83-Bthin, Daisy-Ni83-Bmiddle, and Daisy-Ni82-Bthick. The generated heats were normalised to 670 J g⁻¹, 584 J g⁻¹, 544 J g⁻¹, and 423 J g⁻¹, respectively.

The higher peak temperatures and lower amounts of heat generated in the DSC test indicated improved thermal stability after boron-related doping and coating modification. Compared with Daisy-Ni83-Bthin, Daisy-Ni83-Bmiddle exhibited better thermal stability, which was ascribed to the higher boron content for doping and coating. Although ICP-OES implies Daisy-Ni83-Bthick has the smallest mole ratio of boron in the modified samples, owing to the stripping of B₂O₃ during the process of mixing with the lithium source in the ball mill machine, Daisy-Ni83-Bthick exhibits superior thermal stability compared to Daisy-Ni83-Bmiddle, which can possibly be attributed to the poor Li/Ni ordering. This is because, from the viewpoint of thermodynamics, the phase transition reactions of Daisy-Ni83-Bthick become difficult. The disordered Li/Ni arrangement of Daisy-Ni83-Bthick would involve some spinel phases and/or rock-salt phase, which appears better thermal stability compared with the layered phase.

Although Daisy-Ni83-Bthick exhibited the best thermal stability, the poor Li/Ni

ordering and unstable cycling performances under most test conditions reduced the application value of Daisy-Ni83-Bthick. Compared with Daisy-Ni83-Bthin, Daisy-Ni83-Bmiddle is a more ideal Ni-rich cathode material with excellent long-term cycling stability at both the high cut-off voltage and the high current density and also exhibits superior thermal stability. The achievement of Daisy-Ni83-Bmiddle can be attributed to the fact that by retaining the radial structure, a completely smooth and dense boron-related coating and near-surface doping can improve thermal stability and effectively inhibit electrolyte decomposition and transition metal dissolution. This embodies the advantages of the three-in-one effect of the coating and doping with an intrinsic daisy-like structure.

5.4. Conclusion

In the step of determining the optimal lithiation calcination condition, the four factors of good crystallinity with ordered layered structure, clean surface without obvious lithium residues, reduced gaps among primary particles, and the daisy-like radially aligned structure are demonstrated to be important for such special structured Ni-rich cathode material to achieve high discharge capacity over 200 mAh g⁻¹ between 2.8-4.3 V and nearly 240 mAh g⁻¹ between 2.8-4.5 V. In the sol/antisolvent B₂O₃ coating on the precursor of the daisy-like structure followed by the optimal lithiation calcination condition, the modification process does not destroy the special daisy-like structure, but realises the combined boron-related coating and doping together with the radially aligned primary particles. Meanwhile, the synthesised coating layer appeared very

smooth and dense with nanosized thickness and was identified as the material of the glass amorphous LiBO_2 . Boron doping was concentrated in the near-surface area of the secondary particles of the cathode material. Owing to these boron-related coating and doping, the modified Ni-rich cathode materials Daisy-Ni83-Bthin and Daisy-Ni83-Bmiddle exhibited better long-term cycling stability, rate capability, and thermal stability than the unmodified Daisy-Ni83. The difference is that Daisy-Ni83-Bthin is subjected to an incomplete coating for the secondary particle, while Daisy-Ni83-Bmiddle is subjected to a complete coating of the secondary particle. Sufficient protection from the complete coating on the secondary particle of Daisy-Ni83-Bmiddle leads to superior cycling performances at the high cut-off voltage and high current density. For Daisy-Ni83-Bthick, the relatively lean lithium source for lithiation causes the material to exhibit poor Li/Ni ordering, which is responsible for its poor cycling performance under most test conditions.

Overall, with the help of sol/antisolvent B_2O_3 treatment on the specially structured precursor and the subsequent lithiation calcination, the three-in-one effect of the radially aligned microstructure and the incorporated coating and doping can be achieved. Compared with the separate doping or coating modification, the benefit of the three-in-one effect is obvious. This study plays a positive role in promoting the development of Ni-rich cathode materials by providing new ideas and references.

Chapter 6 Sol/Antisolvent with Boron Treating for the Modification of LiNiO₂ Cathode

This chapter reports the sol/antisolvent boron treatment with lithiation calcination to modify the end member of the Ni-rich layered oxide LiNiO₂ (LNO). A Ni(OH)₂ sample with a radially aligned structure was used as the precursor. A combination of radially structured and B-doped LNO materials can be achieved. One of the modified LNO materials doped with boron exhibits superior electrochemical performance, even better than the well-formed and similar-sized single-crystal LNO material.

6.1. Introduction

The specific capacity of Ni-rich layered oxide cathode materials increases with increasing Ni content, and the highest discharge capacity of up to 240 mAh g⁻¹ can be attributed to the extremely high Ni content of LiNiO₂ (Markevich et al., 2019). However, as the Ni content increases, the structural stability, interfacial stability, and thermal stability of the Ni-rich layered oxide decrease, particularly for the end member of LiNiO₂ (Qiu et al., 2021, de Biasi et al., 2019). Unlike NCM811, which delivers negligible capacity fading and voltage decay for 50 cycles at 0.5 C (100 mA g⁻¹) with a cut-off voltage of 4.3 V (Wang et al., 2023), LiNiO₂ experiences quick capacity fading at a cut-off voltage of 4.3 V with a smaller current density of 0.1 C (18 mA g⁻¹) (Yoon et al., 2017). Although the rapid capacity fading of LiNiO₂ can be alleviated by

decreasing the cut-off voltage to 4.1 V, the expense is the low discharge capacity of only 179 mAh g⁻¹ at 0.1 C (18 mA g⁻¹) (Yoon et al., 2017). It is mainly due to the most detrimental effect of H2 phase to H3 phase transformation above 4.1 V, which involves a sharp shrinkage of the unit cell volume and a sudden collapse of the structure leading to harmful impacts on the material's stability (de Biasi et al., 2019).

Many studies have been conducted to mitigate the rapid capacity fading of LiNiO₂ above 4.1 V. The main strategies for modifying LiNiO₂ are almost the same as those for NCM811, which include doping and coating treatment. For example, the Mg/Al co-doping strategy can achieve better cycling stability and rate capability of LiNiO₂ (Shen et al., 2023). Li_xW_yO_z amorphous coating for LiNiO₂ can restrict primary particle growth during synthesis and increase the resistance of the secondary particles to microcracking (Geng et al., 2022). In addition, synthesising LiNiO₂ with a well-formed and similar-sized single-crystal structure (SC-LNO) can enhance the rate capability or achieve high cycling stability, which is correlated with the different shapes and dominant surface facets of the single crystals (Kim et al., 2022).

Considering that the sol/antisolvent boron-related treatment is beneficial for improving the electrochemical performance of NCM with Ni content greater than 80 % (Zhang et al., 2022), the sol/antisolvent boron treatment is further adopted for the modification of the ultra-high Ni material of LiNiO₂. Ni(OH)₂ with a radially aligned arrangement of primary particles was used as the starting material to synthesise LiNiO₂. The modified LiNiO₂ was obtained by sol/antisolvent B₂O₃ treating on the Ni(OH)₂ along with the subsequent lithiation calcination. It is noteworthy that the alteration can render LiNiO₂

as ordered and well-crystallised primary particles, which are accompanied by enhanced discharge capacities and rate capabilities. One of the modified LiNiO₂ named LiNiO₂-more B can deliver as high as the initial discharge capacity of 186.5 mAh g⁻¹ at 0.3 C (60 mA g⁻¹) with a capacity retention of 74.7 % after 100 cycles between 2.8-4.3 V, the initial discharge capacity of 202.6 mAh g⁻¹ at 0.3 C (60 mA g⁻¹) with the capacity retention of 69.1 % after 100 cycles between 2.8-4.5 V, and the initial discharge capacity of 197.7 mAh g⁻¹ at 0.3 C (60 mA g⁻¹) with the capacity retention of 62.3 % after 100 cycles between 2.8-4.6 V. This result is superior to the two types of well-formed and similar-sized SC-LNO reported by Kim et al. (Kim et al., 2022). Moreover, beyond the H2–H3 phase transition that occurs for the modified LiNiO₂, another harmful phase transition of H3–H4 above 4.4 V is also detected, which is different from NCM811 and is rarely mentioned in the study of LiNiO₂ (de Biasi et al., 2019, Xu et al., 2020, Kurzhals et al., 2021).

6.2. Experimental Section

6.2.1. LiNiO₂, LiNiO₂-less B, and LiNiO₂-more B preparation

Radially aligned Ni(OH)₂ was purchased from Hebei Guifa Alloy Wear-Resistant Materials Co. Ltd. Such specially structured Ni(OH)₂ was used as a precursor to synthesise LiNiO₂. SEM images of Ni(OH)₂ precursor are shown in **Figure 6. 1** with various magnifications. Several secondary particles of Ni(OH)₂ can be found in **Figure 6. 1. (a)** at relatively low magnification. The sizes of Ni(OH)₂ secondary particles were not uniform. However, the roundness was good, as shown in **Figure 6. 1. (b)**. The

radially aligned structures of Ni(OH)₂ particles are illustrated in **Figure 6. 1. (c)** and **Figure 6. 1. (d)** with cross-section observations at different angles. It is clear that the arrangement of the primary particles is in the radial direction, and the shape of the primary particles in each radial direction is very thin, so many radiant streaks can be observed. Moreover, the light-green colour of the Ni(OH)₂ precursor powders in the bottle can be easily recognized, as shown in **Figure 6. 1. (d)**. Pristine LiNiO₂ samples were synthesised by mixing specially structured Ni(OH)₂ powders with dried LiOH.H₂O with a mole ratio of Li/Ni of 1.02:1, followed by calcination in a tubular furnace in a pure oxygen atmosphere. The mixed powders were first heated to 500 °C for 5 h to melt the LiOH, and then the temperature was increased to 685 °C for 13 h with subsequent natural cooling to obtain the final pristine LiNiO₂ samples. These lithiation calcination conditions were also applied to get the modified LiNiO₂. To synthesis sol/antisolvent boron-treated LiNiO₂ samples, the sol/antisolvent process for treating Ni(OH)₂ powders was the same as that for treating Ni_{0.83}Co_{0.05}Mn_{0.12}(OH)₂ powders, as described in Chapter 5. The difference is that only the mole mass ratio of boron to the precursor of 0.075 was adopted. B₂O₃ ethanol sol with a certain concentration was prepared using an ultrasonic instrument. Chapter 4 demonstrated that a greater amount of antisolvent can induce a thicker coating thickness in the sol/antisolvent process. To distinguish the treatments using different dosages of antisolvent, the modified LiNiO₂ with the Ni(OH)₂ precursor subjected to 35 ml tetrahydrofuran (THF) antisolvent treatment is named LiNiO₂-less B, and the modified LiNiO₂ with the Ni(OH)₂ precursor subjected to 140 ml THF antisolvent treating is named LiNiO₂-more B.

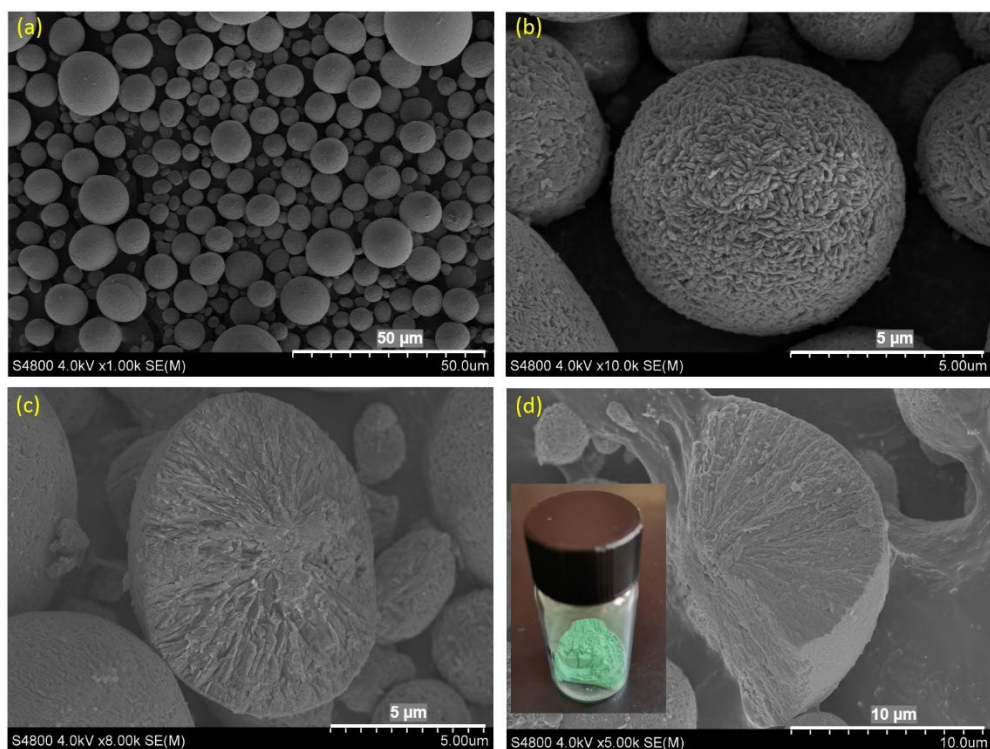


Figure 6. 1. SEM images of Ni(OH)₂ precursor at different magnifications: (a) various sized spherical secondary particles; (b) a high degree of roundness for a secondary particle; and (c, d) cross-sectional observations at different angles with a picture of Ni(OH)₂ powder in a bottle inserted in panel (d).

6.2.2. Electrochemical Tests and Material Characterisation

The electrochemical properties of the pristine LiNiO₂, LiNiO₂-less B, and LiNiO₂-more B were assessed using 2032 coin-cells. The cathode material was mixed with a Super P conductor and PVDF binder at a mass ratio of 8:1:1 in N-methyl pyrrolidone (NMP) to form the cathode slurry. After the slurry was coated onto Al foil, the coated foil was dried in a blast drying oven, then the dried coated foil was pressed into discs with a diameter of 14 mm to form the cathodes. The prepared cathode was assembled with a Celgard M825 separator, lithium metal anode, and 100 μL of 1 M LiPF₆ in the volume ratio of 3:7 ethylene carbonate (EC)/dimethyl carbonate (DMC) electrolyte. The coin-

cell assembly was completed in an argon-filled glove box with O₂ less than 0.5 ppm and H₂O less than 0.5 ppm (MBRAUN UniLab). The mass loading of the active material was approximately 4 mg cm⁻² for each coin cell. The charge-discharge tests of these coin cells were performed using a LAND cell test system at room temperature. Mainly the galvanostatic cyclings at the current density of 0.3 C (1 C = 200 mA g⁻¹) with the potential limitation measurements between 2.8-4.3 V, 2.8-4.5 V, and 2.8-4.6 V (vs. Li/Li⁺) and the rate performance at different current densities were investigated.

The crystal structures of the pristine LiNiO₂, LiNiO₂-less B, and LiNiO₂-more B were analysed by high-performance X-ray diffraction (XRD, D8 DISCOVER, Bruker) from 5° to 90° at a scan rate of 3°/min with Cu K α radiation. A scanning electron microscope (SEM, S4800, Hitachi) was carried out to observe the microstructures and morphologies of the pristine LiNiO₂, LiNiO₂-less B, and LiNiO₂-more B in secondary electron mode with an accelerating voltage of 4 KV and an emission current of 7 μ A.

6.3. Results and Discussion

6.3.1. Electrochemical Performances of LiNiO₂, LiNiO₂-less B, and LiNiO₂-more B

All samples of the pristine LiNiO₂, LiNiO₂-less B, and LiNiO₂-more B undergo 0.3 C (1 C = 200 mA g⁻¹) cycling for 100 cycles with the initial two activation cycles at 0.1 C with the different cut-off voltages of 4.3, 4.5, and 4.6 V. The 0.3 C cycling performance comparison of the pristine LiNiO₂, LiNiO₂-less B, and LiNiO₂-more B in the voltage range of 2.8-4.3 V, 2.8-4.5 V, and 2.8-4.6 V are separately shown in **Figure 6. 2.** (a), (b),

and (c). The black, red, and green points represent the pristine LiNiO₂, LiNiO₂-less B, and LiNiO₂-more B, respectively. According to **Figure 6. 2.** (a), (b), and (c), it can be found that the initial discharge capacities at 0.1 C and 0.3 C increased after the precursor was subjected to the sol/antisolvent boron treatment, and LiNiO₂-more B exhibits the highest initial discharge capacities in each test voltage range. Meanwhile, the capacity fading rate of all samples increased with increasing cut-off voltage, as shown in **Figure 6. 2.** (a), (b), and (c). The fastest capacity fading appears for the cut-off voltage of 4.6 V for all samples by comparing the slopes of the capacity fade curves. Although LiNiO₂-more B suffers quicker capacity fading rates than the pristine LiNiO₂ and LiNiO₂-less B under most test conditions, the delivered specific capacity of LiNiO₂-more B at each cycle is always higher than that of the other two samples in the voltage range of 2.8-4.3 V and 2.8-4.5 V.

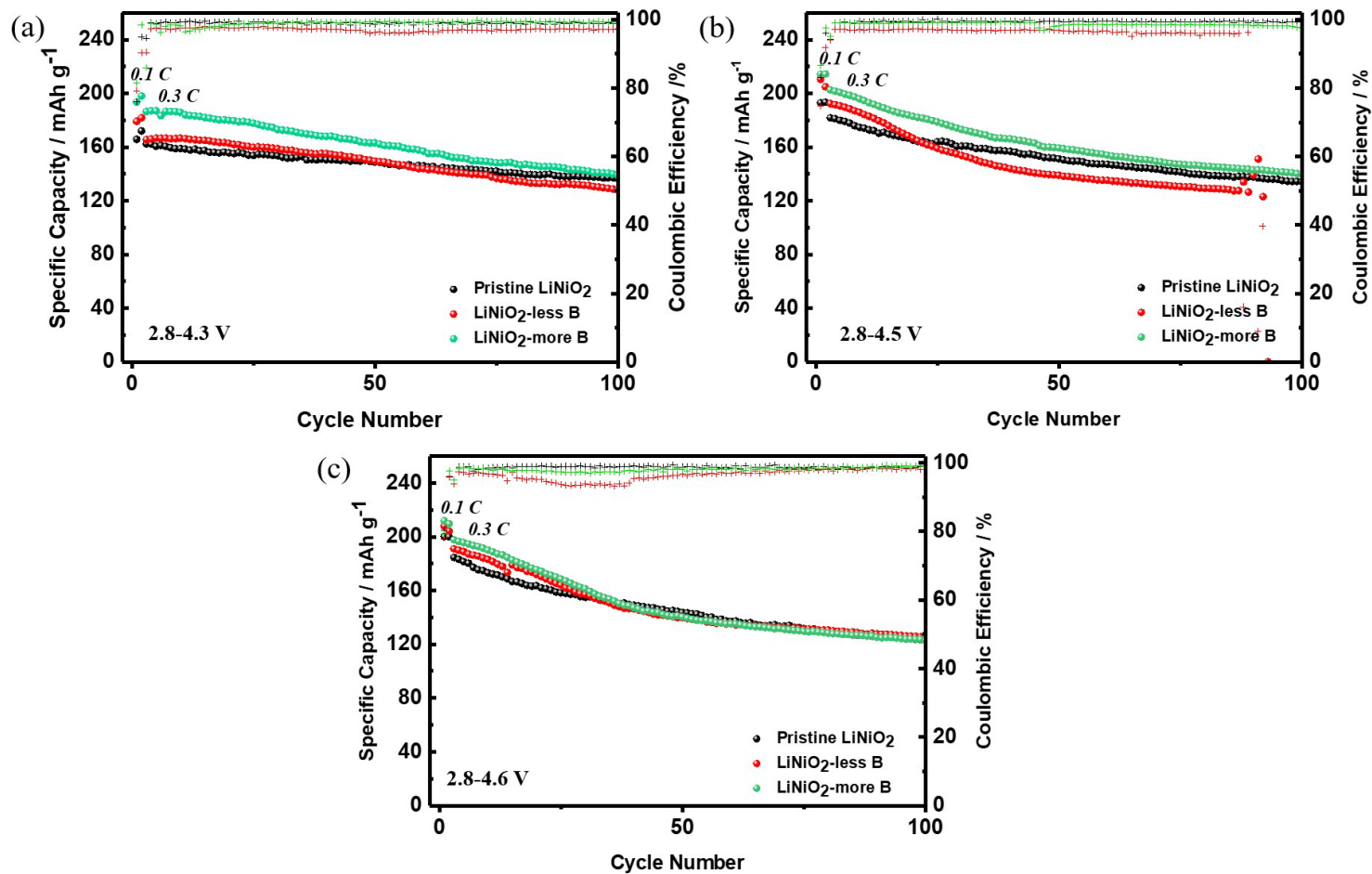


Figure 6. 2. 0.3 C cycling performances of pristine LiNiO₂, LiNiO₂-less B, and LiNiO₂-more B at different cut-off voltages: (a) the voltage range of 2.8-4.3 V, (b) the voltage range of 2.8-4.5 V, and (c) the voltage range of 2.8-4.6 V.

Table 6. 1. Summary of the initial discharge capacity, the last cycle discharge capacity, and the capacity retention with full cycles at 0.3 C in 2.8-4.3 V, 2.8-4.5 V, and 2.8-4.6 V for pristine LiNiO₂, LiNiO₂-less B, and LiNiO₂-more B.

Sample	Discharge capacity for the initial cycle at 0.3 C between 2.8-4.3 V (mAh g ⁻¹)	Discharge capacity for the last cycle at 0.3 C between 2.8-4.3 V (mAh g ⁻¹)	Capacity retention
Pristine LiNiO ₂	162.4	136.3	83.9%
LiNiO ₂ -less B	165.6	128.3	77.5%
LiNiO ₂ -more B	186.5	139.3	74.7%
Sample	Discharge capacity for the initial cycle at 0.3 C between 2.8-4.5V (mAh g ⁻¹)	Discharge capacity for the last cycle at 0.3 C between 2.8-4.5 V (mAh g ⁻¹)	Capacity retention
Pristine LiNiO ₂	181.8	134.1	73.8%
LiNiO ₂ -less B	192.3	0 (127.5 @ 87 th cycle)	N/A (66.3% @ 87 th cycle)
LiNiO ₂ -more B	202.6	140	69.1%
Sample	Discharge capacity for the initial cycle at 0.3 C between 2.8-4.6 V (mAh g ⁻¹)	Discharge capacity for the last cycle at 0.3 C between 2.8-4.6 V (mAh g ⁻¹)	Capacity retention
Pristine LiNiO ₂	184.6	122.9	66.6%
LiNiO ₂ -less B	191	125.4	65.7%
LiNiO ₂ -more B	197.7	123.2	62.3%

The detailed data of the initial discharge capacity, the last cycle discharge capacity, and the capacity retention with full cycles at 0.3 C in 2.8-4.3 V, 2.8-4.5 V, and 2.8-4.5 V for pristine LiNiO₂, LiNiO₂-less B, and LiNiO₂-more B are gathered in **Table 6. 1**. In 2.8-4.3 V, the discharge capacity for the initial cycle at 0.3 C is 162.4 mAh g⁻¹, 165.6 mAh g⁻¹, and 186.5 mAh g⁻¹ for the pristine LiNiO₂, LiNiO₂-less B, and LiNiO₂-more B, respectively. The discharge capacity for the last cycle at 0.3 C after the full 100 cycles becomes 136.3 mAh g⁻¹, 128.3 mAh g⁻¹, and 139.3 mAh g⁻¹ for the pristine LiNiO₂, LiNiO₂-less B, and LiNiO₂-more B, respectively. The capacity retention with full cycles at 0.3 C was calculated to be 83.9%, 77.5%, and 74.7% for each sample between 2.8-4.3 V. This indicates that the antisolvent process with a longer time for LiNiO₂-more B can produce a more significant effect on enhancing the initial specific capacity. The higher initial specific capacity also triggered quicker capacity fading, which conforms to the general electrochemical characteristics of LiNiO₂ (Yoon et al., 2017).

In 2.8-4.5 V, the initial discharge capacities at 0.3 C for all samples are raised, which becomes 181.8 mAh g⁻¹, 192.3 mAh g⁻¹, and 202.6 mAh g⁻¹ respectively for the pristine LiNiO₂, LiNiO₂-less B, and LiNiO₂-more B. The average specific capacity increase in the first cycle between 2.8-4.5 V was approximately 20 mAh g⁻¹ for these samples relative to the cut-off voltage of 4.3 V. However, the discharge capacities for the last cycle at 0.3 C between 2.8-4.5 V are similar to those in 2.8-4.3 V with the value of 134.1 mAh g⁻¹ and 140 mAh g⁻¹ for the pristine LiNiO₂ and LiNiO₂-more B, due to the attenuated capacity retentions. Because of the overcharging possibly triggered by the local micro internal short circuit after the 87th cycle, LiNiO₂-less B exhibited a severe

fluctuation in the delivered specific capacity until complete failure. The capacity retentions were calculated to be 73.8%, 0%, and 69.1% for the pristine LiNiO₂, LiNiO₂-less B, and LiNiO₂-more B after the full 0.3 C cycling in 2.8-4.5 V.

When the cut-off voltage is increased to 4.6 V, the initial discharge capacity at 0.3 C becomes 184.6 mAh g⁻¹, 191 mAh g⁻¹, and 197.7 mAh g⁻¹ for the pristine LiNiO₂, LiNiO₂-less B, and LiNiO₂-more B, respectively. Different from all samples showing about 20 mAh g⁻¹ capacity rise after increasing the cut-off voltage from 4.3 V to 4.5 V, only the pristine LiNiO₂ appears a slight capacity rise of 2.8 mAh g⁻¹ at the first cycle at 0.3 C after increasing the cut-off voltage from 4.5 V to 4.6 V. While LiNiO₂-less B and LiNiO₂-more B appear slight capacity downs of 1.3 mAh g⁻¹ and 4.9 mAh g⁻¹ at the first cycle at 0.3 C after increasing the cut-off voltage from 4.5 V to 4.6 V. The discharge capacities for the last cycle at 0.3 C and 2.8-4.6 V are 122.9 mAh g⁻¹, 125.4 mAh g⁻¹, and 123.2 mAh g⁻¹, respectively, with the lowest values among the different cut-off voltages. The capacity retentions at the cut-off voltage of 4.6 V were also the worst, being less than 67% for all samples at the three different cut-off voltages of 4.3, 4.5, and 4.6 V. It can be concluded an operating voltage of 4.6 V can greatly accelerate the capacity decay of pristine LiNiO₂ and sol/antisolvent boron-treated LiNiO₂

Referring to the 0.3 C (54 mA g^{-1}) cycling performances of the well-formed and similar-sized SC-LNO in 2.7-4.3 V and 2.7-4.6 V as reported by Kim et al. shown in **Figure 6. 3**, the performances of 0.3 C (60 mA g^{-1}) cycling of LiNiO₂-more B in 2.8-4.3 V and 2.8-4.6 V shown in **Figure 6. 2**. are generally superior. The octahedron-shaped SC-LNO (Oct), T-poly-SC-LNO (T-poly), and cubic-SC-LNO (Cubic) exhibit different dominant surfaces or mixed surface facets (Kim et al., 2022). The active mass loading of the radially structured LiNiO₂ in this study was approximately 4 mg cm^{-2} , which was twice the active mass loading of SC-LNO ($\sim 2 \text{ mg cm}^{-2}$).

At higher active material loading and slightly higher current density, after two cycles of activation, the initial discharge capacity of LiNiO₂-more B (186.5 mAh g^{-1}) is almost the same as that of octahedron-shaped SC-LNO ($\sim 187.5 \text{ mAh g}^{-1}$) and is higher than that of T-poly-SC-LNO ($\sim 179.1 \text{ mAh g}^{-1}$) at a cut-off voltage of 4.3 V. After 100 cycles at a cut-off voltage of 4.3 V, the discharge capacity of LiNiO₂-more B was 139.3 mAh g^{-1} higher than those of octahedron-shaped SC-LNO (135 mAh g^{-1}) and T-poly-SC-LNO (120 mAh g^{-1}). The discharge capacities at the last cycle of octahedron-shaped SC-LNO and T-poly-SC-LNO achieved 96.9% and 86.1% of the value of LiNiO₂-more B at a cut-off voltage of 4.3 V. The capacity retention was also higher for LiNiO₂-more B (74.7%) than octahedron-shaped SC-LNO (72%) and T-poly-SC-LNO (67%).

A similar phenomenon was also observed for cycling between 2.8-4.6 V. After two cycles of activation, the initial capacity of LiNiO₂-more B (197.7 mAh g^{-1}) is almost the same as the values of octahedron-shaped SC-LNO ($\sim 200 \text{ mAh g}^{-1}$) and T-poly-SC-LNO ($\sim 202.4 \text{ mAh g}^{-1}$) at a cut-off voltage of 4.6 V. After 100 cycles at a cut-off voltage of

4.6 V, the discharge capacity of LiNiO₂-more B was 123.2 mAh g⁻¹, which is much higher than the values of octahedron-shaped SC-LNO (102 mAh g⁻¹) and T-poly-SC-LNO (85 mAh g⁻¹). The discharge capacities at the last cycle of octahedron-shaped SC-LNO and T-poly-SC-LNO achieved only 82.8% and 69% of the value of LiNiO₂-more B at the cut-off voltage of 4.6 V. The corresponding capacity retention was also higher for LiNiO₂-more B (62.3%) than that for octahedron-shaped SC-LNO (51%) and T-poly-SC-LNO (42%). Compared with the cubic SC-LNO, as shown in **Figure 6.3**, the performance of LiNiO₂-more B was slightly inferior, with an average of 2.6 mAh g⁻¹ and an average 2% differences in the initial discharge capacities and capacity retentions after full cycling at cut-off voltages of 4.3 and 4.6 V.

The electrochemical performance of LiNiO₂-more B is comparable to that of cubic-SC-LNO but superior to that of octahedron-shaped SC-LNO and T-poly-SC-LNO. This demonstrates that the radially arranged structure combined with the sol/antisolvent boron treatment can enable LiNiO₂ to achieve superior electrochemical performance, even better than the well-formed and similar-sized octahedron-shaped SC-LNO and T-poly-SC-LNO, especially in terms of capacity retention under a nearly similar initial discharge capacity.

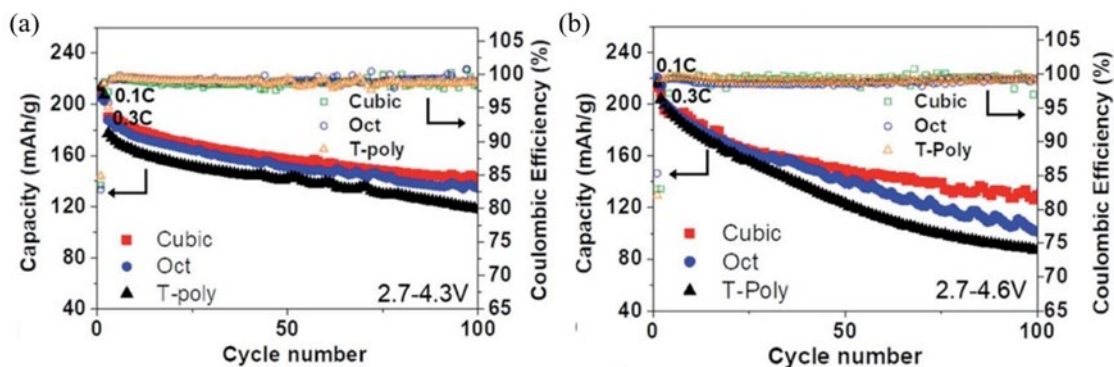


Figure 6. 3. Discharge capacity and Coulombic efficiency as a function of the cycle number from 2.7-4.3 V (a), and from 2.7-4.6 V (b) for the well-formed and similar-sized SC-LNO (Kim et al., 2022).

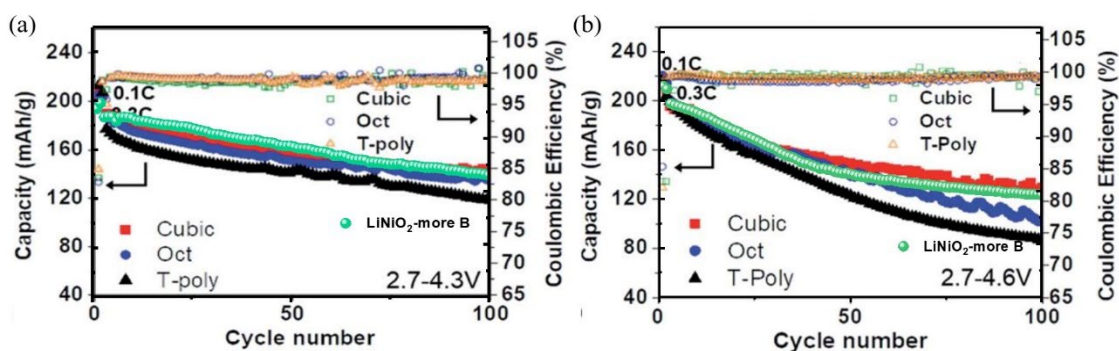


Figure 6. 4. Combined cycling data of $\text{LiNiO}_2\text{-more B}$ and the well-formed and similar-sized SC-LNO: (a) with a cut-off voltage of 4.3 V, (b) with a cut-off voltage of 4.6 V.

Figure 6. 4 combines the cycling data of $\text{LiNiO}_2\text{-more B}$ and the well-formed and similar-sized SC-LNO. The advantage of $\text{LiNiO}_2\text{-more B}$ relative to the well-formed and similar-sized octahedron-shaped SC-LNO and T-poly-SC-LNO becomes intuitive, where $\text{LiNiO}_2\text{-more B}$ delivers a higher discharge capacity at almost every cycle in long-term cycling under similar initial discharge capacities, a relatively higher current density, and a relatively higher discharge cut-off voltage. This also means that the

delithiation/lithiation kinetics of LiNiO_2 -more B are better than those of the well-formed and similar-sized octahedron-shaped SC-LNO and T-poly-SC-LNO, and even LiNiO_2 -more B, which has a higher active mass loading.

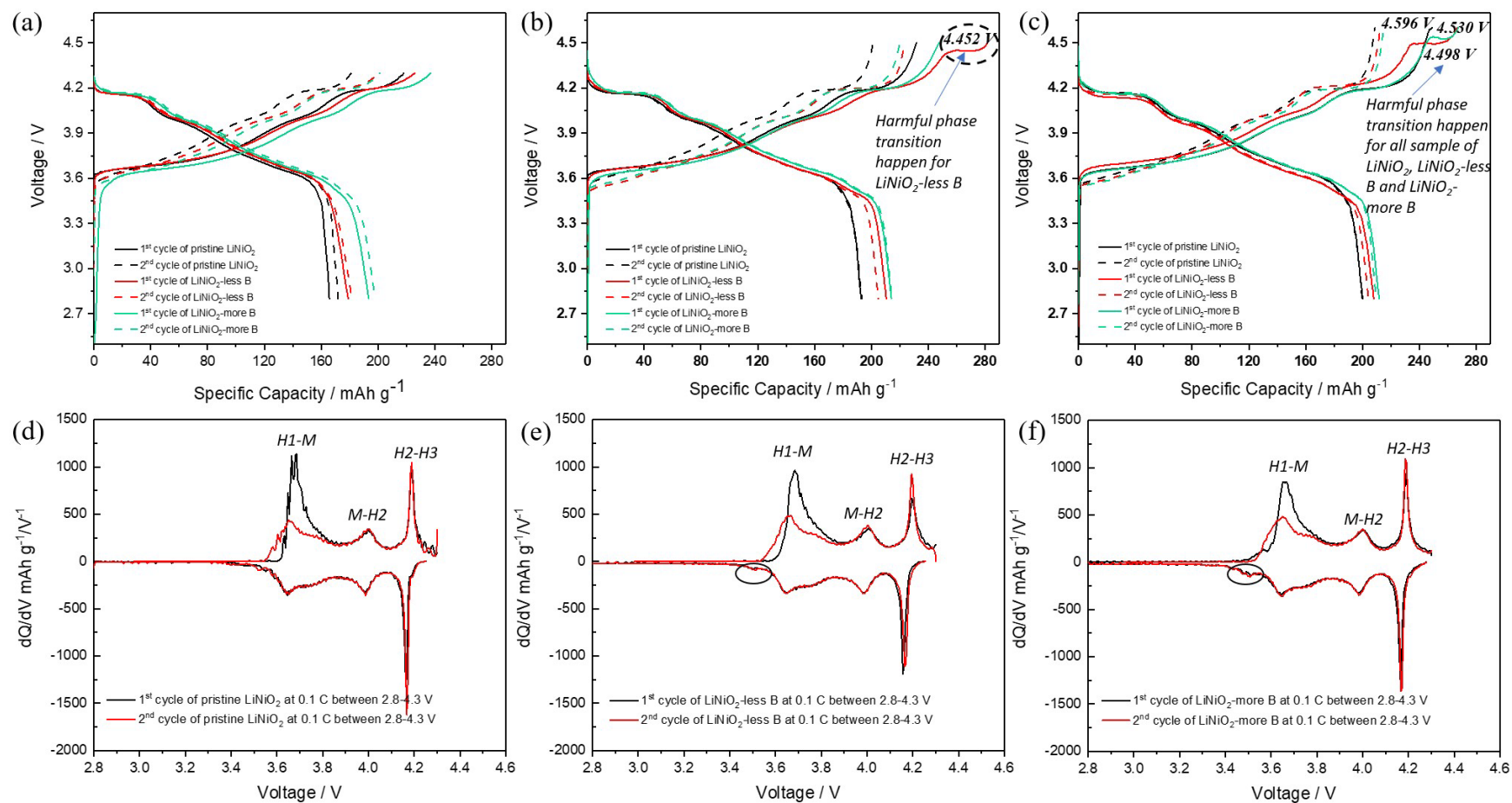


Figure 6. 5. The first and second cycles charge/discharge profiles of all samples at 0.1 C in 2.8-4.3 V(a), 2.8-4.5 V(b), and 2.8-4.6 V(c) from **Figure 6. 2** and the corresponding dQ/dV curves at 0.1 C in 2.8-4.3 V for pristine LiNiO₂(d), LiNiO₂-less B(e), and LiNiO₂-more B(f).

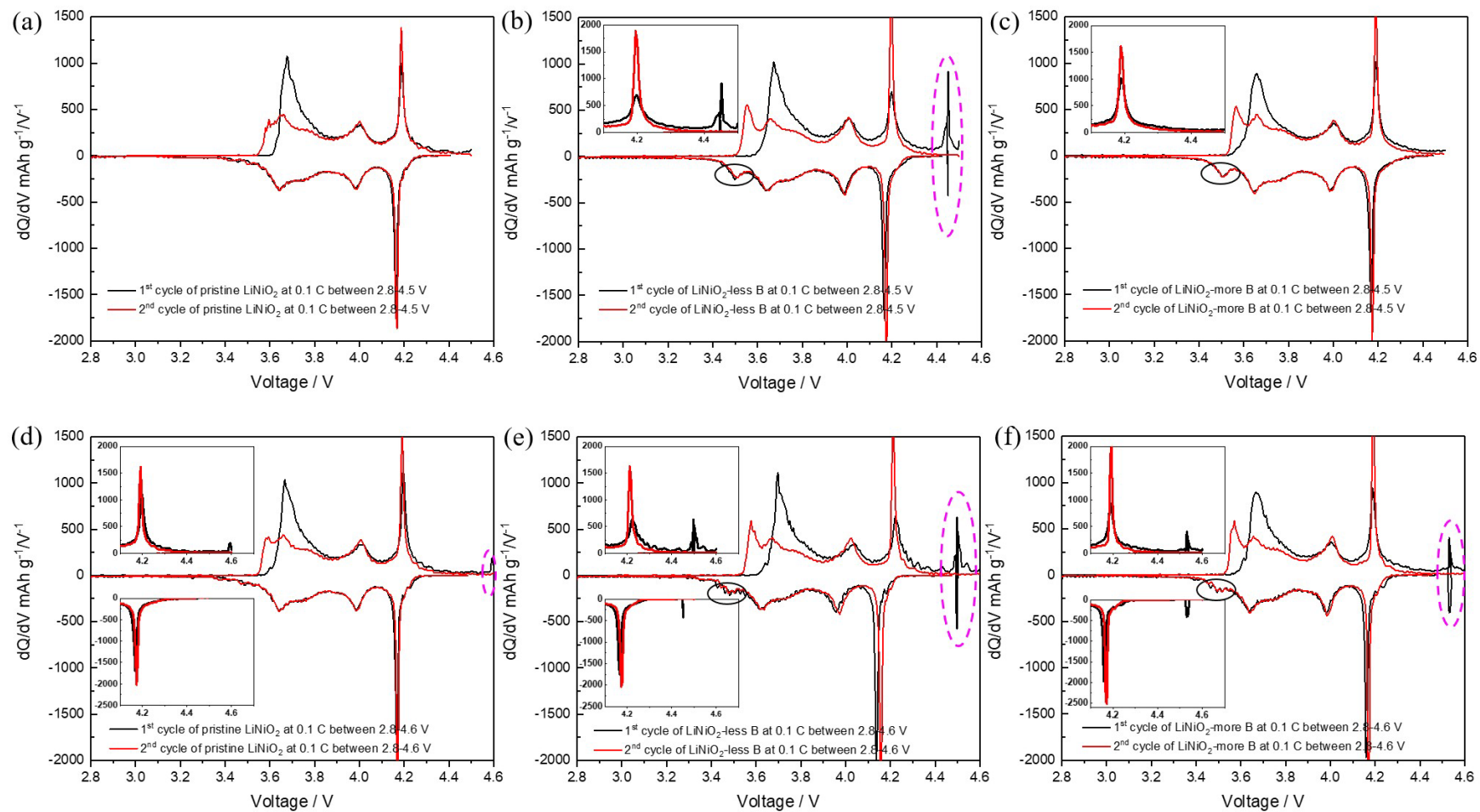


Figure 6. 6. The dQ/dV curves at 0.1 C in 2.8-4.5 V and 2.8-4.6 V: (a, d) pristine LiNiO_2 ; (b, e) LiNiO_2 -less B, and (c, f) LiNiO_2 -more B.

Figure 6. 5. (a), (b), and (c) present the first and second cycles charge/discharge profiles of pristine LiNiO₂, LiNiO₂-less B, and LiNiO₂-more B at 0.1 C in 2.8-4.3 V, 2.8-4.5 V, and 2.8-4.6 V separately from the activation region of 0.3 C cycling test in **Figure 6. 2**.

According to **Figure 6. 5.** (a), the charging capacity at the first cycle at 0.1 C is 218.1 mAh g⁻¹, 226.1 mAh g⁻¹, and 237.2 mAh g⁻¹ respectively for pristine LiNiO₂, LiNiO₂-less B, and LiNiO₂-more B in 2.8-4.3 V, along with the initial Coulombic efficiency (ICE) of 76%, 79.21%, and 81.58% for each sample. The highest ICE and charging capacity in the first cycle in the voltage range of 2.8-4.3 V can be considered responsible for the highest discharge capacity delivered by LiNiO₂-more B.

When the cut-off voltage was increased to 4.5 V, a new voltage plateau around 4.452 V appeared for LiNiO₂-less B, as shown in **Figure 6. 5.** (b). This harmful phase transition should be the direct reason for the quickest capacity degradation of LiNiO₂-less B at 0.3 C cycling with 0.1 C activations in the voltage range of 2.8-4.5 V, since such phenomenon does not happen for pristine LiNiO₂ and LiNiO₂-more B in 2.8-4.5 V. The emergence of such phase transition can also be considered as a reason leading to the accelerated capacity fading for all samples between 2.8-4.6 V, because of the detection of such harmful phase transition above 4.4 V for all samples as shown in **Figure 6. 5.**

(c). The corresponding voltages for these phase transitions are indicated. For pristine LiNiO₂, the plateau voltage value of this harmful phase transition is 4.596 V higher than that of 4.530 V for LiNiO₂-more B and 4.498 V for LiNiO₂-less B. The width of the platform on that phase transition was the longest for the LiNiO₂-less B. The lowest phase transition voltage and the deepest phase transition degree imply such harmful phase

transition can easily occur for LiNiO₂-less B than the other two samples of pristine LiNiO₂ and LiNiO₂-more B. However, the fastest capacity decaying in 2.8-4.6 V is LiNiO₂-more B rather than LiNiO₂-less B, mainly because not only the phase transition above 4.4 V detrimental to the performance of LNO samples but also H₂–H₃ phase transition at about 4.2 V can deteriorate the performance of LNO samples. This is because the H₂–H₃ phase transition induces sharp shrinkage of the unit cell along with high stains in the material of LNO, which can easily produce microcracks and weaken the structural stability of LNO (Xu et al., 2020).

The differential capacity analysis (dQ/dV) curves of the first and second cycles charge/discharge profiles of all samples at 0.1 C in 2.8-4.3 V are shown in **Figure 6. 5.** (d) for pristine LiNiO₂, **Figure 6. 5.** (e) for LiNiO₂-less B, and **Figure 6. 5.** (f) for LiNiO₂-more B. Three pairs of redox peaks corresponding to H₁–M, M–H₂, and H₂–H₃ phase transitions can be identified for all samples. “H” represents hexagonal phases and “M” represents monoclinic phases. According to **Figure 6. 5.** (d), (e), and (f), the charge/discharge degree at phase transitions of H₁ → M → H₂ → H₃ becomes increasingly deeper from the pristine LiNiO₂ to LiNiO₂-less B and then to LiNiO₂-more B along with the larger and larger areas under the differential capacity analysis curves. Meanwhile, the capacity from the redox reactions at 3.5 V can be extracted after the sol/antisolvent boron treatment of LiNiO₂-less B and LiNiO₂-more B with the appearance of a small peak, as indicated by the black circles in **Figure 6. 5.** (e) and (f), which cannot be observed in the pristine LiNiO₂ (**Figure 6. 5.** (d)). Other research suggests that the disappearance of the 3.5 V plateau of LNO can be ascribed to a

kinetically sluggish process (Kim et al., 2022). Our findings reveal that both LiNiO₂-less B and LiNiO₂-more B can better activate the redox process in this region at about 3.5 V than the pristine LiNiO₂. The dQ/dV curves at 0.1 C in 2.8-4.5 V and 2.8-4.6 V of pristine LiNiO₂, LiNiO₂-less B, and LiNiO₂-more B are presented in **Figure 6. 6** in two rows. The first row presents the dQ/dV curves of different samples at 0.1 C in 2.8-4.5 V, the second row presents the dQ/dV curves of different samples at 0.1 C in 2.8-4.6 V. Likewise, it can be found that the small peak in the dQ/dV curves corresponding to the 3.5 V plateau appears for LiNiO₂-less B (**Figure 6. 6.** (b) and (e)), and LiNiO₂-more B (**Figure 6. 6.** (c) and (f)), but not for the pristine LiNiO₂ (**Figure 6. 6.** (a) and (d)). These data in 2.8-4.5 V and 2.8-4.6 V further confirm that sol/antisolvent boron treatment of LiNiO₂-less B and LiNiO₂-more B can enhance the kinetic of the delithiation/lithiation process of LNO material with delivering more specific capacities.

The redox peaks corresponding to the phase transition above 4.4 V of all samples can be easily distinguished in **Figure 6. 6**, which are circled by the dotted pink lines in **Figure 6. 6.** (b), (d), (e), and (f). To better compare the differences in the phase transitions above 4.1 V, zoomed-down images of the redox peaks in that region are shown in **Figure 6. 6**. It seems that the emergence of the new phase transition at 4.452 V of LiNiO₂-less B in the first cycle at 0.1 C can greatly enhance the peak intensity of the H2–H3 phase transition in the second cycle at 0.1 C as shown in **Figure 6. 6.** (b). The enhanced H2–H3 phase transition intensity of LiNiO₂-less B was even higher than that of LiNiO₂-more B in the second cycle in 2.8-4.5 V as shown in **Figure 6. 6.** (c). The speculation on the negative effect of the last phase transition above 4.4 V on the H2–H3

phase transition is further confirmed by the test in 2.8-4.6 V, where the peak intensity of H2–H3 phase transition at the second cycle of LiNiO₂-more B becomes much stronger after the appearance of the harmful phase transition at 4.53 V as shown in **Figure 6. 6.** (f). The peak intensity of the H2–H3 phase transition at the second cycle for LiNiO₂-more B reaches 2000 mAh g⁻¹/V⁻¹ (**Figure 6. 6.** (f)) at the cut-off voltage of 4.6 V much higher than that of LiNiO₂-more B at the cut-off voltage of 4.5 V around 1500 mAh g⁻¹/V⁻¹ (**Figure 6. 6.** (c)). The curves for the pristine LiNiO₂ are shown in **Figure 6. 6.** (a) and (d), the emergence of the harmful phase transition at 4.596 V also strengthens H2–H3 phase transition in the second cycle, with a peak of intensity over 1500 mAh g⁻¹/V⁻¹ (**Figure 6. 6.** (d)) at the cut-off voltage of 4.6 V higher than the sample at the cut-off voltage of 4.5 V with the intensity of lower than 1500 mAh g⁻¹/V⁻¹ (**Figure 6. 6.** (a)).

Although LiNiO₂-less B presents the highest peak intensity for the last phase transition among the three samples between 2.8-4.6 V, this harmful phase transition cannot be regarded as the only factor inducing the performance decay. The combined effect of the H2–H3 phase transition at about 4.2 V and the newly emerged phase transition at the voltage over 4.4 V jeopardizes the cycling stability of LNO material. For LNO material, the newly emerged last phase transition is the H3–H4 phase transition when extremely slow charging to 4.45 V (Xu et al., 2020). H4 is another hexagonal phase formed when LNO approaches the fully delithiated state. It has been suggested that crystallites closest to the ideal stoichiometry form an H4 phase that is stable at high potential, while others lead to an H4 phase that transforms into the H3' phase through Ni migration from the slab to the inter-slab space, thus making part of the material inactive and affecting the

overall reversibility of the material (Bianchini et al., 2019). In this study, because of impurity elements and the addition of the boron, the synthesised LNO cannot have the ideal stoichiometry of LNO, and the H3–H4 phase transition only occurs in the first cycle and disappears in the second cycle as shown in **Figure 6. 6.** (b), (d), (e), and (f), precisely due to the unstable H4 phase irreversibly transforms to a related hexagonal one called H3' through Ni³⁺ migration into the inter-slab. Furthermore, for samples with an anti-site defect concentration greater than 7%, the H3–H4 phase transition in LNO can no longer be observed, and the observations of the H3–H4 phase transition of LNO materials are rare (Xu et al., 2020). This also implies that the synthesised LNO materials in this study had fewer anti-site defects.

The dQ/dV curves demonstrate that after sol/antisolvent boron treatment, LiNiO₂-less B and LiNiO₂-more B can activate the redox process in 3.5 V region, along with more delivered specific capacity. Regarding the structure and cycling stability of the material, it is necessary to prevent the occurrence of the H3–H4 phase transition because such a phase transition can enhance the intensity of another harmful phase transition of H2–H3. The combination of these two harmful phase transitions can worsen the cycling stability of the LNO materials. Beyond the appearance of the H3→H4 transition in itself is extremely detrimental to the structural stability as it requires a gliding of the transition metal slab with the results of stacking faults (Xu et al., 2020), the report about the occurrence of H3–H4 phase transition can strengthen the intensity of the H2–H3 phase transition through the analysis of dQ/dV curves is very rare to the best of our knowledge.

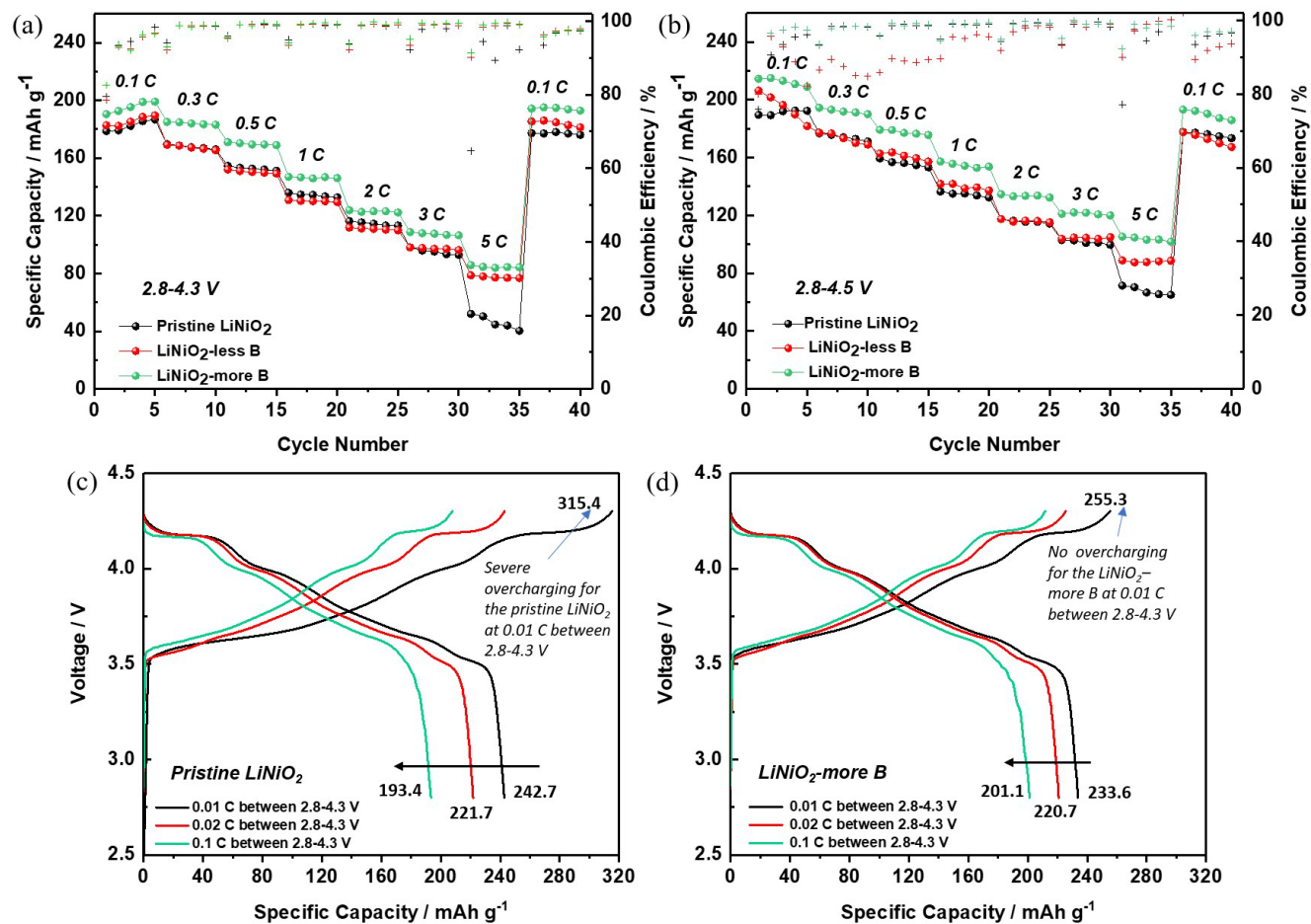


Figure 6. 7. (a) Rate performances of pristine LiNiO_2 , LiNiO_2 -less B, and LiNiO_2 -more B between 2.8-4.3 V; (b) Rate performances of pristine LiNiO_2 , LiNiO_2 -less B, and LiNiO_2 -more B between 2.8-4.5 V; (c) Charge/discharge curves at 0.01 C, 0.02 C, and 0.1 C between 2.8-4.3 V for pristine LiNiO_2 ; (d) Charge/discharge curves at 0.01 C, 0.02 C, and 0.1 C between 2.8-4.3 V for LiNiO_2 -more B.

Furthermore, the rate performances are carried out for the pristine LiNiO₂, LiNiO₂-less B, and LiNiO₂-more B between 2.8-4.3 V and 2.8-4.5 V with every five cycles at 0.1 C, 0.3 C, 0.5 C, 1 C, 2 C, 3 C, 5 C, and back to 0.1 C. The corresponding results are shown in **Figure 6. 7.** (a) and (b). It can be seen that, compared with the pristine LiNiO₂, both LiNiO₂-less B and LiNiO₂-more B exhibit better rate capabilities. In particular, LiNiO₂-more B delivered the highest discharge capacity at each current density in both 2.8-4.3 V and 2.8-4.5 V. This means that the rate performance can be enhanced after sol/antisolvent boron treatment. LiNiO₂-more B showed the best rate property among all the samples.

The excellent rate capability of LiNiO₂-more B is also reflected at smaller current densities. **Figure 6. 7.** (c) and (d) present the charge/discharge test with the current density of 0.01 C, 0.02 C, and 0.1 C for the pristine LiNiO₂ and LiNiO₂-more B, separately. For LiNiO₂-more B, the smaller polarisation and overpotential make the discharge curves close to each other, and a relatively high discharge capacity of 201.1 mAh g⁻¹ at 0.1 C can be delivered by LiNiO₂-more B after the charge/discharge cycles at 0.01 C and 0.02 C. In contrast, pristine LiNiO₂ delivers a discharge capacity of 193.4 mAh g⁻¹ at 0.1 C even with an initial discharge capacity of 242.7 mAh g⁻¹ at 0.01 C. The initial discharge capacity of LiNiO₂-more B at 0.01 C is 233.6 mAh g⁻¹ lower than the pristine LiNiO₂, but no overcharging is observed for LiNiO₂-more B, and the ICE at 0.01 C of LiNiO₂-more B is 91.5% much higher than the ICE of 76.9% for pristine LiNiO₂ at 0.01 C.

In summary, the radial polycrystalline structure combined with the sol/antisolvent boron

treatment is beneficial for delivering high specific capacity, high cycling stability, and enhanced rate capability of LNO material. Even at a higher active mass loading and slightly higher current density, the cycling stability of LiNiO₂-more B is better than that of the well-formed and similar-sized SC-LNO (octahedron-shaped SC-LNO and T-poly-SC-LNO) and is comparable to the optimised cubic-SC-LNO reported by other researchers (Kim et al., 2022). The effect of boron addition on the crystal structure and material morphology of the intrinsic radially structured LNO is discussed in the following material characterisation.

6.3.2. Exploring the Origin of Different Electrochemical Performances for LiNiO₂, LiNiO₂-less B, and LiNiO₂-more B

The crystal structures of pristine LiNiO₂, LiNiO₂-less B, and LiNiO₂-more B were identified using XRD analysis. The results are shown in **Figure 6. 8.** (a), (b), and (c) for each sample. All main peaks matched well with the standard pattern of α -NaFeO₂ layered structure with $R\bar{3}m$ LiNiO₂ (JCPDS No. 09-0063). According to the information of JCPDS No. 09-0063, the diffraction peaks at 18.785°, 36.649°, 38.100°, 38.268°, 44.369°, 48.873°, 58.763°, 64.476°, 64.727°, 68.027°, 76.734°, 77.547° are corresponded to (003), (101), (006), (012), (104), (015), (107), (018), (110), (113), (021), and (116) facets of the hexagonal LiNiO₂. Beyond the main diffraction peaks coinciding with the α -NaFeO₂ layered structure of LiNiO₂, small amounts of impurities (LiCO₃ and NiO) were also detected for all LNO samples by comparing the JCPDS data (Song et al., 2006), as shown in **Figure 6. 8.** (a) for pristine LiNiO₂. This is because the excess

lithium source is used for synthesising the LNO material, which produces by-products of Li_2CO_3 in the atmosphere. Pure stoichiometric LiNiO_2 is difficult to synthesise because of lithium vacancies compensated by excess nickel within the lithium layer, which contains a certain amount of inactive cubic phase (Kalyani and Kalaiselvi, 2005, Moses et al., 2007).

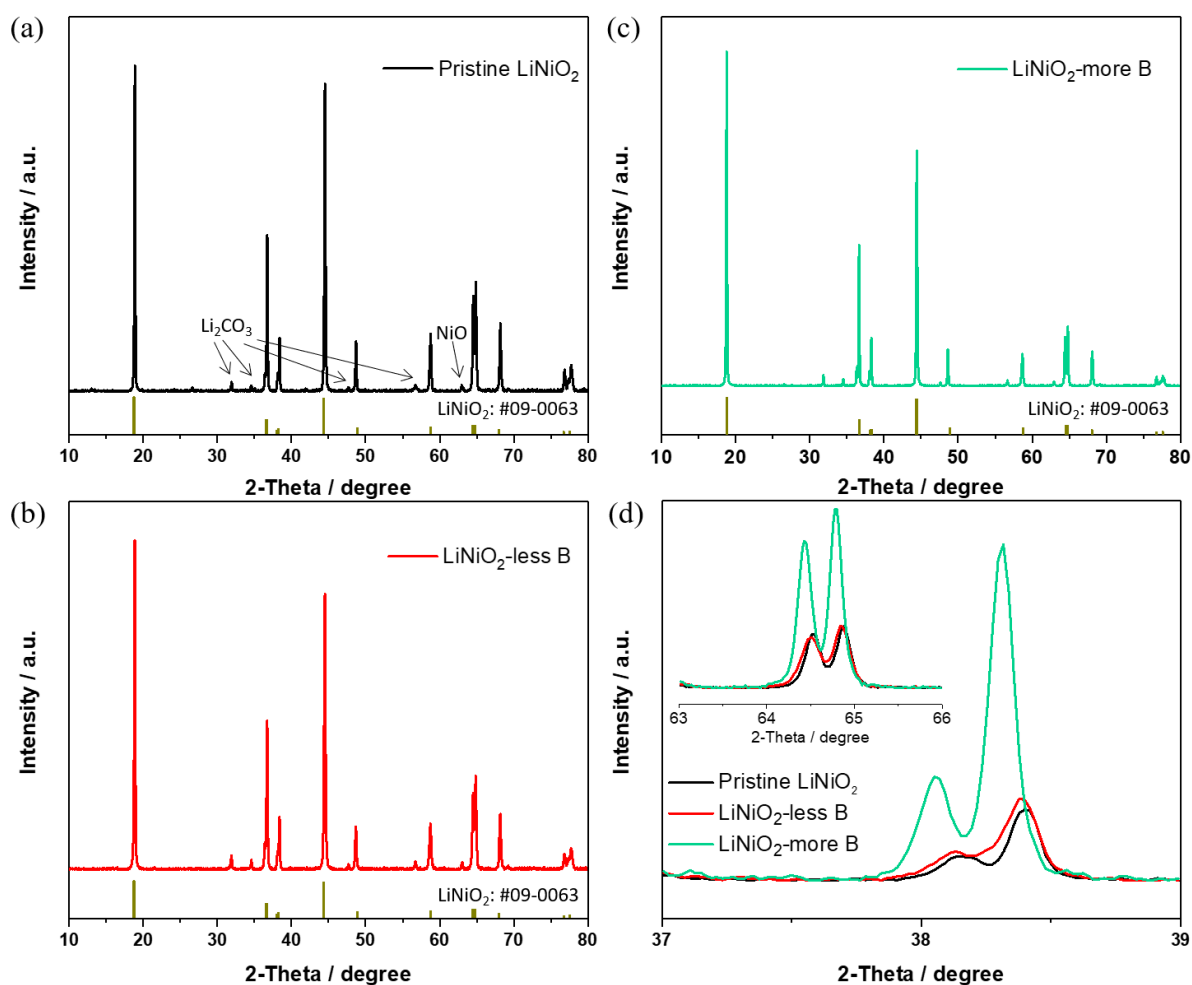


Figure 6. 8. XRD patterns of (a) pristine LiNiO_2 , (b) LiNiO_2 -less B, (c) LiNiO_2 -more B, and (d) enlarged XRD patterns of all LNO samples in 2-Theta ranges of 37° to 39° and 63° to 66° .

Table 6. 2. I(003)/I(104) ratio of pristine LiNiO₂, LiNiO₂-less B, and LiNiO₂-more B.

Sample	Pristine LiNiO ₂	LiNiO ₂ -less B	LiNiO ₂ -more B
I(003)/I(104)	1.06	1.2	1.42

The intensity ratio of (003)/(104) peaks (I(003)/I(104)) of the XRD spectrum can also be used as a criterion to show the level of Li/Ni disordering in the LNO material. The lower intensity of the (003) peaks is likely a result of lower lithium availability triggered by an increased degree of cation mixing (Yuwono et al., 2023). The intensity ratio of (003)/(104) peaks should be more than 1.2 to enhance the electrode performance of LNO material (Lee et al., 1999). The calculated I(003)/I(104) ratios for the pristine LiNiO₂, LiNiO₂-less B, and LiNiO₂-more B are listed in **Table 6. 2** with values of 1.06, 1.2, and 1.42, respectively.

The I(003)/I(104) ratio of pristine LiNiO₂ is the lowest and is lower than the threshold of 1.2, which means that pristine LiNiO₂ suffers from the highest extent of cation mixing. The lowest initial specific capacity and the best capacity retention of the pristine LiNiO₂ at 0.3 C cycling as listed in **Table 6. 1** can be attributed to this reason. This is because the redox active Ni in the transition metal layer, which contributes to the capacity of the material, decreases owing to its migration to the lithium layer. Meanwhile, the side reactions between the active material and electrolyte can be mitigated by less Ni⁴⁺ catalysis, leading to more stable cycling (Xue et al., 2020). On the other hand, the highest initial specific capacity along with the reduced capacity retention of LiNiO₂-more B at 0.3 C cycling as listed in **Table 6. 1** can be attributed to the best Li/Ni ordering, since such a well-ordered structure can provide more redox-active Ni, but also triggers

more side reactions because of the catalytic activity of Ni^{4+} . LiNiO_2 -less B is at a median level with respect to the initial specific capacity and capacity retention at 0.3 C cycling owing to the middle value of the I(003)/I(104) ratio.

Figure 6. 8. (d) presented the enlarged XRD patterns of two speaks of (006) and (102) facets for all LNO samples in the 2-Theta range of 37° to 39° , as well as the two peaks of (108) and (110) facets for all LNO samples in the 2-Theta range of 63° to 66° as an insert. The splittings of (006)/(102) peak and (108)/(110) peak are much clearer for LiNiO_2 -more B than pristine LiNiO_2 and LiNiO_2 -less B. This also suggests the cation mixing of LiNiO_2 -more B is the lowest among the three samples. Moreover, the peaks of the (006) and (102) facets shifted to a lower degree in the sequence of pristine LiNiO_2 to LiNiO_2 -less B and then to LiNiO_2 -more B. The same trend of peak shift can also be detected for the peaks of the (108) and (110) facets. This shift is due to doping (Amalraj et al., 2021). The lower degree shift indicates the expansion of the unit cell volume by doping boron (B) at the interstitial site of the packed oxygen in the nickel and lithium layers. The lower the degree, the more B doping occurs at the interstitial site with the bond to oxygen in tri- or tetra-coordination (Chen et al., 2018). The XRD analysis demonstrated that boron was successfully incorporated into the lattice of the LNO material, and LiNiO_2 -more B was subjected to a greater amount of boron doping owing to the longer antisolvent treatment time. A higher amount of B-doping can achieve a better degree of Li/Ni ordering in the LNO material.

Figure 6. 9 presents the SEM surface images of the three LNO samples and Ni(OH)₂ precursor at different magnifications. **Figure 6. 9.** (a1-a3) are the images of pristine LiNiO₂ with different scale bars. The surfaces of the primary particles of pristine LiNiO₂ appeared relatively rounded (**Figure 6. 9.** (a1)). The primary particles were very close to each other with good fusion, as shown in **Figure 6. 9.** (a2). Such a dense surface can help prevent the electrolyte from infiltrating the particle's interior, thus reducing the side reactions between the active material and the electrolyte. The best capacity retention of the pristine LiNiO₂ at 0.3 C cycling can also be correlated to the dense surface of the material.

SEM surface images of LiNiO₂-less B and LiNiO₂-more B are shown in **Figure 6. 9.** (b1-b3) and (c1-c3), respectively, which are completely different from those pristine LiNiO₂. LiNiO₂-less B and LiNiO₂-more B show clear crystal planes with edges and corners on the surface of the primary particles, such developed morphology is the same as the B-doped LiNi_{0.86}Co_{0.08}Mn_{0.06}O₂ samples reported by other people (Chen et al., 2023). Density functional theory calculations based on a model structure of LiNiO₂ demonstrate that the surface energy of the (003) facet of B-doped LNO is much lower than that of non-B-doped LNO; therefore B doping tends to expose the (003) crystal plane in stable crystals with a flat shaped crystal structure (Chen et al., 2023). Meanwhile, the size of the primary particles of LiNiO₂-less B and LiNiO₂-more B became much smaller than that of the primary particles of pristine LiNiO₂, as shown in **Figure 6. 9.** The geometry (shape and size) of the primary particles of LNO can be refined by boron doping. Furthermore, comparing **Figure 6. 9.** (b1) and (c1), the aspect

ratio of the primary particles of LiNiO₂-more B is larger than LiNiO₂-less B, due to more amounts of boron doping. The crystallinity of the primary particles changed after the sol/antisolvent boron treatment, showing the image of the well-crystallised primary particles with clear crystal planes with edges and corners: more gaps emerged among the primary particles of LiNiO₂-less B and LiNiO₂-more B than the pristine LiNiO₂. Such structure can accelerate electrolyte infiltrating into the interior of the particle through the gaps, the contact surfaces between the active material and the electrolyte can also be increased, which can provide more chances for the side reactions, being a factor to the weakened capacity retentions of LiNiO₂-less B and LiNiO₂-more B.

Figure 6. 9. (d1-d3) presents the SEM surface images of Ni(OH)₂ precursor at different magnifications. The size of the primary particles of the pristine LiNiO₂ (**Figure 6. 9. (a2)**) is much larger than that of the Ni(OH)₂ precursor (**Figure 6. 9. (d2)**). The primary particles of the LiNiO₂-less B (**Figure 6. 9. (b2)**) and LiNiO₂-more B (**Figure 6. 9. (c2)**) approached the size of the primary particles of the Ni(OH)₂ precursor (**Figure 6. 9. (d2)**), which demonstrates again that boron doping can inhibit the growth of primary particle in the calcination process. Meanwhile, some of the small spherical particles with a diameter of less than 1 μm adhered on the outside surface of the secondary particles of all LNO samples, as shown in **Figure 6. 9. (a3)**, **(b3)**, and **(c3)**, these particles were the smaller-sized LNO material since there are many smaller-sized Ni(OH)₂ particles in the precursors, as shown in **Figure 6. 1. (a)**. The adhered smaller-sized LNO particles, looking like the island coatings, disrupt the continuity of the entire conductive network of the cathode electrode, which is not beneficial for the electrochemical performance of

the battery. It can be speculated that better performance in terms of specific capacity and capacity retention would be achieved using the uniform-sized radially structured precursor than the non-uniform-sized ones.

Figure 6. 10 presents the SEM cross-sectional images of the three LNO samples and Ni(OH)₂ precursor at different magnifications. The primary particles in the cross-sectional region exhibited the same variations as the primary particles located on the surface of the LNO samples. After sol/antisolvent boron treatment, LiNiO₂-less B (**Figure 6. 10. (b1)**) and LiNiO₂-more B (**Figure 6. 10. (c1)**) also show clear crystal planes of the primary particles at the cross-section, which is completely different from the rounded surface of the primary particles of the pristine LiNiO₂ with the image shown in **Figure 6. 10. (a1)**. The sizes of the primary particles of LiNiO₂-less B and LiNiO₂-more B are much smaller than those of pristine LiNiO₂ at the cross-section. All LNO samples inherited the radially aligned structure from the precursor as shown in **Figure 6. 10. (a2), (b2), (c2), and (d2)**.

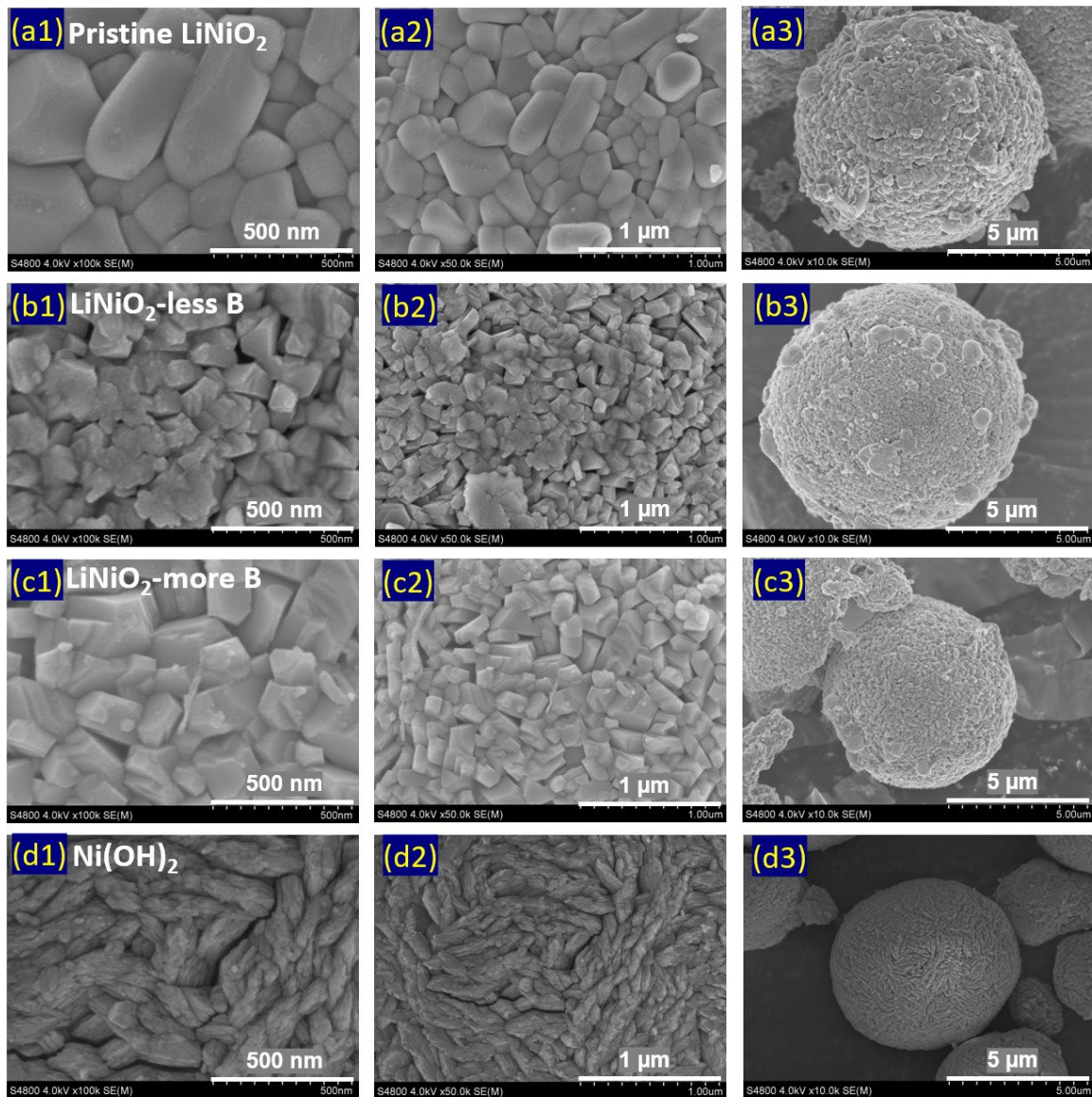


Figure 6. 9. SEM images: (a1-a3) surface images of pristine LiNiO_2 at different magnifications; (b1-b3) surface images of LiNiO_2 -less B at different magnifications; (c1-c3) surface images of LiNiO_2 -more B at different magnifications; and (d1-d3) surface images of Ni(OH)_2 precursor at different magnifications.

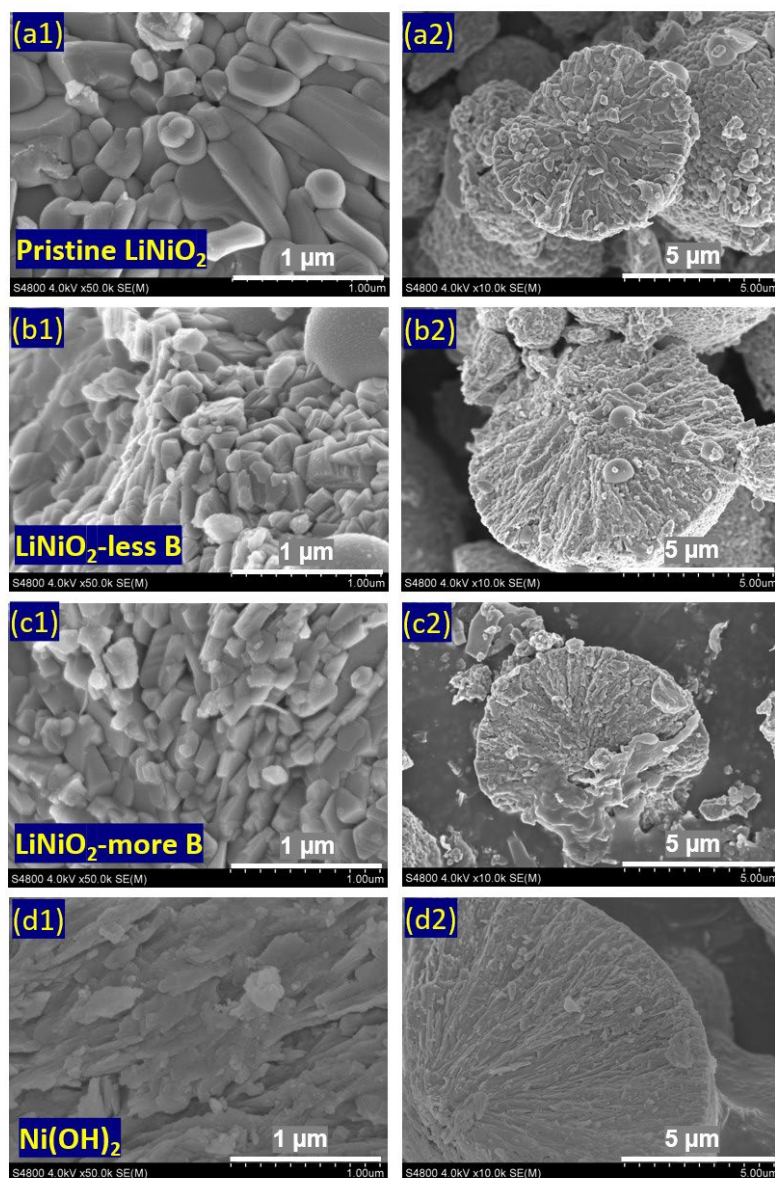


Figure 6. 10. SEM images: (a1-a2) cross-section images of pristine LiNiO_2 at different magnifications; (b1-b2) cross-section images of LiNiO_2 -less B at different magnifications; (c1-c2) cross-section images of LiNiO_2 -more B at different magnifications; and (d1-d2) cross-section images of Ni(OH)_2 precursor at different magnifications.

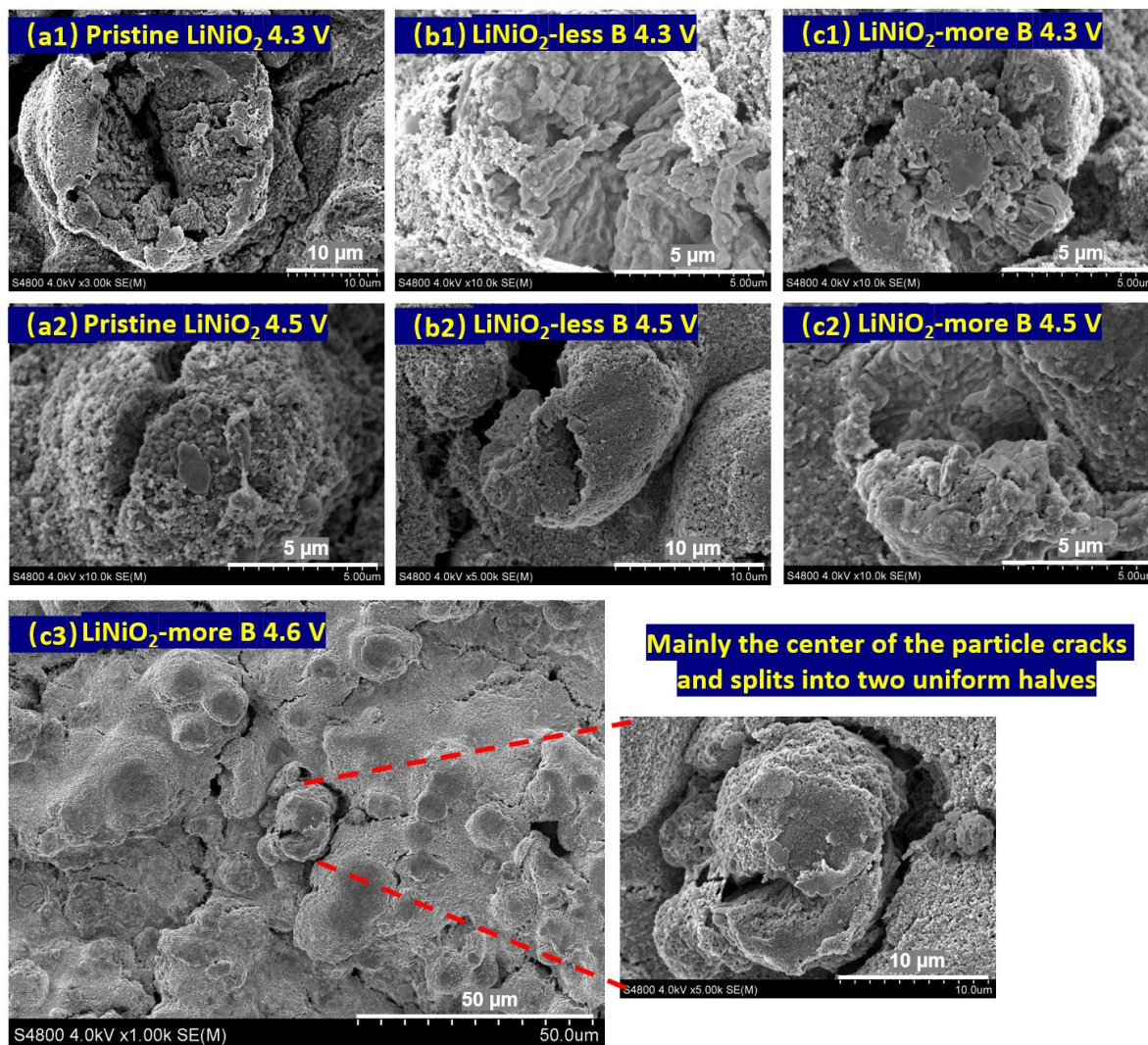


Figure 6. 11. The cracked particles after 0.3 C cycling of LNO cathode: (a1, a2) pristine LiNiO_2 at the cut-off voltage of 4.3 V and 4.5 V; (b1, b2) LiNiO_2 -less B at the cut-off voltage of 4.3 V and 4.5 V; (c1, c2, c3) LiNiO_2 -more B at the cut-off voltage of 4.3 V, 4.5 V and 4.6 V.

Figure 6. 11 presents cracked particles after 0.3 C cycling of the pristine LiNiO_2 , LiNiO_2 -less B, and LiNiO_2 -more B cathodes. **Figure 6. 11.** (a1, a2), (b1, b2), and (c1, c2) correspond to the pristine LiNiO_2 at the cut-off voltage of 4.3 V and 4.5 V, LiNiO_2 -less B at the cut-off voltage of 4.3 V and 4.5 V, and LiNiO_2 -more B at the cut-off voltage of 4.3 V and 4.5 V, respectively. It can be found that, beyond the sample in **Figure 6. 11.**

(c1) appearing the rupture like the opening of the flower with discrete cracks, all other samples in **Figure 6. 11.** (a1, a2), (b1, b2), and (c2) suffer centre cracking, which causes the particles to split into two uniform halves. Similarly, a sample of LiNiO₂-more B at the cut-off voltage of 4.6 V as shown in **Figure 6. 11.** (c3) also suffers rupture from the centre, with the entire particle being divided into two halves. This observation implies that the stress, which is induced by the anisotropic volume change during Li-ion extraction/insertion, is concentrated mainly in the centre of the secondary particles of the radially structured LNO material. The centre of such LNO materials can be considered as the mechanically weakest part of the entire particle. A radially aligned structure with a hole in the centre may be a good way to alleviate such stress concentration and reduce cracking (Kalluri et al., 2020). Undoubtedly, the high intensity of the phase transition of H2–H3 in the images shown in **Figure 6. 5** and **Figure 6. 6** is responsible for such high degree of cracking of LNO materials.

6.4. Conclusion

Sol/antisolvent boron treatment and subsequent lithiation calcination have been utilised to produce ordered and well-crystallised primary particles for LNO materials. LiNiO₂-more B is subjected to a longer antisolvent boron treatment time, resulting in more boron doping than LiNiO₂-less B, as reviewed by the XRD analysis. Comparing the three samples of pristine LiNiO₂, LiNiO₂-less B, and LiNiO₂-more B, LiNiO₂-more B exhibits the best Li/Ni ordering, which can provide the largest amount of redox-active Ni, which is a positive factor for achieving the highest specific capacity and rate

capability. Analysis of the dQ/dV curves implies that LiNiO_2 -less B and LiNiO_2 -more B with boron doping can better activate the redox process, which is beneficial for delivering a higher specific capacity than pristine LiNiO_2 . At a higher active material loading, the superior performances of LiNiO_2 -more B in terms of specific capacity and capacity retention compared to the well-formed and similar-sized single-crystal LiNiO_2 reflects the advantage of the radically arranged and B-doped polycrystalline LNO material. The harmful H3–H4 phase transition above 4.4 V can enhance the intensity of the H2–H3 phase transition. It is necessary to avoid or inhibit the harmful phase transitions of H2–H3 and H3–H4 at high voltages.

Chapter 7 Conclusions and Prospects

The research objective of this thesis is to modify and characterise Ni-rich layered oxide (NLO) cathodes for advanced LIBs for EVs applications. This chapter summarises the conclusions of each experimental study and discusses the prospects for future work.

7.1. Conclusions

In this thesis, a novel sol/antisolvent method is developed to modify different NLO materials. The importance of developing NLO with stoichiometric ratios of $\text{Ni} \geq 0.8$ as the dominant cathode material of LIBs for next-generation passenger EVs, is first highlighted in **Chapter 1**. The mechanism of the performance degradation of NLO and the current proposed strategies to strengthen its electrochemical performance are reviewed in **Chapter 2**. The studies in **Chapter 1** and **Chapter 2** aim to understand NLO as a critical material for high-energy LIBs and cultivate meaningful modification works to develop NLO as a superior cathode material for LIBs for EVs applications. After the materials and equipment of the thesis are introduced in **Chapter 3**, **Chapters 4, 5, and 6** present novel and effective modifications of different NLO materials along with the corresponding results and discussions. With the assistance of the developed sol/antisolvent modification method, different kinds of NLO materials with stoichiometric ratios of $\text{Ni} > 0.8$ achieve better electrochemical properties in this thesis. The conclusions of each experimental study on different NLO materials in this thesis are summarised.

In **Chapter 4**, a fast and convenient sol/antisolvent wet coating is developed to achieve nanocrystalline LiBO₂ coating of LiNi_{0.85}Co_{0.1}Mn_{0.05}O₂ in an anhydrous environment.

The conclusions of this work are listed as follows:

- (1) Compared with conventional sol/gel coating and solvent/antisolvent coating, a homogeneous coating layer can be easily realised using a novel sol/antisolvent coating. There are four main advantages of sol/antisolvent coating: the aqueous environment is avoided, coating with different morphologies is available, no high-temperature evaporation occurs, and the coating thickness can be tuned by changing the antisolvent dosage.
- (2) The coating layer was confirmed to be an α - and γ -mixed LiBO₂. Owing to such coating modification, the modified battery exhibits a high ICE and better fast charging ability. The smaller polarisation, strengthened electrochemical reversibility of the H1–M phase transition, depressed H2–H3 phase transition, and enhanced Li-ion diffusion coefficient in the electrode are the reasons for the improved battery performance.
- (3) Beyond the uniform LiBO₂ nano-spherical particle coating, bandage-like LiBO₂ nanorods also deposit on the intrinsic crack, so a double protection against electrolytes is built. The predominant problem of microcracks during the cycling of PC-NLO was also effectively alleviated by such a sol/antisolvent nano LiBO₂ coating.
- (4) The proposed nanoparticle dispersion and aggregation by the sol/antisolvent method for the wet coating of an NLO cathode was demonstrated to be feasible.

In **Chapter 5**, a sol/antisolvent B_2O_3 coating is applied for the precursor of $LiNi_{0.83}Co_{0.05}Mn_{0.12}O_2$ with a daisy-like structure, followed by lithiation calcination to realise the combined boron-related coating and doping with the intrinsic radially aligned structure. The conclusions of this work are listed as follows:

- (1) In the lithiation calcination process, the four factors of good crystallinity with an ordered layered structure, clean surface without obvious lithium residues, reduced gaps among primary particles, and daisy-like radially aligned structures were identified as important factors for achieving a high discharge capacity (≥ 200 mAh g^{-1}) at a cut-off voltage of 4.3 V.
- (2) A high discharge capacity can be considered an important indicator for the preparation of superior NLO materials. The modified NLO named Daisy-Ni83-Bthin and Daisy-Ni83-Bmiddle with a special radially aligned structure and the combined boron-related coating and doping can deliver extremely high discharge capacities of over 220 mAh g^{-1} at 0.1 C between 2.8-4.3 V and approaching 240 mAh g^{-1} at 0.1 C between 2.8-4.5 V.
- (3) Characterisation of the materials demonstrated that the designed sol/antisolvent B_2O_3 coating modification on the precursor followed by lithiation calcination does not destroy the special daisy-like structure, but can realise a smooth and dense coating layer with nano-sized thickness and near-surface boron doping with radially aligned primary particles. The coating layer was identified as a faster ion conductor of glass amorphous $LiBO_2$. Beyond the extremely high discharge capacity, Daisy-Ni83-Bthin and Daisy-Ni83-Bmiddle also exhibited better cycling stability, rate

capability, and thermal stability than unmodified Daisy-Ni83.

- (4) Since B_2O_3 concentration in ethanol sol for synthesising Daisy-Ni83-Bthin is relatively lower than that for synthesising Daisy-Ni83-Bmiddle. Daisy-Ni83-Bthin is subjected to the incomplete coating for the secondary particle, Daisy-Ni83-Bmiddle is subjected to the complete coating for the secondary particle. Owing to sufficient protection from the complete coating on the secondary particle, Daisy-Ni83-Bmiddle exhibited the best cycling performance at high cut-off voltage and elevated current density.
- (5) The integration of the advantages of the radially aligned structure and the combined effects of coating and doping can boost the potential of NLO as an excellent cathode material. In contrast to separate doping or coating modification, the benefit of the three-in-one effect of the radially aligned microstructure and the incorporated coating and doping is obvious.

In **Chapter 6**, a sol/antisolvent boron treatment is further adopted for the modification of the ultrahigh Ni material of $LiNiO_2$. The modified $LiNiO_2$ was obtained by sol/antisolvent B_2O_3 treatment on radially structured $Ni(OH)_2$ along with subsequent lithiation calcination. The conclusions of this work are listed as follows:

- (1) Ordered, well-crystallised, and B-doped $LiNiO_2$ material with clear crystal planes of the primary particles were realised after modification. Different times of antisolvent treatment induced different degrees of boron doping. $LiNiO_2$ -more B exhibits more boron doping than $LiNiO_2$ -less B owing to the longer antisolvent

treatment time.

- (2) B-doping can activate the redox process in some kinetically sluggish regions, which is beneficial for delivering a higher discharge capacity than that of pristine LiNiO₂. B doping can also improve the Li/Ni ordering of the LNO material. The highest discharge capacity and the best rate capability of LiNiO₂-more B were matched with the highest Li/Ni ordering.
- (3) Compared with the well-formed and similar-sized single-crystal LiNiO₂, the polycrystalline radially aligned LiNiO₂-more B performs better in terms of both the discharge capacity and long-term cycling stability, which indicates that the benefit of the radially arranged structure and B-doping is also applicable for LNO materials.
- (4) In contrast to NCM811, H3–H4 phase transitions were detected for all the LNO materials. The emergence of the H3–H4 phase transition above 4.4 V can enhance the degree of the phase transition of H2–H3 at approximately 4.2 V, and further accelerate the performance deterioration. To optimise radially aligned and B-doped polycrystalline LNO, avoiding or inhibiting the harmful phase transitions of H2–H3 and H3–H4 at high voltages is necessary.

7.2. Prospects

NLO cathodes with superior electrochemical performance for advanced LIBs for EVs applications have been realised by the developed sol/antisolvent boron-related modification of different NLO materials. The outcome of the experimental work presented in this thesis is fascinating. Prospects for future work are as follows:

- (1) In addition to boron-related materials, such as LiBO_2 and B_2O_3 , other coating materials can also be studied using the sol/antisolvent method to expand the application of this method for modifying NLO materials.
- (2) In addition to tetrahydrofuran (THF), which is used as an antisolvent, other organic solutions exhibiting relatively lower polarities than ethanol can also be tried, and accordingly broaden the selection of antisolvents.
- (3) Achieving a complete surface coating on all the secondary particles poses a significant challenge, and more effort is needed. For example, the exploration of advanced equipment capable of ensuring a more uniform distribution of the micro-sized particles (i.e. the cathode material itself or its precursor) and nano-sized particles (i.e. the coating material) in the ethanol sol is a direction.
- (4) At a high specific capacity, LiNiO_2 undeniably demonstrates inferior cycling performance compared with NCM811, and strategies for inhibiting the harmful phase transitions of H2–H3 and H3–H4 should be developed. This endeavour necessitates a deeper comprehension and meticulous analysis of the underlying mechanisms driving these two detrimental phase transitions, thereby informing the development of targeted mitigation approaches.

Bibliography

- AGENCY, U. S. E. P. 1980. *EPA 560/11*, Health Review Division, Office of Toxic Substances, Environmental Protection Agency.
- AHALIABADEH, Z., KONG, X., FEDOROVSKAYA, E. & KALLIO, T. 2022. Extensive comparison of doping and coating strategies for Ni-rich positive electrode materials. *Journal of Power Sources*, 540.
- AIJAZ, I. & AHMAD, A. 2022. Electric Vehicles for Environmental Sustainability. In: AGARWAL, P., MITTAL, M., AHMED, J. & IDREES, S. M. (eds.) *Smart Technologies for Energy and Environmental Sustainability*. Cham: Springer International Publishing.
- AMALRAJ, S. F., RAMAN, R., CHAKRABORTY, A., LEIFER, N., NANDA, R., KUNNIKURUVAN, S., KRAVCHUK, T., GRINBLAT, J., EZERSKY, V., SUN, R., DEEPAK, F. L., ERK, C., WU, X., MAITI, S., SCLAR, H., GOOBES, G., MAJOR, D. T., TALIANKER, M., MARKOVSKY, B. & AURBACH, D. 2021. Boron doped Ni-rich $\text{LiNi}_{0.85}\text{Co}_{0.10}\text{Mn}_{0.05}\text{O}_2$ cathode materials studied by structural analysis, solid state NMR, computational modeling, and electrochemical performance. *Energy Storage Materials*, 42, 594-607.
- AMIN, R. & CHIANG, Y.-M. 2016. Characterization of Electronic and Ionic Transport in $\text{Li}_{1-x}\text{Ni}_{0.33}\text{Mn}_{0.33}\text{Co}_{0.33}\text{O}_2$ (NMC333) and $\text{Li}_{1-x}\text{Ni}_{0.50}\text{Mn}_{0.20}\text{Co}_{0.30}\text{O}_2$ (NMC523) as a Function of Li Content. *Journal of The Electrochemical Society*, 163, A1512-A1517.
- ANDERSSON, A. M., ABRAHAM, D. P., HAASCH, R., MACLAREN, S., LIU, J. & AMINE, K. 2002. Surface Characterization of Electrodes from High Power Lithium-Ion Batteries. *Journal of The Electrochemical Society*, 149, A1358.
- ARROYO Y DE DOMPABLO, M. E. & CEDER, G. 2003. First-principles calculations on Li_xNiO_2 : phase stability and monoclinic distortion. *Journal of Power Sources*, 119-121, 654-657.
- BAK, S.-M., HU, E., ZHOU, Y., YU, X., SENANAYAKE, S. D., CHO, S.-J., KIM, K.-B., CHUNG, K. Y., YANG, X.-Q. & NAM, K.-W. 2014. Structural Changes and Thermal Stability of Charged $\text{LiNi}_x\text{Mn}_y\text{Co}_z\text{O}_2$ Cathode Materials Studied by Combined In Situ Time-Resolved XRD and Mass Spectroscopy. *ACS Applied Materials & Interfaces*, 6, 22594-22601.
- BASALAEV, Y. M., BOLDYREVA, E. S. & DUGINOVA, E. B. 2019. Electronic and Vibrational Properties of LiBO_2 Crystals. *Russian Physics Journal*, 61, 1868-1875.
- BI, Y., WANG, T., LIU, M., DU, R., YANG, W., LIU, Z., PENG, Z., LIU, Y., WANG, D. & SUN, X. 2016. Stability of Li_2CO_3 in cathode of lithium ion battery and its influence on electrochemical performance. *RSC Advances*, 6, 19233-19237.
- BIANCHINI, M., ROCA-AYATS, M., HARTMANN, P., BREZESINSKI, T. & JANEK, J. 2019. There and Back Again-The Journey of LiNiO_2 as a Cathode Active Material. *Angewandte Chemie*.
- BINDER, J. O., CULVER, S. P., PINEDO, R., WEBER, D. A., FRIEDRICH, M. S., GRIES, K. I., VOLZ, K., ZEIER, W. G. & JANEK, J. 2018. Investigation of Fluorine and Nitrogen as Anionic Dopants in Nickel-Rich Cathode Materials for Lithium-Ion Batteries. *ACS Applied Materials & Interfaces*, 10, 44452-44462.
- BRANDT, K. 1994. Historical development of secondary lithium batteries. *Solid State Ionics*, 69, 173-183.
- BUTT, A., JAMIL, S., BATOOL, M., FASEHULLAH, M., SHARIF, R. & ALI, G. 2022. Elevated Li^+ diffusivity in Ni-rich layered oxide by precursor pre-oxidation. *Ceramics International*, 48, 30176-

30183.

- CAIRNS, E. J. & SHIMOTAKE, H. 1969. High-Temperature Batteries. *Science*, 164, 1347.
- CELINE BUECHEL, L. B., AND SAMANTHA WIETLISBACH. 2021. *As lithium-ion battery materials evolve, suppliers face new challenges* [Online]. Available: <https://www.spglobal.com/commodityinsights/en/ci/research-analysis/lithium-ion-battery-materials-evolve-suppliers-face-new-challenges.html> [Accessed].
- CHAKRABORTY, A., KUNNIKURUVAN, S., KUMAR, S., MARKOVSKY, B., AURBACH, D., DIXIT, M. & MAJOR, D. T. 2020. Layered Cathode Materials for Lithium-Ion Batteries: Review of Computational Studies on $\text{LiNi}_{1-x-y}\text{Co}_x\text{Mn}_y\text{O}_2$ and $\text{LiNi}_{1-x-y}\text{Co}_x\text{Al}_y\text{O}_2$. *Chemistry of Materials*, 32, 915-952.
- CHAKRABORTY, P., PARKER, R., HOQUE, T., CRUZ, J., DU, L., WANG, S. & BHUNIA, S. 2022. Addressing the range anxiety of battery electric vehicles with charging en route. *Scientific Reports*, 12.
- CHEN, J., WANG, X. L., JIN, E. M., MOON, S.-G. & JEONG, S. M. 2021. Optimization of B_2O_3 coating process for NCA cathodes to achieve long-term stability for application in lithium ion batteries. *Energy*, 222.
- CHEN, S., HE, T., SU, Y., LU, Y., BAO, L., CHEN, L., ZHANG, Q., WANG, J., CHEN, R. & WU, F. 2017. Ni-Rich $\text{LiNi}_{0.8}\text{Co}_{0.1}\text{Mn}_{0.1}\text{O}_2$ Oxide Coated by Dual-Conductive Layers as High Performance Cathode Material for Lithium-Ion Batteries. *ACS Appl Mater Interfaces*, 9, 29732-29743.
- CHEN, S., NIU, C., LEE, H., LI, Q., YU, L., XU, W., ZHANG, J.-G., DUFEK, E. J., WHITTINGHAM, M. S., MENG, S., XIAO, J. & LIU, J. 2019. Critical Parameters for Evaluating Coin Cells and Pouch Cells of Rechargeable Li-Metal Batteries. *Joule*, 3, 1094-1105.
- CHEN, T., JIN, Y., LV, H., YANG, A., LIU, M., CHEN, B., XIE, Y. & CHEN, Q. 2020. Applications of Lithium-Ion Batteries in Grid-Scale Energy Storage Systems. *Transactions of Tianjin University*, 26, 208-217.
- CHEN, T., LI, X., WANG, H., YAN, X., WANG, L., DENG, B., GE, W. & QU, M. 2018. The effect of gradient boracic polyanion-doping on structure, morphology, and cycling performance of Ni-rich $\text{LiNi}_{0.8}\text{Co}_{0.15}\text{Al}_{0.05}\text{O}_2$ cathode material. *Journal of Power Sources*, 374, 1-11.
- CHEN, T., WEN, C., WU, C., QIU, L., WU, Z., LI, J., ZHU, Y., LI, H., KONG, Q., SONG, Y., WAN, F., CHEN, M., SAADOUNE, I., ZHONG, B., DOU, S., XIAO, Y. & GUO, X. 2023. Manipulating the crystal plane angle within the primary particle arrangement for the radial ordered structure in a Ni-rich cathode. *Chemical Science*, 14, 13924-13933.
- CHEN, Z., QIN, Y., AMINE, K. & SUN, Y. K. 2010. Role of surface coating on cathode materials for lithium-ion batteries. *Journal of Materials Chemistry*, 20, 7606-7612.
- CHO, D.-H., JO, C.-H., CHO, W., KIM, Y.-J., YASHIRO, H., SUN, Y.-K. & MYUNG, S.-T. 2014. Effect of Residual Lithium Compounds on Layer Ni-Rich $\text{Li}[\text{Ni}_{0.7}\text{Mn}_{0.3}]\text{O}_2$. *Journal of The Electrochemical Society*, 161, A920-A926.
- CHOI, J. U., VORONINA, N., SUN, Y. K. & MYUNG, S. T. 2020. Recent Progress and Perspective of Advanced High-Energy Co-Less Ni-Rich Cathodes for Li-Ion Batteries: Yesterday, Today, and Tomorrow. *Advanced Energy Materials*, 10.
- DAI, Z., LI, Z., CHEN, R., WU, F. & LI, L. 2023. Defective oxygen inert phase stabilized high-voltage nickel-rich cathode for high-energy lithium-ion batteries. *Nature Communications*, 14, 8087.

- DE BIASI, L., SCHWARZ, B., BREZESINSKI, T., HARTMANN, P., JANEK, J. & EHRENBERG, H. 2019. Chemical, Structural, and Electronic Aspects of Formation and Degradation Behavior on Different Length Scales of Ni-Rich NCM and Li-Rich HE-NCM Cathode Materials in Li-Ion Batteries. *Advanced Materials*, 31, 1900985.
- DE BIASI, L., SCHIELE, A., ROCA-AYATS, M., GARCIA, G., BREZESINSKI, T., HARTMANN, P. & JANEK, J. 2019. Phase Transformation Behavior and Stability of LiNiO₂ Cathode Material for Li-Ion Batteries Obtained from In Situ Gas Analysis and Operando X - Ray Diffraction. *ChemSusChem*, 12, 2240-2250.
- DEAN, J. A. Lange's Handbook of Chemistry. 1978.
- DELMAS, C., MÉNÉTRIER, M., CROGUENNEC, L., LEVASSEUR, S., PÉRÈS, J. P., POUILLERIE, C., PRADO, G., FOURNÈS, L. & WEILL, F. 1999. Lithium batteries: a new tool in solid state chemistry. *International Journal of Inorganic Materials*, 1, 11-19.
- DENG, X., ZHANG, R., ZHOU, K., GAO, Z., HE, W., ZHANG, L., HAN, C., KANG, F. & LI, B. 2022. A Comparative Investigation of Single Crystal and Polycrystalline Ni-Rich NCMs as Cathodes for Lithium-Ion Batteries. *Energy & Environmental Materials*, 6.
- DING, Y., CANO, Z. P., YU, A., LU, J. & CHEN, Z. 2019. Automotive Li-Ion Batteries: Current Status and Future Perspectives. *Electrochemical Energy Reviews*, 2, 1-28.
- DU, M., YANG, P., HE, W., BIE, S., ZHAO, H., YIN, J., ZOU, Z. & LIU, J. 2019. Enhanced high-voltage cycling stability of Ni-rich LiNi_{0.8}Co_{0.1}Mn_{0.1}O₂ cathode coated with Li₂O-2B₂O₃. *Journal of Alloys and Compounds*, 805, 991-998.
- EVERTZ, M., HORSTHEMKE, F., KASNATSCHEEW, J., BÖRNER, M., WINTER, M. & NOWAK, S. 2016. Unraveling transition metal dissolution of Li_{1.04}Ni_{1/3}Co_{1/3}Mn_{1/3}O₂ (NCM 111) in lithium ion full cells by using the total reflection X-ray fluorescence technique. *Journal of Power Sources*, 329, 364-371.
- FAN, Q., YANG, S., LIU, J., LIU, H., LIN, K., LIU, R., HONG, C., LIU, L., CHEN, Y., AN, K., LIU, P., SHI, Z. & YANG, Y. 2019. Mixed-conducting interlayer boosting the electrochemical performance of Ni-rich layered oxide cathode materials for lithium ion batteries. *Journal of Power Sources*, 421, 91-99.
- FANG, C., TRAN, T.-N., ZHAO, Y. & LIU, G. 2021. Electrolyte decomposition and solid electrolyte interphase revealed by mass spectrometry. *Electrochimica Acta*, 399, 139362.
- FENG, Z., RAJAGOPALAN, R., ZHANG, S., SUN, D., TANG, Y., REN, Y. & WANG, H. 2020. A Three in One Strategy to Achieve Zirconium Doping, Boron Doping, and Interfacial Coating for Stable LiNi_{0.8}Co_{0.1}Mn_{0.1}O₂ Cathode. *Advanced Science*, 8.
- FU, C., LI, G., LUO, D., LI, Q., FAN, J. & LI, L. 2014. Nickel-rich layered microspheres cathodes: lithium/nickel disordering and electrochemical performance. *ACS Appl Mater Interfaces*, 6, 15822-31.
- GALIMBERTI, M., BARBERA, V. & SIRONI, A. 2020. Chapter 3 - Functionalized sp² carbon allotropes as fillers for rubber nanocomposites. In: VALENTINI, L. & LOPEZ MANCHADO, M. A. (eds.) *High-Performance Elastomeric Materials Reinforced by Nano-Carbons*. Elsevier.
- GAMBLE, F. R., OSIECKI, J. H., CAIS, M., PISHARODY, R., DISALVO, F. J. & GEBALLE, T. H. 1971. Intercalation complexes of lewis bases and layered sulfides: a large class of new superconductors. *Science (New York, N.Y.)*, 174, 493-497.
- GAUTHIER, M., CARNEY, T. J., GRIMAUD, A., GIORDANO, L., POUR, N., CHANG, H. H., FENNING, D. P., LUX, S. F., PASCHOS, O., BAUER, C., MAGLIA, F., LUPART, S., LAMP, P. & SHAO-HORN,

- Y. 2015. Electrode–electrolyte interface in Li-ion batteries: current understanding and new insights. *J Phys Chem Lett*, 6, 4653–72.
- GENG, C., RATHORE, D., HEINO, D., ZHANG, N., HAMAM, I., ZAKER, N., BOTTON, G. A., OMESSI, R., PHATTHARASUPAKUN, N., BOND, T., YANG, C. & DAHN, J. R. 2022. Mechanism of Action of the Tungsten Dopant in LiNiO₂ Positive Electrode Materials. *Advanced Energy Materials*, 12, 2103067.
- GONG, Y., ZHANG, P., JIANG, P. & LIN, J. 2015. Metal(ii) complex based on 5-[4-(1H-imidazol-1-yl)phenyl]-2H-tetrazole: the effect of the ligand on the electrodes in a lead-acid battery. *CrystEngComm*, 17, 1056–1064.
- GOURDIN, G., SMITH, P. H., JIANG, T., TRAN, T. N. & QU, D. 2013. Lithiation of amorphous carbon negative electrode for Li ion capacitor. *Journal of Electroanalytical Chemistry*, 688, 103–112.
- GREY, C. P. & HALL, D. S. 2020. Prospects for lithium-ion batteries and beyond—a 2030 vision. *Nature Communications*, 11, 6279.
- GU, M., BELHAROUAK, I., ZHENG, J., WU, H., XIAO, J., GENG, A., AMINE, K., THEVUTHASAN, S., BAER, D. R., ZHANG, J.-G., BROWNING, N. D., LIU, J. & WANG, C. 2013. Formation of the Spinel Phase in the Layered Composite Cathode Used in Li-Ion Batteries. *ACS Nano*, 7, 760–767.
- GUAN, P., ZHOU, L., YU, Z., SUN, Y., LIU, Y., WU, F., JIANG, Y. & CHU, D. 2020. Recent progress of surface coating on cathode materials for high-performance lithium-ion batteries. *Journal of Energy Chemistry*, 43, 220–235.
- GUÉGUEN, A., STREICH, D., HE, M., MENDEZ, M., CHESNEAU, F. F., NOVÁK, P. & BERG, E. J. 2016. Decomposition of LiPF₆ in High Energy Lithium-Ion Batteries Studied with Online Electrochemical Mass Spectrometry. *Journal of The Electrochemical Society*, 163, A1095–A1100.
- HA, Y., SCHULZE, M. C., FRISCO, S., TRASK, S. E., TEETER, G., NEALE, N. R., VEITH, G. M. & JOHNSON, C. S. 2021. Li₂O-Based Cathode Additives Enabling Prelithiation of Si Anodes. *Applied Sciences*, 11, 12027.
- HASHIGAMI, S., KATO, Y., YOSHIMI, K., FUKUMOTO, A., CAO, Z., YOSHIDA, H., INAGAKI, T., HASHINOKUCHI, M., HARUTA, M., DOI, T. & INABA, M. 2019a. Effect of Lithium Silicate Addition on the Microstructure and Crack Formation of LiNi_{0.8}Co_{0.1}Mn_{0.1}O₂ Cathode Particles. *ACS Appl Mater Interfaces*, 11, 39910–39920.
- HASHIGAMI, S., KATO, Y., YOSHIMI, K., YOSHIDA, H., INAGAKI, T., HASHINOKUCHI, M., DOI, T. & INABA, M. 2018. Influence of lithium silicate coating on retarding crack formation in LiNi_{0.5}Co_{0.2}Mn_{0.3}O₂ cathode particles. *Electrochimica Acta*, 291, 304–310.
- HASHIGAMI, S., YOSHIMI, K., KATO, Y., YOSHIDA, H., INAGAKI, T., HARUTA, M., HASHINOKUCHI, M., DOI, T. & INABA, M. 2019b. Improvement of Cycleability and Rate-Capability of LiNi_{0.5}Co_{0.2}Mn_{0.3}O₂ Cathode Materials Coated with Lithium Boron Oxide by an Antisolvent Precipitation Method. *ChemistrySelect*, 4, 8676–8681.
- HE, B., ZHANG, F., XIN, Y., XU, C., HU, X., WU, X., YANG, Y. & TIAN, H. 2023. Halogen chemistry of solid electrolytes in all-solid-state batteries. *Nature Reviews Chemistry*, 7, 826–842.
- HEENAN, T. M. M., WADE, A., TAN, C., PARKER, J. E., MATRAS, D., LEACH, A. S., ROBINSON, J. B., LLEWELLYN, A., DIMITRIJEVIC, A., JERVIS, R., QUINN, P. D., BRETT, D. J. L. & SHEARING, P. R. 2020. Identifying the Origins of Microstructural Defects Such as Cracking within Ni-Rich

- NMC811 Cathode Particles for Lithium-Ion Batteries. *Advanced Energy Materials*, 10.
- HINUMA, Y., MENG, Y. S., KANG, K. & CEDER, G. 2007. Phase Transitions in the $\text{LiNi}_0.5\text{Mn}_0.5\text{O}_2$ System with Temperature. *Chemistry of Materials*, 19, 1790-1800.
- HIROSE, E., KATAOKA, K., NAGATA, H., AKIMOTO, J., SASAKI, T., NIWA, K. & HASEGAWA, M. 2019. Lithium ionic conductivities of α - LiBO_2 with two-dimensional Li-Li networks and γ - LiBO_2 with three-dimensional ones synthesized under high pressure. *Journal of Solid State Chemistry*, 274, 100-104.
- HU, W., ZHANG, C., JIANG, H., ZHENG, M., WU, Q.-H. & DONG, Q. 2017. Improving the electrochemistry performance of layer $\text{LiNi}_0.5\text{Mn}_0.3\text{Co}_0.2\text{O}_2$ material at 4.5V cutoff potential using lithium metaborate. *Electrochimica Acta*, 243, 105-111.
- HUANG, B., WANG, M., YANG, X., XU, G. & GU, Y. 2019. Enhanced electrochemical performance of the layered nickel-rich oxide cathode by KMnO_4 treatment precursor. *Journal of Alloys and Compounds*, 808.
- HUANG, Y., LIN, Y.-C., JENKINS, D. M., CHERNOVA, N. A., CHUNG, Y., RADHAKRISHNAN, B., CHU, I.-H., FANG, J., WANG, Q., OMENYA, F., ONG, S. P. & WHITTINGHAM, M. S. 2016. Thermal Stability and Reactivity of Cathode Materials for Li-Ion Batteries. *ACS Applied Materials & Interfaces*, 8, 7013-7021.
- HUANG, Z., CHU, M., WANG, R., ZHU, W., ZHAO, W., WANG, C., ZHANG, Y., HE, L., CHEN, J., DENG, S., MEI, L., KAN, W. H., AVDEEV, M., PAN, F. & XIAO, Y. 2020. Optimizing the structure of layered cathode material for higher electrochemical performance by elucidating structural evolution during heat processing. *Nano Energy*, 78, 105194.
- HUY, N. D., BADILESCU, S., DJAOUED, Y., GIROUARD, F. E., BADER, G., ASHRIT, P. V. & TRUONG, V.-V. 1996. Preparation and characterization of lithium metaborate thin films obtained by a sol-gel method. *Thin Solid Films*, 286, 141-145.
- HWANG, S., CHANG, W., KIM, S. M., SU, D., KIM, D. H., LEE, J. Y., CHUNG, K. Y. & STACH, E. A. 2014. Investigation of Changes in the Surface Structure of $\text{Li}_x\text{Ni}_0.8\text{Co}_0.15\text{Al}_0.05\text{O}_2$ Cathode Materials Induced by the Initial Charge. *Chemistry of Materials*, 26, 1084-1092.
- IRLE, V. 2021. *EV-Volumes-The Electric Vehicle World Sales Database* [Online]. Available: <https://finance.sina.com.cn/tech/2021-02-22/doc-ikftssap7971173.shtml> [Accessed].
- JAMIL, S., YU, R., WANG, Q., FASEHULLAH, M., HUANG, Y., YANG, Z., YANG, X. & WANG, X. 2020. Enhanced cycling stability of nickel-rich layered oxide by tantalum doping. *Journal of Power Sources*, 473, 228597.
- JEONG, M., KIM, H., LEE, W., AHN, S.-J., LEE, E. & YOON, W.-S. 2020. Stabilizing effects of Al-doping on Ni-rich $\text{LiNi}_0.8\text{Co}_0.15\text{Mn}_0.05\text{O}_2$ cathode for Li rechargeable batteries. *Journal of Power Sources*, 474.
- JULIEN, C. M., MAUGER, A., ZAGHIB, K. & GROULT, H. Comparative Issues of Cathode Materials for Li-Ion Batteries. 2014.
- JUNG, R., METZGER, M., MAGLIA, F., STINNER, C. & GASTEIGER, H. A. 2017. Oxygen Release and Its Effect on the Cycling Stability of $\text{LiNi}_x\text{Mn}_y\text{Co}_z\text{O}_2$ (NMC) Cathode Materials for Li-Ion Batteries. *Journal of The Electrochemical Society*, 164, A1361-A1377.
- KALLURI, S., CHA, H., KIM, J., LEE, H., JANG, H. & CHO, J. 2020. Building High-Rate Nickel-Rich Cathodes by Self-Organization of Structurally Stable Macrovoid. *Advanced Science*, 7, 1902844.
- KALYANI, P. & KALAISELVI, N. 2005. Various aspects of LiNiO_2 chemistry: A review. *Science and*

Technology of Advanced Materials, 6, 689-703.

- KANNO, R. 2006. Structural Aspects of Materials for Lithium Battery Electrodes. *GS Yuasa Technical Report*, 3, 11.
- KASNATSCHEEW, J., EVERTZ, M., STREIPERT, B., WAGNER, R., KLÖPSCH, R., VORTMANN, B., HAHN, H., NOWAK, S., AMERELLER, M., GENTSCHKEV, A. C., LAMP, P. & WINTER, M. 2016a. The truth about the 1st cycle Coulombic efficiency of LiNi_{1/3}Co_{1/3}Mn_{1/3}O₂ (NCM) cathodes. *Physical Chemistry Chemical Physics*, 18, 3956-3965.
- KASNATSCHEEW, J., RODEHORST, U., STREIPERT, B., WIEMERS-MEYER, S., JAKELSKI, R., WAGNER, R., LASKOVIC, I. C. & WINTER, M. 2016b. Learning from Overpotentials in Lithium Ion Batteries: A Case Study on the LiNi_{1/3}Co_{1/3}Mn_{1/3}O₂(NCM) Cathode. *Journal of The Electrochemical Society*, 163, A2943-A2950.
- KIM, H., KIM, M. G., JEONG, H. Y., NAM, H. & CHO, J. 2015. A new coating method for alleviating surface degradation of LiNi_{0.6}Co_{0.2}Mn_{0.2}O₂ cathode material: nanoscale surface treatment of primary particles. *Nano Lett*, 15, 2111-9.
- KIM, J.-H., PARK, K.-J., KIM, S. J., YOON, C. S. & SUN, Y.-K. 2019. A method of increasing the energy density of layered Ni-rich Li[Ni_{1-2x}CoxMnx]O₂ cathodes (x = 0.05, 0.1, 0.2). *Journal of Materials Chemistry A*, 7, 2694-2701.
- KIM, M., ZOU, L., SON, S.-B., BLOOM, I. D., WANG, C. & CHEN, G. 2022. Improving LiNiO₂ cathode performance through particle design and optimization. *Journal of Materials Chemistry A*, 10, 12890-12899.
- KIM, U.-H., PARK, G.-T., SON, B.-K., NAM, G. W., LIU, J., KUO, L.-Y., KAGHAZCHI, P., YOON, C. S. & SUN, Y.-K. 2020. Heuristic solution for achieving long-term cycle stability for Ni-rich layered cathodes at full depth of discharge. *Nature Energy*, 5, 860-869.
- KIM, U. H., JUN, D. W., PARK, K. J., ZHANG, Q., KAGHAZCHI, P., AURBACH, D., MAJOR, D. T., GOOBES, G., DIXIT, M., LEIFER, N., WANG, C. M., YAN, P., AHN, D., KIM, K. H., YOON, C. S. & SUN, Y. K. 2018. Pushing the limit of layered transition metal oxide cathodes for high-energy density rechargeable Li ion batteries. *Energy & Environmental Science*, 11, 1271-1279.
- KIPPER, R. A. 2007. *Properties of substance: lithium metaborate* [Online]. Available: <http://chemister.ru/Database/properties-en.php?id=4304>. [Accessed].
- KONAROV, A., MYUNG, S.-T. & SUN, Y.-K. 2017. Cathode Materials for Future Electric Vehicles and Energy Storage Systems. *ACS Energy Letters*, 2, 703-708.
- KONG, D., ZHANG, M., XIAO, Y., HU, J., ZHAO, W., HAN, L. & PAN, F. 2019. Insights into the structural evolution and Li/O loss in high-Ni layered oxide cathodes. *Nano Energy*, 59, 327-335.
- KURZHALS, P., RIEWALD, F., BIANCHINI, M., SOMMER, H., GASTEIGER, H. A. & JANEK, J. 2021. The LiNiO₂ Cathode Active Material: A Comprehensive Study of Calcination Conditions and their Correlation with Physicochemical Properties. Part I. Structural Chemistry. *Journal of The Electrochemical Society*, 168, 110518.
- KURZWEIL, P. 2010. Gaston Planté and his invention of the lead-acid battery—The genesis of the first practical rechargeable battery. *Journal of Power Sources*, 195, 4424-4434.
- LAI, J., ZHANG, J., LI, Z., XIAO, Y., HUA, W., WU, Z., CHEN, Y., ZHONG, Y., XIANG, W. & GUO, X. 2020. Structural elucidation of the degradation mechanism of nickel-rich layered cathodes during high-voltage cycling. *Chemical Communications*, 56, 4886-4889.

- LAZANAS, A. C. & PRODROMIDIS, M. I. 2023. Electrochemical Impedance Spectroscopy—A Tutorial. *ACS Measurement Science Au*, 3, 162-193.
- LEE, S.-H., JIN, B.-S. & KIM, H.-S. 2019. Superior Performances of B-doped $\text{LiNi}_{0.84}\text{Co}_{0.10}\text{Mn}_{0.06}\text{O}_2$ cathode for advanced LIBs. *Scientific Reports*, 9.
- LEE, Y. S., SUN, Y. K. & NAHM, K. S. 1999. Synthesis and characterization of LiNiO_2 cathode material prepared by an adipic acid-assisted sol-gel method for lithium secondary batteries. *Solid State Ionics*, 118, 159-168.
- LEI, L., HE, D., HE, K., QIN, J. & WANG, S. 2009. Pressure-induced coordination changes in LiBO_2 . *Journal of Solid State Chemistry*, 182, 3041-3048.
- LEI, Y., AI, J., YANG, S., JIANG, H., LAI, C. & XU, Q. 2019. Effect of flower-like $\text{Ni}(\text{OH})_2$ precursors on $\text{Li}^+/\text{Ni}^{2+}$ cation mixing and electrochemical performance of nickel-rich layered cathode. *Journal of Alloys and Compounds*, 797, 421-431.
- LI, H., LIU, S., HUANG, C., ZHOU, Z., LI, Y. & FANG, D. 2011. Characterization and supercapacitor application of coin-like β -nickel hydroxide nanoplates. *Electrochimica Acta*, 58, 89-94.
- LI, L., XU, M., YAO, Q., CHEN, Z., SONG, L., ZHANG, Z., GAO, C., WANG, P., YU, Z. & LAI, Y. 2016. Alleviating Surface Degradation of Nickel-Rich Layered Oxide Cathode Material by Encapsulating with Nanoscale Li-Ions/Electrons Superionic Conductors Hybrid Membrane for Advanced Li-Ion Batteries. *ACS Applied Materials & Interfaces*, 8, 30879-30889.
- LI, M., CHENG, L., ZHANG, B., DENG, P., XIAO, Z., MING, L., ZHAO, Y., XU, B. & OU, X. 2022. The effect of $\text{B}_2\text{O}_3/\text{Li}_3\text{BO}_3$ coating and B^{3+} doping on electrochemical properties in nickel-rich single-crystal $\text{LiNi}_{0.7}\text{Co}_{0.2}\text{Mn}_{0.1}\text{O}_2$ cathodes. *Journal of Alloys and Compounds*, 907.
- LI, M., LU, J., CHEN, Z. & AMINE, K. 2018. 30 Years of Lithium-Ion Batteries. *Advanced Materials*, 30, 1800561.
- LI, Q., ZHUANG, W., LI, Z., WU, S., LI, N., GAO, M., LI, W., WANG, J. & LU, S. 2020a. Realizing Superior Cycle Stability of a Ni-Rich Layered $\text{LiNi}_{0.83}\text{Co}_{0.12}\text{Mn}_{0.05}\text{O}_2$ Cathode with a B_2O_3 Surface Modification. *ChemElectroChem*, 7, 998-1006.
- LI, T., YUAN, X.-Z., ZHANG, L., SONG, D., SHI, K. & BOCK, C. 2019. Degradation Mechanisms and Mitigation Strategies of Nickel-Rich NMC-Based Lithium-Ion Batteries. *Electrochemical Energy Reviews*, 3, 43-80.
- LI, T., YUAN, X.-Z., ZHANG, L., SONG, D., SHI, K. & BOCK, C. 2020b. Degradation Mechanisms and Mitigation Strategies of Nickel-Rich NMC-Based Lithium-Ion Batteries. *Electrochemical Energy Reviews*, 3, 43-80.
- LI, W., DOLOCAN, A., OH, P., CELIO, H., PARK, S., CHO, J. & MANTHIRAM, A. 2017a. Dynamic behaviour of interphases and its implication on high-energy-density cathode materials in lithium-ion batteries. *Nature Communications*, 8, 14589.
- LI, W., ERICKSON, E. M. & MANTHIRAM, A. 2020c. High-nickel layered oxide cathodes for lithium-based automotive batteries. *Nature Energy*, 5, 26-34.
- LI, W., LIU, X., XIE, Q., YOU, Y., CHI, M. & MANTHIRAM, A. 2020d. Long-Term Cyclability of NCM-811 at High Voltages in Lithium-Ion Batteries: an In-Depth Diagnostic Study. *Chemistry of Materials*, 32, 7796-7804.
- LI, W., SONG, B. & MANTHIRAM, A. 2017b. High-voltage positive electrode materials for lithium-ion batteries. *Chemical Society Reviews*, 46, 3006-3059.
- LIANG, Y., ZHAO, C.-Z., YUAN, H., CHEN, Y., ZHANG, W., HUANG, J.-Q., YU, D., LIU, Y., TITIRICI, M.-M., CHUEH, Y.-L., YU, H. & ZHANG, Q. 2019. A review of rechargeable batteries for

- portable electronic devices. *InfoMat*, 1, 6-32.
- LIAO, J.-Y. & MANTHIRAM, A. 2015. Surface-modified concentration-gradient Ni-rich layered oxide cathodes for high-energy lithium-ion batteries. *Journal of Power Sources*, 282, 429-436.
- LIM, B.-B., MYUNG, S.-T., YOON, C. S. & SUN, Y.-K. 2016. Comparative Study of Ni-Rich Layered Cathodes for Rechargeable Lithium Batteries: $\text{Li}[\text{Ni}_{0.85}\text{Co}_{0.11}\text{Al}_{0.04}]\text{O}_2$ and $\text{Li}[\text{Ni}_{0.84}\text{Co}_{0.06}\text{Mn}_{0.09}\text{Al}_{0.01}]\text{O}_2$ with Two-Step Full Concentration Gradients. *ACS Energy Letters*, 1, 283-289.
- LIM, J.-M., KIM, H., CHO, K. & CHO, M. 2018. Fundamental mechanisms of fracture and its suppression in Ni-rich layered cathodes: Mechanics-based multiscale approaches. *Extreme Mechanics Letters*, 22, 98-105.
- LIM, S. N., AHN, W., YEON, S.-H. & PARK, S. B. 2014. Enhanced elevated-temperature performance of $\text{Li}(\text{Ni}_{0.8}\text{Co}_{0.15}\text{Al}_{0.05})\text{O}_2$ electrodes coated with $\text{Li}_2\text{O}-2\text{B}_2\text{O}_3$ glass. *Electrochimica Acta*, 136, 1-9.
- LIU, C., NEALE, Z. G. & CAO, G. 2016. Understanding electrochemical potentials of cathode materials in rechargeable batteries. *Materials Today*, 19, 109-123.
- LIU, H., WOLF, M., KARKI, K., YU, Y.-S., STACH, E. A., CABANA, J., CHAPMAN, K. W. & CHUPAS, P. J. 2017. Intergranular Cracking as a Major Cause of Long-Term Capacity Fading of Layered Cathodes. *Nano Letters*, 17, 3452-3457.
- LIU, T., PAREKH, R., MOCNY, P., BLOOM, B. P., ZHAO, Y., AN, S. Y., PAN, B., YIN, R., WALDECK, D. H., WHITACRE, J. F. & MATYJASZEWSKI, K. 2023. Tailored PVDF Graft Copolymers via ATRP as High-Performance NCM811 Cathode Binders. *ACS Materials Letters*, 5, 2594-2603.
- LIU, T., YU, L., LU, J., ZHOU, T., HUANG, X., CAI, Z., DAI, A., GIM, J., REN, Y., XIAO, X., HOLT, M. V., CHU, Y. S., ARSLAN, I., WEN, J. & AMINE, K. 2021. Rational design of mechanically robust Ni-rich cathode materials via concentration gradient strategy. *Nat Commun*, 12, 6024.
- LIU, W., LI, C., SUN, X., ZHANG, X., WANG, K., LI, Z., HAO, Q. & MA, Y. 2018. Improvement of the high-rate capability of $\text{LiNi}_{1/3}\text{Co}_{1/3}\text{Mn}_{1/3}\text{O}_2$ cathode by adding highly electroconductive and mesoporous graphene. *Journal of Alloys and Compounds*, 758, 206-213.
- LIU, W., OH, P., LIU, X., LEE, M.-J., CHO, W., CHAE, S., KIM, Y. & CHO, J. 2015. Nickel-Rich Layered Lithium Transition-Metal Oxide for High-Energy Lithium-Ion Batteries. *Angewandte Chemie International Edition*, 54, 4440-4457.
- LIU, Y., WANG, X., CAI, J., HAN, X., GENG, D., LI, J. & MENG, X. 2020. Atomic-scale tuned interface of nickel-rich cathode for enhanced electrochemical performance in lithium-ion batteries. *Journal of Materials Science & Technology*, 54, 77-86.
- LUO, L., QIN, X., WU, J., LIANG, G., LI, Q., LIU, M., KANG, F., CHEN, G. & LI, B. 2018. An interwoven $\text{MoO}_3@\text{CNT}$ scaffold interlayer for high-performance lithium-sulfur batteries. *Journal of Materials Chemistry A*, 6, 8612-8619.
- LV, Y., HUANG, S., LU, S., DING, W., YU, X., LIANG, G., ZOU, J., KANG, F., ZHANG, J. & CAO, Y. 2022. $\text{B}_2\text{O}_3/\text{LiBO}_2$ dual-modification layer stabilized Ni-rich cathode for lithium-ion battery. *Journal of Power Sources*, 536.
- MANTHIRAM, A. 2017. An Outlook on Lithium Ion Battery Technology. *ACS Central Science*, 3, 1063-1069.
- MANTHIRAM, A. 2020. A reflection on lithium-ion battery cathode chemistry. *Nat Commun*, 11,

1550.

- MANATHIRAM, A. & GOODENOUGH, J. B. 2021. Layered lithium cobalt oxide cathodes. *Nature Energy*, 6, 323-323.
- MANATHIRAM, A., SONG, B. & LI, W. 2017. A perspective on nickel-rich layered oxide cathodes for lithium-ion batteries. *Energy Storage Materials*, 6, 125-139.
- MÄRKER, K., REEVES, P. J., XU, C., GRIFFITH, K. J. & GREY, C. P. 2019. Evolution of Structure and Lithium Dynamics in LiNi_{0.8}Mn_{0.1}Co_{0.1}O₂ (NMC811) Cathodes during Electrochemical Cycling. *Chemistry of Materials*, 31, 2545-2554.
- MARKEVICH, E., SALITRA, G., HARTMANN, P., KULISCH, J., AURBACH, D., PARK, K.-J., YOON, C. S. & SUN, Y.-K. 2019. New Insights Related to Rechargeable Lithium Batteries: Li Metal Anodes, Ni Rich LiNi_xCo_yMn_zO₂ Cathodes and Beyond Them. *Journal of The Electrochemical Society*, 166, A5265-A5274.
- MIKOLAJCZAK, C., KAHN, M., WHITE, K. & LONG, R. T. 2011. Introduction to Lithium-Ion Cells and Batteries. In: MIKOLAJCZAK, C., KAHN, M., WHITE, K. & LONG, R. T. (eds.) *Lithium-Ion Batteries Hazard and Use Assessment*. Boston, MA: Springer US.
- MIN, K. & CHO, E. 2018. Intrinsic origin of intra-granular cracking in Ni-rich layered oxide cathode materials. *Physical chemistry chemical physics : PCCP*, 20 14, 9045-9052.
- MIN, K., SEO, S.-W., SONG, Y. Y., LEE, H. S. & CHO, E. 2017. A first-principles study of the preventive effects of Al and Mg doping on the degradation in LiNi_{0.8}Co_{0.1}Mn_{0.1}O₂ cathode materials. *Physical Chemistry Chemical Physics*, 19, 1762-1769.
- MITCHELL, A. 2020. *How electric vehicles are driving the nickel sulphate market* [Online]. Available: <https://www.woodmac.com/news/opinion/how-electric-vehicles-are-driving-the-nickel-sulphate-market/#:~:text=There%20has%20been%20a%20surge%20in%20demand%20for,gathers%20speed%2C%20demand%20for%20battery%20materials%20will%20accelerate>. [Accessed].
- MIZUSHIMA, K., JONES, P., WISEMAN, P. & GOODENOUGH, J. 1981. Li_xCoO₂ (0 < x < 1): A new cathode material for batteries of high energy density. *Solid State Ionics*, 171-174.
- MIZUSHIMA, K., JONES, P. C., WISEMAN, P. J. & GOODENOUGH, J. B. 1980. Li_xCoO₂ (0 < x < 1): A new cathode material for batteries of high energy density. *Materials Research Bulletin*, 15, 783-789.
- MOSES, A. W., FLORES, H. G. G., KIM, J.-G. & LANGELL, M. A. 2007. Surface properties of LiCoO₂, LiNiO₂ and LiNi_{1-x}Co_xO₂. *Applied Surface Science*, 253, 4782-4791.
- NISAR, U., MURALIDHARAN, N., ESSEHLI, R., AMIN, R. & BELHAROUAK, I. 2021. Valuation of Surface Coatings in High-Energy Density Lithium-ion Battery Cathode Materials. *Energy Storage Materials*, 38, 309-328.
- NOH, H.-J., YOUN, S., YOON, C. S. & SUN, Y.-K. 2013. Comparison of the structural and electrochemical properties of layered Li[Ni_xCo_yMn_z]O₂ (x = 1/3, 0.5, 0.6, 0.7, 0.8 and 0.85) cathode material for lithium-ion batteries. *Journal of Power Sources*, 233, 121-130.
- OKA, H., NONAKA, T., KONDO, Y. & MAKIMURA, Y. 2023. Quantification of side reactions in lithium-ion batteries during overcharging at elevated temperatures. *Journal of Power Sources*, 580, 233387.
- OSIAK, M., GEANEY, H., ARMSTRONG, E. & O'DWYER, C. 2014. Structuring materials for lithium-ion batteries: advancements in nanomaterial structure, composition, and defined assembly on cell performance. *Journal of Materials Chemistry A*, 2, 9433-9460.

- OZAWA, K. 1994. Lithium-ion rechargeable batteries with LiCoO₂ and carbon electrodes: the LiCoO₂/C system. *Solid State Ionics*, 69, 212-221.
- PARK, K.-J., JUNG, H.-G., KUO, L.-Y., KAGHAZCHI, P., YOON, C. S. & SUN, Y.-K. 2018. Improved Cycling Stability of Li[Ni_{0.90}Co_{0.05}Mn_{0.05}]O₂ Through Microstructure Modification by Boron Doping for Li-Ion Batteries. *Advanced Energy Materials*, 8, 1801202.
- PAYANDEH, S., GOONETILLEKE, D., BIANCHINI, M., JANEK, J. & BREZESINSKI, T. 2021. Single versus poly-crystalline layered oxide cathode materials for solid-state battery applications - a short review article. *Current Opinion in Electrochemistry*.
- PINSON, M. B. & BAZANT, M. Z. 2012. Theory of SEI Formation in Rechargeable Batteries: Capacity Fade, Accelerated Aging and Lifetime Prediction. *Journal of The Electrochemical Society*, 160, A243-A250.
- POURAGHAJAN, F., THOMPSON, A. I., HUNTER, E. E., MAZZEO, B., CHRISTENSEN, J., SUBBARAMAN, R., WRAY, M. & WHEELER, D. 2021. The effects of cycling on ionic and electronic conductivities of Li⁻ion battery electrodes. *Journal of Power Sources*, 492, 229636.
- QIAO, D., WANG, G., GAO, T., WEN, B. & DAI, T. 2021. Potential impact of the end-of-life batteries recycling of electric vehicles on lithium demand in China: 2010–2050. *Science of The Total Environment*, 764, 142835.
- QIU, L., ZHANG, M., SONG, Y., XIAO, Y., WU, Z., XIANG, W., LIU, Y., WANG, G., SUN, Y., ZHANG, J., ZHANG, B. & GUO, X. 2021. Recent advance in structure regulation of high-capacity Ni-rich layered oxide cathodes. *EcoMat*, 3.
- RADIN, M. D., HY, S., SINA, M., FANG, C., LIU, H., VINCKEVICIUTE, J., ZHANG, M., WHITTINGHAM, M. S., MENG, Y. S. & VAN DER VEN, A. 2017. Narrowing the Gap between Theoretical and Practical Capacities in Li-Ion Layered Oxide Cathode Materials. *Advanced Energy Materials*, 7, 1602888.
- RAN, A., CHEN, S., CHENG, M., LIANG, Z., LI, B., ZHOU, G., KANG, F., ZHANG, X. & WEI, G. 2022. A single-crystal nickel-rich material as a highly stable cathode for lithium-ion batteries. *Journal of Materials Chemistry A*, 10, 19680-19689.
- REN, D., YANG, Y., SHEN, L., ZENG, R. & ABRUÑA, H. D. 2020. Ni-rich LiNi_{0.88}Mn_{0.06}Co_{0.06}O₂ cathode interwoven by carbon fiber with improved rate capability and stability. *Journal of Power Sources*, 447.
- ROITZHEIM, C., KUO, L.-Y., SOHN, Y. J., FINSTERBUSCH, M., MÖLLER, S., SEBOLD, D., VALENCIA, H., MELEDINA, M., MAYER, J., BREUER, U., KAGHAZCHI, P., GUILLON, O. & FATTAKHOVA-ROHLFING, D. 2021. Boron in Ni-Rich NCM811 Cathode Material: Impact on Atomic and Microscale Properties. *ACS Applied Energy Materials*, 5, 524-538.
- ROMÁN-TEJEDA, A. & PFEIFFER, H. 2012. $\alpha \rightarrow \gamma$ Lithium borate phase transition produced during the CO₂ chemisorption process. *Journal of Thermal Analysis and Calorimetry*, 110, 807-811.
- ROSLOVA, M., HUANG, Z. & ZOU, X. 2023. Structural studies of inorganic materials by electron crystallography. *Comprehensive Inorganic Chemistry III*.
- ROTH, D. H. D. A. E. P. 2012. A General Discussion of Li Ion Battery Safety. *Electrochemical Society Interface*.
- ROUGIER, A., SAADOUNE, I., GRAVEREAU, P., WILLMANN, P. & DELMASA, C. 1996. Effect of cobalt substitution on cationic distribution in LiNi_{1-y}Co_yO₂ electrode materials. *Solid State*

Ionics, 90, 83-90.

- RYU, H.-H., NAMKOONG, B., KIM, J.-H., BELHAROUAK, I., YOON, C. S. & SUN, Y.-K. 2021. Capacity Fading Mechanisms in Ni-Rich Single-Crystal NCM Cathodes. *ACS Energy Letters*, 6, 2726-2734.
- RYU, H.-H., PARK, N.-Y., YOON, D. R., KIM, U.-H., YOON, C. S. & SUN, Y.-K. 2020. New Class of Ni-Rich Cathode Materials Li[Ni_xCo_yB_{1-x-y}]O₂ for Next Lithium Batteries. *Advanced Energy Materials*, 10, 2000495.
- SCHULZ, N., HAUSBRAND, R., WITTICH, C., DIMESSO, L. & JAEGERMANN, W. 2018. XPS-Surface Analysis of SEI Layers on Li-Ion Cathodes: Part II. SEI-Composition and Formation inside Composite Electrodes. *Journal of The Electrochemical Society*, 165, A833-A846.
- SEIDL, L., MARTENS, S., MA, J., STIMMING, U. & SCHNEIDER, O. 2016. In situ scanning tunneling microscopy studies of the SEI formation on graphite electrodes for Li⁺-ion batteries. *Nanoscale*, 8, 14004-14014.
- SHANNON, R. D. 1976. Revised effective ionic radii and systematic studies of interatomic distances in halides and chalcogenides. *Acta Crystallographica Section A*, 32, 751-767.
- SHARIFI-ASL, S., LU, J., AMINE, K. & SHAHBAZIAN-YASSAR, R. 2019. Oxygen Release Degradation in Li-Ion Battery Cathode Materials: Mechanisms and Mitigating Approaches. *Advanced Energy Materials*, 9, 1900551.
- SHEN, L., DU, F., ZHOU, Q., XU, T., FAN, Z., WEN, Y., WANG, J., WU, J. & ZHENG, J. 2023. Cobalt-free nickel-rich cathode materials based on Al/Mg co-doping of LiNiO₂ for lithium ion battery. *Journal of Colloid and Interface Science*, 638, 281-290.
- SHEPARD, J. 2021. *How to read battery discharge curves* [Online]. Available: <https://www.batterypowertips.com/how-to-read-battery-discharge-curves-faq/> [Accessed].
- SHUAI, C., DUAN, S., GAO, D., WU, P., GAO, C., YANG, Y., LIU, L., YUAN, F., YANG, S. & FENG, P. 2017. Mechanically Strong CaSiO₃ Scaffolds Incorporating B₂O₃-ZnO Liquid Phase. *Applied Sciences*, 7.
- SILBERNAGEL, B. G. & WHITTINGHAM, M. S. 1976. An NMR study of the alkali metal intercalation phase Li_xTiS₂: Relation to structure, thermodynamics, and ionicity. *The Journal of Chemical Physics*, 64, 3670-3673.
- SOCIETY, A. C. 2022. *Common Solvents Used in Organic Chemistry: Table of Properties* [Online]. Available: <https://organicchemistrydata.org/solvents/> [Accessed].
- SONG, M., KWON, I., KIM, H., SHIM, S. & MUMM, D. R. 2006. Synthesis of LiNiO₂ cathode by the combustion method. *Journal of Applied Electrochemistry*, 36, 801-805.
- SONG, Y., CUI, Y., LI, B., GENG, L., YAN, J., ZHU, D., ZHOU, P., ZHOU, J., YAN, Z., XUE, Q., TANG, Y. & XING, W. 2023. Revealing the origin of high-thermal-stability of single-crystal Ni-rich cathodes toward higher-safety batteries. *Nano Energy*, 116, 108846.
- SU, Y., LI, L., CHEN, G., CHEN, L., LI, N., LU, Y., BAO, L., CHEN, S. & WU, F. 2021. Strategies of Removing Residual Lithium Compounds on the Surface of Ni-Rich Cathode Materials†. *Chinese Journal of Chemistry*, 39, 189-198.
- SU, Y., LI, L., CHEN, L., WANG, L., LU, Y., ZHANG, Q., BAO, L. & WU, F. 2022. Enhanced Electrochemical Performance of Ni-Rich Cathode Materials with an In Situ-Formed LiBO₂/B₂O₃ Hybrid Coating Layer. *ACS Applied Energy Materials*, 5, 2231-2241.
- SUGUMARAN, G. & AMUTHA PRABHA, N. 2023. A Comprehensive Review of Various Topologies

- and Control Techniques for DC-DC Converter-Based Lithium-Ion Battery Charge Equalization. *International Transactions on Electrical Energy Systems*, 2023, 3648488.
- SUN, H. & ZHAO, K. 2017. Electronic Structure and Comparative Properties of $\text{LiNi}_x\text{Mn}_y\text{Co}_z\text{O}_2$ Cathode Materials. *The Journal of Physical Chemistry C*, 121, 6002-6010.
- SUN, H. H., RYU, H.-H., KIM, U.-H., WEEKS, J. A., HELLER, A., SUN, Y.-K. & MULLINS, C. B. 2020. Beyond Doping and Coating: Prospective Strategies for Stable High-Capacity Layered Ni-Rich Cathodes. *ACS Energy Letters*, 5, 1136-1146.
- SUN, L., ZHU, L., MI, C., HAN, E., SHANG, M. & ZENG, Z. 2019. The effects of Cr substitution on $\text{LiNi}_{0.65}\text{Co}_{0.1}\text{Mn}_{0.25}\text{O}_2$ for lithium-ion batteries. *Ionics*, 25, 3021-3030.
- SUN, X. 2015. *Development and Characterization of Nano-Structured LiFePO_4 Cathode and $\text{Li}_4\text{Ti}_5\text{O}_{12}$ Anode Materials for High-Performance Li-Ion Battery*. UWSpace.
- SUSAI, F. A., SCLAR, H., SHILINA, Y., PENKI, T. R., RAMAN, R., MADDUKURI, S., MAITI, S., HALALAY, I. C., LUSKI, S., MARKOVSKY, B. & AURBACH, D. 2018. Horizons for Li-Ion Batteries Relevant to Electro-Mobility: High-Specific-Energy Cathodes and Chemically Active Separators. *Advanced Materials*, 30, 1801348.
- SYBIL PAN, Z. L., AND YIWEN JU. 2023. *LFP batteries extend dominance over NCM batteries in China* [Online]. Available: <https://www.fastmarkets.com/insights/lfp-batteries-extend-dominance-over-ncm-batteries-china/#:~:text=LFP%20batteries%20accounted%20for%2065.81%25%20of%20China%E2%80%99s%20total,total%20production%20and%20NCM%2038.77%25%2C%20according%20to%20CA&BIA>. [Accessed].
- TANG, M., YANG, J., CHEN, N., ZHU, S., WANG, X., WANG, T., ZHANG, C. & XIA, Y. 2019. Overall structural modification of a layered Ni-rich cathode for enhanced cycling stability and rate capability at high voltage. *Journal of Materials Chemistry A*, 7, 6080-6089.
- TARASCON, J. M. & ARMAND, M. 2001. Issues and challenges facing rechargeable lithium batteries. *Nature*, 414, 359-367.
- TIAN, J., SU, Y., WU, F., XU, S., CHEN, F., CHEN, R., LI, Q., LI, J., SUN, F. & CHEN, S. 2015. High-Rate and Cycling-Stable Nickel-Rich Cathode Materials with Enhanced Li^+ Diffusion Pathway. *ACS Applied Materials & Interfaces*, 8, 582-587.
- TONG, F. & AZEVEDO, I. M. L. 2020. What are the best combinations of fuel-vehicle technologies to mitigate climate change and air pollution effects across the United States? *Environmental Research Letters*, 15, 074046.
- VENKATRAMAN, S., SHIN, Y. & MANTHIRAM, A. 2003. Phase Relationships and Structural and Chemical Stabilities of Charged $\text{Li}_{1-x}\text{CoO}_{2-\delta}$ and $\text{Li}_{1-x}\text{Ni}_{0.85}\text{Co}_{0.15}\text{O}_{2-\delta}$ Cathodes. *Electrochemical and Solid-State Letters*, 6.
- VIJI, M., SWAIN, P., MOCHERLA, P. S. V. & SUDAKAR, C. 2016. High-rate capability of bamboo-like single crystalline LiFePO_4 nanotubes with an easy access to b-axis 1D channels of olivine structure. *RSC Advances*, 6, 39710-39717.
- WANG, D., KOU, R., REN, Y., SUN, C.-J., ZHAO, H., ZHANG, M.-J., LI, Y., HUQ, A., KO, J. Y. P., PAN, F., SUN, Y.-K., YANG, Y., AMINE, K., BAI, J., CHEN, Z. & WANG, F. 2017. Synthetic Control of Kinetic Reaction Pathway and Cationic Ordering in High-Ni Layered Oxide Cathodes. *Advanced Materials*, 29, 1606715.
- WANG, J., LEI, X., GU, L., WANG, X. & SU, D. 2022. Structure modification of Ni-rich layered oxide cathode toward advanced lithium-ion batteries. *Journal of Materials Research*, 37, 3250-

3268.

- WANG, L., LIU, G., DING, X., ZHAN, C. & WANG, X. 2019a. Simultaneous Coating and Doping of a Nickel-Rich Cathode by an Oxygen Ion Conductor for Enhanced Stability and Power of Lithium-Ion Batteries. *ACS applied materials & interfaces*, 11, 33901-33912.
- WANG, L., SU, Q., HAN, B., SHI, W., DU, G., WANG, Y., LI, H., GU, L., ZHAO, W., DING, S., ZHANG, M., YANG, Y. & XU, B. 2023. Unraveling the degradation mechanism of $\text{LiNi}_0.8\text{Co}_0.1\text{Mn}_0.1\text{O}_2$ at the high cut-off voltage for lithium ion batteries. *Journal of Energy Chemistry*, 77, 428-437.
- WANG, Q., MAO, B., STOLIAROV, S. I. & SUN, J. 2019b. A review of lithium ion battery failure mechanisms and fire prevention strategies. *Progress in Energy and Combustion Science*, 73, 95-131.
- WANG, Y., REN, D., FENG, X., WANG, L. & OUYANG, M. 2021. Thermal kinetics comparison of delithiated $\text{Li}[\text{Ni}_x\text{Co}_y\text{Mn}_{1-x-y}]\text{O}_2$ cathodes. *Journal of Power Sources*, 514, 230582.
- WATANABE, S., KINOSHITA, M., HOSOKAWA, T., MORIGAKI, K. & NAKURA, K. 2014. Capacity fade of $\text{LiAl}_y\text{Ni}_{1-x-y}\text{Co}_x\text{O}_2$ cathode for lithium-ion batteries during accelerated calendar and cycle life tests (surface analysis of $\text{LiAl}_y\text{Ni}_{1-x-y}\text{Co}_x\text{O}_2$ cathode after cycle tests in restricted depth of discharge ranges). *Journal of Power Sources*, 258, 210-217.
- WEIGEL, T., SCHIPPER, F., ERICKSON, E. M., SUSAI, F. A., MARKOVSKY, B. & AURBACH, D. 2019. Structural and Electrochemical Aspects of $\text{LiNi}_0.8\text{Co}_0.1\text{Mn}_0.1\text{O}_2$ Cathode Materials Doped by Various Cations. *ACS Energy Letters*, 4, 508-516.
- WHITTINGHAM, M. S. 1976a. Electrical Energy Storage and Intercalation Chemistry. *Science*, 192, 1126.
- WHITTINGHAM, M. S. 1976b. The Role of Ternary Phases in Cathode Reactions. *Journal of The Electrochemical Society*, 123, 315-320.
- WOLFMAN, M., WANG, X., GARCIA, J. C., BARAI, P., STUBBS, J. E., ENG, P. J., KAHVECIOGLU, O., KINNIBRUGH, T. L., MADSEN, K. E., IDDIR, H., SRINIVASAN, V. & FISTER, T. T. 2022. The Importance of Surface Oxygen for Lithiation and Morphology Evolution during Calcination of High-Nickel NMC Cathodes. *Advanced Energy Materials*, 12.
- WU, F., LI, Q., CHEN, L., ZHANG, Q., WANG, Z., LU, Y., BAO, L., CHEN, S. & SU, Y. 2019a. Improving the Structure Stability of $\text{LiNi}_0.8\text{Co}_0.1\text{Mn}_0.1\text{O}_2$ by Surface Perovskite-like $\text{La}_2\text{Ni}_0.5\text{Li}_0.5\text{O}_4$ Self-Assembling and Subsurface $\text{La}(3+)$ Doping. *ACS Appl Mater Interfaces*, 11, 36751-36762.
- WU, F., TIAN, J., SU, Y., GUAN, Y., JIN, Y., WANG, Z., HE, T., BAO, L. & CHEN, S. 2014. Lithium-active molybdenum trioxide coated $\text{LiNi}_0.5\text{Co}_0.2\text{Mn}_0.3\text{O}_2$ cathode material with enhanced electrochemical properties for lithium-ion batteries. *Journal of Power Sources*, 269, 747-754.
- WU, F., TIAN, J., SU, Y., WANG, J., ZHANG, C., BAO, L., HE, T., LI, J. & CHEN, S. 2015. Effect of Ni^{2+} Content on Lithium/Nickel Disorder for Ni-Rich Cathode Materials. *ACS Applied Materials & Interfaces*, 7, 7702-7708.
- WU, K., LI, Q., DANG, R., DENG, X., CHEN, M., LEE, Y. L., XIAO, X. & HU, Z. 2019b. A novel synthesis strategy to improve cycle stability of $\text{LiNi}_0.8\text{Mn}_0.1\text{Co}_0.1\text{O}_2$ at high cut-off voltages through core-shell structuring. *Nano Research*, 12, 2460-2467.
- WU, L., KORYTTSEVA, A., GROß, C. B. M. & NAVROTSKY, A. 2019c. Thermochemical investigation of lithium borate glasses and crystals. *Journal of the American Ceramic Society*, 102, 4538-

4545.

- WU, X., MA, J., WANG, J., ZHANG, X., ZHOU, G. & LIANG, Z. 2022. Progress, Key Issues, and Future Prospects for Li-Ion Battery Recycling. *Global Challenges*, 6, 2200067.
- XIA, S., MU, L., XU, Z., WANG, J., WEI, C., LIU, L., PIANETTA, P., ZHAO, K., YU, X., LIN, F. & LIU, Y. 2018a. Chemomechanical interplay of layered cathode materials undergoing fast charging in lithium batteries. *Nano Energy*, 53, 753-762.
- XIA, Y., CHEN, A., WANG, K., MAO, Q., HUANG, H., ZHANG, J., HE, X., GAN, Y., XIAO, Z. & ZHANG, W. 2022. Industrial modification comparison of Ni-Rich cathode materials towards enhanced surface chemical stability against ambient air for advanced lithium-ion batteries. *Chemical Engineering Journal*, 450.
- XIA, Y., ZHENG, J., WANG, C. & GU, M. 2018b. Designing principle for Ni-rich cathode materials with high energy density for practical applications. *Nano Energy*, 49, 434-452.
- XIAO, J., LI, Q., BI, Y., CAI, M., DUNN, B., GLOSSMANN, T., LIU, J., OSAKA, T., SUGIURA, R., WU, B., YANG, J., ZHANG, J.-G. & WHITTINGHAM, M. S. 2020. Understanding and applying coulombic efficiency in lithium metal batteries. *Nature Energy*, 5, 561-568.
- XIAO, P., LI, W., CHEN, S., LI, G., DAI, Z., FENG, M., CHEN, X. & YANG, W. 2022. Effects of Oxygen Pressurization on Li⁺/Ni²⁺ Cation Mixing and the Oxygen Vacancies of LiNi_{0.8}Co_{0.15}Al_{0.05}O₂ Cathode Materials. *ACS Applied Materials & Interfaces*, 14, 31851-31861.
- XIE, Q., LI, W., DOLOCAN, A. & MANTHIRAM, A. 2019. Insights into Boron-Based Polyanion-Tuned High-Nickel Cathodes for High-Energy-Density Lithium-Ion Batteries. *Chemistry of Materials*, 31, 8886-8897.
- XIN, F., GOEL, A., CHEN, X., ZHOU, H., BAI, J., LIU, S., WANG, F., ZHOU, G. & WHITTINGHAM, M. S. 2022. Electrochemical Characterization and Microstructure Evolution of Ni-Rich Layered Cathode Materials by Niobium Coating/Substitution. *Chemistry of Materials*, 34, 7858-7866.
- XU, C., REEVES, P. J., JACQUET, Q. & GREY, C. P. 2020. Phase Behavior during Electrochemical Cycling of Ni-Rich Cathode Materials for Li-Ion Batteries. *Advanced Energy Materials*, 11.
- XU, J., HU, E., NORDLUND, D., MEHTA, A., EHRLICH, S. N., YANG, X.-Q. & TONG, W. 2016. Understanding the Degradation Mechanism of Lithium Nickel Oxide Cathodes for Li-Ion Batteries. *ACS applied materials & interfaces*, 8, 31677-31683.
- XU, X., HUO, H., JIAN, J., WANG, L., ZHU, H., XU, S., HE, X., YIN, G., DU, C. & SUN, X. 2019. Radially Oriented Single-Crystal Primary Nanosheets Enable Ultrahigh Rate and Cycling Properties of LiNi_{0.8}Co_{0.1}Mn_{0.1}O₂ Cathode Material for Lithium-Ion Batteries. *Advanced Energy Materials*, 9.
- XUE, R., LIU, N., BAO, L., CHEN, L., SU, Y., LU, Y., DONG, J., CHEN, S. & WU, F. 2020. UiO-66 type metal-organic framework as a multifunctional additive to enhance the interfacial stability of Ni-rich layered cathode material. *Journal of Energy Chemistry*, 50, 378-386.
- YAN, P., ZHENG, J., GU, M., XIAO, J., ZHANG, J.-G. & WANG, C.-M. 2017. Intragranular cracking as a critical barrier for high-voltage usage of layer-structured cathode for lithium-ion batteries. *Nature Communications*, 8, 14101.
- YAN, W., YANG, S., HUANG, Y., YANG, Y. & GUOHUI, Y. 2020. A review on doping/coating of nickel-rich cathode materials for lithium-ion batteries. *Journal of Alloys and Compounds*, 819.
- YANG, H., WU, H.-H., GE, M., LI, L., YUAN, Y., YAO, Q., CHEN, J., XIA, L., ZHENG, J., CHEN, Z., DUAN,

- J., KISSLINGER, K., ZENG, X. C., LEE, W.-K., ZHANG, Q. & LU, J. 2019. Simultaneously Dual Modification of Ni-Rich Layered Oxide Cathode for High-Energy Lithium-Ion Batteries. *Advanced Functional Materials*, 29, 1808825.
- YANG, J., LIANG, X., RYU, H.-H., YOON, C. S. & SUN, Y.-K. 2023. Ni-rich layered cathodes for lithium-ion batteries: From challenges to the future. *Energy Storage Materials*, 63.
- YANG, J. & XIA, Y. 2016. Suppressing the Phase Transition of the Layered Ni-Rich Oxide Cathode during High-Voltage Cycling by Introducing Low-Content Li₂MnO₃. *ACS Applied Materials & Interfaces*, 8, 1297-1308.
- YANG, S.-J., HU, J.-K., JIANG, F.-N., YUAN, H., PARK, H. S. & HUANG, J.-Q. 2024. Safer solid-state lithium metal batteries: Mechanisms and strategies. *InfoMat*, 6, e12512.
- YE, Z., QIU, L., YANG, W., WU, Z., LIU, Y., WANG, G., SONG, Y., ZHONG, B. & GUO, X. 2021. Nickel-Rich Layered Cathode Materials for Lithium-Ion Batteries. *Chemistry*, 27, 4249-4269.
- YIN, J., ZHOU, G., GAO, X., CHEN, J., ZHANG, L., XU, J., ZHAO, P. & GAO, F. 2019. alpha- and beta-Phase Ni-Mg Hydroxide for High Performance Hybrid Supercapacitors. *Nanomaterials (Basel)*, 9.
- YIN, S., DENG, W., CHEN, J., GAO, X., ZOU, G., HOU, H. & JI, X. 2021. Fundamental and solutions of microcrack in Ni-rich layered oxide cathode materials of lithium-ion batteries. *Nano Energy*, 83, 105854.
- YOON, C. S., JUN, D.-W., MYUNG, S.-T. & SUN, Y.-K. 2017. Structural Stability of LiNiO₂ Cycled above 4.2 V. *ACS Energy Letters*, 2, 1150-1155.
- YOON, M., DONG, Y., HUANG, Y., WANG, B., KIM, J., PARK, J.-S., HWANG, J., PARK, J., KANG, S. J., CHO, J. & LI, J. 2023. Eutectic salt-assisted planetary centrifugal deagglomeration for single-crystalline cathode synthesis. *Nature Energy*, 8, 482-491.
- YOON, M., DONG, Y., HWANG, J., SUNG, J., CHA, H., AHN, K., HUANG, Y., KANG, S. J., LI, J. & CHO, J. 2021. Reactive boride infusion stabilizes Ni-rich cathodes for lithium-ion batteries. *Nature Energy*, 6, 362-371.
- YOSHINO, A. 2013. リチウムイオン電池総論. *ぶんせき*, 580-584.
- YOSHINO, A. 2014. 1 - Development of the Lithium-Ion Battery and Recent Technological Trends. In: PISTOIA, G. (ed.) *Lithium-Ion Batteries*. Amsterdam: Elsevier.
- YU, Z., QU, X., WAN, T., DOU, A., ZHOU, Y., PENG, X., SU, M., LIU, Y. & CHU, D. 2020. Synthesis and Mechanism of High Structural Stability of Nickel-Rich Cathode Materials by Adjusting Li-Excess. *ACS Appl Mater Interfaces*, 12, 40393-40403.
- YUWONO, R. A., WANG, F.-M., WU, N.-L., CHEN, Y.-C., CHEN, H., CHEN, J.-M., HAW, S.-C., LEE, J.-F., XIE, R.-K., SHEU, H.-S., CHANG, P.-Y., KHOTIMAH, C., MERINDA, L. & HSING, R. 2023. Evaluation of LiNiO₂ with minimal cation mixing as a cathode for Li-ion batteries. *Chemical Engineering Journal*, 456, 141065.
- ZHANG, C., JIANG, W., HE, W. & WEI, W. 2021a. Heteroepitaxial interface of layered cathode materials for lithium ion batteries. *Energy Storage Materials*, 37, 161-189.
- ZHANG, D., LIU, Y., WU, L., FENG, L., JIN, S., ZHANG, R. & JIN, M. 2019a. Effect of Ti ion doping on electrochemical performance of Ni-rich LiNi_{0.8}Co_{0.1}Mn_{0.1}O₂ cathode material. *Electrochimica Acta*, 328.
- ZHANG, H., XU, J. & ZHANG, J. 2019b. Surface-Coated LiNi_{0.8}Co_{0.1}Mn_{0.1}O₂ (NCM811) Cathode Materials by Al₂O₃, ZrO₂, and Li₂O-2B₂O₃ Thin-Layers for Improving the Performance of Lithium Ion Batteries. *Frontiers in Materials*, 6.

- ZHANG, J.-N., LI, Q., WANG, Y., ZHENG, J., YU, X. & LI, H. 2018a. Dynamic evolution of cathode electrolyte interphase (CEI) on high voltage LiCoO₂ cathode and its interaction with Li anode. *Energy Storage Materials*, 14, 1-7.
- ZHANG, J., WU, F., DAI, X., MAI, Y. & GU, Y. 2021b. Enhancing the High-Voltage Cycling Performance and Rate Capability of LiNi_{0.8}Co_{0.1}Mn_{0.1}O₂ Cathode Material by Codoping with Na and Br. *ACS Sustainable Chemistry & Engineering*, 9, 1741-1753.
- ZHANG, S. S. 2020. Problems and their origins of Ni-rich layered oxide cathode materials. *Energy Storage Materials*, 24, 247-254.
- ZHANG, W., WANG, L., WANG, L. & LIAO, C. 2020. An approximate solution of lithium ion diffusion process in spherical active particles with controllable error. *Solid State Ionics*, 358, 115501.
- ZHANG, X.-Q., CHEN, X., CHENG, X.-B., LI, B.-Q., SHEN, X., YAN, C., HUANG, J.-Q. & ZHANG, Q. 2018b. Highly Stable Lithium Metal Batteries Enabled by Regulating the Solvation of Lithium Ions in Nonaqueous Electrolytes. *Angewandte Chemie International Edition*, 57, 5301-5305.
- ZHANG, X., XIONG, J., CHANG, F., XU, Z., WANG, Z., HALL, P., CHENG, Y. J. & XIA, Y. 2022. Sol/Antisolvent Coating for High Initial Coulombic Efficiency and Ultra-stable Mechanical Integrity of Ni-Rich Cathode Materials. *ACS Appl Mater Interfaces*, 14, 45272-45288.
- ZHANG, X. D., SHI, J. L., LIANG, J. Y., WANG, L. P., YIN, Y. X., JIANG, K. C. & GUO, Y. G. 2019c. An Effective LiBO₂ Coating to Ameliorate the Cathode/Electrolyte Interfacial Issues of LiNi_{0.6}Co_{0.2}Mn_{0.2}O₂ in Solid-State Li Batteries. *Journal of Power Sources*, 426, 242-249.
- ZHAO, S., MA, J., XU, R., LIN, X., CHENG, X., HAO, S., ZHAO, X., DENG, C. & LIU, B. 2019. Synthesis and Characterization of Zirconium Nitride Nanopowders by Internal Gelation and Carbothermic Nitridation. *Scientific Reports*, 9, 19199.
- ZHAO, W., ZHANG, H. & YANG, H. 2022a. Improving the electrochemical performance of Ni-rich LiNi_{0.6}Co_{0.2}Mn_{0.2}O₂ cathode at high cutoff voltage coated with LiBO₂. *Ionics*, 28, 5015-5024.
- ZHAO, W., ZOU, L., ZHANG, L., FAN, X., ZHANG, H., PAGANI, F., BRACK, E., SEIDL, L., OU, X., EGOROV, K., GUO, X., HU, G., TRABESINGER, S., WANG, C. & BATTAGLIA, C. 2022b. Assessing Long-Term Cycling Stability of Single-Crystal Versus Polycrystalline Nickel-Rich NCM in Pouch Cells with 6 mAh cm⁻² Electrodes. *Small*, 18.
- ZHENG, J., MYEONG, S., CHO, W., YAN, P., XIAO, J., WANG, C., CHO, J. & ZHANG, J.-G. 2017. Li- and Mn-Rich Cathode Materials: Challenges to Commercialization. *Advanced Energy Materials*, 7, 1601284.
- ZHENG, J., YAN, P., ESTEVEZ, L., WANG, C. & ZHANG, J.-G. 2018. Effect of calcination temperature on the electrochemical properties of nickel-rich LiNi_{0.76}Mn_{0.14}Co_{0.10}O₂ cathodes for lithium-ion batteries. *Nano Energy*, 49, 538-548.
- ZHOU, J., HAN, Z., ZHANG, Y., ZHU, A., HE, X., WU, H., CHEN, X., WANG, Q. & ZHANG, Y. 2021. Design and host-involved in situ fabrication of La₄NiLiO₈ coating on Ni-rich cathode materials towards superior structural stability. *Journal of Materials Chemistry A*, 9, 3427-3440.
- ZHU, H., WANG, Z., CHEN, L., HU, Y., JIANG, H. & LI, C. 2022. Strain Engineering of Ni-Rich Cathode Enables Exceptional Cyclability in Pouch-Type Full Cells. *Advanced Materials*, 35.
- ZUBI, G., DUFO-LÓPEZ, R., CARVALHO, M. & PASAOGLU, G. 2018. The lithium-ion battery: State of the art and future perspectives. *Renewable and Sustainable Energy Reviews*, 89, 292-

308.

ZUO, D., TIAN, G., LI, X., CHEN, D. & SHU, K. 2017. Recent progress in surface coating of cathode materials for lithium ion secondary batteries. *Journal of Alloys and Compounds*, 706, 24-40.